The effect of the bacterial amyloid CsgA on enteroendocrine cell function and crosstalk with macrophages and enteric neurons: implications for Parkinson's disease

Dissertation

zur Erlangung des Grades eines Doktors der Naturwissenschaften

der Mathematisch-Naturwissenschaftlichen Fakultät

und

der Medizinischen Fakultät

der Eberhard-Karls-Universität Tübingen

vorgelegt

von

Fokion Spanos

aus Thessaloniki, Griechenland

2026

Tag der mündlichen Prüfung: 13-10-2026

Dekan der Math.-Nat. Fakultät: Prof. Dr. Thilo Stehle

Dekanin der Medizinischen Fakultät: Prof. Dr. Sara Y. Brucker

1. Berichterstatter: PD Dr. Christian Johannes Gloeckner

2. Berichterstatter: Dr. Dr. Michela Deleidi

Prüfungskommission: Dr. Dr. Michela Deleidi
PD Dr. Christian Johannes Gloeckner
Prof. Dr. Eric Kemen
Prof. Dr. Lisa Maier

Erklärung / Declaration:

Ich erkläre, dass ich die zur Promotion eingereichte Arbeit mit dem Titel: „ The effect of the bacterial amyloid CsgA on enteroendocrine cell function and crosstalk with macrophages and enteric neurons: implications for Parkinson's disease " selbständig verfasst, nur die angegebenen Quellen und Hilfsmittel benutzt und wörtlich oder inhaltlich übernommene Stellen als solche gekennzeichnet habe. Ich versichere an Eides statt, dass diese Angaben wahr sind und dass ich nichts verschwiegen habe. Mir ist bekannt, dass die falsche Abgabe einer Versicherung an Eides statt mit Freiheitsstrafe bis zu drei Jahren oder mit Geldstrafe bestraft wird.

I hereby declare that I have produced the work entitled "The effect of the bacterial amyloid CsgA on enteroendocrine cell function and crosstalk with macrophages and enteric neurons: implications for Parkinson's disease", submitted for the award of a doctorate, on my own (without external help), have used only the sources and aids indicated and have marked passages included from other works, whether verbatim or in content, as such. I swear upon oath that these statements are true and that I have not concealed anything. I am aware that making a false declaration under oath is punishable by a term of imprisonment of up to three years or by a fine.

Tübingen, den ....

Datum / Date Unterschrift /Signature

Content

Statement of contribution……..8

Personal contributions……..8

Contributions of others……..8

1 Summary……...9

1.1 Zusammenfassung……..9

1.2 Summary……11

2 Introduction……13

2.1 Parkinson's disease: α-synuclein aggregation and inflammation……...13

2.2 Gut microbiota and bacterial amyloids in Parkinson's disease……18

2.3 Enteroendocrine cells and their involvement in Parkinson's disease……22

2.4 Organelle and proteasome involvement in Parkinson's disease……23

2.4.1 Mitochondria……..23

2.4.2 Lysosomes and intracellular trafficking……..25

2.4.3 Proteasome……28

2.5 Extracellular vesicles and exosomes in intestinal homeostasis and α-SYN pathology propagation……...28

2.6 Microfluidics model systems in intestinal research……...30

3 Aim……..33

4 Materials & Methods……..34

4.1 CsgA cloning and sequencing……..34

4.1.1 CsgA cloning and bacterial transformation……..34

4.1.2 Polymerase Chain Reaction (PCR) ……..34

4.2 Protein purifications, processing, and labelling……...35

4.2.1 CsgA monomer purification……..35

4.2.2 Curli purification……..36

4.2.3 CsgA and Curli labelling……..36

4.2.4 A-SYN PFF generation……..36

4.2.5 A-SYN PFF and curli sonication……..37

4.3 Bacteria cultures……...37

4.3.1 *E. coli* culture for biofilm formation……..37

4.3.2 *E. coli*-HuTu-80 co-culture……...37
4.3.3 *E. coli* bacterial growth assay……..…….37
4.3.4 *A. muciniphila* culture……..…….38
4.4 Cell culture……..……38
4.4.1 HuTu-80 cell culture……..……...38
4.4.2 Colo-320DM cell culture ……..……38
4.4.3 THP-1 cell culture……..……39
4.4.4 Human iPSC and NPC maintenance……..……39
4.4.5 Embryonic body differentiation for macrophage precursor production…….39
4.4.6 Macrophage differentiation and treatments……..…….40
4.4.7 Peripheral neuron differentiation……..……..40
4.4.8 Peripheral neuron and macrophage co-culture……..……..41
4.4.9 Microfluidics peripheral neuron/enteroendocrine cell co-culture……41
4.4.10 Intestinal organoids……..…...41
4.4.11 Cell treatments……..……..42
4.4.12 HuTu-80-TMEM192-3xHA line generation……..……44
4.5 Characterization assays…….……..44
4.5.1 Thioflavin T (ThT) assay……..……44
4.5.2 Transmission electron microscopy (TEM) ……..……44
4.5.3 Nanoparticle Tracking Analysis (NTA) ……..……45
4.5.4 Coomassie staining……..……45
4.6 Experimental assays……..……..45
4.6.1 Extracellular vesicle purification……..……..…….45
4.6.2 A-SYN seed amplification assay……..……..46
4.6.3 Enzyme-linked immunosorbent Assay (ELISA)…….. ……46
4.6.4 Chemokine and cytokine multiplex measurements……..……46
4.6.5 TMEM192-3xHA Lysosomal Immunoprecipitation……..…….47
4.6.6 Western blot……..……47
4.6.7 Cell lysis for detergent-soluble/insoluble fractionation……..……..48
4.6.8 Seahorse……..……..49
4.6.9 Proteasome Assay……..……..49

4.6.10 Intestinal organoid fixation and cryosectioning……..……..49

4.6.11 Cell fixation and immunostaining……..50

4.6.12 Live cell imaging……..……50

4.6.13 Image quantification……..……51

4.6.14 Flow Cytometry……..……51

4.6.15 Fluorescence-activated cell sorting (FACS)…….. ……52

4.6.16 Quantitative Reverse Transcription Polymerase Chain Reaction (qRT-PCR)……..52

4.6.17 Glucocerebrosidase (GCase) Assay……..……..……...52

4.7 Proteomics……..……...53

4.7.1 TMT-based quantitative proteomics sample preparation……..……..……53

4.7.2 LC-MS/MS……..……...…53

4.7.3 Mass Spectrometry Data analysis…….……54

4.8 Statistics……..……...55

5 Results……..……..56

5.1 Part 1: CsgA as a trigger of intestinal Parkinson's disease……..……..56

5.1.1 Question 1: Do enteroendocrine cells uptake CsgA? ……..……..56

5.1.1.1 Cloning of CsgA-R12343 in pET-11d……..……...56

5.1.1.2 Purification and characterization of CsgA and curli……..……..58

5.1.1.3 Selection of HuTu-80 as an enteroendocrine cell model……..……59

5.1.1.4 CsgA is uptaken and localized to the lysosomes of HuTu-80 cells……..…….60

5.1.2 Question 2: How do enteroendocrine cells respond to CsgA?…….. ……66

5.1.2.1 Generation and characterization of the HuTu-80-TMEM192-3xHA lyso-IP line..66

5.1.2.2 Proteomics analysis reveals cellular stress and altered intracellular trafficking in enteroendocrine cells upon CsgA-WT exposure……..…….67

5.1.2.3 CsgA-WT downregulates the expression of mitochondrial antioxidant proteins and complex subunit proteins, without affecting superoxide levels or mitochondrial respiration in enteroendocrine cells……....73

5.1.2.4 Reduction in HSP90 chaperone and proteasome subunit levels by CsgA-WT without an impact on chymotrypsin-like proteasome activity in enteroendocrine cells…74

5.1.2.5 CsgA-WT induces downregulation of lysosomal trafficking and upregulation of extracellular vesicle release in human enteroendocrine cells……78

5.1.3 Question 3: What is the immune response of enteroendocrine cells exposed to CsgA? ……..……..……...82

5.1.3.1 HuTu-80 upregulate chemokine secretion and antigen presentation upon CsgA-WT treatment, and their extracellular vesicles sustain macrophage cytokine release associated with immune exhaustion properties…… ……...82

5.1.4 Question 4: Can CsgA initiate α-SYN pathology in the human intestine?…….. ……86

5.1.4.1 CsgA does not provoke A-SYN aggregation in HuTu-80……..……..86

5.1.4.2 Extracellular vesicles from CsgA-WT-treated HuTu-80 induce α-SYN seeding competency in peripheral neuron and macrophages……..……..92

5.2 Part 2: Development of neuron-EEC models to monitor pathology propagation…….…….98

5.2.1 Human iPSC-derived intestinal organoids……..……..98

5.2.2 Human iPSC-derived peripheral neurons co-cultured with HuTu-80 in microfluidics chips……..……..100

6 Discussion……..……..103

6.1 The HuTu-80 response to CsgA and relevance for Parkinson's disease……..……..105

6.1.1 CsgA: lysosomes and intracellular trafficking……..……105

6.1.2 Gut bacterial products and Parkinson's disease……..……107

6.1.2.1 The bacterial-human amyloid cross-seeding: CsgA and α-SYN……..……107

6.1.2.2 Other bacterial metabolites that promote α-SYN aggregation: *A. muciniphila* secretome and nitric oxide……..……109

6.1.3 CsgA-mediated EEC immune response and macrophage activation……..……110

6.1.3.1 The immune response of enteroendocrine cells……..……110

6.1.3.2 The immune response of macrophages exposed to enteroendocrine cell extracellular vesicles……..……..112

6.1.3.3 The mechanistic pathway driving the immune response to CsgA.……113

6.1.4 Mitochondrial changes by CsgA in EECs……..……114

6.1.5 Bacterial amyloids in the human intestine……..……..116

6.2 Human intestinal organoids and the microfluidics co-culture system……..……117

6.3 Limitations of the study……..……119

6.4 Conclusion……..……120

7 Outlook……..……122

8 References……..……125

9 Appendix……..……150

10 Acknowledgements……..……159

Statement of contribution

The data related to mitochondrial subunit quantification by Western blot and MitoSOX intensity (Figures 12C-D) as well as the LysoTracker quantification (Figure 4E) were presented in the master's thesis of Anouk Kletz in 2025.

Personal contribution

I conducted most of the experiments and collected most of the data. I designed the experiments and performed data analysis with help and supervision from Michela Deleidi (MD). I prepared the figures and wrote the thesis draft. I received help for the following figures: for figure 2D, Katharina Hipp at Max Planck Institute of Tuebingen obtained images of the samples (left side) and Alain Schmitt at Institut Cochin obtained images shown on the right side of the panel; for Figure 2F, Federico Bertoli conducted the ELISA for the CsgA monomer samples; for Figure 4E, Anouk Kletz (AK) performed the lysosomal quantification; for figures 5E and 11D, AK developed the Western blots; for figures 8B-D and 9, Mandy Rettel ran the proteomics samples and Frank Stein (FrS) performed the proteomics analysis; figure 10 was generated by FrS ; for figure 11E, Ivan Nemazanyy at the SFR Metabolomic Analysis Facility performed the Seahorse Assay; for figures 12D and 15F, Malvina Dubroux (MD) developed the Western blots; for figure 14A, Karim Ourahmoun at the ICM.Quant Platform at the Institut du Cervau took the electron microscopy images; for figure 14E, Marie Maumus at the EVe facility at the IRMB run the nanoparticle tracking analysis; for figure 15B, MD performed one of the three replicates; for Figure 21A, Christin Weissleder performed the imaging; for Figures 23B-C, Matilde Bongianni at the University of Verona ran the the SAA assay; for Figure 22B, Jerome Megret performed the sorting; for figures 24B,D, AK took the images.

Contribution from others

MD supervised the doctoral project, acquired the funding for the position and the experimental work, and reviewed the thesis. FrS discussed the proteomics data produced by the facility. Bernd Gilsbach helped in the initial optimization of CsgA monomer purification and provided the Coomassie staining protocol. Daniel Otzen provided the pET-11d-CsgA-WT-6xHis plasmid. Matthew Chapman provided the *Escherichia coli* K12 WT and Δ*csgBAC* strains. Benoit Chassaing provided the *Akkermansia muciniphila* bacteria and Maeva Duquesnoy helped with their anaerobic culture. Ganna Panasyuk provided the pLJC5-Tmem192-3xHA lentivirus and Edouard Le Guillou the lyso-IP protocol. Graziella Cappelletti provided the α-SYN monomers.

1. Summary

Zusammenfassung

Zunehmende Hinweise deuten darauf hin, dass sich die Parkinson-Krankheit (PD) im Darm durch gastrointestinale Funktionsstörungen, eine Aggregation von α-SYN und Entzündungen manifestiert, die die Pathologie auf das zentrale Nervensystem übertragen. Insbesondere die bei PD-Patienten beobachtete veränderte Zusammensetzung der Darmmikrobiota ist ein aktives Forschungsgebiet, in dem deren Kausalität bei der Krankheitsentstehung untersucht wird. Während das funktionelle bakterielle Amyloid CsgA die PD-Pathologie in Tiermodellen beschleunigt, sind die zugrunde liegenden molekularen Mechanismen und die Relevanz für den menschlichen Darm bislang unbekannt. Wir stellten die Hypothese auf, dass CsgA von enteroendokrinen Zellen aufgenommen wird – also von Darmhormone freisetzenden Zellen, die als Sensoren zwischen dem Lumen und dem Wirt fungieren – und deren Funktion stört, wodurch eine Prädisposition für PD entsteht. Wir stellten die Hypothese auf, dass CsgA von enteroendokrinen Zellen aufgenommen wird, also von Darmhormone freisetzenden Zellen, die als Sensoren zwischen dem Lumen und dem Wirt fungieren, und deren Funktion stört, wodurch eine Prädisposition für die Krankheitspathologie entsteht. Unter Verwendung von HuTu-80-Enteroendokrinen Zellen, die mit CsgA-WT, CsgA-R12343 (nicht-amyloidogene Kontrolle) und Curli (reife CsgA-Fasern) behandelt wurden, untersuchten wir die CsgA-Aufnahme, proteomische Veränderungen, die α-SYN-Proteostase sowie die interzelluläre Kommunikation mit gewebsresidenten Neuronen und Makrophagen. CsgA-WT und Curli wurden von HuTu-80 aufgenommen und zur Degradation in die Lysosomen transportiert, wie durch Western-Blot-Analysen und Live-Cell-Imaging in Zellen gezeigt wurde, die mit den lysosomalen alkalisierenden Reagenzien Bafilomycin A1 und Chloroquin behandelt wurden. .Trotz der durch die bakteriellen Amyloide verursachten Veränderungen in Anzahl und Größe der Lysosomen zeigten sich keine Auswirkungen auf die Autophagie-Marker P62 und LC3B. Eine umfassende Bewertung der Reaktionen enteroendokriner Zellen auf CsgA erfolgte mittels Proteomanalyse in Ganzzell- und lysosomenangereicherten HuTu-80-Lysaten. Nur CsgA-WT, nicht jedoch CsgA-R12343 oder Curli, induzierte Veränderungen der Proteinkonzentrationen in Ganzzellen und Lysosomen. Konkret löste CsgA-WT Veränderungen in verschiedenen zellulären Komponenten aus, darunter Mitochondrien, Proteasom, Chaperone, Komponenten des intrazellulären Transports und die Freisetzung extrazellulärer Vesikel (EV). Dennoch gab es keinen signifikanten Einfluss auf die mitochondriale Atmung, die Superoxidspiegel oder die Proteasomaktivität, was darauf hindeutet, dass CsgA-WT nicht ausreicht, um diese zellulären Funktionen zu stören. Stattdessen wurden die lysosomalen Transportkomponenten DYNC1I2 und LAMP2 parallel zur lysosomalen α-SYN-

Bindung herunterreguliert. Dies ging mit einer erhöhten α-SYN-Freisetzung im Überstand und in den EVs einher, was auf einen veränderten α-SYN-Transport hindeutet. Die erhöhten CD63-Spiegel in den EVs und die erhöhten RAB27A-Spiegel in den Gesamtzelllysaten bestätigten zudem, dass HuTu-80 über den EV-Signalweg auf das bakterielle Amyloid CsgA-WT reagiert. Die damit einhergehende Hochregulation der HLA-DR-Oberflächenpräsentation sowie die Freisetzung der Chemokine IL-8 und MIP-1α deuteten auf die immunmodulatorischen Eigenschaften von HuTu-80 hin, das CsgA-WT ausgesetzt war. Interessanterweise verringerten die EV von mit CsgA behandelten HuTu-80-Zellen die Freisetzung der proinflammatorischen Zytokine IL-1β, IL-6 und IL-23 in Makrophagen im Vergleich zu den EV der Kontrollgruppe aus HuTu-80-Zellen. Makrophagen, die EV aus CsgA-behandelten HuTu-80-Zellen ausgesetzt waren, zeigten jedoch auch nach Entfernung der EV aus dem Überstand eine anhaltende Freisetzung von IL-1β, IL-6, TNFα und IL-10. In diesem Zusammenhang reagierten diese Makrophagen nicht auf einen sekundären LPS-Reiz, was darauf hindeutet, dass CsgA eine anhaltende Aktivierung und einen immunsuppressiven Zustand in Makrophagen induziert. Die EVs aus CsgA-WT-behandelten HuTu-80 förderten die α-SYN-Seed-Bildung sowohl in aus induzierten pluripotenten Stammzellen gewonnenen peripheren Neuronen als auch in Makrophagen, was die Rolle von EVs enteroendokriner Zellen in der α-SYN-Pathologie unterstreicht. Schließlich etablierten wir ein Mikrofluidik-Co-Kulturmodell aus EEC und peripheren Neuronen, das die Untersuchung der Auslösung und Ausbreitung der PD-Pathologie ermöglicht. Zusammenfassend liefern wir Belege für einen neuartigen Mechanismus, durch den CsgA die Proteostase enteroendokriner Zellen stört, um die Freisetzung von α-SYN auszulösen und eine anhaltende, jedoch erschöpfte Entzündungsreaktion zu fördern, die das langfristige Gleichgewicht der Mikrobiota und die intestinale Homöostase stören und so zu den frühen Stadien der PD-Pathologie beitragen könnte.

Summary

Burgeoning evidence suggests that Parkinson's disease (PD) manifests in the gut with gastrointestinal dysfunction, α-SYN aggregation, and inflammation propagating the pathology to the central nervous system. Particularly, the altered gut microbiota composition observed in PD patients is an active area of investigation with respect to studying its causality in disease pathogenesis. While the functional bacterial amyloid CsgA accelerates PD pathology in animal models, the underlying molecular mechanisms and relevance to the human intestine remain unknown. We hypothesized that CsgA is uptaken by enteroendocrine cells, gut hormone releasing cells acting as sensors between the lumen and the host, perturbing their function to predispose to PD. Using HuTu-80 enteroendocrine cells treated with CsgA-WT, CsgA-R12343 (non-amyloidogenic control), and curli (mature CsgA fibers), we evaluated CsgA uptake, proteomics changes, α-SYN proteostasis, and intercellular communication with tissue-resident neurons and macrophages. CsgA-WT and curli were uptaken by HuTu-80 and targeted to the lysosomes for degradation as shown by Western blot and live-cell imaging in cells treated with lysosomal alkalizing reagents bafilomycin A1 and chloroquine. Despite the changes in lysosomal number and size by the bacterial amyloids, there was no effect on the autophagy markers P62 and LC3B. Comprehensive evaluation of enteroendocrine cell responses to CsgA was achieved by proteomics analysis in whole-cell and lysosome-enriched HuTu-80 lysates. Only CsgA-WT, but not CsgA-R12343 or curli, induced whole-cell and lysosome protein level alterations. Specifically, CsgA-WT evoked changes in various cellular components including mitochondria, proteasome, chaperones, intracellular trafficking components, and extracellular vesicle (EV) release. Nonetheless, there was no robust effect on mitochondrial respiration, superoxide levels or proteasome activity, suggesting that CsgA-WT a is not sufficient to perturb these cellular functions. Instead, the lysosomal trafficking components DYNC1I2 and LAMP2 were downregulated alongside lysosomal α-SYN targeting. This was accompanied by elevated α-SYN release in the supernatant and EVs, implying altered α-SYN trafficking. The increased CD63 levels in EVs, and RAB27A levels in whole-cell lysates, further corroborated that HuTu-80 respond to the bacterial amyloid CsgA-WT via the EV pathway. The accompanied upregulation of HLA-DR surface exposure and IL-8 and MIP-1α chemokine release, indicated the immune-modulatory properties of HuTu-80 exposed to CsgA-WT. Interestingly, EVs from CsgA-treated HuTu-80 decreased IL-1β, IL-6, and IL-23 pro-inflammatory cytokine release in macrophages compared to control HuTu80 EVs. However, macrophages exposed to EVs from CsgA-treated HuTu-80 displayed sustained IL-1β, IL-6, TNFα, and IL-10 release even after removal of the EVs from the supernatant. In the same line, these macrophages did not respond to a secondary LPS stimulus, suggesting CsgA induces a sustained activation and immunosuppressed state in macrophages.

The EVs from CsgA-WT-treated HuTu-80 promoted α-SYN seed formation in both induced pluripotent stem cell-derived peripheral neurons and macrophages, highlighting the role of enteroendocrine cell EVs in α-SYN pathology. Finally, we established an EEC-peripheral neuron microfluidics co-culture model that permits investigation of PD pathology initiation and propagation. Conclusively, we provide evidence for a novel mechanism by which CsgA perturbs enteroendocrine cell proteostasis to trigger α-SYN release and promote a sustained yet exhausted inflammatory response which could disrupt long-term microbiota balance and intestinal homeostasis contributing to early stages of PD pathology.

Introduction

2.1 Parkinson's disease: α-synuclein aggregation and inflammation

PD is a complex movement disorder with increasing prevalence in the aging and aged population which is expected to reach 25 million people worldwide in the year 2050 [1]. The disease's complexity stems from the intricate interaction between genetics and the environment with age being the major risk factor [1-4]. Only 15% of the patients are familial, while the majority of PD is sporadic [5], denoting that there is not known genetic cause. PD patients develop a set of motor symptoms, such as tremors, bradykinesia, rigidity, and postural instability. These symptoms mark the late stages of the disease as they manifest after a significant loss of dopaminergic neurons in the substantia nigra pars compacta (SNpc) has occurred. At the histopathological level, patients exhibit intraneuronal inclusion bodies termed Lewy Bodies (LBs) in which a major protein component is α-SYN in its aggregated form [6]. A-SYN is classified as an intrinsically disordered protein with its structure depending on its cellular localization. The protein remains unstructured and monomeric in the cytosol while it acquires an alpha-helical structure and is bound as multimers to lipid membranes [7]. Membrane binding is mediated by the amphipathic N-terminal region of the protein, whereas the acidic C-terminal domain is essential for protein-protein interactions [8-10]. A-SYN regulates neuronal vesicle clustering and release at the pre-synapses, [11, 12] and modulates the immune system [13]. However, the structure and function of α-SYN are perturbed during PD pathogenesis. A-SYN transitions towards a beta-sheet conformation where multimer formation occurs by excessive monomer stacking [14]. Aggregation is promoted by the hydrophobic non-amyloid-beta-component (NAC) domain located in the middle of the protein [14]. The resulting multimers are detrimental to cellular health and provoke persistent pro-inflammatory responses, with the larger aggregates being insoluble and accumulating within LBs [6, 15-17]. The beta-sheet conformation is characteristic of amyloid proteins, a term introduced by Mathias Schleiden to describe plant starch substances [18]. Later, Rudolf Virchow stained corpora amylacea, granular bodies forming with normal aging or neurodegeneration, with iodine. Due to the staining properties of corpora amylacea he believed they were starch-like, hence denominated them "amyloids" [18]. Currently, several human amyloid proteins are associated with neurodegenerative disorders, such as amyloid-beta for Alzheimer's disease (AD) and Huntingtin (HTT) for Huntington's disease [19]. Despite the identification of pathologic human amyloids in neurodegenerative disorders since the last century [18, 20, 21], the exact disease mechanisms of amyloid formation are not entirely known.

Since the last century, LBs were reported in neurons lining the mucosal and submucosal plexus of the intestine at early disease stages in a subset of PD patients [20, 21]. Combined with the nonmotor symptoms of PD, including sleep disturbances, depression, cognitive decline, low blood pressure, and gastrointestinal dysfunction [22, 23], researchers have focused on other tissues as origins of the pathology. Importantly, constipation may appear up to 20 years before the onset of movement problems [23, 24], further hinting that gut dysfunction is involved in early disease pathogenesis. Indeed, PD may start in the gut and propagate to the brain [20, 21, 25]. The principal questions of gut-derived PD include its pathological origin and manner of propagation to the brain. The intestinal origin of PD is not yet known, but it is speculated to be a combination of genetic and environmental factors that promote chronic inflammation and α-SYN accumulation (i.e., *LRRK2* variants, infections, microbiota imbalance) [26-30]. Specifically, gut microbiota dysregulation has been reported in PD patients and meta-genomics analysis revealed bacterial molecules implicated in disease pathogenesis [31], as will be introduced in the following section. In this section, we will introduce the link between the gut and the brain related to α-SYN pathology propagation and inflammation.

One of the routes of gut-to-brain pathology propagation is the vagus nerve. The vagus nerve connects the enteric nervous system with the central nervous system (CNS) [32] through which α-SYN pathology travels transneuronally in a prion-like manner [33-35]. Indeed, truncal vagotomy reduced the risk for developing PD in individuals [36] and hindered gut-to-brain transmission of α-SYN pathology in mice [35]. Braak had already discovered the gut-to-brain axis by monitoring PD progression to anatomically connected areas [37]. Medulla oblongata pathology reflected early disease stages (stage 1), specifically in the dorsal motor nucleus that connects the vagus nerve to the brain [37]. The subsequent stages were characterized by lesions in the coeruleus complex (stage 2), the midbrain (stage 3), and finally cortical areas (stage 4-6) [37]. The exact mechanisms of pathological transmission are not entirely known but include lysosomal exocytosis and extracellular vesicle (EV) transfer, which are described in more detail later. Over the years, two non-mutually exclusive models of PD pathology development have been described, the brain-first and body-first PD. During brain-first PD, the pathology commences in the olfactory bulb, expanding into anatomically connected areas, the amygdala and the nigrostriatal pathway, and spreading to the periphery, such as the intestine and the heart [25]. By contrast, the body-first PD may start in the intestine and over the disease course spread via the vagus nerve into the brainstem and the SN, and through the sympathetic nervous system to the heart [25].

Other than α-SYN aggregation and dopaminergic neuron death, PD is characterized by extensive and chronic (neuro)inflammation. Moreover, the immune system’s capacity to respond to antigens

declines during normal aging and is heavily impacted in PD [38]. Indeed, astrocyte reactivity, microglial activation (the brain resident immune cells), peripheral T-cell infiltration and increased cytokine levels are detected and are associated with α-SYN pathology, and neuronal death in the CNS of PD patients [39-44]. Neuroinflammation is partially triggered by microglia and astrocytes that recognize α-SYN aggregates as pro-inflammatory molecules [45-47]. The persistence of insoluble α-SYN aggregates is thought to maintain the chronic inflammatory response which contributes to disease progression [48]. Due to these observations, the combination of pro-inflammatory cytokines and aggregated α-SYN as pre-formed firbrils (PFFs) has been used to model PD pathology in neuronal/glial co-cultures. The cytokine IFNg is elevated in the serum of PD patients [49]. Co-stimulation of stem cell-derived dopaminergic neurons and microglia in co-culture with IFNg and α-SYN PFFs provoked formation of LB-like structures in the neurons, where α-SYN PFFs alone did not [50]. These results further highlighted the importance of the immune system and cytokines in PD pathology development.

In the intestine, elevated numbers of T-cells, B-cells, and antigen-presenting (HLA-DR+) cells were reported in PD patients compared to non-affected individuals [51]. Mechanistically, $CD4^+$ T-cells developed autoimmunity against the α-SYN epitope HLA-DRB1∗15:01, which resulted in enteric neuron death and constipation [52]. In another mouse study, intestinal CD4+ T-cells exposed to segmented filamentous bacteria initiated local inflammation and migrated through the circulation into the CNS [53], providing an alternative route of gut-to-brain pathology propagation through blood circulation. Within the CNS, CD4+ T-cells were re-activated by host proteins (ERBB2, TRO1, and ANACP2) through molecular mimicry eliciting neuroinflammation [53], suggesting a link between gut bacteria and auto-immunity in PD. The innate immune system is also implicated in intestinal disease progression. A recent study discovered that early α-SYN pathology, identified as the capacity of the protein to act as an amyloid seed, was observed in proximal muscularis macrophages and not enteric neurons in α-SYN transgenic mice (carrying three *SCNA* mutations: E35K/E46K/E61K) or mice injected with human PD-derived α-SYN fibrils [54]. Depletion of the muscularis macrophages prevented CNS α-SYN pathology, dopaminergic neuron death, T-cell expansion, and motor complications, suggesting the pivotal role of intestinal macrophages in early PD pathogenesis [54]. These studies highlight that both innate and adaptive immunity are involved in the mechanisms of PD pathology. The significance of inflammation in Parkinson's is further corroborated by epidemiological and meta-analysis studies showing that inflammatory bowel diseases (IBD) significantly augment the risk for developing PD, yet the results vary between studies [55, 56]. One marker used to evaluate α-SYN pathology is the elevation of α-SYN phosphorylation at serine 129 (pS129-α-SYN), though the exact contribution of this post-translation modification in disease progression is still debated [57-61]. The dextran

sulfate sodium (DSS) mouse model of IBD, displayed increased pS129-α-SYN in the intestine and midbrain, and dopaminergic neuron loss in the SN [62]. The pS129-α-SYN elevation was validated in mucosa, submucosa, and muscularis externa colon samples from patients with ulcerative colitis [62]. These results link intestinal inflammatory diseases and PD and are an active area of investigation. Conclusively, the immune system connects the CNS with the periphery and contributes to both early and late stages of the disease.

A-SYN itself has a direct role in immune function under physiological conditions. Mice that were αβγ-SYN$^{-/-}$ did not display a robust phenotype in neurodevelopment, and only aged animals had neuronal firing dysfunction and reduced survival [63], suggesting that synucleins are not as crucial for neuronal function as initially thought. On the contrary, αβγ-SYN$^{-/-}$ mice had impaired immune responses and survival when exposed to *Salmonella typhimurium* or the West Nile virus [64, 65]. Accordingly, *SNCA* was upregulated upon RNA viral exposure in CNS neurons from wild-type animals with reported α-SYN/viral particle co-localization in the endoplasmic reticulum [64], implying that the protein participates in the physiological response to the virus. Biopsies from children with reported upper gastrointestinal tract inflammation had increased α-SYN intensity which correlated with the number of mononuclear cells and neurotrophils in the tissue [66]. Both monomeric and oligomeric α-SYN acted by attracting macrophages and neutrophils in a CD11b-dependent manner, and by inducing dendritic cell maturation by upregulation of surface CD80, CD83, CD86, and HLA-ABC expression [66]. Intraperitoneal administration of peptidoglycan and thioglycolate bacterial molecules evoked intestinal α-SYN upregulation in mice [13]. Following administration, α-SYN was responsible for leucocyte attraction, pro-inflammatory cytokine (IL-1β, TNFα, and IL-12p70) production, and Toll-like receptor 4 (TLR4)-dependent dendritic cell activation [13]. TLRs are a family of cell surface receptors that bind bacterial molecules initiating NF-κB-dependent immune responses [67]. Additionally, exposure to the TLR4- and TLR2-binding bacterial molecules lipopolysaccharide (LPS) and Pam3CSK4 triggered α-SYN upregulation and release by enteroendocrine cells [68]. Altogether, these results highlight TLR pathway significance in driving α-SYN-induced immune responses. The bacteria-derived short-chain fatty acid sodium butyrate induced α-SYN elevation in a FFA2/3-dependent manner [68], suggesting that multiple bacterial ligands and host receptors may participate in intestinal immune regulation. Thus, α-SYN is a crucial immune modulator under physiological conditions that is required for host responses to pathogens.

The beneficial and detrimental immune responses in neurodegenerative diseases are still being uncovered. While an initial inflammatory response is necessary to eradicating pathogens and unhealthy cells, removal of the antigen results in eventual resolution of the response. However,

the persistence of a stimulus, such as α-SYN in PD, may lead to chronic and deleterious immune activation. As an emerging concept, immune cell exhaustion has been proposed to contribute to neurodegenerative disease progression. Immune cell exhaustion has been initially described in chronic viral infections and primarily for CD8+ T-cells [69]. Sustained T-cell receptor signalling, imbalanced cytokine environment with upregulation of the anti-inflammatory IL-10, and crosstalk with immunosuppressive regulatory immune cells are mechanisms contributing to persistent T-cell activation [70, 71]. In this state, however, T-cells are not entirely functional. They display decreased cell numbers, proliferation, metabolism, cytokine release, and cytotoxicity [72-74], meaning their ability to remove antigens is declined. Immune cell exhaustion has also been reported in CD4+ T-cells, B-cells, and natural killer cells, as well as for other human diseases including cancer [69]. The exhausted immune cell phenotype has been introduced in the field of neurodegeneration for AD. Elevated T-cell activation and TNFα, IFNg, and IL-2 cytokine production were measured in amyloid positive but cognitively normal patients [75]. Instead, amyloid positive individuals with mild cognitive impairments presented CD4+ and CD8+ T-cell populations with declined granzyme B (cytotoxic function), TNFα, IFNg, and IL-2 levels, suggesting their immune function is compromised. In a PD mouse model with microglial-specific *SNCA*^{G420A} expression**,** while microglia displayed elevated *Il1a*, *Il1b*, *Il18*, and *Ifng* pro-inflammatory cytokine expression accompanied by reactive oxygen species (ROS) and nitric oxide production, the authors reported diminished synaptosome phagocytosis which they termed phagocytic exhaustion [76]. The phenotypes and mechanisms of immune cell exhaustion in neurodegenerative disorders, however, are still being characterized. Regarding the innate immune system, studies report dysregulated response during chronic bacterial infection with macrophages described as chronically-stimulated rather than exhausted [77, 78]. For instance, *Salmonella* infection in the liver promoted an M2-like phenotype (increased *Ym1*, *M6pr*, *Tgfb1*, and decreased *Nos2*, *Il12p40* expression) of macrophages that is more associated with an anti-inflammatory response [79]. However, it is unknown whether macrophages become immunosuppressed due to the constant presence of the pathogen or due to *Salmonella* actively undermining the host immune response [80]. Recently, repetitive LPS treatments have been used to model macrophage exhaustion *in vitro* where reduced NF-κB pathway activation, declined cytokine release, impaired mitochondrial metabolism were reported [78, 81]. Consequently, immune cell exhaustion, immunosuppressive reprogramming and the underlying mechanisms are ongoing areas of research within the field of neurodegenerative diseases.

2.2 Gut microbiota and bacterial amyloids in Parkinson's disease

The gut microbiota mainly consists of beneficial bacteria that promote proper intestinal development and host health, while changes in gut microbiota composition have been implicated in PD [82]. The relevance of these pathological alterations has been investigated by 16S rRNA or shotgun metagenomic sequencing methods. Significant differences in the gut microbiota composition were reported between PD and non-affected individuals, with over-representation of opportunistic and rare pathogenic species, such as *Escherichia coli*, *Actinomyces turicensis*, *Klebsiella pneumoniae*, and *Streptococcus* [31, 83]. In the same line, increased relative *Enterobacteriaceae* abundance was associated with augmented severity of gait difficulty and postural instability [84]. PD patients with constipation had increased abundances of *Bifidobacteriales*, *Desulfovibrionales,* and *Lactobacilalles* [85]. On the contrary, beneficial species, including *Roseburia intestinalis*, *Eubacterium rectale*, and *Prevotella*, were under-represented and were associated with reduced anti-inflammatory short-chain fatty acid production [31, 83]. In the same direction, the reduction in *Roseburia* correlated with more severe cognitive decline [85]. Therefore, the gut microbiota is closely linked to PD pathology and symptoms. It should be noted that metagenomics studies have discovered multiple alterations in species abundance, however due to the geographical and culture variability certain species may be omitted. Further complexity is added by the fact that the role of certain bacterial species in PD pathogenesis is difficult to discern. One example is *Akkermansia muciniphila* that displayed increased abundance only in certain cohorts of PD patients [31, 83]. While *A. muciniphila* can promote mucin production and enhanced gut barrier integrity [86-88], its secretome can induce α-SYN aggregation in enteroendocrine cells [89]. The difficulty to discern the beneficial and detrimental aspects of *A. muciniphila* stems from the fact that gut microbiota composition is affected by lifestyle and geographical region, and bacteria function as a community rather than individually in the host's intestine [90-92]. Thus, the field of microbiota alterations, the intricate relations between microbes and the host, and their involvement in PD is an ongoing area of research. An approach to better comprehend the cellular pathways and biomolecules by which bacterial species contribute to PD is by analyzing enriched bacterial gene families in PD cohorts. One example is LPS [31, 83], which is produced by Gram-negative bacteria and is a fundamental structural component of the outer side of the cell membrane [93]. Due to the surface exposure of LPS, host cells recognize it as a pathogen-associated molecular pattern via TLR4 to trigger immune responses [94]. LPS has endotoxin properties and, thus, was used to model inflammatory conditions both *in vivo* and *in vitro* [95, 96]. For example, LPS stimulated macrophage activation and inflammatory cytokine production via the NF-κB and IRF3 pathways [96, 97]. Another family of upregulated genes in the gut bacterial community of PD patients were the genes *csgA*, *csgC*,

csgG [31]. These genes are expressed by the *Enterobacteriaceae* family [98] revealing a broad mechanism by which intestinal bacteria may contribute to PD.

The operons *csgBAC* and *csgDEFG* are expressed by *Enterobacteriaceae* under biofilm-forming conditions [99]. Bacteria can exist as singular free-floating cells (planktonic), or as densely populated microbial aggregates (biofilm). Biofilm is a type of extracellular matrix (ECM) produced by various bacterial species that confers protection against the environment (i.e., mechanical stress, toxins, other microorganisms, antibiotics) [99, 100]. The model of biofilm formation, initially described in *Pseudomonas aeruginosa*, is a five-step process that begins with reversible surface attachment of planktonic bacteria (step 1) [101, 102]. This attachment and grouping of multiple planktonic bacteria into a monolayer initiates intracellular changes (i.e., extracellular polymeric substance production, antibiotic resistance gene expression, metabolic alterations), and intercellular communication (i.e., quorum sensing, oligopeptides) to facilitate the transition into biofilm growth (step 2: irreversible attachment). Over time, multiple layers form (step 3: maturation I) and the biofilm acquires structural complexity appearing as mushroom-like (step 4: maturation II). The biofilm is composed of various molecules including proteins, saccharides, lipids, and deoxyribonucleic acid (DNA) [103, 104]. Biofilm dispersion (step 5) releases planktonic bacteria that can migrate and colonize other areas [102, 104]. While this model of biofilm formation is still being used, it is appreciated that it does not sufficiently reflect all forms of biofilms observed in nature and in laboratory settings [104].

In *Enterobacteriaceae*, the major protein component of biofilms is CsgA [105, 106]. CsgA is termed a functional bacterial amyloid and the CsgA fibrils in the biofilm are called curli. Being an amyloid protein, similar to α-SYN, it is intrinsically disordered and forms aggregates by sequential stacking of CsgA monomers with a beta-sheet conformation [107, 108]. Particularly, CsgA contains five imperfect repeats (R1-5) with each spanning 19-23 amino acids in length and containing a Ser-X5-Gln-X4-Asn-X5-Gln consensus sequence. By performing Ala mutagenesis, Wang et al [107] discovered that Q49A and N144A mutations completely hindered biofilm formation as assessed by Congo Red staining, which binds and stains beta-sheet structures. The mutant CsgA-slowgo, where Q49 and N54 in repeat 1 and Q139 and N144 in repeat 5 were all replaced by alanine, had a substantially reduced ability to aggregate into fibrils. This suggested that the R1 and the R5 sequences are important for CsgA monomer aggregation and nucleation with CsgB. Indeed, cryo-EM structures of CsgA fibrils displayed that the R1 or R5 of one monomer interacted with the R1 or R5 of the subsequent monomer (termed head-to-tail, head-to-head, or tail-to-tail interactions) [109, 110]. The intrinsic beta-sheet forming ability of CsgA, contrary to α-SYN, confers the rapid aggregation capacity needed for biofilm production [108]. Regarding the

two operons, CsgD is the master transcriptional regulator of *csgBAC* and *csgDEFG*, and it is activated by various environmental cues that benefit biofilm formation including low temperature and starvation [111-113]. Once produced, CsgA remains soluble and monomeric within the cell due to its binding by the chaperone CsgC [114, 115]. CsgC prevents both CsgA and α-SYN aggregation by binding to the following consensus sequences: D-Q-Φ-$X_{0,1}$-G-K-N-ζ-E [115]. Since this sequence is not present in amyloid beta, CsgC does not hinder its aggregation [115]. CsgA is produced by Gram-negative bacteria meaning it must pass through the cell membrane into the periplasm, and then through the outer membrane to reach the extracellular milieu. For the first step, CsgA carries a secretion signal (SEC) in its N-terminus which is recognized and cleaved by the protein complex SecYEG during CsgA's translocation [105]. CsgG forms a pore in the outer bacterial membrane through which CsgC and CsgE secrete CsgA to the extracellular space [116, 117]. CsgB and CsgF are bound on the extracellular side of CsgG, with CsgB acting as the nucleator where CsgA binds and begins aggregating [118-120]. These two *csg* operons tightly regulate the amyloid aggregation process of CsgA that, in contrast to human amyloids, does not detrimentally occur within the cell.

The effect of CsgA and curli in PD was studied in animal models overexpressing human *SNCA* [121-124] or expressing human *LRRK2* variants associated with sporadic PD (R1628P or G2385R) [125]. The animals were repeatedly exposed to *E. coli* WT or Δ*csgBAC* via different administration methods (drinking water, oral gavage, colonic injection) prior to intestinal and brain pathology evaluation [121-125]. The duration of the experiments ranged between 9-24 weeks for mice and up to 6 days for *C. elegans* [121-125]. *E. coli* WT induced elevated α-SYN aggregation and phosphorylation at serine 129 in the intestine of mice and *C. elegans* compared to *E. coli* Δ*csgBAC*, with the pathology extending to the SN of mice [121-125]. This was accompanied by increased astrocyte and microglial activation measured by the increased number of GFAP+ and IBA1+ cells, respectively, augmented IL-6, TNFα, and TLR2 levels in the brain, and motor impairments in *E. coli* WT-colonized versus *E. coli* Δ*csgBAC*-colonized mice [121, 122, 124, 125]. SN dopaminergic neuron loss was reported in the *LRRK2* mutant mice colonized with *E. coli* WT but not in *SNCA* overexpressing mice [122, 125]. Accordingly, intestinal injection with the synthetic CsgA peptide QYGGNN (derived from CsgA's conserved amyloidogenic sequence) promoted motor impairments in *Thy1-SNCA* overexpressing mice from 20 days and up to 70 days post-injection when compared to the non-amyloidogenic peptide QYGGNA [122]. Finally, epigallocatechin gallate (EGCG), which blocks α-SYN and CsgA aggregation, ameliorated motor scores, pS129-α-SYN levels, and IBA1+ cell number and density in the SN compared to the vehicle control in *E. coli* WT-colonized mice [122]. Thus, *csgA* upregulation and increased *E. coli*

levels reported in PD patients could aggravate PD progression through both α-SYN aggregation and inflammation.

Mechanistically and in the context of peripheral inflammation, *Salmonella* curli fibers bound to TLR2 and promoted macrophage IL-6, IL-8, and IL-10 production via NF-κB [126-129], showing that innate immune cells recognize curli as a pathogen-associated molecular pattern. The association between curli with intestinal pathology and neurodegeneration was reported in AD and amyloid lateral sclerosis (ALS). In the Tg2576 AD mouse model (APP-KM670/671NL), increased curli burden, epithelial barrier integrity loss, and TLR2 activation were observed in the gut [130]. *E. coli*-derived curli upregulated TLR2 in human ileal organoids, though inflammation was not further evaluated [130]. Additionally, elevated *Tlr2* and *Arg1* expression in skeletal muscles, as well as increased blood-circulating $CD19^+$ B-cells were reported in male *SOD1*-G93A ALS mice colonized with curli-producing vs non-curli-producing *E. coli* [131]. On the contrary, a trend for reduced IL-22 levels in the distal colon, and decreased dendritic cell, activated T-helper and T-cytotoxic cell numbers were reported in the blood of *SOD1*-G93A ALS mice colonized with curli-producing *E. coli* [131]. This suppressed immunity was hypothesized to occur due to the binding of curli on major histocompatibility complexes (MHC) class I [132], highlighting the potential detrimental role of CsgA through both activation or downregulation of immunity depending on disease context and cell type analyzed. Nevertheless, CsgA and curli have also been described to be homeostatic regulators of the immune system. Oral gavage rather than peritoneal injection of curli fibers is anti-inflammatory by promoting IL-10 release [133], suggesting that intestinal lumen curli is part of gut commensal flora-derived homeostasis. Under inflammatory conditions, such as in the DSS mouse model of IBD, *E. coli* and orally administered curli fibers ameliorated inflammation and improved gut histopathological score [133, 134]. Similarly, *E. coli* Nissle 1914 reduced peripheral blood T-cell cycling and IL-2, TNFα, IFNg production, while it increased anti-inflammatory IL-10 levels in CD3-stimulated lamina propria T-cells [135]. The cytokine level changes by *E. coli* were not observed in *Tlr2*$^{-/-}$ mice [135], suggesting the effect is partially mediated through curli. These results together with the findings of the ALS study [131] imply that T-cell activation is suppressed by *E. coli* and curli. Overall, curli can be either pro- or anti-inflammatory depending on the cell type, tissue localization and disease context. Despite this information, how curli is exposed to intestinal and immune cells in humans has not been described in detail. Biofilms were reported in healthy individuals, and their prevalence was increased in IBD patients [136-139]. Therefore, intestinal cells could uptake CsgA or CsgA could infiltrate past the damaged gut barrier reported in irritable bowel syndrome (IBS) and ulcerative colitis [136]. Other than canonical secretion for biofilm formation, CsgA is released via exosomes by *E. coli* in the mouse gut [125]. The CsgA-carrying exosomes promoted pS129-α-SYN phosphorylation and

insoluble α-SYN formation in the LRRK2-R1628P mouse model [125], suggesting that different routes of intestinal bacterial amyloid exposure may be present. Conclusively, CsgA is linked to altered inflammation and worsened pathology, yet it remains to be investigated how the bacterial amyloid disrupts intestinal homeostasis to promote PD pathogenesis.

Other than TLR2, curli fibers bind to fibronectin and MHC class I molecules. Fibronectin is a ubiquitously expressed ECM protein involved in cell adhesion, differentiation, migration, and growth [140]. One manner of fibronectin-cytoskeleton coupling is via integrins, transmembrane proteins forming heterodimers between α and β subunit members [140]. Particularly, the RGD (arginine–glycine–aspartic acid) integrin family (α_v, α_{IIb}, β_3, β_5, β_6, β_8) binds fibronectin [141]. Curli binds fibronectin in an RGD-dependent manner resulting in *E. coli* internalization in T24 and HeLa cells, since bacterial uptake was blocked by co-treatment with competing RGD peptides [142]. Except for fibronectin, *E. coli* curli binds to MHC-I, proteins involved in antigen presentation to adaptive immune cells [143]. The curli-MHC-I interaction promoted *E. coli* adherence on murine macrophages [132]. However, it did not affect the ability of macrophages to phagocytose bacteria, bind ovalbumin peptides, and induce proliferation of CD3-stimulated T-cells [144], implying that antigen presentation is not affected by curli. Thus, curli bind to fibronectin and MHC-I molecules to facilitate bacterial adherence on host cells, yet the uptake or downstream cellular effects have yet to be investigated.

2.3 Enteroendocrine cells and their involvement in Parkinson's disease

The intestinal epithelial cell (IEC) layer consists of multiple cell types, including intestinal stem cells which are necessary for regeneration of the tissue [145]. Enterocytes uptake and process nutrients [146], while Paneth cells participate in host defense by secreting antimicrobial peptides [147]. Goblet cells produce mucin, the protective layer restricting bacterial growth near the gut epithelium [148], and enteroendocrine cells (EECs) release hormones to control digestion, gut motility and immunity following their exposure to luminal nutrients [149, 150]. EECs were classically divided based on the hormone they produced, e.g. enterochromaffin cells produce 5-hydroxytryptamine (5-HT or serotonin) and L cells produce glucagon-like peptide-1 (GLP-1), though it is currently appreciated that each EEC type secretes multiple hormones [151, 152]. A widely used marker for EECs is chromogranin A (CHGA), a glycoprotein involved in the biogenesis and maintenance of secretory granules that contain hormones and neurotransmitters in neuroendocrine cells [153]. EECs additionally function as immunity regulators through functional TLR expression [154], hormone release (i.e., GLP1, cholecystokinin) [149], and chemokine and

cytokine (i.e., GROα, MIP2, TNFα, and IL-32) secretion to IECs and immune cells [149, 154-157]. A subset of EECs, called enterochromaffin cells, consist of a basal neuropod structure that forms a synapse with enteric neurons [158]. These EECs produce 5-HT, CCK, or PYY following nutrient exposure to regulate intestinal motility via enteric neurons [158, 159]. Due to their neuron-like properties, EECs express α-SYN [160] and exposure to bacterial ligands, such as LPS, Pam3CSK4, and sodium butyrate, induces upregulation of both *SNCA* transcription and α-SYN levels [68], further corroborating their role in immune system regulation and suggesting their involvement in PD pathogenesis [160]. Indeed, *A. muciniphila* secretome promoted intracellular calcium overload followed by increased mitochondrial ROS release with subsequent elevation of pS129-α-SYN and α-SYN-GFP aggregation in mouse STC-1 EECs [89]. Nitrite, produced by intestinal *Enterobacteriaceae* and an oxidizing molecule, was also potent in inducing α-SYN aggregation *in vitro* and in STC-1 EECs [161]. The pathology of α-SYN can be propagated from EECs to proximal enteric neurons to eventually reach the hindbrain [162], rendering EECs as an integral component in PD pathogenesis. One mechanism of transmission requires cell-to-cell contact between STC-1 EECs and SH-SY5Y-derived neurons and is mediated via RAB35 [163]. RAB35 participates in endocytic recycling [164] and its silencing in EECs induced increased α-SYN targeting to the lysosomes and diminished α-SYN fibril propagation to neurons [163]. Thus, EEC intracellular trafficking pathways are implicated in PD pathology. However, exogenously-generated α-SYN PFF were used as seeds to induce pathology [163], while physiologically relevant inducers of pathology (i.e., genetic variants, microbial molecules) were not evaluated. The *SNCA* mutation A53T is implicated in familial PD through autosomal dominant inheritance and has been used to model the disease [165, 166]. Mouse primary intestinal organoids with human *SNCA*-A53T expression displayed α-SYN seeding capacity with aggregates being transmitted to *SNCA*$^{-/-}$ nodose ganglia neurons [162]. Therefore, EECs are implicated in intestinal α-SYN aggregation upon fibril exposure or familial *SNCA* mutations and propagate the α-SYN pathology to enteric neurons, nevertheless whether and how sporadic PD manifests in EECs is not yet known.

2.4 Organelle and proteasome involvement in α-SYN homeostasis and pathology

2.4.1 Mitochondria

The field of mitochondrial biology in neurodegenerative diseases developed from studying CNS neurons. Neurons, particularly dopaminergic, are highly metabolic and rely heavily on proper

mitochondrial function [167]; thus, any mitochondrial activity perturbation is lethal if not resolved. Genetically, multiple mitochondrial function-related genes are implicated in neurodegenerative diseases. *PARK7* is responsible for an autosomal recessive form of familial PD [168]. PARK7, also known as DJ-1, is a multifunctional protein which counteracts oxidative stress, regulates proper respiratory function and mitochondrial dynamics [169-171], exerts antioxidant function to maintain neuron survival [172], and prevents α-SYN aggregation in its oxidized state [173, 174], linking overall mitochondrial health status with PD pathology. Another protein, SOD1 functions as a cellular antioxidant by converting superoxide (O_2^-) to hydrogen peroxide (H_2O_2). A fraction of SOD1 is localized to mitochondria, and genetic mutations are implicated in ALS [175-177]. Yet dysfunctional wild-type SOD1 resulting from post-translation modifications is reported to accumulate in LBs of PD patients [178], suggesting that protein function is perturbed in PD without genetic perturbations. Dysfunctional SOD1 induced excessive mitochondrial ROS (mtROS) production which promoted cellular oxidative stress [179]. Excessive oxidative stress may increase the rate of both α-SYN aggregation and propagation and, additionally, damage the neurons causing neurodegeneration in the context of PD [180-183]. The mitochondrial respiratory chain (MRC), responsible for generating the majority of adenosine triphosphate (ATP) in the cell, is another source of PD-related mitochondrial dysfunction. The MRC consists of 5 complexes, complex I-V, containing multiple subunits each [184]. Complex deficiency was reported during natural aging and robust complex I impairment was described in the SN of PD patients [185-187]. There is no clear genetic cause for MRC dysfunction in PD [188], whereas the environment, e.g. pesticides, has a key role [189, 190]. The importance of mitochondria is further highlighted by the 1-methyl-4-phenyl-1,2,3,6-tetrahydropyridine (MPTP) mouse model of PD. MPTP is a potent toxin that induces dopaminergic neuron death by blocking mitochondrial respiration and provoking aberrant superoxide production [191]. This elicits SN dopaminergic neuron death inducing parkinsonian-like features in mice [191]. Overall, mitochondria damage and dysfunction are heavily implicated in PD in the brain and their role in the periphery is emerging.

EECs exhibit neuron-like properties, as they release both hormones and neurotransmitters, and therefore rely heavily on mitochondrial energy production to sustain their function [192-194]. From early development, the gut microbiota modulates the EEC transcriptome, particularly genes involved in mitochondrial activity and dynamics [192]. Notably, mitochondrial localization at the basal side of EECs, where hormone and synaptic vesicle release occurs, was observed in conventionalized (CV) but not germ-free (GF) zebrafish [192]. Using linoleic acid as a nutrient stimulant, EECs in GF animals failed to increase mitochondrial and cytosolic calcium levels compared to EECs in CV animals, suggesting that the microbiota is required for proper EEC nutrient responsiveness [192]. Consistently, a preprint study using amino acids as stimuli reported

that GLP-1 secretion depended on oxidative phosphorylation and the tricarboxylic acid (TCA) cycle [194], further linking mitochondrial activity to EEC hormonal release and function. EECs additionally contribute to the maintenance of overall intestinal mitochondrial function and metabolism, as demonstrated by EEC ablation studies in mice [195], indicating that proper EEC signalling is essential for intestinal metabolic homeostasis. However, mitochondrial homeostasis can be disrupted inducing α-synuclein (α-SYN) pathology, as shown in the *A. muciniphila* secretome study [89]. In this context, α-SYN-pS129 and α-SYN-GFP aggregation were rescued by restoring mitochondrial calcium balance, which prevented excessive, non-physiological ROS production [89]. Thus, mitochondria are central to EEC function and intestinal homeostasis, and their dysfunction may contribute to PD pathogenesis.

2.4.2 Lysosomes and intracellular trafficking

Lysosomes are cytoplasmic organelles and consist the endpoint of intracellular vesicle trafficking where biomolecule degradation occurs [196]. The relevance of lysosomes in PD was highlighted by the study of the lysosomal storage disorder Gaucher's disease (GD). GD is caused by biallelic mutations in *GBA1* encoding for the lysosomal enzyme glucocerebrosidase (GCase) which catabolizes glucosylceramide into glucose and ceramide [197]. A GWAS study identified monoallelic *GBA1* mutations as the major genetic risk factor for PD [198]. In the loss-of-function hypothesis, *GBA1* variants impede GCase enzymatic activity leading to glucosylceramide accumulation in the lysosomes, which hinders proper lysosomal function and lysosomal degradation of α-SYN [199] promoting a vicious cycle of α-SYN accumulation. GCase dysfunction in PD is modelled using PD-linked genetic mutations (i.e., L444P, N370S, E326K) [200-203], genetic knock-down [199], or by blocking its enzymatic function using the chemical inhibitor conduritol-b-epoxide (CBE) [204-206]. In the intestine, injection of α-SYN PFF in mouse duodenum diminished GCase enzymatic function to 50% over 7 days which completely recovered after 4 months [207]. The mice displayed increased intestinal α-SYN-pS129, gastrointestinal dysfunction, and decreased enteric neuron function, all of which were partially rescued by *GBA1* gene delivery [207], suggesting that GCase also plays a role in intestinal PD pathology. Overall, GCase dysfunction can contribute to α-SYN aggregation in PD pathogenesis, though the field of intestinal *GBA1* PD has yet to be explored in detail.

Extracellular or intracellular cargo is sorted and distributed to endosomes which traffic the molecules to different compartments within the cell. In principle, early endosomes transition to late endosomes, also called multivesicular bodies (MVBs) due to the appearance of membrane invaginations, accompanied by a reduction in pH prior to fusion with lysosomes [208]. An alternative fate of late endosomal content is release via exocytosis [209] which will be mentioned

later. In PD, various endosomal trafficking mechanisms and lysosomal degradation are perturbed which contribute to disease progression [210-212]. This section will provide a summary of relevant proteins involved in intracellular α-SYN trafficking in the context of PD.

Lysosomal degradation is termed autophagy and is classically described as a mechanism occurring during starvation or disease when the cell recycles its own molecules [213]. Multiple autophagy pathways exist in the cell. The principal manner of intracellular lysosomal α-SYN targeting is via chaperone-mediated autophagy (CMA) [214-216]. In CMA, proteins with KFERQ-like sequences ($_{95}$VKKDQ$_{99}$ for α-SYN) are bound by the lysosomal membrane protein LAMP2A which, together with the help of HSPA8, co-chaperones and ATP, results in lysosomal import of the target proteins [217]. The A53T or A30P mutant α-SYN forms bind to LAMP2A but are not internalized, thus preventing their degradation of α-SYN and other proteins (GAPDH in the study) via CMA [215]. This data suggested that mutant α-SYN acted in a toxic gain-of-function manner. On the other hand, multiple pathways of extracellular monomeric, oligomeric, or fibrillar α-SYN uptake have been described in literature, including macropinocytosis, dynamin-dependent endocytosis, clathrin-mediated endocytosis (CME), or receptor-mediated endocytosis [218-224]. Many of these pathways converge into lysosomes with multiple intracellular trafficking-related proteins interacting directly or indirectly with physiological and pathologic α-SYN. Initially, a crucial component of the CME is the AP2 adaptor complex consisting of five subunits AP2A1, AP2A2, A2PB1, AP2M1, and AP2S1 [225]. Under physiological conditions, α-SYN recruits AP2 followed by clathrin to the synaptic membrane to facilitate CME [226]. Lack of *SNCA* reduced AP2 synaptic membrane localization potentially affecting the early steps of neurotransmitter endocytosis [226], though a redundance for synaptic vesicle trafficking with other synucleins was reported [227]. However, the AP2 complex and clathrins have also been discovered in DLB inclusions, suggesting that CME is linked to α-SYN amyloid disease [228].

The importance of lysosomal α-SYN trafficking was further highlighted by studies of the dynein complex and autophagy. Dynein consists of multiple subunits categorized as heavy, intermediate, light intermediate, and light chains [229]. Dynein is a large motor protein carrying organelles towards the minus end of microtubules, meaning towards the nucleus [230]. Autophagosomes, double-membraned vesicles containing material for degradation [231], are carried by dynein towards lysosomes near the minus end of microtubules [232]. Genetic silencing of the dynein heavy chain induced an increase in α-SYN A53T levels and half-life in PC12 cells [233]. On the contrary, enhancing dynein activity via exogenous expression of N-acetylglucosamine kinase (NAGK) prevented α-SYN-A53T aggregation in HEK293T cells and primary rat cortical cultures [234]. Dynein is implicated in autophagy as shown by elevated SQSTM1/P62 and LC3B-II levels,

and accumulation of LC3+/LAMP1+ autophagic vacuoles in PC12 cells silenced for the dynein heavy chain [233]. P62 functions by capturing ubiquitinated cargo for delivery to autophagosomes where it is degraded [235]. The levels of P62 decrease upon autophagy activation, thus this protein has been used as an autophagy marker. P62 directly interacts with microtubule-associated protein 1 light chain 3 (MAP1LC3 or LC3) required for autophagosome formation. LC3 is cleaved at the C-terminus by ATG4A to yield the cytosolic form LC3-I. A series of ATG proteins act in a ubiquitin-like manner to apply a phosphatidylethanolamine modification to the C-terminal of LC3-I. In this manner, LC3-I converts to LC3-II which associates with the autophagosome membrane and correlates with autophagosome formation [236-238], meaning the ratio of LC3-II-to-LC3-I is marker of autophagic flux similar to P62. Conclusively, the upregulation of P62 and LC3-II upon dynein silencing [234] suggests that dynein participates in autophagic degradation α-SYN.

Vacuolar protein sorting 35 (VPS35) and VPS26A are additional intracellular trafficking proteins implicated in PD. VPS35, VPS26A, and VPS29 form together the retromer complex which participates in endosomal sorting [239]. Mutations in *VPS35* cause familial or sporadic PD [240], whereas certain variants in *VPS26A* are implicated only in sporadic PD [240, 241]. The mechanisms linking VPS35 and VPS26A mutations to PD are not entirely known and are mostly derived from studying VPS35. *Vps35*$^{+/-}$ mice display decreased LAMP2A and MFN2, and increased α-SYN in dopaminergic neurons, suggesting that retromer dysfunction impacts CMA and mitochondrial fusion which could be responsible for the dopaminergic neuron death observed in these animals [43]. There is no reported interaction between α-SYN and VPS26A, but VPS26A is required for proper processing of APP and Tau, two amyloid proteins involved in AD [242]. Downregulation of VPS26 by high glucose led to APP retention in endosomes accompanied by increased Aβ levels and augmented phospho-Tau levels [243], both of which are pathologic hallmarks in AD [242]. Using the retromer pharmacological chaperone R33, VPS26A downregulation was rescued leading to recovered APP and Tau levels, and improved cathepsin D activity and lysosomal localization [243], suggesting that retromers are necessary for proper lysosomal enzyme function. Indeed, a recent multi-omics study discovered that retromer function is fundamental for endo-lysosomal homeostasis while *VPS35* deletion elicited severe lysosomal and cell surface proteome changes, and lysosomal dysfunction (autolysosome formation, lysosomal number) [244]. These effects were due to the ability of retromers to bind effector proteins on the lysosomal membrane [244]. As a compensatory mechanism to lysosomal perturbations, cells displayed elevated lysosomal exocytosis [244] which could present a mechanism of aggregated α-SYN release [245]. Therefore, the retromer is an intracellular trafficking component linking pathologic amyloids to lysosomal dysfunction.

Overall, defects in intracellular trafficking and impaired lysosomal targeting disrupt α-SYN homeostasis, promoting its pathological aggregation and propagation.

2.4.3 Proteasome

Lastly, α-SYN degradation also occurs in proteasomes [246]. The proteasome is a multi-ring-like complex consisting of structural and catalytic subunits. 20S proteasome is the smallest complex divided into α and β subunits, with the α subunits forming the two outer rings of the complex [247]. The normal catalytic β subunits are PSMB5, PSMB6, and PSMB7 [248-250], with each protein catalyzing the breakdown of different protein sequences. Due to their sequence specificity, PSMB5 displays chymotrypsin-like activity, PSMB6 has caspase-like activity, and PSMB7 performs trypsin-like activity [251, 252]. The 19S proteasome is a regulatory complex in the form of a cap that binds on the outer rings of the 20S proteasome [248]. The resulting structure is the 26S or 30S proteasomes depending whether one or two caps bind on the 20S proteasome [248]. The 26S proteasome degrades ubiquitinated proteins compared to the 20S which displays broader protein degradative activity [248]. Proteasome function is reduced in PD patients [253, 254], and α-SYN can directly impair proteasome subunit levels and its activity [255-259]. Interestingly, α-SYN, amyloid-beta 1-42, and HTT Q53 oligomers were all able to impair the proteasome chymotrypsin-like activity, suggesting a common mechanism of amyloid-induced proteasome impairment [260], which could also occur upon exposure to bacterial amyloid oligomers. Thus, amyloids disrupt proteasome activity as a mechanism of proteostasis impairment linked to neurodegenerative diseases.

2.5 Extracellular vesicles and exosomes in intestinal homeostasis and α-SYN pathology propagation

Extracellular vesicles (EVs) are defined as cell-released particles enclosed by a lipid bilayer that are incapable of replication [28]. They carry various molecules such as proteins, metabolites, microRNAs (miRNAs), and DNA, and are important for intercellular communication and homeostasis maintenance [261]. EVs are typically characterized as small (<200 nm) or large (>200 nm) though no unanimous cut-off is defined in literature, and their intracellular origin can vary [28]. Marker proteins include ALIX, FLOT1, and tetraspanins. ALIX is an accessory protein of the endosomal sorting complex required for transport (ESCRT) which participates in EV biogenesis [262]. FLOT1 is a scaffold protein for lipid rafts that aids in membrane trafficking for the EV pathway [263]. Tetraspanins are cell surface molecules, including CD81, CD9, and CD63,

that define membrane protein microdomains [264] and their role in EVs will be introduced later. One of the most studied EV subsets are the exosomes. Exosomes are typically characterized by their endosomal origin, when MVBs fuse with the plasma membrane, and their <200 nm size [28].

In the intestinal epithelium, exosomes perform various roles to maintain tissue homeostasis. IEC exosomes maintain barrier integrity, regulate microbiota growth, control immune cell responses, and promote tissue repair [265]. These functions are controlled by protein (i.e., chemokines, cytokines, MHC class I/II molecules for immune regulation) and miRNA cargo in exosomes [265]. For instance, adaptive immune activation can be initiated via IEC antigen presentation on exosomes. MHC-I/II-exposed antigens on the exosomal membrane promote dendritic cell and subsequent T-cell activation [266-269]. Antigen presentation efficiency is further enhanced by the presence of tetraspanins CD81, CD9, and CD63, which arrange MHC-I/II molecules and their co-receptors in membrane microdomains augmenting immune signal transmission [270-273]. IEC-derived EVs are necessary for intestinal tolerogenic responses. The transfer of integrin αvβ6 from IEC-derived EVs to dendritic cells induced active TGF-β release resulting in regulatory T-cell production and T-cell helper 2 suppression to promote antigen tolerance [274]. Importantly, direct exposure of dendritic cells to food antigens promoted latent TGF-β secretion without downstream adaptive immunity tolerance [274]. Indeed, TGF-β1-associated EVs from IECs were immunosuppressive and inhibited CD4+ T-cell proliferation under control conditions *in vitro* [275]. In the DSS-induced IBD mouse model, IEC ERK pathway activation upregulated EV TGF-β1 levels which ameliorated intestinal inflammation (decreased IL-1β, IL-6, TNFα, IL-10, IL-22, and MPO production; recovered body weight and colon length) through induction of regulatory T-cells and suppression of dendritic cell activation [275]. In contrast, CD63+ EVs derived from IECs of rats that underwent trauma and hemorrhagic shock showed upregulated MHC class II and Fas ligand molecules compared to EVs from sham rats [276]. These EVs induced dendritic cell death and suppressed surviving dendritic cell maturation as shown by the reduced CD80, CD86, and MHC class II surface expression [276]. Concomitant with the effect of EVs from trauma rats to downregulate dendritic cell-mediated lymphocyte proliferation [276], these findings suggest IEC-derived EV cargo impairs host immune responses. While the immune-modulatory effect of IEC-derived EVs in macrophages has not yet been explored, serum from DSS-induced colitis mice promoted ERK activation, TNFα production, and proteomics alterations involving 56 acute-phase proteins and immunoglobulins in macrophages, suggesting their immune activation [277]. In the context of PD, the role of IEC exosomes has yet to be uncovered but considering α-SYN is transported via these vesicles [278, 279], it could describe a potential mechanism of intestinal immune regulation. Thus, extracellular vesicles and exosomes are important for cell-cell

communication, homeostatic and pathologic immune responses, and α-SYN transfer, suggesting their involvement in gut-derived PD pathogenesis.

Pathologic α-SYN transfer occurs via multiple pathways, including lysosomal exocytosis, tunnelling nanotubes, cell death, or exosomal release, all of which have been proposed as pathology propagation mechanisms [245, 280-285]. Due to the involvement of EVs in intestinal cell communication and immune modulation, the exosomal transport α-SYN will be introduced [265]. Exosomes isolated from the cerebrospinal fluid (CSF) of dementia with Lewy bodies (DLB) patients induced α-SYN pathology in the mouse brain [286]. A-SYN PFFs were detected in MVBs where they co-localized with the exosomal marker CD63, implying they are sorted for exosomal release [287]. Upon release, the majority of α-SYN PFFs were localized on the membrane of the CD63+ exosomes as evaluated by transmission electron microscopy experiments [287]. A-SYN oligomers were also detected in the exosomal membrane, though a fraction of oligomers was discovered in the exosomal lumen [281]. Both α-SYN oligomer- or PFF-carrying exosomes were transferred from donor to recipient cells *in vitro* and this effect was blocked by the exosome biogenesis inhibitor manumycin A [281, 287, 288], suggesting that exosomes are a major pathway of α-SYN pathology propagation. The EV-mediated α-SYN release mechanism could act in a compensatory manner against intracellular α-SYN accumulation as reported in LUHMES neurons where *ATG5* was silenced to inhibit autophagy [282]. Consistently, EV α-SYN transfer occurs between different cell types. Neuron-released exosomes containing α-SYN PFF were uptaken by microglia which subsequently released their own exosomes to further propagate the pathology to proximal neurons [283]. The specificity of the exosomal pathway was shown *in vitro* using the chemical inhibitor GW4869 [283], which blocks neutral sphingomyelinase 2 involved in ceramide-dependent exosome generation [289]. This was further corroborated by use of patient CSF-derived exosomes that were CD11b+ (a marker of microglia) and induced α-SYN pathology when injected into the brains of healthy mice [283]. Thus, exosomes participate in α-SYN pathology propagation between neurons and immune cells. However, the field of α-SYN propagation through EVs is still debated, due to the difficulties of obtaining pure EV fractions [290]. Overall, intracellular trafficking perturbations promote exosomal release of pathological α-SYN which contributes to PD progression.

2.6 Microfluidics model systems in intestinal research

Microfluidics chips are micrometer-scale systems where small liquid volumes are processed and are typically fabricated using polydimethylsiloxane (PDMS) offering optical transparency, mechanical manipulation, oxygen permeability, and biocompatibility [291]. The technology was first introduced to permit capillary electrophoresis in 1990 [292]. Over the years, microfluidics

chips have been used as cell culture model systems which provide multiple advantages over animal models are regular 2D cultures. The chips are highly modifiable and can be compartmentalized to separate cell types or tissue-like structures. Cells are seeded in channels carved within the PDMS through inlets and different segments are connected via microchannels (same z-plane as the channels), microgrooves (lower z-plane than the channels), or a thin and porous PDMS membrane. The channel layout can be modified to establish a specific structure, for instance intestinal invaginations, and medium flow permits constant nutrient exchange [293]. Additionally, the combination of microfluidics pressure applied by the medium flow and the suction-induced mechanical PDMS deformation at a frequency of 0.15 Hz, mimicking the human intestinal lumen, promoted villi formation in 2D-seeded Caco-2 intestinal epithelial cells [294]. In the same direction, primary human colonic organoids cultured in microfluidics chips resembled the anatomy, cell type variability, and transcriptome of human duodenum [295]. Polarity was spontaneously achieved with the apical side towards the flowing medium and the basal side on top of the PDMS membrane. These resulting cultures formed a tight epithelial barrier, metabolized sucrose, and secreted mucin, suggesting their functionality [295]. Overall, gut microfluidic chip models and protocols with structural and functional resemblance to the human intestine have been developed which allow researchers to perform research in more complex and translatable systems. Here, we introduce microfluidics models designed to facilitate human intestinal research focusing on the epithelium, microbiota, immune cells, and enteric neurons.

Caco-2 intestinal cells were cultured in microfluidics devices with different commensal or pathogenic bacterial strains under the absence or presence of peripheral blood mononuclear cells (PBMCs) as an immune cell model [294, 296, 297]. Technically, devices permitting either aerobic or anaerobic bacterial cultures together with or without constant flow were designed and characterized. Overall, the combination of Caco-2 with commensal bacteria (probiotic species mixture VSL#3, or *Lactobacillus rhamnosus* GG strain and *Bifidobacterium longum*) improved transcriptomic similarity to the human intestine compared to the absence of bacteria or Caco-2 cultures outside the chip [294, 296, 297]. Luminal addition of a pathogenic enteroinvasive *E. coli* (EIEC) strain (serotype O124:NM) promoted barrier permeability and induced loss of the spontaneously formed villi structures [294]. LPS and commensal *E. coli* induced the same detrimental effects only when combined with PBMCs cultured in the apical side of Caco-2 cells [294], suggesting the importance of including immune cells in microbiota-intestinal models. From the immune cell perspective, certain chemokines and several pro-inflammatory cytokines (IL-1α, IL-1β, IL-2, IL-6, IL-8, IL-12, IFNγ, TNFα, and GM-CSF) were augmented following exposure to LPS or EIEC [294, 296]. Thus, immune cell-intestinal epithelium microfluidics co-cultures are useful in investigating immune-mediated changes in intestinal health under bacterial exposure. In

contrast, the VSL#3 probiotic mixture prevented the EIEC-induced epithelial layer damage [294], suggesting the beneficial role commensal bacterial and their competition with pathogenic strains.

One of the three microbiota-epithelial cell models [297] was further elaborated and published as a protocol to include a neuronal chamber below the intestinal epithelial layer, yet it was not characterized and the chambers required custom preparation [298]. A feasible neuro-epithelial interface was modelled by de Hoyos-Vega et al [299] where primary human colonic organoids and primary mouse myenteric ganglia were cultured in two separate microfluidics channels linked by microgrooves. Neurons projections extended towards the colonic tissue channel within 3 days, and the culture was maintained up to 6 days [299]. Nevertheless, immunohistochemical characterization of the cultures or electrophysiological recordings were not performed. Thus, while the field of microfluidics provides promising approaches to obtain complex human intestine-like models and study host cell type or microbiota-host crosstalk, it is still being developed. The microfluidics system difficulties arise from the inherited drawbacks, including the requirement for training, reduced affordability, lack of standardization, and low throughput during the initial stages. Regarding cell biology, it is necessary to compromise for varying medium and ECM requirements for each cell type and optimize the cell culture/differentiation protocol, particularly for human induced pluripotent stem-cell(hiPSC)-derived models. A microfluidics gut-to-brain axis is relevant to understanding pathology propagation in Parkinson's disease, where lumen-exposed EECs transfer α-SYN aggregates to synaptically-connected enteric neurons [162, 163]. We focused on using iPSC-derived models due to published intestinal organoid or neuron differentiation protocols [300, 301], the ability to biobank iPSCs, and potential to perform personalized studies. Therefore, we differentiated enteric-like neurons on one channel of a commercially available microfluidics system. We aimed to derive hiPSC-derived colonic organoids or use commercial enteroendocrine cells (HuTu-80) for culture in the second channel of the chip, a microfluidics model which could be generally employed to study EEC-neuron crosstalk following bacterial cell or bacterial product exposure to EECs.

3. Aim

The cellular pathways and triggers of intestinal-derived PD pathogenesis are an active area of investigation, particularly in the context of microbiota dysbiosis. The bacterial amyloid CsgA has been shown to exacerbate neurodegenerative disease progression; however, whether and through which mechanisms it can initiate PD in the human intestine remains unclear.

The primary objective of this doctoral project is therefore to determine how CsgA impairs EEC function and whether this contributes to the initiation of PD pathogenesis. To address this, the human intestinal cell line HuTu-80 was treated with purified CsgA or curli fibers derived from *E. coli*, followed by live-cell imaging to monitor cellular uptake. A comprehensive characterization of EEC alterations associated with PD-related processes was obtained through proteomic analyses. The immune effect of CsgA-exposed EECs was studied by treating HuTu-80-derived extracellular vesicles to hiPSC-derived macrophages. A-SYN pathology was assessed following direct exposure of HuTu-80-derived EECs to CsgA or *E. coli*, as well as indirectly through treatment of peripheral neuron-macrophage co-cultures with EEC-derived extracellular vesicles. Finally, a peripheral neuron-enteroendocrine microfluidics co-culture was developed to enhance model complexity and physiological relevance, enabling the validation of candidate pathways.

To investigate the hypothesis of this project, the following points were addressed:

Part 1 – CsgA as a trigger of intestinal Parkinson's disease:

1) Do enteroendocrine cells uptake CsgA?
2) How does CsgA impact enteroendocrine cell function?
3) What is the immune response of enteroendocrine cells exposed to CsgA?
4) Can CsgA initiate α-SYN pathology in the human intestine?

Part 2 – Development of a neuron-enteroendocrine microfluidics co-culture model to monitor pathology propagation

4. Materials & Methods

4.1 CsgA cloning and sequencing

4.1.1 CsgA cloning and bacterial transformation

The plasmid pET-11d containing the CsgA-WT sequence without the secretion signal and with a 6xHis-tag at the C-terminus was provided by the Otzen laboratory. The DNA oligonucleotide of CsgA-R12343 without the secretion signal and with a 6xHis-tag at the C-terminus was obtained from Integrated DNA Technologies and was cloned into the pET-11d plasmid. Both CsgA-WT and CsgA-R12343 lacked the secretion signal (first 20 amino acids with the exception of the start codon) to maintain the produced proteins within the bacteria. CsgA-R12343 (100 ng) was digested with 0.1 U NcoI (ThermoFisher) and 0.1 U BamHI (ThermoFisher) in 1x Tango Buffer (ThermoFisher) in 50 µL total volume at 37ºC for 20 minutes. A total of 1 µg of pET-11d-CsgA-WT was digested with the same enzymes at 1 U each to obtain the digested pET-11d vector. Restriction enzymes were inactivated by a 20-minute incubation at 80ºC. Successful digestion of the vector was verified by loading 100 ng of digested DNA onto 1.5% agarose (Sigma Aldrich) gel with 4% Midori Green Advance (Dutscher). The digested vector was excised from the gel using the QIAquick Gel Extraction Kit (QIAGEN) and its concentration was quantified by nanodrop. CsgA-R12343 was ligated to pET-11d by mixing 50 ng of of vector with 11.46 ng insert, 1x T4 DNA ligase buffer (New England Biolabs), and 1 µL T4 DNA Ligase (New England Biolabs) at 20 µL total volume. The reaction mixture was incubated at room temperature for 2 hours. The ligated product was cloned in One Shot TOP10 Chemically Competent *E. coli* (ThermoFisher) following manufacturer's instructions using 100 ng/mL ampicillin (Carl Roth) to select for transformed bacteria. Ten colonies were picked to be lysed and to perform a sequencing PCR (see section below). After sequence verification, 1 ng of pET-11d-CsgA-R12343 or pET-11d-CsgA-WT was transformed in NiCo21 (New England Biolabs) following manufacturer's instructions. The plasmid and CsgA sequences are in the Appendix.

4.1.2 Polymerase Chain Reaction (PCR)

The plasmids pET-11d-CsgA-WT-6xHis and pET-11d-CsgA-R12343-6xHis were extracted from bacteria using the QuickLyse Miniprep Kit (QIAGEN). DNA input of 100 ng was mixed with 1 µM forward and reverse primers, 0.2 mM dNTPs (ThermoFisher), 1x Colorless Reaction Buffer (Promega), and GoTaq Polymerase (Promega) in ddH2O to a total of 20 µL. PCR was performed in a VeritiPro (Agilent Biosystems) thermocycler with the following settings: 95ºC for 2 minutes, 30x (95oC for 15 seconds, 57ºC for 20 seconds, 72ºC for 1 minute), 72ºC for 5 minutes, store at

4ºC. Part of the resulting product (5 µL) was tested by running a 1.5% agarose (Sigma Aldrich) gel with 4% Midori Green Advance. The remaining PCR reaction underwent sodium acetate/ethanol precipitation (120 mM sodium acetate in EtOH) and the DNA pellet was resuspended in 10 µL ddH2O. DNA input of 4 µL was mixed with 1 µM of primer (one primer per reaction), 1.4 µL of BigDye v3.1 (ThermoFisher) and 1x Terminator Sequencing buffer to a total volume of 15 µL. PCR was performed following manufacturer's instructions, prior to sodium acetate/ethanol precipitation. The DNA pellets were resuspended in 14 µL ddH2O and half of the preparation was mixed with 10 µL formamide (Sigma Aldrich) and 3 µL of ddH2O. The solution was sequenced using a 3500 Genetic Analyzer (Agilent Biosystems). PCR primer sequences are written in the Appendix (**Supplementary Table 1**). Sequences were aligned using Clustal Omega (RRID:SCR_001591, https://www.ebi.ac.uk/jdispatcher/msa/clustalo).

4.2 Protein purifications, processing, and labeling

4.2.1 CsgA monomer purification

The same purification procedure was used for both CsgA-WT and CsgA-R12343. Small cultures were grown overnight at 37°C in commercial Luria-Bertani broth (LB, Carl Roth) containing 100 µg/mL ampicillin. The next day, cultures were diluted 1:100 in 5 L Erlenmeyer flasks containing 900 mL of 1:1 LB and Terrific Broth (TB) mixture supplemented with 100 µg/mL ampicillin. TB consisted of 24 g/L yeast extract (Gibco), 20 g/L tryptone (Gibco), 0.4% v/v glycerol (Sigma-Aldrich), 17 mM KH_2PO_4 (Sigma-Aldrich) and 72 mM K_2HPO_4 (Carl Roth). When the cultures reached an optical density (OD) of 1.7, CsgA expression was induced with 100 µM isopropyl-β-D-thiogalactopyranoside (IPTG, Invitrogen). After 2 hours, the bacteria were pelleted and resuspended in lysis buffer containing 6 M guanidine hydrochloride (Sigma-Aldrich), 50 mM Tris-HCl (pH 7.3) and 40 mM imidazole (Sigma-Aldrich). Lysis was performed overnight at 4°C with gentle shaking. The following day, lysates were sonicated at 30% amplitude for 30 seconds (Q700, QSonica) and centrifuged at 17,000 × g for 20 minutes. The supernatant was filtered through a 0.22 µm PES filter (Thermo Fisher) and applied to an equilibrated 6×His fast protein liquid chromatrography (FPLC) column (two Cytiva HisTrap™ FF 5 mL columns) using an ÄKTA purifier system. The bound protein was eluted with a gradient of elution buffer (6 M guanidine hydrochloride, 50 mM Tris, 500 mM imidazole, pH 7.3). The eluted protein was concentrated using Amicon Ultra-4 3 kDa cut-off filter units (Millipore). Purified CsgA was stored at -80°C until use. For assays or treatments, the protein was desalted by passing through a HiTrap Desalting 5 mL column (Cytiva) and replacing the buffer with PBS.

4.2.2 Curli purification

Curli was purified from *E. coli* according to the published protocol Sivaranjani et al [302]. Small overnight cultures grown at 37°C were diluted 1:100 in 2 × 150 mL YESCA medium [10 g/L casamino acids (Gibco), 1 g/L yeast extract] in 250 mL Erlenmeyer flasks supplemented with 4% dimethylsulfoxide (DMSO, Sigma-Aldrich). Cultures were incubated at 26°C for 3 days at 150 rpm to promote biofilm formation. Bacteria were pelleted by centrifugation and resuspended in 10 mM Tris-HCl (pH 8.0, Sigma-Aldrich) containing RNase A (Sigma-Aldrich), DNase I (Sigma-Aldrich) and 1 mM MgCl2 (Sigma-Aldrich). The suspension was incubated at 37°C for 20 minutes, followed by treatment with lysozyme (Sigma-Aldrich) for 40 minutes and incubation with 1% SDS (Carl Roth) at 37°C for 20 minutes. Curli were pelleted by centrifugation at 15,300 × g for 10 minutes and resuspended in 10 mM Tris-HCl (pH 8.0). The suspension was boiled at 95°C for 10 minutes, followed by a second round of RNase A, DNase I and lysozyme treatment. Curli was again pelleted at 15,300 × g for 10 minutes, washed with 10 mM Tris-HCl (pH 8.0) and resuspended in 2× reducing Laemmli SDS sample buffer (Thermo Fisher). The sample was loaded onto a 12% polyacrylamide gel (with a 3% stacking gel) and electrophoresed at 120 V for 2 hours. Curli was collected from the top of the stacking gel with a needle, washed three times with distilled water and resuspended in 1 mL PBS. Protein concentration was assessed using BCA assay (ThermoFisher) and the protein was aliquoted and stored at -80ºC at a final concentration of 1.5-2.0 mg/mL.

4.2.3 CsgA and Curli labelling

CsgA-WT was labeled using the Alexa Fluor™ 594 Protein Labeling Kit (Cat #A10239, Thermo Scientific) according to the manufacturer's instructions using 200 µL of 2 mg/mL CsgA-WT diluted in PBS. Curli were labeled using the PE/Atto 594 Conjugation Kit – Lightning-link® (Cat #ab269900, Abcam) according to the manufacturer's instructions using 60 µL of 1 mg/mL sonicated curli in PBS.

4.2.4 A-SYN PFF generation

A-SYN PFFs were generated as described by Singh et al [303]. Lyophilized monomers were resuspended at a concentration of 5 mg/mL in 500 µL of A-SYN buffer containing 50 mM Tris-HCl, 150 mM KCl (Sigma Aldrich), pH 7.5. The concentration was measured at 280 nm using a nanodrop and applying the Beer-Lambert's law using a molar absorption coefficient (ε) of 5,960 M^{-1} cm^{-1}. The resuspended monomers were centrifuged at 23,000 x g for 30 minutes at 4ºC to pellet any aggregates. The supernatant (α-SYN monomers) was moved into a new tube and incubated at 37ºC for 168 hours (one week) at 1,000 rpm. Generated fibrils were centrifuged at

23,000 x g for 10 minutes at room temperature and then resuspended in 250 µL of α-SYN buffer. A small amount (5 µL) of fibrils was mixed with equal volume of 8 M guanidine hydrochloride and incubated for 1 hour at room temperature. This aliquot was used to measure fibril concentration using a nanodrop as described for the α-SYN monomers. The α-SYN PFF concentration was adjusted to 5 mg/mL, aliquoted, and stored at -80^{o}C.

4.2.5 A-SYN PFF and curli sonication

A-SYN PFFs and curli were sonicated using a cup horn attached to the Q700 sonicator (Qsonica). The temperature was set at 15oC, and sonication was performed with the following settings: 30% amplitude, 22.5 minutes of sonication time, 3 seconds on, 2 seconds off. The sonicated proteins were used immediately afterwards for cell treatments.

4.3 Bacteria cultures

4.3.1 *E. coli* culture for biofilm formation

For biofilm formation, *E. coli* K12 (WT) and *E. coli* K12 Δ*csgBAC* [107] were grown on YESCA with 20 g/L agar (Gibco) plates for 48 hours at 26°C. To assess biofilm formation, 25 µg/mL of Congo Red (Sigma-Aldrich) was added either to the YESCA agar prior to preparing the plates or directly into the liquid YESCA medium. Bacterial optical density was measured at 600 nm using a VICTOR Nivo Microplate Reader. A standard curve of bacterial ODs with known colony forming units per mL (CFU/mL) was prepared by growing serial dilutions on agar plates and counting the colonies. These values were used to convert bacterial ODs to CFU/mL for *E. coli*-HuTu-80 co-cultures.

4.3.2 *E. coli*-HuTu-80 co-culture

For the co-culture of HuTu-80 cells with *E. coli*, bacteria were first scraped off the agar plates into 1 mL of YESCA medium, and the OD600 was measured. An MOI of 100 was used for 4 hours of co-culture, after which 20 µg/mL of gentamycin (Carl Roth) were added. The medium was refreshed every other day, with fresh *E. coli* added each time, for a total duration of 7-10 days in vitro (DIV) of the HuTu-80 culture.

4.3.3 *E. coli* bacterial growth assay

For the effect of HuTu-80 supernatant and α-SYN on *E. coli* growth, the strain *E. coli* K12 was grown overnight in LB medium at 37^{o}C at 200 rpm. Conditioned HuTu-80 supernatant was concentrated approximately 13-fold using Amicon Ultra-4 3 kDa cut-off filter units (Millipore) by

centrifuging at 3,220 x g for 30 minutes at 4°C. These filter units remove any antibiotics from the conditioned medium. Bacterial OD at 600 nm was measured, the bacteria were pelleted by centrifugation at 3,220 x g for 5 minutes and resuspended at OD = 1. Concentrated conditioned HuTu-80 supernatant at 50% v/v, or ampicillin (100 µg/mL) were mixed with *E. coli* at a final volume 200 µL in LB medium, and each sample was pipetted in triplicate in 96-well Half Area Black/Clear Flat Bottom Polystyrene non-binding surface Microplates (Corning). The starting OD for each experiment is indicated in the respective graphs. The plate was sealed with optical adhesion film and was placed in a VICTOR Nivo (Revvity) spectrophotometer pre-equilibrated at 37°C. Bacteria OD at 600 nm was measured every 2 hours for up to 16 hours.

4.3.4 *A. muciniphila* culture

A. municiphila was grown by inoculating $2x10^9$ CFU/mL in 50 mL brain-heart infusion broth (BHI, 37 g per 1 L of ddH_2O, Sigma-Aldrich) and incubating at 37°C for 42 hours under anaerobic and static conditions at Benoit Chassaing's laboratory at Paris Pasteur Institute. The bacteria were centrifuged at 3,220 x g for 20 minutes at 4°C, and the supernatant was concentrated in Amicon Ultra-4 3 kDa cut-off filter units by centrifuging twice at 3,220 x g for 30 minutes at 4°C. The concentrated supernatant was passed through a 0.22 µm PES filter and stored as aliquots at -80°C. Concentrated BHI medium was used as the negative control.

4.4 Cell culture

4.4.1 HuTu-80 cell culture

HuTu-80 (RRID:CVCL_1301, Cytion) were cultured in Dulbecco's modified Eagle's medium (DMEM) with 10% FBS and 1X Penicillin/Streptomycin (all from Gibco). Medium was changed twice a week, the cells were split once a week with Accutase (Stem Cell Technolgoies), and they were grown at 37°C and 5% CO_2. For experiments cells were seeded at a density of 200,000 cells per well in 12-well plates for 3 days or 10,000 cells per well in 6-well plates (Corning) for 8-11 days of culture.

4.4.2 Caco-2, Colo-320DM, and HT-29 cells

Caco-2 (Cat #300137, RRID:CVCL_0025, Cytion) and HT-29 cells (Cat #300215, RRID:CVCL_0320, Cytion) were cultured using cultured using EMEM with 2 mM Glutamine, 2.2 g/L NaHCO3, and EBSS (Cat #820100a, Cytion). Colo-320DM (Cat #300153, RRID:CVCL_0219, Cytion) were cultured using Ham's F12 with 1.0 mM stable Glutamine, 1.0 mM Sodium pyruvate, and 1.1 g/L NaHCO3 (Cat #820600a, Cytion). Cells were seeded at a density of 300,000 cells per

well of a 12-well plate and medium was refreshed twice a week. Confluent 6-well plates were lysed and the protein was quantified as described in the “Western blot” section.

4.4.3 THP-1 cell culture

THP-1 cells (RRID:CVCL_0006) were purchased from Sigma Aldrich and cultured in RPMI-1640 (Sigma Aldrich) with 10% FBS, 1X GlutaMAX (Gibco), and 1X Penicillin/Streptomycin. Cells were maintained at 37°C in a humidified incubator with 5% CO_2 and split once a week. For differentiation into macrophages, THP-1 cells were seeded at a density of 800,000 cells per well in 12-well plates (Corning) and treated with 50 ng/mL phorbol 12-myristate 13-acetate (PMA, Sigma-Aldrich) for 48 hours. Following differentiation, the cells were cultured for an additional 48 hours without PMA before treatment. Cells were then exposed to PBS (Gibco), CsgA-WT, CsgA-R12343, or Curli for 6 hours. After treatment, the supernatant was collected, and the cells were lysed for further analysis.

4.4.4 Human iPSC and neural precursor cell (NPC) maintenance

KOLF2.1J (RRID:CVCL_B5P3, Jackson Laboratory) and control cell line 1 iPSCs [304] were kept on 300 µg/mL Matrigel-coated plates and were maintained in mTeSR plus (Stem Cell Technologies) medium at 37 °C and 5% CO_2. Medium was changed every other day, and cells were split with Accutase once a week. Control cell line 1 NPCs (previously derived using the protocol from Reinhardt et al [301]) were kept on 300 µg/mL Matrigel-coated plates and were maintained in NPC basal medium [50% Advanced DMEM/F12 (Gibco), 50% Neurobasal (Gibco), 0.5x N-2 (Fisher Scientific), 0.5x B-27 without vitamin A (ThermoFisher), 1x GlutaMAX, 1x Penicillin/Streptomycin] supplemented with 3 µM CHIR99021 (Sigma), 0.5 µM purmorphamine (Merck), and 150 µM ascorbic acid (Sigma) at 37 °C and 5% CO_2. Medium was changed every other day, and cells were split with Accutase once a week. Y-27632 (Selleck Chemicals) was included during the splitting, freezing, and thawing of the cells, and was removed the following day.

4.4.5 Embryonic body differentiation for macrophage precursor production

Human induced pluripotent stem cells were detached with Accutase and seeded in an AggreWell 800 (Stem Cell Technologies) at a density of 4 million cells per well. The differentiation was performed using the protocol from Haenseler et al [305]. Medium was changed daily between day 0 and day 7. The medium between day 0 and 3 consisted of mTeSR Plus supplemented with 50 ng/mL BMP4 (Proteintech), 50 ng/mL VEGF (ImmunoTools), and 20 ng/mL SCF (ImmunoTools). On day 4, embryonic bodies (EBs) were collected from the AggreWell and were transferred to a

40 µm strainer over a 50 mL falcon tube. Then, the EBs were moved to a 6-well plate using a cropped tip at a density of 15-20 EBs per well. From day 4 onwards, the medium consisted of basal factory medium of X-Vivo15 (Biozym) containing 1X Glutamax (Gibco), 1X Penicillin/Streptomycin, and 55 µM b-mercaptoethanol (Sigma) supplemented with 100 ng/mL M-CSF (Proteintech) and 25 ng/mL IL-3 (Immunotools). From this point onwards the medium was changed once a week.

4.4.6 Macrophage differentiation and treatments

Floating macrophage precursors were collected from the medium of producing EB factories and were seeded at a density of 200,000 cells per well in a 12-well plate pre-coated with Matrigel (Corning). The precursors were cultured for 7 DIV with basal factory medium supplemented with 100 ng/mL M-CSF. The medium was changed every 3-4 days. After 7 DIV, the macrophages were treated with HuTu-80 EVs at a concentration of 2 µg/mL for 48 hours. For the 48 hours endpoint, the supernatant and cell lysates were collected for cytokine measurements and protein quantification with the bicinchoninic acid (BCA, Fisher Scientific) assay, respectively. If the experiment continued to evaluate the macrophage response to a second inflammatory trigger (LPS), cells were washed and allowed to rest in macrophage medium for 48 hours. Macrophages were then treated with 100 ng/mL LPS (or H_2O control) for an additional 24 hours prior to supernatant and cell lysate collection.

4.4.7 Peripheral neuron differentiation

Peripheral neurons were differentiated from NPCs using the protocol from Reinhardt et al [301]. NPCs were seeded at a density of 1.4 million cells / well in a 6-well plate pre-coated with Matrigel in NPC basal medium supplemented with 3 µM CHIR99021, 0.5 µM purmorphamine, and 150 µM ascorbic acid. Two days post-seeding, the medium was switched to NPC basal supplemented with 3 µM CHIR99021 to initiate differentiation (Day 0). On day 2, 10 ng/mL BMP4 were supplemented to NPC basal medium. The medium was refreshed every other day until day 10. On day 10, the medium was switched to final neuronal medium [NPC basal medium supplemented with 10 ng/mL BDNF (Peprotech), 10 ng/mL GDNF (Peprotech), and 500 µM dibutyryl-cAMP (MedChem Express)] for 24 hours. On the same day, 12-well plates were pre-coated with Matrigel for 30 minutes at 37°C followed by 1 µg/mL laminin (ThermoFisher) diluted in PBS overnight at 37°C. On day 11, cells were split with Accutase and seeded at a density of 100,000 cells / cm^2 (corresponding to 380,000 cells in a well of a 12-well plate) in final neuronal medium supplemented with 10 µM Y-27632 (Selleck Chemicals). On day 12, the medium was

refreshed to remove Y-27632, and cells were fed by half medium changes every other day. Cells were considered mature from day 21 onwards.

4.4.8 Peripheral neuron and macrophage co-culture

Induced PSC-derived macrophages precursors were first cultured in 12-well plates for 7 days as described in the “Macrophage differentiation and treatments” section. Peripheral neurons and macrophages were combined on day 21 of the peripheral neuron differentiation protocol, considered day 0 of the co-culture. Macrophages were detached with a 5-minute Accutase incubation and were seeded at a density of 380,000 cells / well of a 12-well plate either with control line 1 NPC-derived peripheral neurons or alone. On day 1, the cells were used for treatments.

4.4.9 Microfluidics peripheral neuron/enteroendocrine cell co-culture

Netri Dualink Ultra microfluidics chips were activated and hydrated as by manufacturer’s instruction and were coated with 300 µg/mL Matrigel in DMEM for 30 minutes at 37^{o}C followed by 10 µg/mL laminin in PBS at 37oC overnight. Control NPC line 1 [304] neural crest-like cells on day 11 of differentiation were seeded in one side channel of the microfluidics chip at a density of 150,000 cells / cm^2 in neuronal maturation medium. The medium was also added in the other channels. Following 48 hours, the volume of the second side channel was reduced to half but the medium composition included double BDNF and GDNF concentration (20 ng/mL) to promote neuronal projection growth towards this channel. Half-medium changes were performed every other day in the chips following manufacturer’s instructions for the whole duration of the protocol. At day 22 of the peripheral neuron differentiation protocol (11 days after seeding the NCLCs in the chips), HuTu-80 were seeded in the second channel at a density of 15,000 cells / cm^2 in 50% Advanced DMEM/F12, 50% Neurobasal, 0.5x N-2, 0.5x B-27 without vitamin A, 1x GlutaMAX, 10% FBS, 1x penicillin/streptomycin, 10 ng/mL BDNF, 10 ng/mL GDNF, and 500 µM dibutyryl-cAMP. The medium in the middle channel consisted of neuronal maturation medium. The cells were kept in culture until day 29 of the peripheral neuron differentiation protocol (day 7 of the co-culture).

4.4.10 Intestinal organoids

Intestinal organoids were generated from iPSCs following the protocol from Crespo et al [300]. 80-85% confluent hIPSCs were switched to RPMI medium supplemented with 1x GlutaMAX/Penicillin/Streptomycin (basal medium 1) with 3 µM CHIR and 100 ng/mL Activin A (ImmunoTools) on day 1. The medium was changed to basal medium 1 with Activin A and 0.2%

FBS on day 2. The FBS concentration increased to 2% on day 3. On days 4-7, basal medium 1 was supplemented with 1x B27 without vitamin A (basal medium 2), 3 μM CHIR, and 500 ng/ml FGF4 (Proteintech) and the medium was changed daily. On day 8, the cells were switched to the final human intestinal organoid (HIO) medium, which consisted of basal medium 2 with 3μM CHIR, 300 nM LDN193189 (Axon MedChem), and 100 ng/ EGF (Sigma-Aldrich). The medium was changed every other day and on days 15-20 floating intestinal organoids were collected with a needle and a tip and were cultured in Matrigel domes. HIOs in domes were split every 8-12 days and were kept in culture for up to 10 passages. For culture in 2D using 12-well plate transwells (CellQART), organoids were dissociated as single cells using Accutase for 10 minutes and gentle pipetting. Cells were centrifuged at 300 x g for 3 minutes prior to being seeded at a density of 3.75 x 10^5 cells / cm^2. Cells were allowed to grow until the covered the whole surface of the transwell (8-10 DIV).

4.4.11 Cell treatments

HuTu-80 cells were treated with 50 μg/mL CsgA-WT or CsgA-R12343, or 20 μg/mL sonicated curli fibers for 48 hours. PBS was used as a negative control. Lysosomal degradation was blocked by use of 10 nM bafilomycin A1 (bafA1, Invivogen) or 10 μM chloroquine (CQ, Invivogen) for 4 hours prior to amyloid treatment, and an additional 48 hours post-treatment. IFNg was added at a concentration of 0.2 ng/mL every other day for up to 10 DIV (for α-SYN aggregation experiments). A-SYN monomers were treated to HuTu-80 at a concentration of 50 μg/mL for 48 hours and were refreshed every 48 hours for up to 10 DIV. A-SYN PFF were treated at a concentration of 0.5 μM every other day for HuTu-80 or 2 μM at day 1 and day 3 for the neuron/macrophage co-cultures (concentrations corresponding to monomers). CBE (MedChemExpress) was added at a concentration of 50 μM for 48 hours and refreshed every 48 hours for experiments up to 10 DIV. Lipopolysaccharide (LPS) from *E.coli O111:B4* (Invivogen) was added at a concentration of 10, 100, 1000 ng/mL for 48 hours and was refreshed every 48 hours for up to 10 DIV. Sodium nitrite ($NaNO_2$, Sigma-aldrich) was added at a concentration of 20 μM for 48 hours and was refreshed every 48 hours for up to 10 DIV. A summary of all reagents is given on the table below.

Table 1. Proteins and chemicals used for HuTu-80 treatments.

Reagent	Concentration	Duration	Up to 10 DIV?
CsgA-WT	50 µg/mL	48 hours	In certain experiments
CsgA-R12343	50 µg/mL	48 hours	No
Sonicated curli	20 µg/mL	48 hours	In certain experiments
BafA1	10 nM	4+48 hours	No
CQ	10 µM	4+48 hours	No
IFNg	0.2 ng/mL	48 hours	In certain experiments
A-SYN monomers	50 µg/mL	48 hours	Yes
A-SYN PFF	0.5 µM (for HuTu-80)	48 hours	Yes
CBE	50 µM	48 hours	In certain experiments
LPS	10, 100, 1000 µg/mL	48 hours	Yes
$NaNO_2$	20 µM	48 hours	Yes
***A. muciniphila* conditioned medium**	1% or 5%	48 hours	Yes (for 1%) No (for 5%)
E. coli* WT or Δ*csgBAC	MOI 100	48 hours	Yes

THP-1 derived macrophages were treated with 50 µg/mL CsgA-WT or CsgA-R12343, or 20 µg/mL sonicated curli fibers for 48 hours. PBS was used as a negative control. Human iPSC-derived macrophages were treated on day 7 with 2 µg/mL HuTu-80 extracellular vesicles for 48 hours. On day 7, LPS was used as a positive control for cytokine release at a concentration of 100 ng/mL for 24 hours. For certain experiments, macrophages were washed and allowed to recover for 48 hours following EV treatment, when 100 ng/mL LPS or vehicle control (H_2O) were added for an additional 24 hours. On day 1 of the co-culture, human iPSC-derived peripheral neuron/macrophage co-cultures were treated with 2 µg/mL EVs derived from HuTu-80 treated with PBS, CsgA-WT, or CsgA-R12343 or curli. A-SYN monomers were co-treated with EVs at a concentration of 50 µg/mL. Certain wells were only treated with 50 µg/mL α-SYN monomers or 2 µM sonicated α-SYN pre-formed fibrils, as negative and positive controls, respectively, for the α-SYN seed amplification assay (SAA). On day 3, a second treatment with the same conditions was performed. The cells were washed on day 5, a medium change was performed on day 7, and cells sorted on day 8.

4.4.12 HuTu-80-TMEM192-3xHA line generation

HuTu-80 stably expressing TMEM192-3xHA were generated by lentiviral (ΔU3 SIN) transduction with pLJC5-Tmem192-3xHA (RRID:Addgene 102930). Transduction was performed by splitting the cells at 60% confluence and infecting them with 10 µL of virus (or medium as the non-infected control) using 1 µg/mL polybrene (Sigma-Aldrich) in 5 mL of DMEM without FBS or antibiotics. After 6 hours, 5 mL of complete DMEM (supplemented with FBS and penicillin/streptomycin) were added to the cells. Forty-eight hours post-infection, cells were selected in medium containing 0.5 µg/mL puromycin (Invivogen) for 72 hours, after which the concentration was reduced to 0.25 µg/mL for an additional 72 hours. Single cells were then plated in a 96-well plate (Corning) with selection medium to allow for colony formation. The resulting colonies were maintained in culture in standard growth medium without puromycin and were biobanked prior to experimentation.

4.5 Characterization Assays

4.5.1 Thioflavin-T (ThT) assay

Freshly purified CsgA-WT or CsgA-R12343 monomers, or sonicated curli fibers were mixed with 20 µM thioflavin T (ThT; Sigma-Aldrich, T3516) in PBS (pH 7.4) at the concentrations and time periods indicated in the respective figure legends. For cross-seeding experiments, 2 µM CsgA-WT were incubated with 50 µg/mL α-SYN monomers. All mixtures were incubated at 37ºC under constant shaking conditions. Fluorescence readings (excitation at 450 nm, emission at 510 nm) were taken every 5 minutes for the first 24 hours and then every 24 hours thereafter. The assays were performed in a 96-well black/clear flat-bottomed polystyrene non-binding surface microplate (Corning) using the VICTOR Nivo Microplate Reader.

4.5.2 Transmission electron microscopy (TEM)

A total of 20 µM of pure CsgA-WT, CsgA-WT-594, CsgA-R12343, curli, or sonicated curli were loaded on Formvar/Carbon Supported Copper Grids (Electron Microscopy Sciences) for 2 minutes. Excess liquid was discarded from the grid using a Whatman Quantitative Filter Paper (Sigma-Aldrich). A total of 2 µg of extracellular vesicles were loaded on the same grids until the droplet dried. Negative staining was performed by a 2-minute incubation (for bacterial amyloids) or a 30-second incubation (for EVs) of the grids with 2% uranyl acetate solution. The dye was first passed through a 0.22 µm filter to remove chunks. Excess liquid was removed using a Whatman filter paper. For bacterial amyloids, the grids were washed three times with 2-minute incubations of double-distilled water (ddH_2O). Grids were stored at RT until imaging. Image acquisition was

performed by the Quant platform of the Paris Brain Institute (ICM) using a JEOL JEM-1011 electron microscope.

4.5.3 Nanoparticle Tracking Analysis (NTA)

Extracellular vesicles samples in (1 µg in 100 µL) of PBS pH 7.4 were diluted 1 in 250. NTA analysis (particle concentration, size) was performed using the ZetaView x30 (Particle Metrix) instrument and the ZetaView 1.1 software (Particle Metrix). The analysis was performed by the EVe facility at the Institute for Regenerative Medicine and Biotherapy at Montpellier.

4.5.4 Coomassie staining

SDS-page gels were washed three times for 10 minutes each in distilled water and incubated with Colloidal Coomassie solution overnight at room temperature. The staining solution consisted of 0.02% (w/v) Coomassie Brilliant Blue G 250 (Merck), 5% (w/v) $NH_4Al(SO_4)_2$ (Merck), 10% (v/v) ethanol (VWR), and 2% (v/v) ortho-phosphoric acid (Sigma). The gel was washed three 5-minute washes with ddH2O prior to imaging using a ChemiDoc MP (BioRad). The gel was imaged using a ChemiDoc MP.

4.6 Experimental Assays

4.6.1 Extracellular vesicle purification

Extracellular vesicle-free FBS was generated by ultra-centrifuging FBS at 100,000 x g using the rotor SW41 (Beckman) overnight at 4°C. HuTu-80 were cultured in extracellular vesicle-free medium for the duration of the treatments (1x 10 cm dish per condition). Following the 48-hour cell treatment, cell culture supernatant was collected and subjected to serial centrifugations of increasing g force as described by Théry et al [306]. All centrifugations were performed at 4°C. Initially, the supernatant was centrifuged at 300 x g for 5 minutes to pellet the cells. The resulting supernatant was centrifuged at 2,000 x g for 20 minutes, followed by centrifugation at 10,000 x g for 30 minutes to pellet dead cells and debris, respectively. The new supernatant was ultracentrifuged at 100,000 x g for 80 minutes using the rotor SW41 to pellet the extracellular vesicles. The supernatant was discarded, and the pellet was resuspended in 1.5 mL PBS and transferred to 1.5 mL polypropylene ultracentrifuge tubes to be centrifuged at 100,000 x g for 70 minutes using the rotor TLA-55 (Beckman). The supernatant was again discarded and the extracellular vesicles were resuspended in PBS (for transmission electron microscopy, nanoparticle tracking analysis, or macrophage treatment) or lysed directly with 50 µL of 1% Triton X (Carl Roth) in TBST [Tris-Buffered Saline containing 0.1% Tween-20 (Sigma-Aldrich)]

supplemented with protease and phosphatase inhibitors (for Western blot or ELISA). The preparations were kept at 4°C (in PBS) up to 3 days or at -80°C (as lysates). Protein concentration was determined using the MicroBCA Protein Assay Kit (ThermoFisher).

4.6.2 A-SYN seed amplification assay (SAA) by real-time quaking-induced conversion (RT-QuIC)

Peripheral neuron or macrophage cell lysates (1.6 µg in 85 µL in 1% Triton X in PBS) of each treatment condition and biological replicate were prepared. Cell sample (1 µL) was transferred into tubes containing 120 µL PBS. For each test, 2 µL of the diluted sample was plated in 98 µl of reaction buffer composed of 40 mmol/L phosphate buffer (ThermoFisher), 170 mmol/L NaCl, 10 µmol/L ThT, 0.1 mg/ml recombinant α-SYN, and 0.0015% SDS, and 6 silica beads of 0.8 mm diameter (OPS Diagnostic). The plate was sealed with a plate sealer film (Nalgene Nunc International, Rochester, NY) and then incubated at 42°C in a BMG FLUOstar Omega plate reader with cycles of 1-minute shaking (400 rpm double orbital) and 1-minute rest. The fluorescence measurements (450 ± 10 nm excitation and 480 ± 10 nm emission; bottom read) were taken every 45 min. Three technical replicate reactions were tested for each sample. Single reactions were considered positive if their fluorescence exceeded 10% of the plate's maximum. Samples were considered positive when 2 out of 3 replicate wells exceeded the ThT threshold within the established cut-off at 30 h.

4.6.3 Enzyme-linked immunosorbent Assay (ELISA)

TNFα levels were measured in the diluted (1:50) supernatant of THP-1-derived macrophage culture medium using the Human TNF-alpha DuoSet ELISA kit (R&D Systems, DY210), according to the manufacturer's instructions. A-SYN levels in HuTu-80 cell supernatant (final dilution 1:500) or EV lysates (final dilution 1:50) were quantified using the LEGEND MAX Human α-Synuclein (Colorimetric) ELISA Kit (BioLegend, 448607), according to the manufacturer’s instructions. Measurements were taken at 450 nm and 570 nm using the VICTOR Nivo (Revvity) spectrophotometer.

4.6.4 Chemokine and cytokine multiplex measurements

Chemokines measurements were performed in HuTu-80 supernatants 48 hours post-treatment using the LEGENDplex human chemokine panel 1 (13-plex, Biolegend #740985) following manufacturer’s instructions and using undiluted samples. Cytokine measurements were performed in KOLF2.1J macrophage supernatants 48 hours post-treatment using the LEGENDplex human inflammatory panel 1 (Biolegend #740809). Samples were either undiluted

or diluted 1:100 to obtain cytokine data within the assay's standard curve. The readouts were performed using the Novocyte Penteon flow cytometer (Agilent) with the following channels: B572 (for PE) and R660 (for APC). Data was analyzed using the Qognit online software (Biolegend).

4.6.5 TMEM192-3xHA Lysosomal Immunoprecipitation

Lysosomal immunoprecipitation was performed by modifying the protocol published from Eapen et al [307]. Cells grown in 10-cm dishes (Falcon) were washed twice with ice-cold PBS (Gibco) and scraped into PBS containing protease and phosphatase inhibitors (ThermoFisher). Cells were centrifuged at 300 × g for 4 minutes at 4°C and resuspended in PBS with inhibitors. An aliquot of 25 µL (2.5%) was used as the input (total cell lysate) by adding 1× reducing Laemmli Sodium Dodecyl Sulfate (SDS) sample buffer (Fisher Scientific) and heating at 95°C for 10 minutes. The remaining cells (975 µL) were gently homogenized by passing them 25 times through a 21G needle (Terumo) and samples were centrifuged at 1,000 × g for 2 minutes at 4°C to remove debris. The supernatant was incubated with 150 µL of anti-HA magnetic beads (ThermoFisher), pre-washed three times in PBS, for 10 minutes at 4°C. Using a magnetic separation rack (New England Biolabs), the flow-through was collected in separate tubes, and the beads containing the immunoprecipitated lysosomes were washed five times with ice-cold PBS. The lysosomes were eluted with 20 µL of 50 mM NaOH on ice for 5 minutes and neutralized with 20 µL of 25 mM HCl (Sigma-Aldrich). Lysosomes were lysed by adding 20 µL 3% SDS (Carl Roth) in 150 mM HEPES (Sigma-Aldrich), supplemented with fresh protease and phosphatase inhibitors. The mixture was incubated at 95ºC for 5 minutes, and protein concentration was determined using the BCA assay. Samples were analyzed by proteomics or Western blot.

4.6.6 Western blot

Cell pellets (HuTu-80, HuTu-80-TMEM192-3xHA, Caco-2, Colo-320DM, or HT-29) were lysed in 1% Triton X in TBS supplemented with fresh protease and phosphatase inhibitors by incubation on ice for 30 minutes. Lysates were centrifuged at 13,000 x g for 10 minutes at 4ºC, and protein concentration was determined using the BCA Protein Assay Kit. Lysosomes and extracellular vesicles were lysed as described in the respective "Methods" sections. Whole-cell lysates (30–50 µg), lysosomal fraction lysates (5-8 µg), or extracellular vesicle lysates (1 µg) were mixed with 1x reducing Laemmli SDS sample buffer and boiled at 95ºC for 10 minutes prior to loading onto pre-cast 4–12% Bis-Tris Protein Gels (GenScript). Proteins were transferred to methanol-activated PVDF membranes at 1.3 A and 2.5 V over 7 minutes using the Trans-Blot Turbo System (BioRad). Membranes were blocked in TBST (TBS containing 0.1% Tween-20) with 5% skimmed milk (Dutscher) or 5% bovine serum albumin (BSA, Fisher Scientific). Primary antibody incubation

was performed overnight at 4°C in the blocking solution. The following day, the membranes were washed three times with 5-minute TBST incubations prior to secondary antibody (HRP-conjugated or fluorescence-conjugated) incubation for 1 hour at room temperature. Following three TBST washes, HRP-conjugated antibodies were detected using SignalFire Elite ECL Reagent (Cell Signalling Technology). Image acquisition was performed using a ChemiDoc MP. Membranes were stripped by two 10 minute-incubations with soft stripping buffer [1.5% (w/v) glycine (Sigma Aldrich), 0.1% (w/v) SDS, 1% (v/v) Tween 20, pH 2.2] if the new set of antibodies did not overlap with the bands of the previous blots. The antibodies are listed in the Appendix (**Supplementary Tables 2-3**). Total membrane protein staining was performed with Ponceau S solution (Sigma).

4.6.7 Cell lysis for detergent-soluble/insoluble fractionation

The protocol to separate detergent-soluble and detergent-insoluble protein lysate fractions was derived from Stojkovska and Mazulli [308]. HuTu-80 cell pellets from a 6-well plate were collected and lysed with 100 uL Triton X extraction buffer consisting of 1% Triton X, 150 mM NaCl (Sigma), 20 mM HEPES (pH 7.4), 1 mM EDTA (Sigma), 1.5 mM $MgCl_2$, 10% glycerol, 50 mM NaF (Sigma), 2 mM Na_3VO_4 (Sigma), 0.5 mM PMSF (Sigma), and protease/phosphatase inhibitors. The samples were incubated in 1.5 mL tubes on a rotating wheel at 45 rpm for 30 minutes at 4°C. The samples were frozen/thawed three times by transferring them from dry ice to a 37°C water bath to disrupt lipid bilayers. Lysates were ultracentrifuged at 100,000 x g for 35 minutes at 4°C using the rotor TLA-55. The supernatant, corresponding to the Triton X-soluble fraction, was transferred to a new 1.5 mL tube and left on ice. The pellet was washed three times with 50 µL of Triton X extraction buffer and then resuspended in 60 µL SDS extraction buffer consisting of 2% SDS, 50 mM Tris (pH 7.4), and protease/phosphatase inhibitors. The samples were boiled at 100°C for 10 min, followed by sonication in a Q700 sonicator with a cup horn at 30% amplitude for 10 minutes at 20°C. The samples were boiled once again at 100°C for 10 minutes, then centrifuged 100,000 x g for 35 minutes at room temperature. The supernatant was moved into a new 1.5 mL tube and corresponded to the Triton X-insoluble fraction. Protein concentration was determined by the BCA assay kit, and 50 µg of each fraction were loaded for Western blot.

4.6.8 Seahorse

HuTu-80 cells were seeded in Seahorse XFe96/XF Pro Cell Culture Microplates (Agilent) at a density of 15,000 cells per well. The following day, the cells were treated with PBS, CsgA-WT, CsgA-R12343, or curli as in the “Cell treatments” Method’s section adjusting for a final volume of 150 µL per well and including six technical replicates per condition. The wells A1, H1, A12, and

H12 were empty (calibration blank). Before running the assay, the cells were washed once with 100 µL Seahorse XF DMEM assay medium pack, pH 7.4 (Agilent) and maintaining the cells in 180 µL of Seahorse medium. The mitochondrial respiration assay was performed using the Equipment XFe 96 Extracellular Flux Analyzer (Agilent) at the SFR Necker Metabolic Analyses platform. The following drug concentrations were used: 2 µM oligomycin, 2 µM FCCP, 1 µM antimycin A, and 1 µM rotenone. Basal respiration was calculated by subtracting the oxygen consumption rate (OCR) after rotenone/antimycin A treatment from the OCR without drug treatment. ATP-linked respiration was calculated by subtracting the OCR after oligomycin treatment from the OCR without drug treatment. Maximal respiratory capacity was calculated by subtracting the OCR after rotenone/antimycin A treatment from the OCR after FCCP treatment [309]. Data were exported from the Seahorse Analytics software (Agilent) and were analyzed using GraphPad prism.

4.6.9 Proteasome Assay

The chymotrypsin-like activity of the proteasome was measured using the substrate Suc-Leu-Leu-Val-Tyr-AMC (MedChemExpress). HuTu-80 protein lysates (10 µg) were mixed with assay buffer containing 50 mM Tris-HCl pH = 7.5, 100 mM KCl, 0.5 mM $MgCl_2$, 25 µg/mL BSA, and 0.1 mM ATP (Sigma-Aldrich) to a total volume of 100 µL. Each sample was split into two separate tubes, one containing 25 µL of 3 µM bortezomib (MedChemExpress) and another containing DMSO diluted in assay buffer. The substrate was diluted to 20 µM in 150 µL assay buffer and added to each sample to a final concentration of 10 µM. Each sample was pipetted in three technical triplicates (45 µL per well) in a low-binding half-area black wall 96-well plate (Corning). The plate was placed into a VICTOR Nivo (Revvity) spectrophotometer set at 37°C, and measurements were taken every 5 min for up to 2 hours using an excitation wavelength of 340 nm and an emission wavelength of 450 nm.

4.6.10 Intestinal organoid fixation and cryosectioning

Organoids were fixed in 4% paraformaldehyde (PFA, Carl Roth) for 2 hours at room temperature, followed by three PBS washes, and an overnight incubation in 30% sucrose at 4°C. The following day, organoids were embedded with Tissue-Tek OCT Compound (Gentaur) in Tissue-Tek Cryomold Molds/Adapters, Sakura Finetek, Biopsy Cryomold, L x W x D=10 mm x 10 mm x 5 mm (Sakura Finetek USA Inc) and frozen by immersion in a -80°C isopropanol bath. Embedded samples were stored at -80°C until sectioning. Organoids were cryosectioned at 20 µm thickness using an Epredia CryoStar NX50 cryostat at -20°C. Eight sections spanning the whole organoid

were placed on each slide, and slides were stored at -80ºC until they were immunostained as described in the following section.

4.6.11 Cell fixation and immunostaining

Cells were fixed with 4% PFA for 10 minutes and washed three times with 5-minute PBS incubations. After fixation, cells were permeabilized and blocked with 10% normal goat serum containing 0.1% (increased to 0.5% for organoid sections) Triton X in TBS for 1 hour at room temperature. Normal donkey serum was used instead of normal goat serum for secondary antibodies produced in goat. Primary antibodies were incubated in 5% normal goat/donkey serum containing 0.1% (increased to 0.5% for organoid sections) Triton X in TBS overnight at 4°C. The following day, samples were washed and secondary antibodies were applied in the same Triton X buffer for 2 hours at room temperature. A list of the antibodies used can be found in the Appendix (**Supplementary Tables 2-3**). DAPI (Sigma) staining was performed at 0.1 µg/mL for 10 minutes at room temperature. Wheat germ agglutinin (WGA) Alexa Fluor 488 conjugate (ThermoFisher) was used at 3.33 µg/mL for 15 minutes after secondary antibody incubation. Phalloidin-594 (Abcam) was diluted 1:500 in PBS and incubated for 15 minutes at room temperature after secondary antibody incubation. Coverslips were mounted onto microscope slides using Fluorescence Mounting Medium (DAKO) and allowed to dry before imaging. In the case of organoid sections, a glass cover was placed on top of the stained slides covered with Fluorescence Mounting Medium. Cells in microfluidics devices were imaged in PBS, since the mounting medium was too viscous to enter the channels. Images were captured using a ZEISS Axio Observer Z1 equipped with a Yokogawa CSU-X1 spinning disc head and an SD ORCA-Flash 4.0 S-CMOS camera (C1144022CU) with 40x (NA 1.4) or 63x (NA 1.46) oil objectives at the Imagine Institute Cell Imaging Platform.

4.6.12 Live cell imaging

Cells were cultured on 25 mm round coverslips (Carl Roth) or in u-Slide 8-well glass-bottom chambers (Ibidi). HuTu-80 were treated with CsgA-WT-594 or curli-594 as in the “Cell Treatments” section. Prior to treatment with dyes, cells were washed once with PBS. The following dyes and markers were used to label cellular compartments: lysosomes - 200 nM LysoTracker Blue DND-22 (Thermo Fisher) for 30 minutes; early endosomes - CellLight Early Endosomes-GFP, BacMam 2.0 (Thermo Fisher) at 30 particles per cell, incubated overnight; mitochondria – 100 nM MitoTracker Green (ThermoFisher) for 10 minutes. Prior to imaging, cells were washed three times with PBS and fresh growth medium was added. Live cell imaging was performed using a ZEISS Axio Observer Z1 equipped with a Yokogawa CSU-X1 spinning disc head and an SD

ORCA-Flash 4.0 S-CMOS camera (C1144022CU) at the Imagine Institute Cell Imaging Platform. A 63× oil immersion objective (NA 1.46) was used for image acquisition. Five images per condition and biological replicate were taken at different positions within each well.

4.6.13 Image quantification

ImageJ (RRID:SCR_003070, version 1.54p) was used for image quantification. Lysosomal counts were performed by thresholding (Image>Adjust>Threshold) the image to separate the LysoTracker or CsgA-WT-594/Curli-594 signal from the background. Curli-594 co-localization with LysoTracker was quantified by applying a threshold to the corresponding channel and using "Image Calculator" with the operation "AND" to filter for the co-localizing signal. The number of LysoTracker+ particles, the average area (in μm^2) of the LysoTracker+ or curli-594+/LysoTracker+ particles per image, and the degree of co-localization (expressed as percentage of curli-594+/LysoTracker+ particles versus LysoTracker+ particles) were measured and plotted.

4.6.14 Flow Cytometry

HuTu-80 cells were washed with PBS, detached by a 5-minute Accutase incubation, counted by trypan blue with LUNA-II (Logos Biosystems), and equal number of cells were stained in 100 µL buffer (described below). Dead cell staining was initially performed with 1:1,000 Zombie NIR (Biolegend) in PBS for 20 minutes on ice. After one wash, the cells were resuspended in 150 µL PBS + 2% FBS (FACS buffer) for direct measurement. For dye labelling, cells were resuspended in 100 µL FACS buffer and incubated with 5 µM MitoSOX Red and 100 nM MitoTracker Green for 10 minutes. For antibody labelling, the cells were instead stained with the desired fluorescently conjugated antibody (Appendix - **Supplementary Table 2**) diluted in 100 µL FACS buffer for 20 minutes on ice. After two washes, the samples were analyzed using a Novocyte Penteon flow cytometer (Agilent). The forward- and side-scatter were plotted to select for the cells, followed by a second gate on the forward scatter area and height to select singlets. From these cells, the Zombie NIR- population was selected, then, plotted for the median fluorescence intensity (MitoSOX) normalized over the MitoTracker signal intensity, or for the percentage of marker-positive cells (for HLA-DR or Zombie NIR) against the unstained control for each marker of interest, and the data were exported for quantifications and plotting. Data was analyzed using the NovoExpress software (Agilent).

4.6.15 Fluorescence-activated cell sorting (FACS)

Control cell line 1 NPC-derived peripheral neurons and macrophages were dissociated into single cells by a 5-minute incubation with Accutase followed by gentle pipetting using a P1000 pipette.

The cells were centrifuged in 10 mL FACS buffer at 300 x g for 5 minutes at 4ºC and were resuspended in 100 µL FACS buffer. Surface staining was performed by a 30-minute ice incubation using CD56/NCAM (FITC) or CD45 (Alexa Fluor 700) diluted 1:100. The cells were centrifuged at 300 x g for 5 minutes at 4ºC, washed with 200 µL FACS buffer, centrifuged again, and resuspended in 200 µL FACS buffer. Sytox Blue (ThermoFisher) was added at 2.5 µM final concentration for 2 minutes prior to sorting. Sytox Blue was used instead of ZombieNIR to avoid cross-bleeding with the CD45-Alexa700 antibody. Cell sorting was performed by the SFR Necker Cytometry Platform using a Sony MA900. The antibodies are described in the Appendix (**Supplementary Table 2**).

4.6.16 Quantitative Reverse Transcription Polymerase Chain Reaction (qRT-PCR)

RNA was extracted from cell pellets using the RNeasy Mini Kit (QIAGEN) according to the manufacturer's instructions. The QuantiTect Rev. Transcription Kit (QIAGEN) was used for cDNA synthesis. The qPCR was performed with the QuantiTect SYBR Green PCR Kit (QIAGEN) using 5 ng of input RNA and of 1 µM of primer mix. The list of qPCR primers is displayed in the Appendix (**Supplementary Table 4**). The reaction and measurements were performed using the Viia7 (ThermoFisher). Quantification and comparisons were performed using the ddCt method.

4.6.18 Glucocerebrosidase (GCase) Assay

HuTu-80 cell lysates (5 µg) were diluted in 45 µL ddH_2O and mixed with 25 µL McIlvaive buffer pH 6.0 consisting of 126.3 µM Na_2HPO_4 and 36.85 µM citric acid (Sigma Aldrich). Two additional tubes were prepared as controls, one without cell lysate and one with control (PBS-treated) cell lysate that would not include the assay's substrate. Each sample was divided into two different tubes, where either 5 µL of ddH2O or 5 µL of 1 mM CBE were added. The samples were incubated for 30 minutes at room temperature to allow CBE to block GCase enzymatic function. Fresh assay substrate was prepared by dissolving 4-Methylumbelliferyl β-D-glucopyranoside (MedChemExpress) in ddH_2O to obtain a 6 mM solution. The substrate was dissolved by heating it at 55ºC and 25 µL were pipetted per sample. No substrate was added to the "no substrate" control. The samples were incubated at 37ºC for 2 hours in the dark. The reaction was stopped by pipetting 585 µL of 0.2 M glycine, pH 10.2 (adjusted with NaOH) to each tube, followed by pipetting of each sample in triplicate in a 96-well Half Area Black/Clear Flat Bottom Polystyrene non-binding surface Microplate. Measurements were performed at an excitation wavelength of 355 nm and an emission wavelength of 460 nm using the Victor NIVO spectrophotometer. For each sample, the average of each experimental triplicate with CBE was subtracted from the average without CBE to calculate the GCase I-specific enzymatic activity.

4.7 Proteomics

4.7.1 TMT-based quantitative proteomics sample preparation

HuTu80 cells were washed once with PBS and collected by scraping. Cells were centrifuged at 300 x g for 3' at 4ºC and lysed with 1% SDS (Carl Roth) with 50 mM HEPES (Sigma) supplemented with fresh protease/phosphatase inhibitors. Lysosomal-enriched fractions were processed with the same buffer (details in the "TMEM192-3xHA Lysosomal Immunoprecipitation" section). The mixture was incubated at 95ºC for 5 minutes and was cooled on ice prior to adding 50 U Benzonase / 100,000 cells. The lysates were incubated at 37ºC for 30 minutes, centrifuged at 13,000 x g for 10 minutes at room temperature, and the protein concentration of the supernatant was quantified by using the BCA Protein Assay Kit. For proteomics analysis, 20 µg (total lysates) or 5 µg (lysosomes) of protein at a concentration of 0.4 µg/µL were snap frozen in liquid nitrogen and shipped to the EBML Proteomics Core Facility on dry ice. Proteins were subjected to the SP3 protocol [310] conducted on the KingFisher Apex (Thermo Fisher Scientific). For digestion, trypsin was used in a 1:20 ratio (protease:protein) in 50 mM HEPES supplemented with 5 mM TCEP and 20 mM chloroacetamide. Digestion was caried out for 5 hours at 37°C. Peptides were labelled with TMTpro [311] Isobaric Label Reagent (ThermoFisher) according the manufacturer's instructions. Samples were combined for multiplexing and an OASIS® HLB µElution Plate (Waters) was used for further sample clean up. Offline high pH reverse phase fractionation was carried out on an Agilent 1200 Infinity high-performance liquid chromatography system, equipped with a Gemini C18 column (3 µm, 110 Å, 100 x 1.0 mm, Phenomenex), resulting in 12 fractions for lysosomes and lysate samples respectively [312].

4.7.2 LC-MS/MS

An UltiMate 3000 RSLC nano LC system (Dionex) fitted with a trapping cartridge (µ-Precolumn C18 PepMap 100, 5µm, 300 µm i.d. x 5 mm, 100 Å) and an analytical column (nanoEase M/Z HSS T3 column 75 µm x 250 mm C18, 1.8 µm, 100 Å, Waters). Trapping was carried out with a constant flow of trapping solution (0.05% trifluoroacetic acid in water) at 30 µL/min onto the trapping column for 6 minutes. Subsequently, peptides were eluted via the analytical column running solvent A (3%DMSO, 0.1% formic acid in water) with a constant flow of 0.3 µL/min, with increasing percentage of solvent B (3% DMSO, 0.1% formic acid in acetonitrile). The outlet of the analytical column was coupled directly to an Orbitrap QExactive plus Mass Spectrometer (Thermo) using the Nanospray Flex ion source in positive ion mode. The peptides were introduced into the QExactive plus via a Pico-Tip Emitter 360 µm OD x 20 µm ID; 10 µm tip (CoAnn Technologies) and an applied spray voltage of 2.3 kV. The capillary temperature was set at 320°C. Full mass scan was acquired with mass range 375-1200 m/z in profile mode with resolution of

70000. The filling time was set at maximum of 10 ms with a limitation of 3x106 ions. Data dependent acquisition (DDA) was performed with the resolution of the Orbitrap set to 35000, with a fill time of 120 ms and a limitation of $2x10^5$ ions. A normalized collision energy of 30 was applied. The isolation window of the quadrupole was set to 0.7 m/z. Dynamic exclusion time of 30 seconds was used. The peptide match algorithm was set to ‘preferred’ and charge exclusion ‘unassigned’, charge states 1, 5 - 8 were excluded. MS2 data was acquired in profile mode.

4.7.3 Mass Spectrometry Data analysis

Raw files were converted to mzML format using MSConvert from ProteoWizard, using peak picking, 64-bit encoding and zlib compression, and filtering for the 1000 most intense peaks. Files were then searched using MSFragger (v4.0) in FragPipe (21.1) against FASTA database merged_FASTA containing common contaminants and reversed sequences. The following modifications were included in the search parameters: Carbamidomethylation (C, 57.0215), TMTpro (K, 304.2072) as fixed modifications; Oxidation (M, 15.9949), Acetylation (protein N-terminus, 42.0106), TMTpro (peptide N-terminus, 304.2072) as variable modifications. For the full scan (MS1) a mass error tolerance of 20 PPM and for MS/MS (MS2) spectra of 20 PPM was set. For protein digestion, 'stricttrypsin' was used as protease with an allowance of maximum 2 missed cleavages requiring a minimum peptide length of 7 amino acids. The false discovery rate on peptide and protein level was set to 0.01. The standard settings of the FragPipe workflow 'TMT16' were used. The following modifications were made: msfragger.misc.fragger.precursor-charge-hi: 6, msfragger.use_topN_peaks: 300, tmtintegrator.allow_unlabeled: true, tmtintegrator.extraction_tool: Philosopher. The raw output files of FragPipe (protein.tsv files) were processed using the R programming language (RRID:SCR_000432, ISBN 3-900051-07-0). Contaminants and reverse proteins were filtered out and only proteins that were quantified with at least 2 razor peptides (Razor.Peptides >= 2) were considered for the analysis. Moreover, only proteins which were identified and quantified in 2 out of 3 replicates for each condition were kept. 7948 proteins passed the quality control filters. Log2 transformed raw DIA intensities ('Intensity' columns) were normalized using the 'normalizeVSN' function of the limma package (VSN - variance stabilization normalization) [313]. Missing values were imputed with the 'knn' method using the 'impute' function of the Msnbase package [314]. Proteins were tested for differential expression using a moderated t-test by applying the limma package ('lmFit' and 'eBayes' functions). The replicate information was added as a factor in the design matrix given as an argument to the 'lmFit' function of limma. Also, imputed values were given a weight of 0.01 while quantified values were given a weight of 1 in the 'lmFit' function. Annotated proteins were considered statistically significantly altered with a log2 fold-change > 0.5 and a False Discovery

Rate (DFR) < 0.2. The list of proteins and their fold-change were input in ShinyGO 0.82 (RRID:SCR_019213) to identify statistically enriched GO pathways (FDR cutoff = 0.05) using the human proteome as a background reference. Lysosomal proteins were filtered using the dataset of Akter et al [315] and were, thereafter, termed “validated” lysosomal proteins. The lysosomal hit proteins additionally underwent a screening of mitochondrial proteins using the human MitoCarta 3.0 (RRID:SCR_018165) dataset. The mass spectrometry proteomics data have been deposited to the ProteomeXchange Consortium via the PRIDE [316] partner repository with the dataset identifier PXD079523.

4.8 Statistics

Statistical analyses were performed with GraphPad Prism version 10.1.2. The Kolmogorov-Smirnov test was used to test for normality. The F-test and the Brown-Forsythe test were employed to asses equal variance between two or more conditions, respectively. For comparisons between two groups the following tests were performed: unpaired two-tailed t-test (normal data, equal variance), Welch’s t-test (normal data, unequal variance), or Mann-Whitney test (non-normal data). For comparisons of more than two groups the following tests were performed: one-way ANOVA with Tukey's post hoc test (normal data, equal variance), Brown-Forsythe and Welch ANOVA test with Dunnet’s post hoc test (normal data, unequal variance), Kruskal-Wallis test with Dunn’s post hoc test (non-normal data). The chemokine (Figure 15D) and cytokine (Figure 16A) datasets were also tested for lognormal distribution on the condition the normal distribution test was not passed, followed by lognormal one-way ANOVA with Tukey’s host test. Two-way ANOVA with Tukey’s post hoc test was used to evaluate statistical significance of macrophage cytokine release between the effect of HuTu-80 EVs or LPS (Figure 16D). For non-normal data (Kolmogorov-Smirnov test), the data were first log-transformed prior to performing the two-way ANOVA analysis. P values less than 0.05 were considered statistically significant.

5. Results

5.1 Part 1: CsgA as a trigger of intestinal Parkinson's disease

5.1.1: Do enteroendocrine cells uptake CsgA?

5.1.1.1 Cloning of CsgA-R12343 in pET-11d

To study the effect of CsgA on EECs, we first acquired the appropriate constructs and bacterial strains to perform protein purification. CsgA-WT without the secretion signal and with a 6xHis-tag sequence at the C-terminus cloned in the pET-11d vector was obtained from the Otzen laboratory. CsgA-R12343 was chosen as negative control for the experiments, as the R5 domain that normally interacts with the R1 domain of the next monomer is replaced by the R3 domain [317]. The R3 domain contains the aspartic acid residues at positions 136 and 149 which inhibit the ability of CsgA to form fibrils [317]. Therefore, we could dissect the effects of CsgA caused by its bacterial origin (CsgA-WT and CsgA-R12343) or its amyloidogenic properties (CsgA-WT versus CsgA-R12343). Using the study from Wang et al [317] as a reference, the double-stranded DNA oligonucleotide of CsgA-R12343 was designed as follows. Fourth-three nucleotides identical to the pET-11d-CsgA-WT vector sequence followed by the *Nco*I restriction site preceded the start codon. The secretion signal (2^{nd}-9^{th} amino acid) was excluded from the CsgA-R12343 sequence, and a 6xHis tag (CATCACCATCACCATCAC) was added before the stop codon. Following the stop codon, a *Bam*HI restriction site and 39 nucleotides identical to the pET-11d-CsgA-WT vector sequence were added. The plasmid pET-11d-CsgA-WT underwent digestion with *Nco*I and *Bam*HI to extract the vector (**Figure 1A**) and was subsequently ligated with the digested CsgA-R12343-6xHis oligonucleotide. The resulting plasmid was transformed into TOP10 chemically competent *E. coli* grown on ampicillin LB-agar plates. Following overnight incubation of selected bacterial colonies, their DNA was extracted. PCR was performed using the CsgA_1_FW and CsgA_1_RV primers (**Supplementary Table 1**) to verify the presence of the CsgA-R12343 insert in the plasmid (**Figure 1B**). Following a sequencing PCR, the results were aligned with Clustal Omega against the *in silico* designed sequence. The sequencing results completely overlapped with the designed sequence (**Figure 1C**), thus the pET-11d-CsgA-R12343 and pET-11d-CsgA-WT plasmid were transformed into NiCo21 (DE3) competent bacteria. NiCo21 is a modification of the BL21 strain, which expresses T7 allowing for lactose-inducible expression of CsgA in our vector. NiCo21 strain was chosen over the BL21 strain as multiple bacterial chaperones, that may contaminate the 6xHis purification procedure, are fused with a chitin-binding domain. In case of contaminating protein elution, they could be removed using chitin-binding beads. In our case,

however, we were able to obtain high purity for both CsgA-WT and CsgA-R12343 (next section, **Figure 2A**).

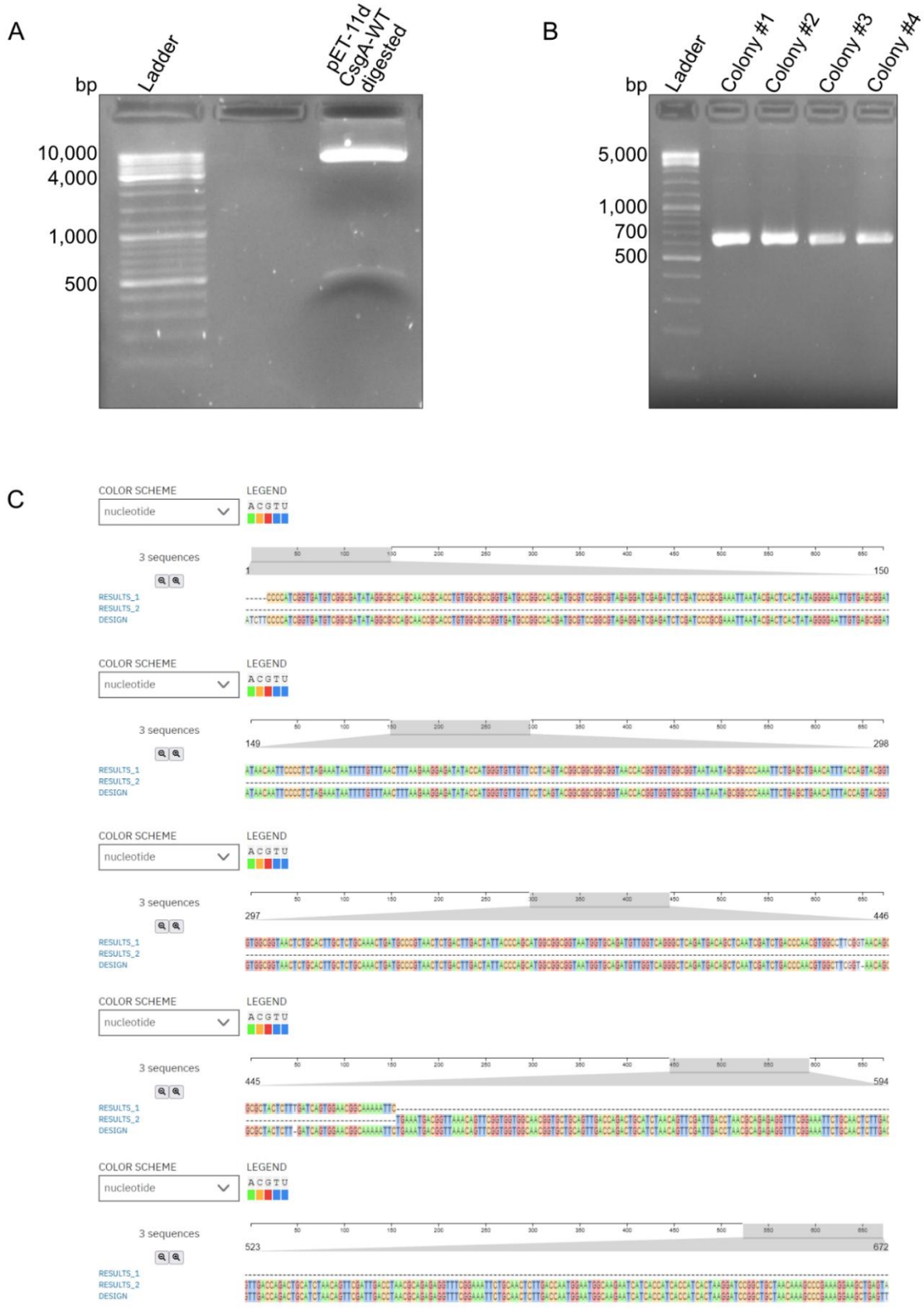


Figure 1. CsgA-R12343 cloning into the pET-11d vector.

A) Agarose gel of pET-11d-CsgA-WT plasmid digested with *Nco*I and *Bam*HI to obtain the cloning vector. The vector corresponds to the ~6,000 bp band, whereas the CsgA-WT insert corresponds to the ~500 bp band.

B) PCR screening of pET-11d-CsgA-R12343-transformed TOP10 colonies using CsgA_1_FW and CsgA_1_RV primers and yielding the expected band at ~650 bp.

C) Clustal Omega multiple sequence alignment result between our designed CsgA-R12343 oligonucleotide ("DESIGN") and the sequencing results ("RESULTS_1" and "RESULTS_2").

5.1.1.2 Purification and characterization of CsgA and curli

The lack of a secretion signal in the CsgA constructs meant that produced CsgA would be retained within the cells. Thus, the protein could be purified from bacterial pellet lysates using nickel-nitrilotriacetic acid (Ni-NTA) beads binding the 6xHis tag. We established in-house CsgA and curli purification methods using published protocols (see Methods). The CsgA monomer purification protocol involved growth of bacteria with the inducible pET-11d vector carrying CsgA-WT or CsgA-R12343, addition of the lactose analogue IPTG to induce the expression of CsgA, and lysis of the bacteria pellet to extract CsgA. Due to CsgA's rapid aggregation, and to completely dissolve potential bacterial inclusion bodies created by its overexpression, the lysis buffer contained the chaotropic reagent guanidine hydrochloride. Protein purification was performed via FPLC with Ni-NTA columns that bound the 6xHis tag which was then eluted by competitive imidazole binding. Prior to conducting the experiments, CsgA-WT and CsgA-R12343 were desalted from the buffer into PBS to allow for the protein to fold in a buffer that is compatible with assays and cell treatments.

Curli fibers were purified from *E. coli* K12 WT bacteria cultured in low-nutrient medium, suboptimal temperature (26^{o}C), low oxygenation (slow shaking – 150 rpm), and in 4% DMSO for 3 days. These parameters provide a stressful environment for the bacteria that promote biofilm production. Notably, the use of DMSO in biofilm formation is controversial, since it is inhibitory for certain species, such as *Pseudomonas aeruginosa* [318, 319]. The produced *E. coli* biofilm was exposed to a series of enzymes and detergents, to release it from nucleotides and lipids. Due to their large size, curli fibers did not enter the SDS-page acrylamide gel and could be separated from other bacterial proteins.

Following CsgA-WT, CsgA-R12343, and curli fiber purification, the proteins were subjected to Coomassie staining and Western blot. Coomassie staining showed high purity for CsgA-WT and CsgA-R12343 with a band at ~17 kDa corresponding to the size of CsgA (**Figures 2A**), which was further validated by Western blot using a His-tag and a CsgA antibody (**Figure 2B**). Curli fibers appeared as a smear with bands at different molecular weights indicative of the insoluble multimers (**Figures 2A-B**).

To validate the ability of CsgA to aggregate and the amyloid nature of curli, we incubated the proteins together with ThT which emits fluorescence upon binding to beta-sheets structures. CsgA-WT, but not CsgA-R12343, displayed initial ThT fluorescence at 1 hour which peaked at around 5 hours (**Figure 2C**), indicative of CsgA-WT's rapid aggregation. Sonicated and non-sonicated curli fibers displayed a baseline fluorescent ThT value that remained stable over time (**Figure 2C**), which verified the amyloid conformation of curli. TEM analysis further confirmed CsgA-WT aggregates 24 hours post-incubation at room temperature, while no visible fibers were seen for CsgA-R12343 at the same time point (Figure 2D). To monitor CsgA-WT uptake in cells, we labelled it with Alexa-594 (CsgA-WT-594). The labelling protocol included a 3-hour room temperature incubation; thus, CsgA fibers were detected by TEM when directly pipetted onto TEM grids without pre-incubation (**Figure 2D**). These results suggested that the labelling procedure did not substantially impact the ability of CsgA to form fibers. Sonicated curli fibers were also visible by TEM with the size and structure being different to CsgA fibers possibly due to the sonication procedure (**Figure 2D**). Non-sonicated curli fibers were too large to be visualized by TEM. CsgA/α-SYN cross-seeding was validated via the ThT assay. Even at 2 μM CsgA-WT was able to aggregate, whereas 50 μM α-SYN monomers did not show any increase in ThT fluorescence over the tested period (**Figure 2E**). When incubated together, CsgA-WT and α-SYN displayed increased lag phase and higher maximal ThT fluorescence (**Figure 2E**), suggesting the primary nucleation phase is slower and the total amyloid content is higher when compared to CsgA-WT alone. Finally, we characterized the pro-inflammatory properties of CsgA and curli by treating THP-1-derived macrophages and measuring TNFα release. CsgA-WT, CsgA-R12343, and curli fibers elicited an increase in TNFα secretion compared to the PBS control (**Figure 2F**), suggesting CsgA triggers a macrophage immune response irrespective of its aggregation state. Thus, we were able to purify and characterize CsgA-WT monomers, CsgA-R12343 monomers, and curli fibers.

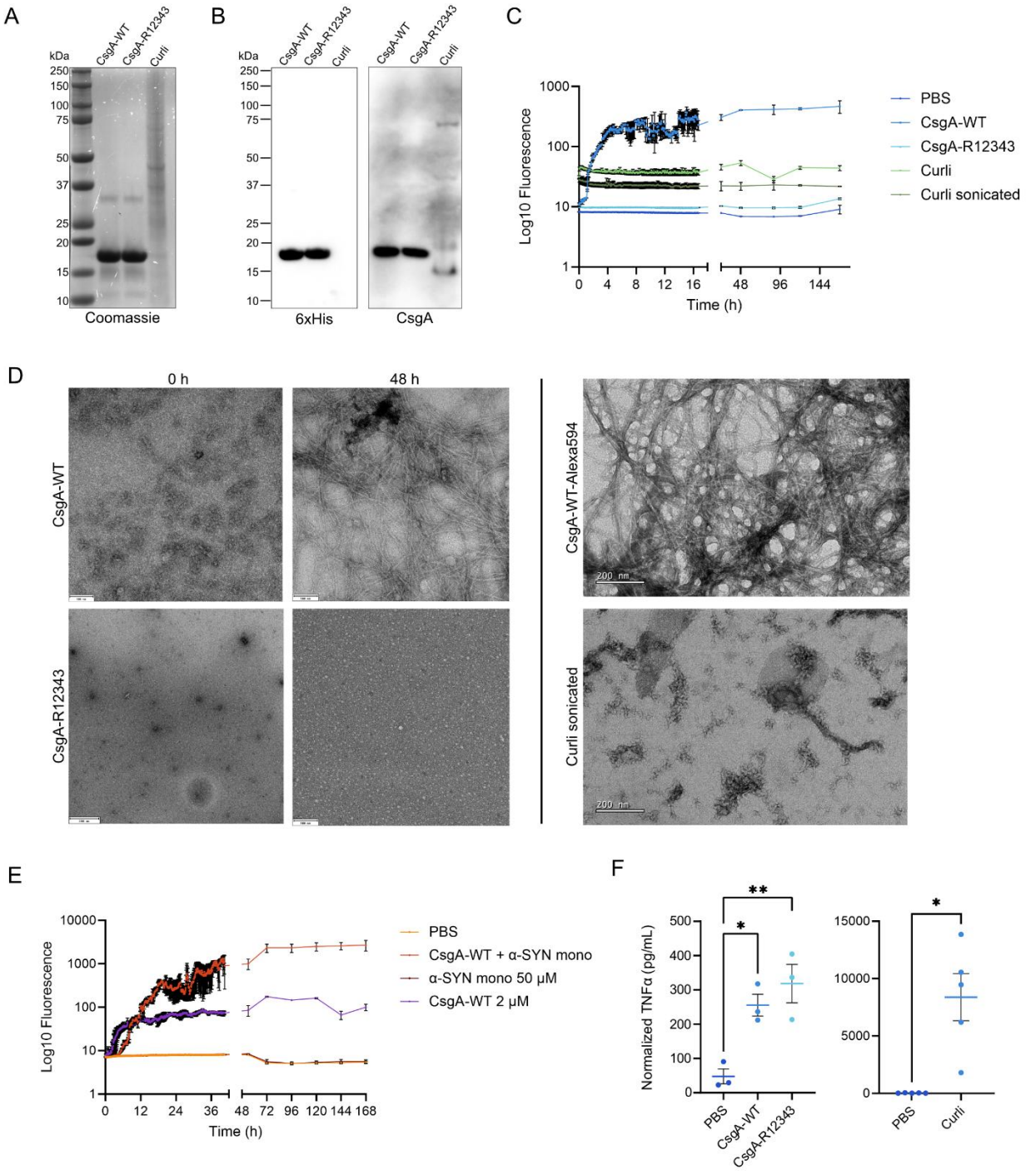


Figure 2. Purification and characterization of CsgA-WT, CsgA-R12343 monomers, and curli fibers.

A) Coomassie staining showing purified CsgA-WT and CsgA-R12343 monomers as a ~17 kDa band, and curli fibers as detergent-insoluble multimers.

B) Western blot analysis confirmed the identity of CsgA and curli using a CsgA-specific antibody. CsgA-WT and CsgA-R12343 were also blotted against a 6xHis-tag-specific antibody.

C) Fibrillization of CsgA-WT, and CsgA-R12343 monomers, and curli fibers monitored by ThT fluorescence (log10 scale). PBS was used as a negative control. Time course of ThT fluorescence change is shown. Mean ± SEM.

D) Representative transmission electron microscopy images of CsgA-WT and CsgA-R12343 at baseline and 48 h, alongside CsgA-WT-594 fibrils and sonicated curli fibers. Scale bars: 100 nm (left panel) and 200 nm (right panel).
E) Fibrillization of CsgA-WT and α-SYN monomers alone or together monitored by ThT fluorescence (log10 scale). PBS was used as a negative control. Time course of ThT fluorescence change is shown. The concentration of each protein is indicated on the graph. Mean ± SEM.
F) ELISA quantification of the pro-inflammatory cytokine TNFα release by human THP-1-derived macrophages following treatment with CsgA monomers or curli fibers. Mean ± SEM; *p<0.05, **p<0.01, one-way ANOVA with Tukey's correction for multiple comparisons (CsgA, n= 3 independent experiments) or unpaired Welch's t-test (curli, n= 5 independent experiments).

5.1.1.3 Selection of HuTu-80 as an enteroendocrine cell model

Due to the absence of a published iPSC-derived EEC protocol, we instead screened commercial immortalized cell lines. Protocols for differentiating iPSCs to intestinal organoids with enteroendocrine cell overrepresentation are available [320, 321], however we needed a simplified 2D homogeneous population to identify cell type-specific effects under bacterial amyloid exposure. The intestinal cell line Caco-2, and the enteroendocrine cell lines HT-29, HuTu-80, and Colo-320DM were blotted against α-SYN and GCase (**Figure 3A**). HuTu-80 were selected due to the higher endogenous levels of α-SYN expression and GCase production compared to the other cell lines tested. As TLR2 is involved in immune responses to CsgA, and EECs are known to have immunomodulatory properties, we blotted against TLR2. However, none of the cell lines screened displayed detectable TLR2 levels by Western blot (**Figure 3A**). HuTu-80 treatment with CsgA-WT, CsgA-R12343, or curli did not induce cell death as assessed by ZombieNIR staining (**Figure 3B**). Thus, HuTu-80 cells were used as our enteroendocrine cell model.

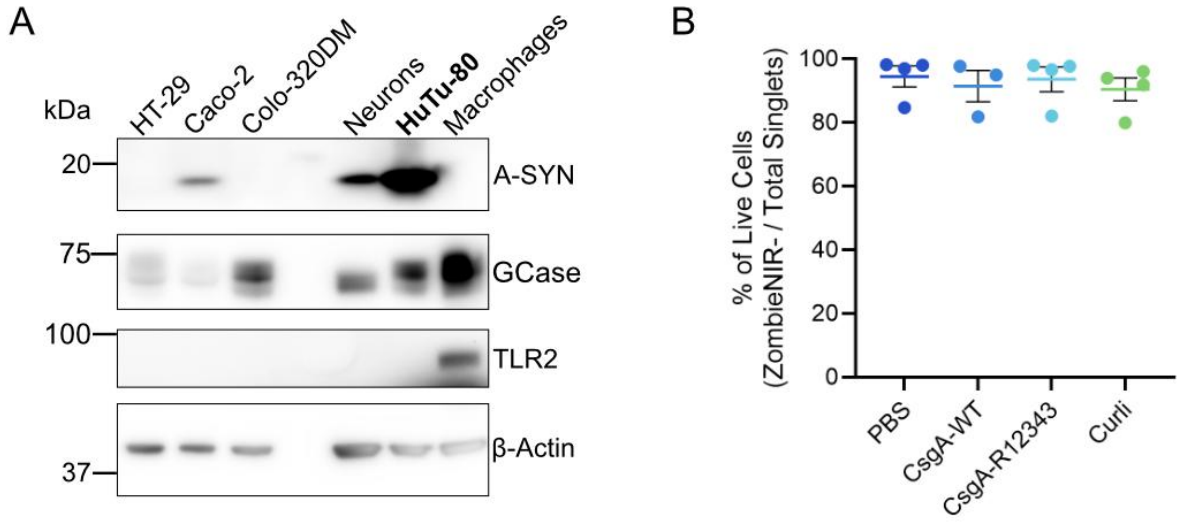


Figure 3. Selection of HuTu-80 as the enteroendocrine cell model and viability assessment of CsgA-treated HuTu-80.
A) Representative Western blots against alpha-synuclein (A-SYN), glucocerebrosidase (GCase), and Toll-like receptor 2 (TLR2) in the intestinal cell line Caco-2 and various enteroendocrine cell lines (HT-29, Colo-320DM, HuTu-80). Human iPSC-derived dopaminergic neurons and THP-1-derived macrophages were included as positive controls for A-SYN, GCase and TLR2 expression. B-actin was used as the loading control.
B) Percentage of live cells measured as the ratio of ZombieNIR- cells over the total number of singlets by flow cytometry for the indicated treatments. Mean ± SEM, one-way ANOVA with Tukey's correction for multiple comparisons, n= 3-4 independent experiments.

5.1.1.4 CsgA is uptaken and localized to the lysosomes of human enteroendocrine cells

We proceeded to assess whether CsgA and curli are uptaken by EECs. CsgA-WT-594 and curli-594 were applied to HuTu-80 cells, and their intracellular localization was analysed. Live-cell imaging revealed that the majority of labelled CsgA and curli co-localized with LysoTracker 48 h post-treatment, suggesting their targeting to lysosomes (**Figure 4A**). This observation was confirmed in fixed cells by immunostaining for the lysosomal marker LAMP1 and with the membrane dye WGA (**Figure 4B-C**). Consistent with lysosomal targeting, we did not detect co-localization of CsgA-WT-594 with early endosomes marked by RAB5A-GFP at 48 h post-treatment (**Figure 4D**). The effect of CsgA on lysosomes was evaluated by quantitative analysis of lysosomal morphology by the LysoTracker signal which revealed a significant reduction in lysosome number following only CsgA-R12343 treatment (**Figure 4E**). Instead, curli provoked an increase in the average lysosomal size (**Figure 4D**). Therefore, CsgA localized to the lysosomes 48-hours post-treatment in HuTu-80 enteroendocrine cells, with monomers and fibers differentially impacting lysosomal morphology parameters.

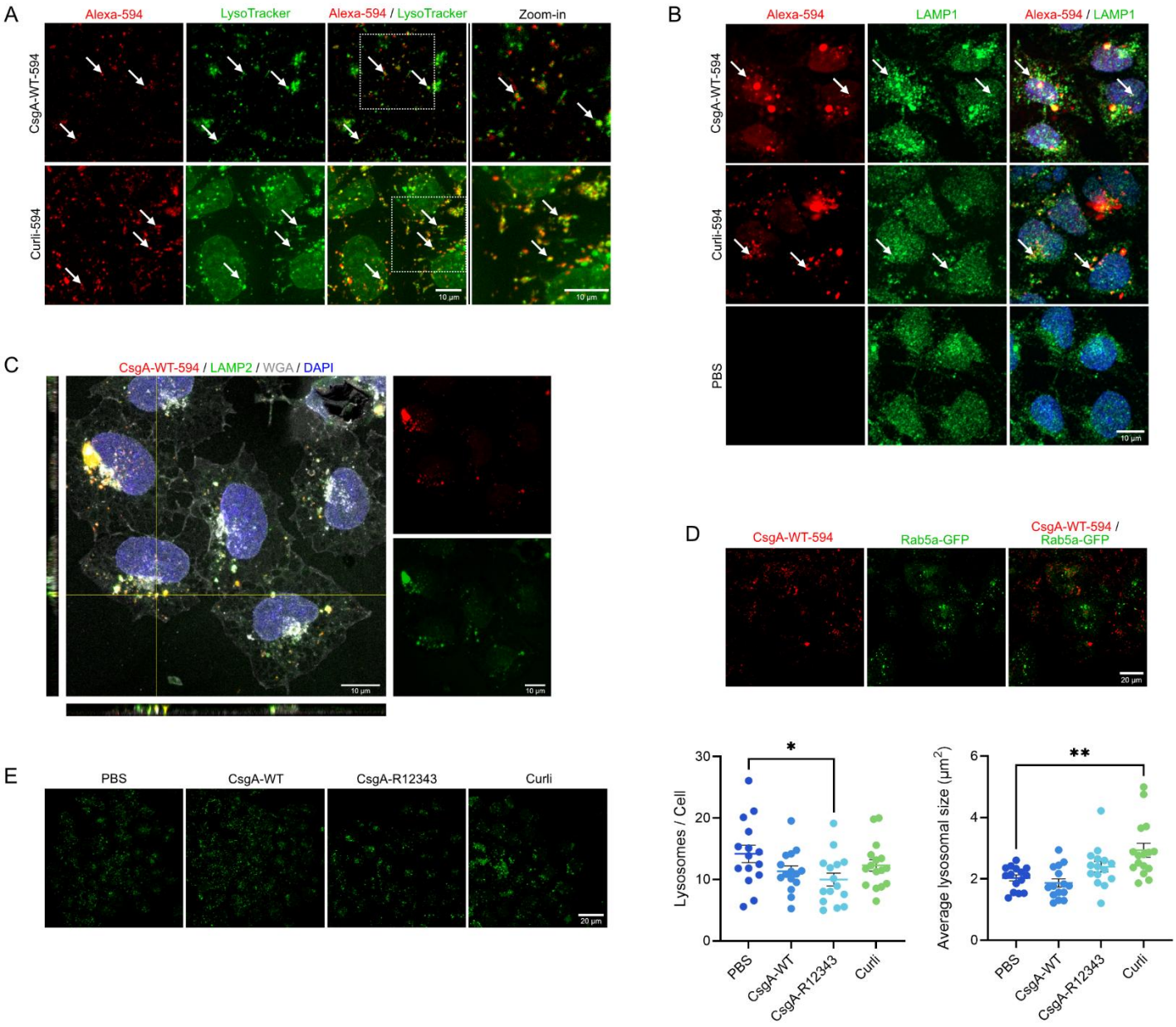


Figure 4. CsgA-WT and curli are targeted to lysosomes in human enteroendocrine cells.
A) Representative live-cell images of HuTu-80 cells treated with CsgA-WT-594 and curli-594 (red) for evaluation of lysosomal localization using LysoTracker (green). Arrows indicate co-localization. Scale bars: 10 μm.
B) Immunostaining of HuTu-80 cells treated with CsgA-WT-594 and curli-594 (red) to confirm lysosomal localization using LAMP1 (green), a lysosomal membrane marker. Arrows indicate co-localization. Scale bar: 10 μm.
C) Representative image of HuTu-80 cells treated with CsgA-WT-594 (red) to confirm intracellular localization using WGA (gray) and lysosomal localization using LAMP1 (green), a lysosomal membrane marker. Yellow lines indicate the Z planes that are presented on the sides of the image. Scale bars: 10 μm.
D) Representative live-cell images of HuTu-80 cells treated with CsgA-WT-594 (red) to evaluate endosomal localization using Rab5a-GFP (green). Scale bar: 20 μm.
E) Representative live-cell images of HuTu-80 cells and labelled with LysoTracker (green) to assess lysosomal morphology for the indicated conditions. Quantitative analysis of the number of lysosomes per

cell and the average lysosomal size per image in μm^2. Scale bar 10 µm. Mean ± SEM, *p<0.05, **p<0.01, one-way ANOVA with Tukey's correction for multiple comparisons, data were obtained from five images per replicate, n=3 independent experiments.

To determine whether CsgA is delivered to lysosomes for degradation, we inhibited lysosomal acidification using bafA1 which targets the vacuolar H^+ ATPase and prevents lysosomal acidification. Successful lysosomal degradation inhibition was verified by accumulation of LC3B-II over LC3B-I following BafA1 treatment (**Figure 5A**). BafA1 resulted in a significant accumulation of CsgA-WT, but not CsgA-R12343, as detected by immunoblotting against the His-tag (**Figure 5A**). A dose curve of the lysosomal degradation inhibitor CQ, which increases lysosomal pH, was also performed to determine the lowest minimum concentration leading to LC3B-II accumulation (10 µM, **Figure 5B**). Both bafA1 and CQ were used to verify curli's lysosomal targeting by live-cell imaging. Lysosomal inhibition did not alter the extent of curli-594/LysoTracker co-localization, yet it led to a significant increase in the average size of curli-594+/LysoTracker+ particles (**Figure 5C-D**), suggesting the accumulation of both lysosomes and curli within lysosomes. Despite these results and the observed changes in lysosomal morphology, we did not detect alterations in the autophagy marker P62 or in the autophagic flux, as assessed by LC3B-II levels before and after BafA1 treatment (**Figures 5E-F**). Together, these data indicate that CsgA and curli are internalized into the lysosomes of HuTu-80 cells, where they undergo degradation without affecting the autophagy markers P62 or LC3B.

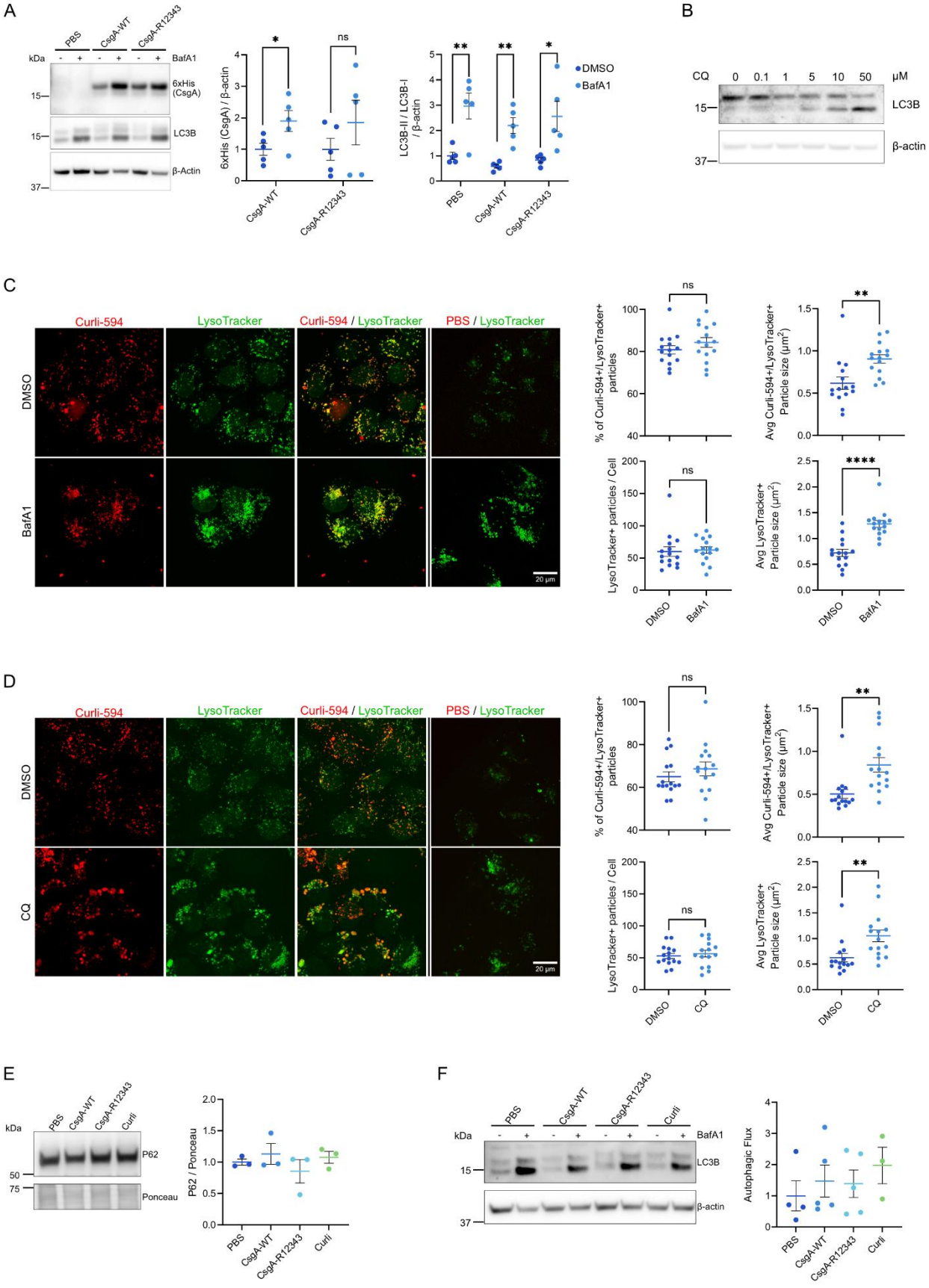

A
PBS
CsgA-WT
CsgA-R12343
kDa
BafA1
6xHis (CsgA)
LC3B
β-Actin
15
37
6xHis (CsgA) / β-actin
ns
LC3B-II / LC3B-I / β-actin
DMSO
BafA1
B
CQ
0
0.1
1
5
10
50
μM
LC3B
β-actin
C
Curli-594
LysoTracker
Curli-594 / LysoTracker
PBS / LysoTracker
DMSO
BafA1
20 μm
% of Curli-594+/LysoTracker+ particles
Avg Curli-594+/LysoTracker+ Particle size (μm²)
LysoTracker+ particles / Cell
Avg LysoTracker+ Particle size (μm²)
D
CQ
E
Curli
P62
Ponceau
P62 / Ponceau
F
Autophagic Flux

Figure 5. CsgA-WT and curli are degraded in the lysosomes of human enteroendocrine cells.
A) Representative Western blots of 6xHis (CsgA) and LC3B in HuTu-80 cells treated with 10 nM Bafilomycin A1 (BafA1) or DMSO (negative control) for 4 hours followed by exposure to CsgA monomers for 48 hours. Quantification of 6xHis levels and LC3B-II/LC3B-I ratio, normalized to β-actin for each treatment, expressed as relative fold-change to PBS. Mean ± SEM, unpaired two-tailed t-test, *p<0.05, **p<0.01, n=5 independent experiments.
B) Representative Western blots of LC3B and β-actin of CQ dose curve for the indicated concentrations in HuTu-80.
C) Representative live-cell images of HuTu-80 cells treated with 10 nM Bafilomycin A1 (BafA1) or DMSO (negative control) for 4 hours followed by exposure to curli-594 (red) for an additional 48 hours. Quantitative analysis of curli-594+/LysoTracker+ and LysoTracker+ counts, and the average curli-594+/LysoTracker+ and LysoTracker+ areas in μm^2. Scale bar 20 μm. Mean ± SEM, **p<0.01, ****p<0.0001, unpaired two-tailed t-test, data were obtained from five images per replicate, n=3 independent experiments.
D) Representative live-cell images of HuTu-80 cells treated with 10 μM chloroquine (CQ) or DMSO (negative control) for 4 hours followed by exposure to curli-594 (red) for an additional 48 hours. Quantitative analysis of curli-594+/LysoTracker+ and LysoTracker+ counts, and the average curli-594+/LysoTracker+ and LysoTracker+ areas in μm^2. Scale bar 20 μm. Mean ± SEM, **p<0.01, unpaired two-tailed t-test, data were obtained from five images per replicate, n=3 independent experiments.
E) Representative Western blot analysis against P62 for the indicated treatments and quantification, normalized to Ponceau, expressed as relative fold change compared to the PBS control. Mean ± SEM, one-way ANOVA with Tukey's correction for multiple comparisons, n= 3 independent experiments.
F) Representative Western blot analysis against LC3B for the indicated treatments and quantification of autophagy flux (LC3B-II intensity in BafA1 subtracting LC3B-II intensity in DMSO for each treatment), normalized to β-actin, expressed as relative fold change compared to the PBS control. Mean ± SEM, one-way ANOVA with Tukey's correction for multiple comparisons, n= 3-5 independent experiments.

5.1.2 Question 2: How does CsgA impact enteroendocrine cell function?

5.1.2.1 Generation and characterization of the HuTu-80-TMEM192-3xHA lyso-IP line

Despite the lysosomal morphology changes by CsgA and curli (**Figure 4E**), we did not detect any alterations in autophagy flux or P62 levels (**Figure 5E-F**). To obtain a comprehensive understanding of the effects of CsgA monomers and curli fibers on HuTu-80, we designed an experiment to analyze whole-cell and lysosomal lysates of treated cells. To permit lysosomal immunoprecipitation, we first generated a HuTu-80 cell line transduced with pLJC5-Tmem192-3xHA lentivirus. HuTu-80 WT were transduced with the lentivirus for 6 hours and, two days later, 0.5 μg/mL puromycin was added to the medium. After clonal selection and expansion, cells were switching to regular medium without puromycin. The resulting HuTu-80-TMEM192-3xHA (HuTu-80-T192) cell line was positive for HA and the signal co-localized with LAMP2 contrary to the background staining in HuTu-80-WT (**Figure 6A**). Following quality control, lysosomal immunoprecipitation (Lyso-IP) was performed in HuTu-80-T192 using HuTu-80-WT as a negative control. We enriched for the tagged TMEM192 protein, the lysosomal membrane protein LAMP1, and the lysosomal lumen protein HEXB by WB, with reduced detection of proteins belonging to other compartments (HSP60 - mitochondria, CANX - endoplasmic reticulum, and GAPDH –

cytosol) in IP fractions (**Figure 6B**). None of these proteins were present in the lyso-IP fractions of HuTu-80-WT cells. Despite observing decreased LAMP1 in the whole-cell lysates of HuTu-80-T192 versus HuTu-80-WT, we purified sufficient lysosomal material for downstream proteomics analysis. Thus, the HuTu-80-T192 line can be used to collect lysosomal fractions through lyso-IP.

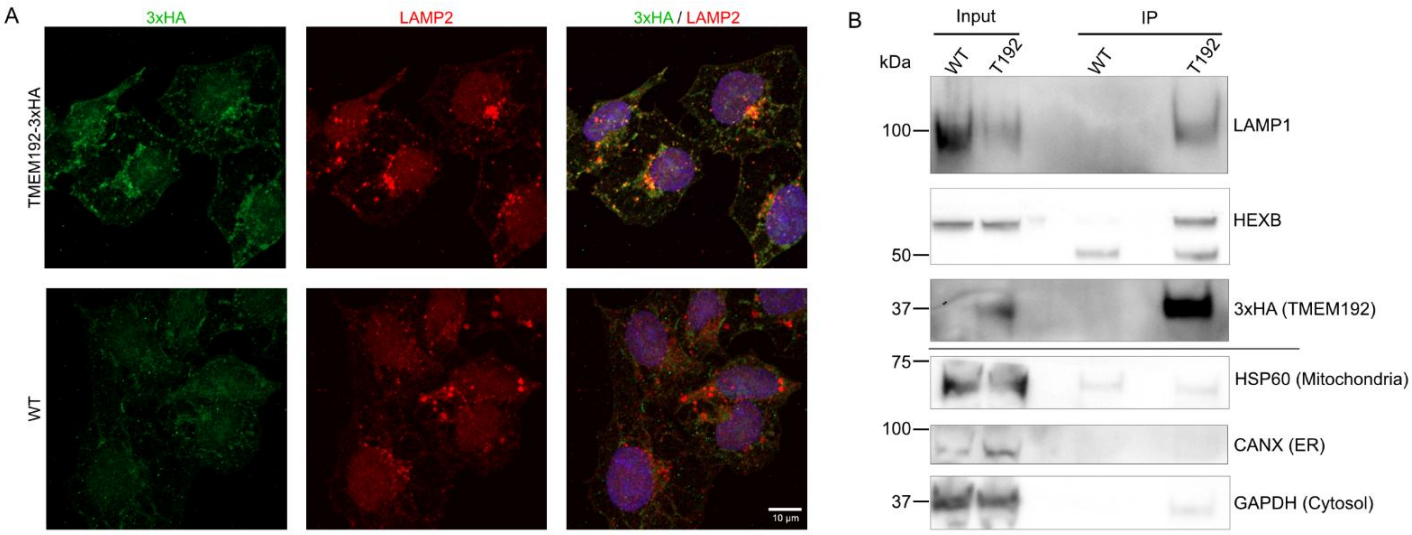


Figure 6. Lysosomal localization of 3xHA-tagged TMEM192 permits lysosomal enrichment by immunoprecipitation in human enteroendocrine cells.
A) Immunostainings against 3xHA (TMEM192, green) to assess its lysosomal membrane localization by using LAMP2 (red) on the top. As a negative control HuTu-80-WT cells were used. DAPI (blue) was used as a nuclei counterstain. Scale bar: 10 µm.
B) Representative lysosomal immunoprecipitation (IP) Western blot using HA antibody-tagged magnetic beads between HuTu-80 WT (WT) and HuTu-80 TMEM192-3xHA (T192) cells. The lysates were blotted against LAMP1, HEXB, 3xHA (TMEM192), HSP60, Calnexin (CANX), and GAPDH. The lower band in the HEXB blot (50 kDa) corresponds to the mouse IgG heavy chain eluted from the beads.

5.1.2.2 Proteomics analysis reveals cellular stress and altered intracellular trafficking in enteroendocrine cells upon CsgA-WT exposure

Following successful establishment and characterization of the HuTu-80-T192 cell line, whole-cell lysates were derived from HuTu-80-WT, while lyso-IP fractions from HuTu-80-T192 (**Figures 7A-B**). Notably, the lysis method of whole-cell preparations for proteomics included an SDS-based buffer, which affected our ability to detect CsgA-R12343 (6xHis) by WB compared to the Triton X lysis buffer (**Figures 7A, C**).

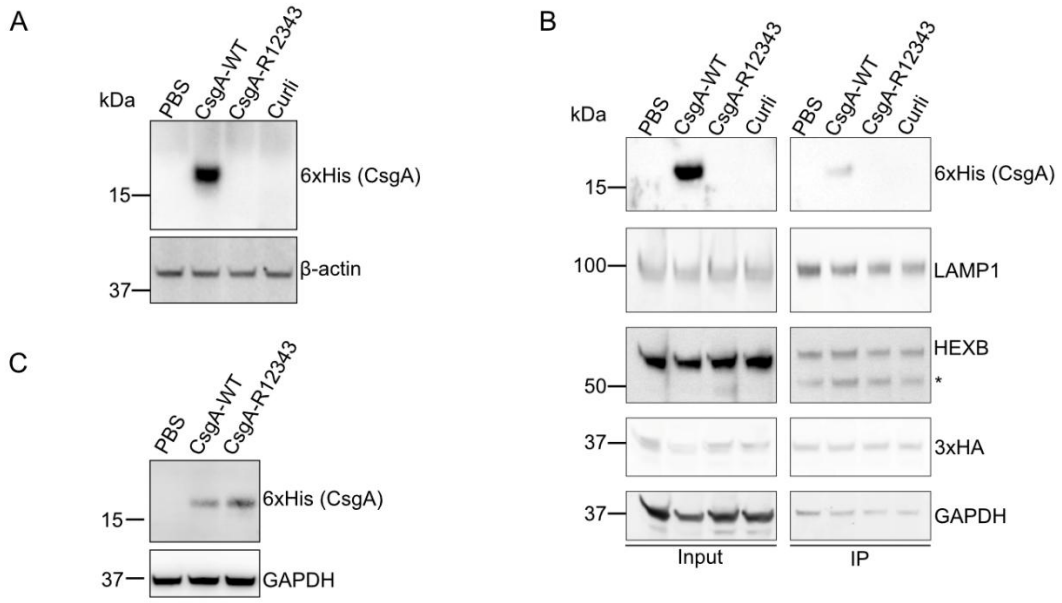


Figure 7. Preparation of human enteroendocrine cells whole-cell lysates and lyso-IP fractions for TMT-based LC-MS/MS proteomics.
A) Western blot analysis of whole-cell lysates using an SDS-based lysis buffer and probing against 6xHis (CsgA) for the indicated conditions. B-actin staining was used to confirm equal total protein loading between the samples.
B) Western blot analysis of lyso-IP samples, probing against 3xHA (TMEM192) to detect CsgA (6xHis) and lysosomal markers (LAMP1, HEXB) for the indicated conditions. GAPDH was used as a loading control for the whole-cell lysates (input). The asterisk corresponds to the mouse IgG eluted from the beads.
C) Western blot analysis of whole-cell lysate using a Triton X-based lysis buffer, probing against 6xHis (CsgA) for the indicated conditions. GAPDH was used as a loading control.

The whole-cell and lysosomal lysates underwent tandem mass tag (TMT) liquid chromatography–mass spectrometry (LC-MS) proteomics (**Figure 8A**). TMT-based proteomics permitted multiplexing of samples and higher accuracy compared to label-free proteomics. Venn diagram representation of hit proteins revealed that only CsgA-WT elicited changes in whole-cell and lyso-IP protein preparations, while curli caused a significant alteration in only 3 proteins in whole-cell lysates (**Figure 8B**). Particularly, volcano plots showed that CsgA-WT induced an upregulation of 371 proteins and a downregulation of 584 proteins when compared to the PBS control (**Figure 8C**). CsgA-R12343 did not alter the HuTu-80 proteome. Despite obtaining a relatively clear lysosomal fraction (**Figure 8B**), we were aware that lyso-IP protocols may still be contaminated with proteins from other organelles [315, 322]. Akter et al [315] developed a dataset where they combined known lysosomal proteins with lysosomal proteins identified from human and mouse cell lines in their study. Their resulting table was used to filter for known lysosomal proteins in our own lyso-IP dataset (“validated lysosomal proteins”) where we identified 42 hits in the CsgA-WT versus PBS condition (**Figure 8C-D**). From these proteins, 7 were upregulated and 35 were

downregulated (**Figure 8D**). Thus, CsgA-WT, but not CsgA-R12343 or curli, altered the HuTu-80 proteome, suggesting that the aggregate-prone CsgA monomers and multimers induced an enteroendocrine cell response.

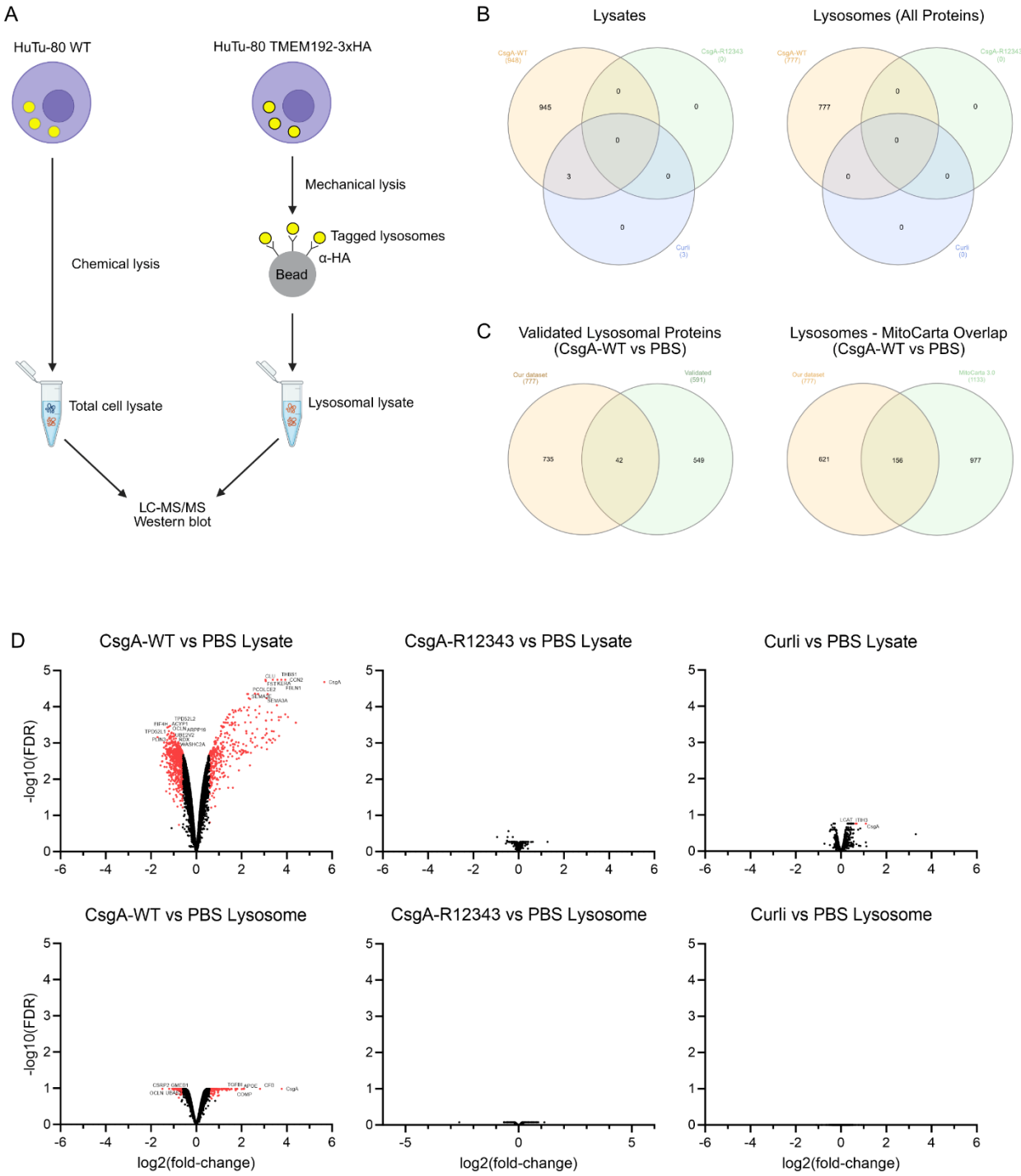


Figure 8. CsgA-WT confers proteomics changes in whole-cell lysates and lysosomes of human enteroendocrine cells.
A) Schematic illustration for total cell (HuTu-80 WT) and lysosome-enriched (HuTu-80-TMEM192-3xHA) lysate collection for subsequent proteomics and Western blot analysis.
B) Venn diagrams showing the overlap of hit proteins from CsgA-WT, CsgA-R12343, and curli treatments compared to PBS controls in whole-cell and lysosomal fractions. Hit proteins were identified as log2FC > |0.5| and false discovery rate < 0.2 using Limma-based analysis for each condition versus the PBS control.
C) Venn diagrams showing the overlap of the lyso-IP CsgA-WT vs PBS hit dataset with known lysosomal proteins [315] or the MitoCarta 3.0 dataset.
D) Volcano plots showing differentially expressed proteins among CsgA-WT, CsgA-R12343, or curli-treated HuTu-80 samples versus PBS. “Lysate” refers to the whole-cell proteome, while “Lysosome” to the validated lysosomal proteins. Hit proteins that differed a log2FC > |0.5| and had a false discovery rate < 0.2 using Limma-based differential analysis are highlighted as red circles.

To understand the cellular and molecular effects of CsgA-WT on HuTu-80, a gene ontology (GO) enrichment analysis was performed based on the hit proteins in the whole-cell and validated lysosomal datasets (**Figure 8B-D**). Traditionally, GO enrichment analysis screens the input dataset against a reference dataset, here the human genome, using a statistical analysis method, in this case a false-discovery rate cut-off. The resulting group of genes, called terms, that are significantly altered are used to infer altered cellular and biochemical pathways. The GO enrichment analysis is divided into three categories: Biological Process (BP, terms describing biological pathways), Molecular Function (MF, terms describing biochemical activities), and Cellular Component (CC, terms describing subcellular locations or organelles). The whole-cell and validated lysosomal hit datasets were input into ShinyGO to identify BFs and CCs (**Figure 9A**). As the hits from the whole-cell lysates were numerous (948 proteins), they were subjected to two additional analyses. The former was the Kyoto Encyclopedia of Genes and Genomes (KEGG) pathway analysis (**Figure 9B**), while the latter was a BP analysis using a maximum pathway size of 100 genes (**Figure 9C**) to identify more specific dysregulated pathways. The whole-cell hit dataset revealed enrichment of terms related to cytoskeletal organization, metabolism, extracellular vesicles, proteasome function, chaperone-mediated complexes, and antigen presentation following CsgA-WT treatment (**Figure 9A-C**). Interestingly, the term “amyloid fibril formation” was detected in CsgA-WT vs PBS whole-cell lysates (**Figure 9C**), which included the upregulated APP and APOE, both involved in AD [323, 324]. Notably, the term “bacterial invasion of epithelial cells” was also enriched, suggesting that HuTu-80 cells recognize CsgA-WT as a bacterial-derived molecule and mount a corresponding cellular response (**Figure 9B**). In lysosome-enriched fractions, GO analysis (CsgA-WT vs PBS) identified “lysosome” as a significantly enriched term, validating the lysosomal immunoprecipitation strategy, along with pathways related to intracellular transport, including endocytosis and vesicle-mediated transport (**Figure 9A**). Together, these data indicate that CsgA-WT elicits a stress response in HuTu-80 by

evoking protein level changes in intracellular functions (mitochondria, proteasome, chaperones, and vesicular trafficking) and intercellular communication pathways (extracellular vesicles and antigen presentation).

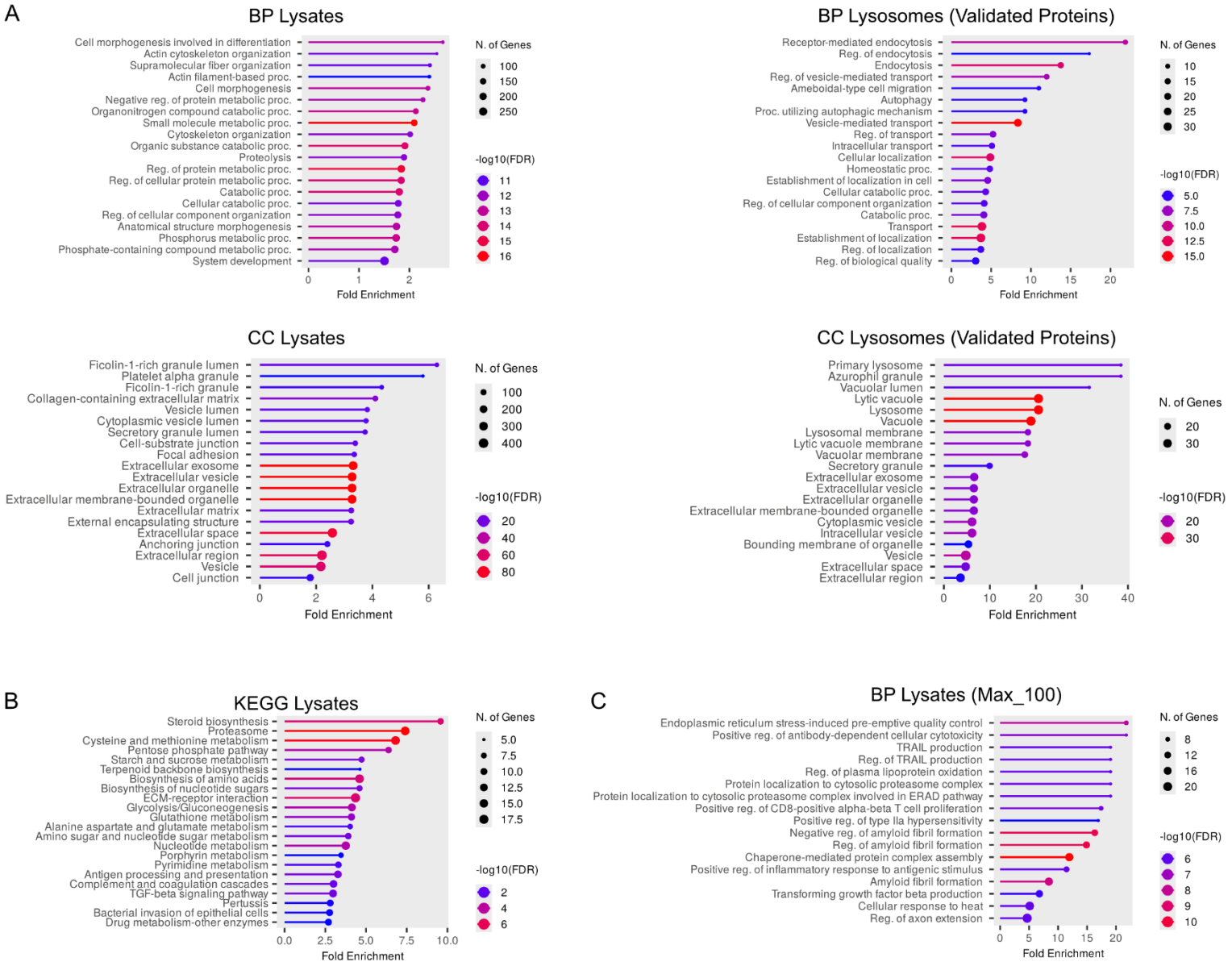


Figure 9. GO analysis reveals cellular stress response and altered intercellular communication in CsgA-WT-treated human enteroendocrine cells.

A) Gene ontology pathway analysis showing the top enriched biological processes (BP) and cellular components (CC) for CsgA-WT vs PBS hit proteins in whole-cell lysates and lysosomes using ShinyGO.

B) KEGG pathway analysis showing the top enriched pathways for hit proteins in the whole-cell lysates for the CsgA-WT vs PBS comparison using ShinyGO.

C) Gene ontology pathway analysis showing the top enriched (BPs) for CsgA-WT vs PBS hit proteins in whole-cell lysates and lysosomes using ShinyGO filtering for a maximum of 100 genes per pathway.

It should be noted that an initial GO enrichment analysis was performed by the proteomics facility without filtering the lysosomal dataset. This analysis revealed altered mitochondrial pathways (**Figure 10**), hence the lysosomal dataset hits in the CsgA-WT versus PBS condition were additionally screened for known mitochondrial proteins using the human MitoCarta 3.0 dataset. A total of 156 hit proteins were mitochondrial in the CsgA-WT versus PBS lysosomal dataset (**Figure 8C**), suggesting that the lyso-IP protocol is not specific for lysosomes and that CsgA-WT impacted mitochondrial protein levels and potentially mitochondrial function.

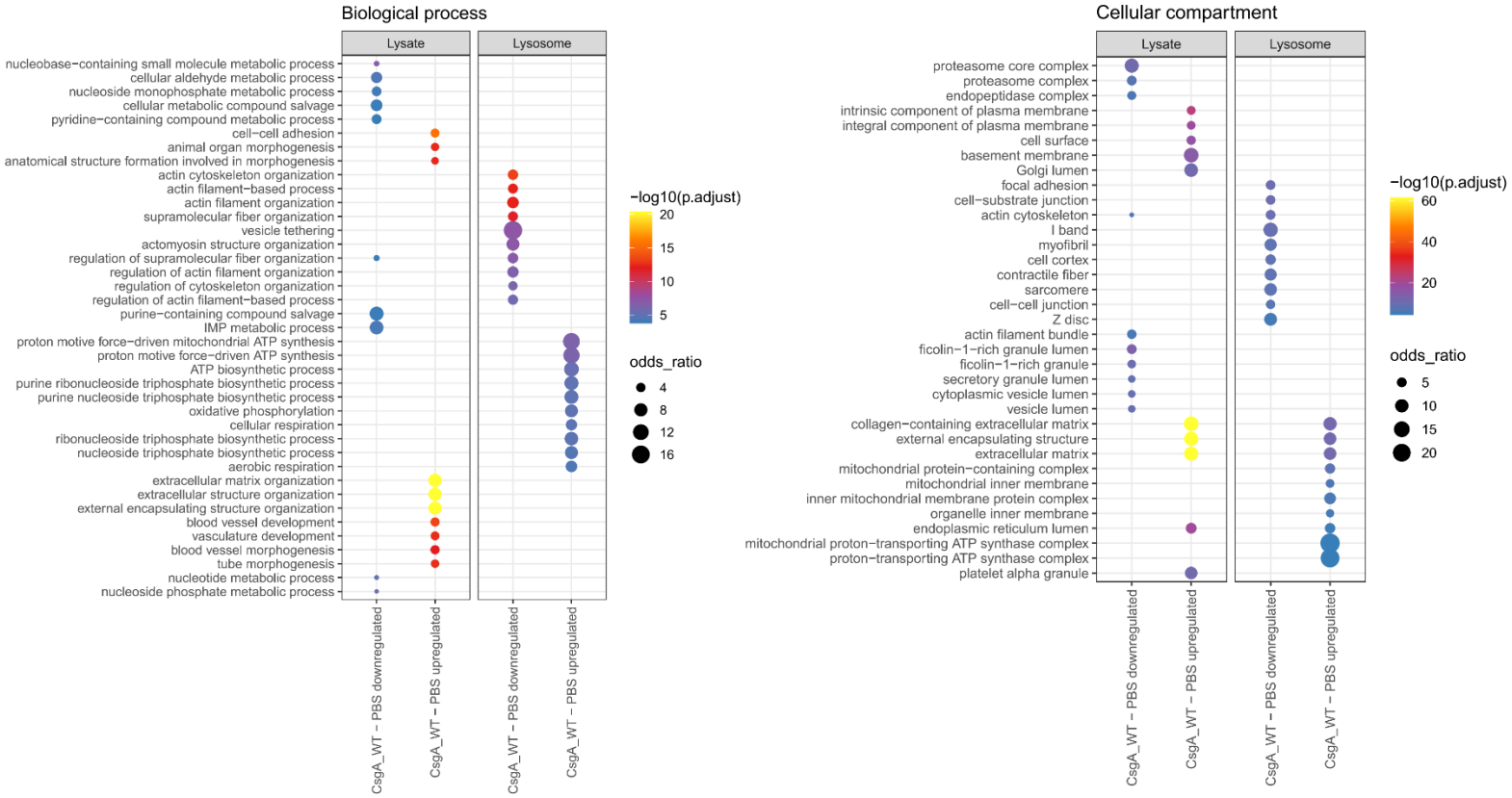


Figure 10. GO analysis uncovers altered mitochondrial pathways in human enteroendocrine cells by CsgA-WT treatment.
GO enrichment analysis showing the top upregulated and downregulated BPs and CCs in whole-cell and lysosome lysates for the CsgA-WT vs PBS comparison provided by the proteomics facility using the “clusterProfiler” and “org.Hs.eg.db” libraries in Rstudio (RRID:SCR_000432).

5.1.2.3 CsgA-WT downregulates the expression of mitochondrial antioxidant proteins and complex subunit proteins, without affecting superoxide levels or mitochondrial respiration in enteroendocrine cells

Mitochondria dysfunction is linked to PD pathogenesis, α-SYN pathology, and neurodegeneration [168, 180-183, 185-187]. Moreover, mitochondria are important for proper EEC function upon nutrient exposure, and the gut microbiota participates in the mitochondrial dynamics and development of EECs [192, 194]. Hence, we argued that the proteomic changes observed by CsgA-WT in HuTu-80 would impede EEC mitochondrial homeostasis and could predispose to mitochondrial-related PD pathology. Particularly, CsgA-WT downregulated the antioxidant proteins PARK7 (DJ-1) and SOD1 in whole-cell HuTu-80 lysates and enriched multiple terms involved in ATP synthesis, oxidative phosphorylation, and mitochondrial membrane potential in the lysosomal dataset (**Figure 10**). Initially, we assessed whether CsgA would have a direct effect on mitochondria by live-cell imaging of fluorescently labelled CsgA and curli together with MitoTracker, a cell-permeable dye which accumulates and fluorescently labels mitochondria with an active membrane potential. Live-cell imaging revealed lack of co-localization between CsgA-WT-594 or curli-594 with mitochondria (**Figure 11A**), suggesting that CsgA-WT affected mitochondria indirectly. No obvious changes in mitochondrial morphology were observed by CsgA-WT-594 or curli-594 treatment compared to the PBS control (**Figure 11A**). Then, we proceeded to validate PARK7 and SOD1 downregulation by CsgA-WT. CsgA-WT caused a significant reduction in SOD1 levels, while the decrease was non-significant for PARK7 (**Figure 11B**). Due to the decrease in SOD1, the mitochondrial superoxide levels were measured using MitoSOX. MitoSOX is targeted at mitochondria in living cells emitting fluorescence upon oxidation by superoxides. As positive controls, we treated cells with H_2O_2 and antimycin A, both of which can increase mitoSOX intensity [325, 326]. Surprisingly, flow cytometry analysis of MitoSOX-stained HuTu-80 did not reveal any change in fluorescence between CsgA-WT and PBS (**Figure 11C**). Instead, we observed a significant increase in MitoSOX fluorescence by curli treatment to a similar extent to H_2O_2 treatment (**Figure 11C**). Therefore, CsgA-WT downregulated SOD1 protein expression without impacting mitochondrial superoxide levels, whereas curli promoted an increase in mitoSOX intensity.

Mitochondrial oxidative phosphorylation capacity was assessed by blotting against mitochondrial complex subunit levels in whole-cell lysates and evaluating oxygen consumption rate (OCR) using the Seahorse assay. We measured the levels of complex I subunits NDUFV1 and NDUFS3, the complex IV subunits COX2 and COX4, and the complex V subunit ATP5A. Except for COX2, the levels of these subunits were increased in the lysosomal fractions of CsgA-WT-treated cells but were unaltered in the whole-cell proteomics dataset. By contrast, CsgA-WT induced a significant

reduction in NDUFV1 and COX2 levels in whole-cell lysates by WB (**Figure 11D**), demonstrating that the function of complexes I and complex IV might be impaired thereby affecting mitochondrial respiration. Mitochondrial ATP production was indirectly measured by the OCR using the Seahorse assay. Treatment with CsgA-WT or curli did not significantly impair basal respiration, ATP-linked respiration, or the maximal respiratory capacity of the cells (**Figure 11E**), suggesting that despite the downregulation of NDUFV1 and COX2, the cells are able to compensate and maintain their mitochondrial respiratory capacity.

Together, these results indicate CsgA-WT reduces the levels of proteins involved in antioxidant response and the mitochondrial respiratory chain, yet not sufficiently to provoke stark superoxide oxidative stress or mitochondrial respiratory dysfunction in enteroendocrine cells.

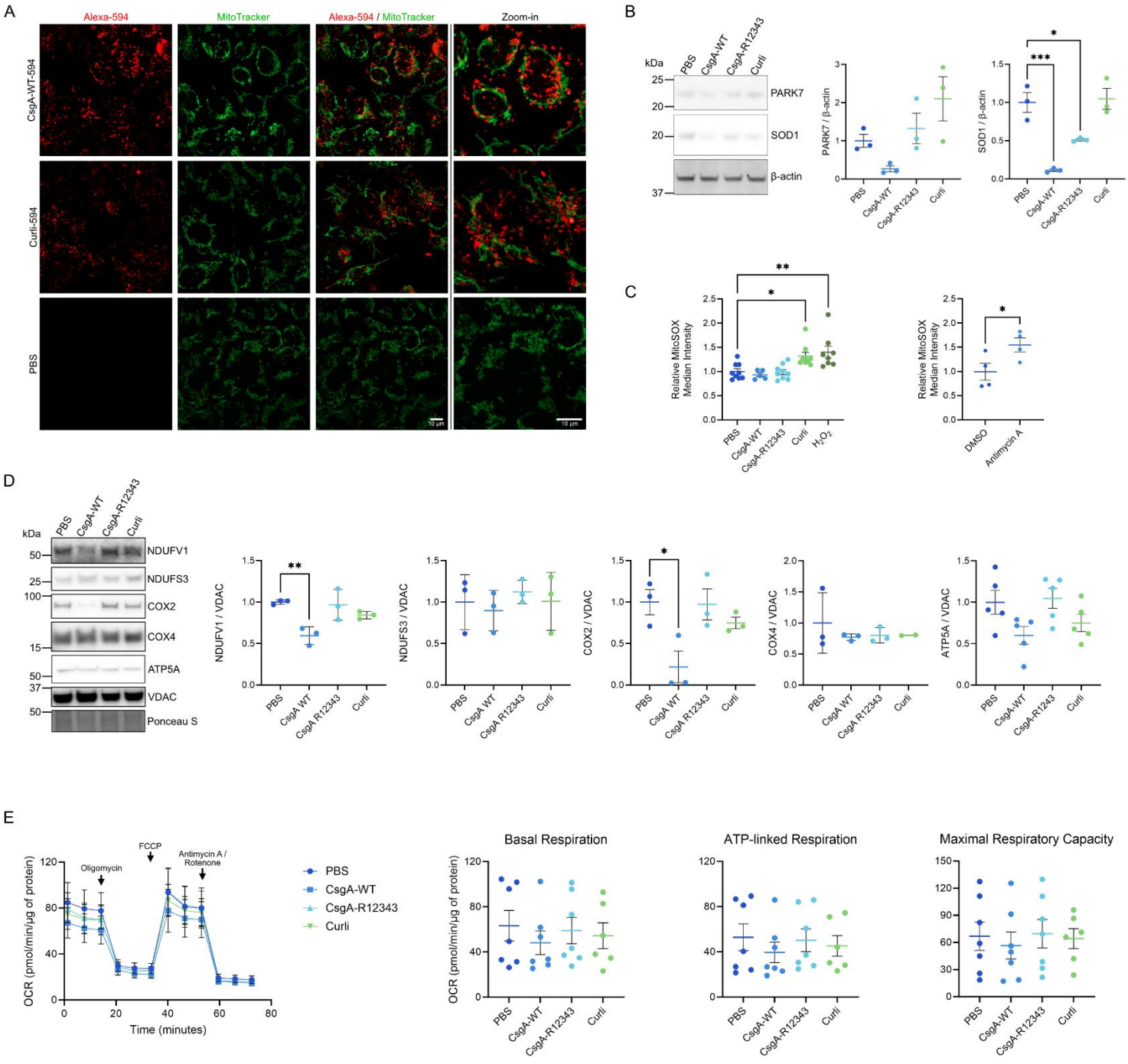


Figure 11. Reduction in SOD1, NFDUV1 and COX2 without perturbed superoxide production or mitochondrial respiration in CsgA-WT-treated human enteroendocrine cells.

A) Representative live-cell images of HuTu-80 cells treated with CsgA-WT-594 and curli-594 (red) and stained with MitoTracker (green) to evaluate mitochondrial localization of the bacterial amyloids. PBS was used as a negative control. Images were taken 48 hours after treatment. Scale bars: 10 µm.

B) Representative Western blot against PARK7 (DJ-1) and SOD1 in HuTu-80. Quantification of PARK7 and SOD1 levels, normalized to β-actin for each treatment, expressed as relative fold-change to PBS. Mean ± SEM, *p<0.05, ***p<0.001, one-way ANOVA with Tukey correction for multiple comparisons, n=3 independent experiments.

C) Representative histogram of MitoSOX median intensity by flow cytometry for the conditions depicted in HuTu-80. Quantification of MitoSOX median intensity expressed as relative fold-change to PBS. H_2O_2 and antimycin A were used as positive controls. Mean ± SEM, *p<0.05, **p<0.01, one-way ANOVA with Tukey correction for multiple comparisons (left graph), unpaired two-tailed t-test (right graph), n=4,8 independent experiments.
D) Representative Western blot against NDUFV1, NDUFS3, COX2, COX4, and ATP5A and quantification of the mitochondrial subunit levels, normalized to VDAC for each treatment, expressed as relative fold-change to PBS. Mean ± SEM, *p<0.05, **p<0.01, one-way ANOVA with Tukey correction for multiple comparisons, n=3-5 independent experiments.
E) Mitochondrial respiration measured through oxygen consumption rate using the Seahorse assay for the indicated conditions. The basal respiration, ATP-linked respiration, and maximal respiratory capacity were calculated from the kinetic measurements using the values after drug treatments as described in the "Materials & Methods" section. Mean ± SEM, one-way ANOVA with Tukey correction for multiple comparisons, n=6 independent experiments.

5.1.2.4 Reduction in HSP90 chaperone and proteasome subunit levels by CsgA-WT without an impact on chymotrypsin-like proteasome activity in enteroendocrine cells

Whole-cell lysate KEGG pathway analysis revealed altered proteasome function and chaperone-mediated complex assembly (**Figure 10B**), hinting towards impaired cellular stress response in CsgA-WT-exposed HuTu80. Both proteasome and chaperone dysfunction are implicated in α-SYN pathology and PD [253-259, 327]. Several proteasome subunits were downregulated by CsgA-WT, and the decrease was verified by WB for the structural subunits PSMA3 and PSMB2, and the chymotrypsin-like catalytic subunit PSMB5 (**Figure 12A**). Interestingly, there was a trend towards a decline for PSMA3 and PSMB2 by CsgA-R12343 (**Figure 12A**). Despite the proteasome subunit reduction by CsgA-WT, the chymotrypsin-like activity of the proteasome, as assessed by fluorescent release of the Suc-Leu-Leu-Val-Tyr-AMC substrate, was unchanged in lysates from CsgA-WT-treated HuTu-80 (**Figure 12B**). Other than the proteasome, chaperones participate in cellular proteostasis. The chaperone with the highest fold-change decrease by CsgA-WT and linked to PD was HSP90 [327], and we verified this reduction by WB (**Figure 12A**). The antibody recognized both HSP90AA1 and HSP90AB1 isoforms, and proteomics displayed a significant downregulation for both although HSP90AB1 was affected to a lesser degree by CsgA-WT. To understand whether the downregulation on the protein or mRNA levels, we performed qRT-PCR in HuTu-80 cDNA preparations against *HSP90AA1* and *HSP90AB1*. *HSP90AA1* expression was unaltered, whereas *HSP90AB1* expression was augmented by CsgA-WT (**Figure 12C**). This could explain why the HSP90AB1 protein levels were decreased to a lesser extent than HSP90AA1 and could describe a compensatory mechanism. Nonetheless, the stark downregulation of HSP90 (50% of the PBS control) implied that the cells could not maintain the chaperone's levels by transcriptional upregulation in response to CsgA-WT. To further evaluate the proteasome subunit and HSP90 chaperone downregulation over the bacterial amyloid

exposure course, their protein levels were measured at 24 hours instead of 48 after treatment. There were no significant changes in PSMBA3, PSMB2, or HSP90 levels over 24 hours (**Figure 12D**). These results together suggest that CsgA-WT did not immediately affect proteasome subunit and HSP90 levels, and rather the accumulation of CsgA-WT over the 24-hour treatment time window was responsible for the observed protein alterations. The cells appeared to compensate as observed by the elevated *HSP90AB1* and the unaltered chymotrypsin-like proteasome activity.

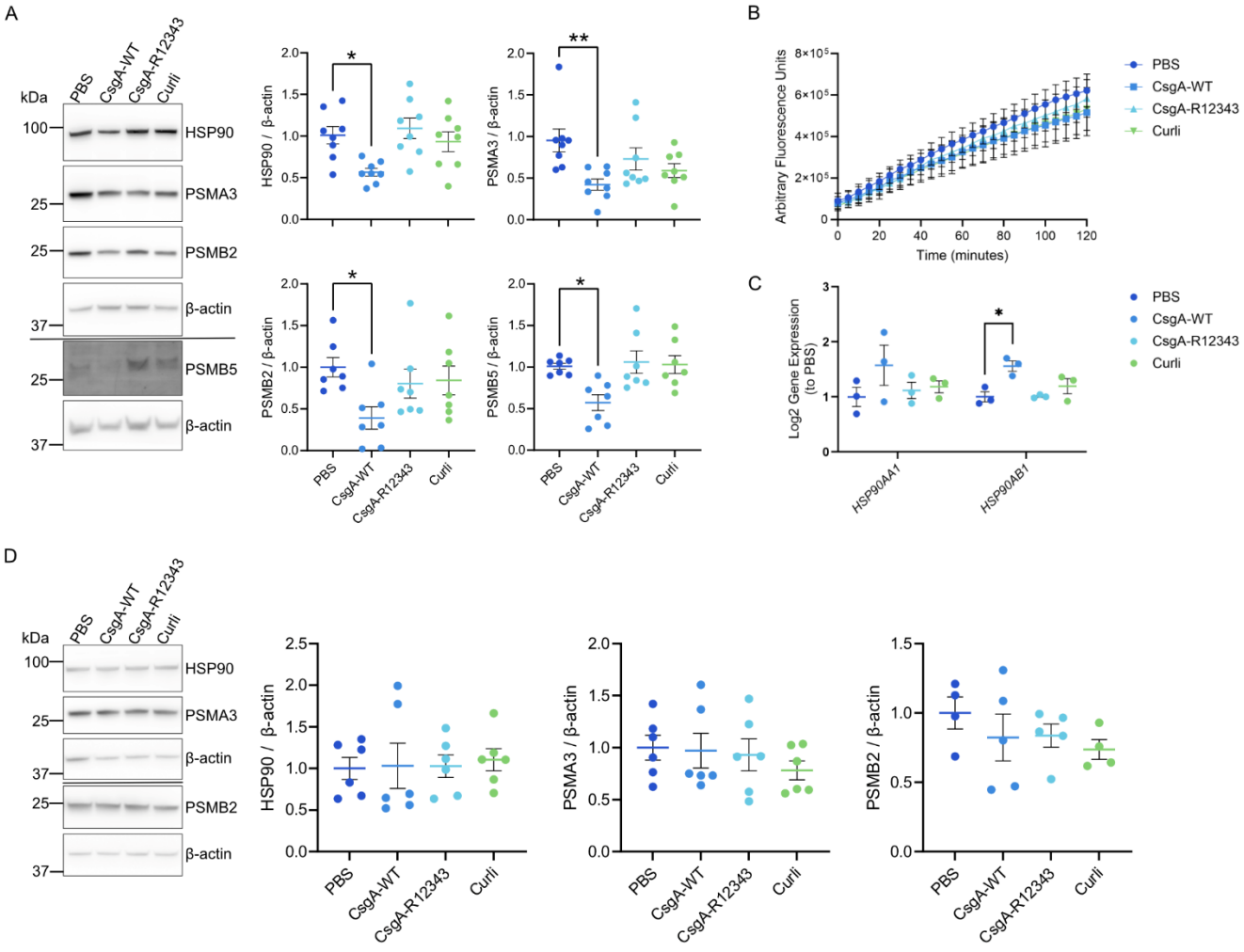


Fig 12. Declined HSP90 and proteasome subunit protein levels pinpoint towards altered stress response in CsgA-WT-treated human enteroendocrine cells.
A) Representative Western blots of HSP90, PSMA3, PSMB2, and PSMB5 in HuTu-80 cells treated for the indicated conditions for 48 hours. Quantification of HSP90, PSMA3, and PSMB2 levels, normalized to β-actin for each treatment, and expressed as relative fold-change to PBS. Mean ± SEM, *p<0,05, **p<0.01, one-way ANOVA with Tukey correction for multiple comparisons; n=7 independent experiments.
B) Proteasome chymotrypsin-like kinetic assay measured by fluorescence emission over time by cleavage of the substrate Suc-Leu-Leu-Val-Tyr-AMC, expressed as fold-change to the PBS control at time point 0. Mean ± SEM; one-way ANOVA with Tukey correction for multiple comparisons (for the endpoint at 2 h), n=5-6 independent experiments.

C) *HSP90AA1* and *HSP90AB1* mRNA expression normalized to *ACTB* expression for the conditions indicated and expressed as relative fold-change to the PBS control. Mean ± SEM, *p<0,05, one-way ANOVA with Tukey correction for multiple comparisons for each gene; n=3 independent experiments.
D) Representative Western blots of HSP90, PSMA3, and PSMB2 in HuTu-80 cells treated for the indicated conditions for 24 hours. Quantification of HSP90, PSMA3, and PSMB2 levels, normalized to β-actin for each treatment, and expressed as relative fold-change to PBS. Mean ± SEM, one-way ANOVA with Tukey correction for multiple comparisons, n=5-6 independent experiments

5.1.2.5 CsgA-WT induces downregulation of lysosomal trafficking and upregulation of alpha-synuclein extracellular vesicle release in human enteroendocrine cells

Even though CsgA-WT elicited a decline in mitochondrial and proteostasis-related proteins, there was not a robust effect on mitochondrial function, proteasome activity, or autophagy. Therefore, we revisited the proteomics dataset and GO analysis, to unravel a homeostatic response of HuTu-80 to CsgA-WT. Combination of whole-cell and lysosomal proteomics analysis revealed altered intracellular processes, such as vesicular trafficking, and pathways associated with intercellular communication, including extracellular vesicles and antigen presentation. Based on these results, we initially focused on lysosomal pathways and validated selected proteins involved in intracellular transport in CsgA-treated samples (**Figure 13A**). Protein hits were selected based on reported interactions with α-SYN (AP2S1, LAMP2), α-SYN trafficking (DYNC1I2) or genetic evidence linking their encoding genes to PD (VPS26A) [226, 233, 240]. Due to the greater effect of CsgA-WT on the HuTu-80 proteome, curli were excluded from the following analyses. CsgA-WT treatment resulted in a significant reduction of AP2S1, DYNC1I2, and LAMP2 in lysosome-enriched fractions, whereas VPS26A levels were unchanged (**Figure 13B**). CsgA-WT did not induce significant differences in AP2S1, DYNC1I2, LAMP2, or VPS26A levels in whole-cell lysates. DYNC1I2 is a component of the dynein motor complex implicated in autophagic trafficking and α-SYN clearance, while LAMP2 plays a key role in CMA of α-SYN [214-216, 232, 233, 328]. Based on these observations, we hypothesized that lysosomal localization of α-SYN is impaired. Consistent with this, CsgA-WT treatment led to a significant reduction of α-SYN in lysosome-enriched fractions, without affecting total cellular α-SYN levels, in HuTu-80-T192A cells (**Figure 13C**). We next investigated the intracellular fate of α-SYN following CsgA-WT treatment. Given that autophagic flux was unchanged (**Figures 5E-F**), *SNCA* mRNA levels remained unaltered (**Figure 13D**), proteasome subunits were downregulated (**Figure 12A**), and multiple lysosomal trafficking proteins were reduced (**Figures 13B**), we reasoned that α-SYN trafficking, rather than its synthesis or degradation, was primarily affected. Accordingly, increased levels of α-SYN were detected in the extracellular supernatant of HuTu-80 cells treated with CsgA-WT (**Figure 13E**). Therefore, CsgA-WT induced a change in α-SYN localization away from lysosomes towards cellular release.

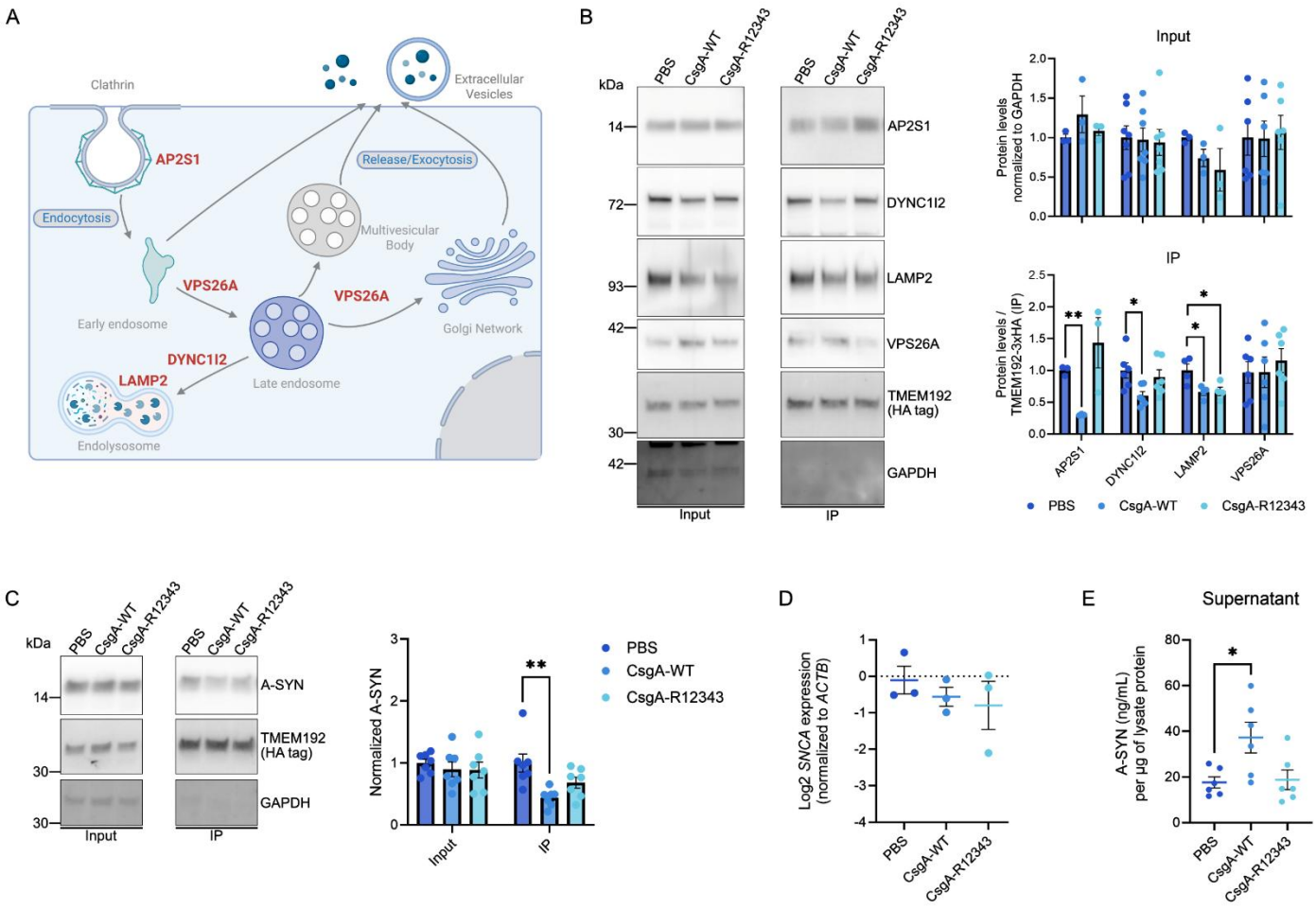


Figure 13. Reduced lysosomal α-SYN localization and increased α-SYN release in CsgA-WT-treated human enteroendocrine cells.

A) Graphical summary displaying the main subcellular location of the intracellular trafficking proteins AP2S1, DYNC1I2, LAMP2, and VPS26A (in red) downregulated in the lysosomal proteomics dataset by the CsgA-WT treatment versus the PBS control.

B) Representative Western blot analysis of AP2S1, DYNC1I2, LAMP2, and VPS26A in whole-cell lysates (input) and lyso-IP (IP) samples for the indicated treatments. Quantification of the indicated proteins, normalized to GAPDH (input) or HA tag (IP), expressed as relative fold-change to the PBS control. Mean ± SEM, *p<0.05, **p<0.01, one-way ANOVA with Tukey's correction for multiple comparisons (DYNC1I2, LAMP2, VPS26A both in input and IP; AP2S1 in input) or Brown-Forsythe and Welch ANOVA with Tukey's correction for multiple comparisons (AP2S1 in IP), n=3-7 independent experiments.

C) Representative Western blot analysis of α-SYN in whole-cell lysates and lysosomal-IP samples for the indicated treatments in HuTu-80-TMEM192-3xHA. Quantification of α-SYN levels, normalized to GAPDH (input) and HA tag (IP), expressed as relative fold change compared to the PBS control. Mean ± SEM, **p<0.01, one-way ANOVA with Tukey's correction for multiple comparisons within the input or IP conditions, n=7 independent experiments.

D) *SNCA* mRNA expression normalized to *ACTB* and expressed as log2 fold-change relative to the PBS control for the conditions indicated. Mean ± SEM, one-way ANOVA with Tukey's correction for multiple comparisons, n=3 independent experiments.

E) ELISA measurements of α-SYN in HuTu-80 supernatants for the conditions indicated. Mean ± SEM, *p<0.05, one-way ANOVA with Tukey's correction for multiple comparisons, n=6 independent experiments.

To investigate the manner of α-SYN release we utilized the whole-cell proteomics data, where the GO term “extracellular vesicles” was the most significant enriched pathway by CsgA-WT vs PBS treatment (**Figure 10A**). Thus, we purified EVs from CsgA-treated HuTu-80 to investigate the levels of α-SYN and EV marker proteins. We were able to purify EVs from all three treatment conditions with sizes ranging from 20-300 μm (**Figures 14A-B**), values comparable to literature [28]. CsgA-WT induced an elevation in EV levels of α-SYN (**Figure 14C**) and a significant increase in whole-cell lysate levels of RAB27A (**Figure 14D**), which is involved in tethering of vesicles to the cell membrane in the exosome secretion pathway [329]. Analysis of EV marker proteins in EV fractions showed a significant increase in CD63, but not in ALIX or FLOT1 from CsgA-WT-treated cells (**Figure 14E**). The levels of CD63 and ALIX were unchanged in whole-cell lysates with FLOT1 showing a non-significant increase by CsgA-WT (**Figure 14D**). The number and size of released EVs was similar between the treatment conditions (**Figure 14E**). Together these results indicate that CsgA-WT alters lysosomal trafficking pathways with concomitant changes of α-SYN localization from lysosomes to extracellular release. The enrichment of α-SYN and CD63 in EVs, both of which are involved in immune cell regulation [13, 330], suggests the acquisition of immune-modulatory properties of HuTu-80 exposed to CsgA-WT.

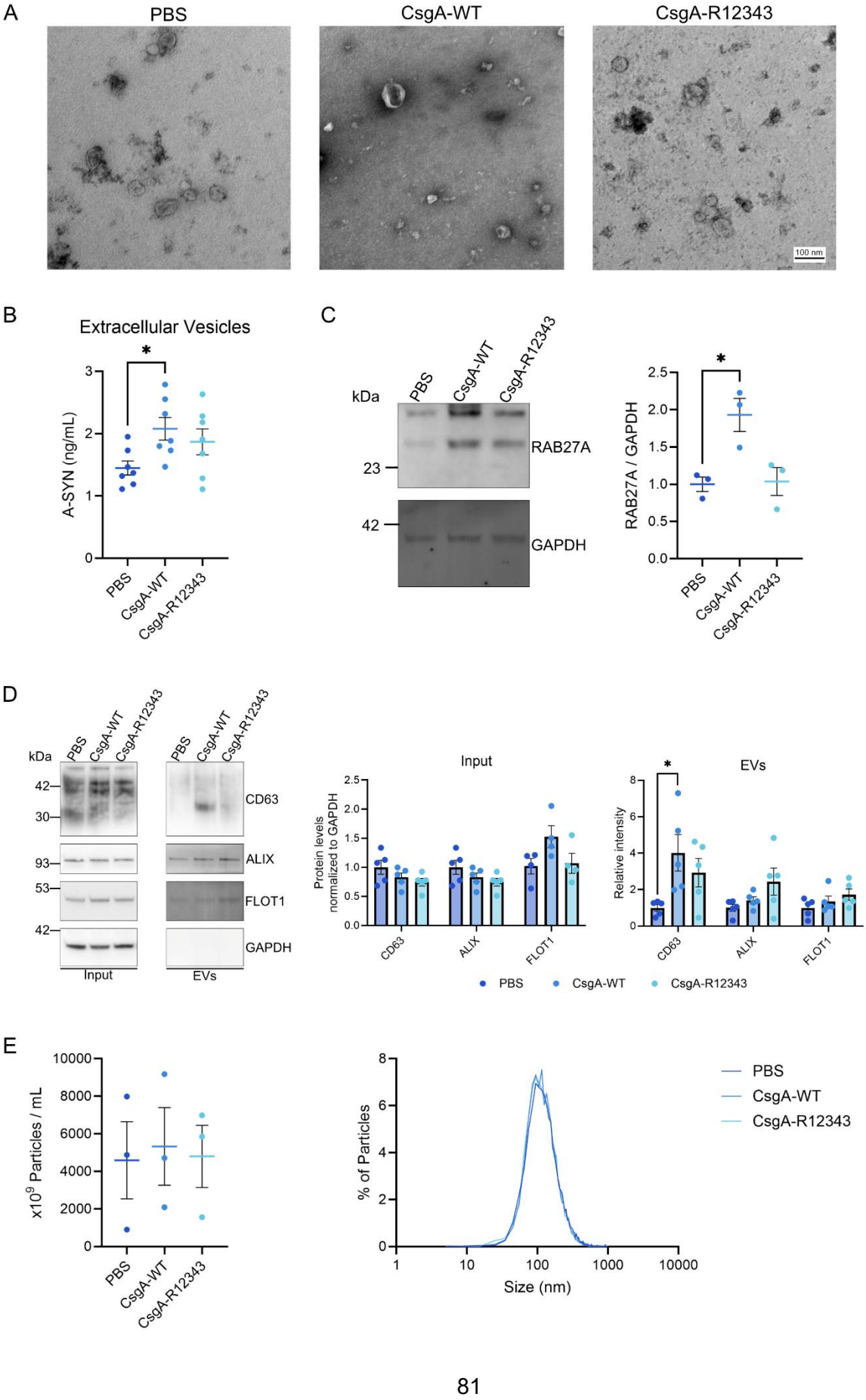

A
PBS
CsgA-WT
CsgA-R12343
100 nm
B
Extracellular Vesicles
A-SYN (ng/mL)
PBS
CsgA-WT
CsgA-R12343
C
kDa
RAB27A
GAPDH
23
42
RAB27A / GAPDH
D
CD63
ALIX
FLOT1
GAPDH
Input
EVs
Protein levels normalized to GAPDH
Relative intensity
E
x10^9 Particles / mL
% of Particles
Size (nm)

Figure 14. Elevated RAB27A in whole-cell lysates accompanied by increased α-SYN and CD63 in EVs of CsgA-WT-treated human enteroendocrine cells .
A) Representative transmission electron microscopy images of negative-stained extracellular vesicle-enriched samples from HuTu-80 supernatant for the indicated treatments. Scale bar: 100 nm.
B) ELISA measurements of α-SYN in HuTu-80 extracellular vesicles for the conditions indicated. Mean ± SEM, *p<0.05, one-way ANOVA with Tukey's correction for multiple comparisons, n=6 independent experiments.
C) Representative Western blot for RAB27A in whole-cell HuTu-80 lysates and the respective quantification normalized to GAPDH, expressed as relative fold change to PBS for the indicated conditions. Mean ± SEM, *p<0.05, one-way ANOVA with Tukey's correction for multiple comparisons, n=3 independent experiments.
D) Representative Western blot against CD63, ALIX, and FLOT1 in extracellular vesicles and whole-cell lysates (input) for the indicated treatments. Quantifications of CD63, ALIX, and FLOT1 for the input (normalized to GAPDH) and the EV fraction, expressed as relative fold change to PBS. Mean ± SEM, *p<0.05, one-way ANOVA with Tukey's correction for multiple comparisons, n=5 independent experiments.
E) Nanoparticle tracking analysis measurements of the number of billion particles per mL and the size frequency distribution (in nm) in EV preparations from HuTu-80 treated with the indicated conditions. Mean ± SEM, one-way ANOVA with Tukey's correction for multiple comparisons, n=3 independent experiments.

5.1.3 Question 3: What is the immune response of enteroendocrine cells exposed to CsgA?

5.1.3.1 HuTu-80 upregulate chemokine secretion and antigen presentation upon CsgA-WT treatment, and their extracellular vesicles sustain macrophage cytokine release associated with immune exhaustion properties.

A-SYN functions as an antimicrobial molecule to elicit immune responses and to limit bacterial growth [64-66, 331]. Considering enteroendocrine cells were exposed to the bacterial protein CsgA-WT which induced α-SYN release (**Figures 13E, 14B**), we evaluated the effect of HuTu-80 secretome on *E. coli* growth and HuTu-80 EVs in macrophage cytokine release. Conditioned medium from CsgA-treated HuTu-80 did not have a significant effect on *E. coli* growth (**Figure 15A-B**), suggesting that the increased α-SYN concentration is not sufficient to prevent bacterial growth.

To study whether CsgA promotes immune activation in EECs, we next measured antigen presentation markers and chemokine release in HuTu-80, as well as EV-mediated cytokine release in macrophages. Flow cytometric analysis revealed a significant increase in cell surface-expressing HLA-DR cells by CsgA-WT (**Figure 15C**) in line with the enrichment of the "antigen presentation" GO term in our proteomics (**Figure 10B**). Accordingly, chemokine measurements showed a significant increase of IL-8 and MIP-1α in CsgA-WT-treated HuTu-80 versus the PBS control (**Figure 15D**) suggesting HuTu-80 acquire immuno-attractive properties in response to CsgA-WT.

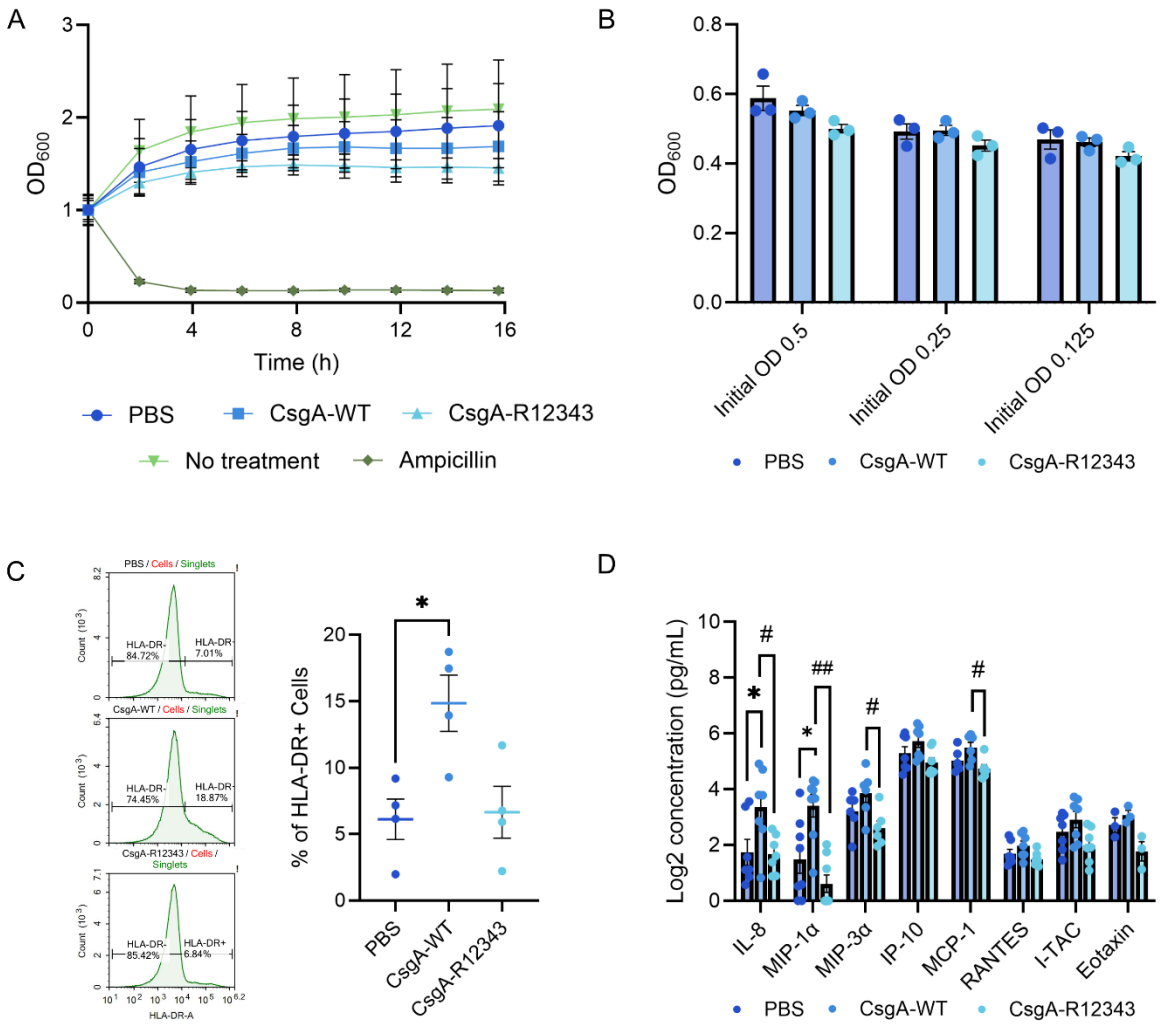


Figure 15. **Conditioned medium from CsgA-WT-treated does not affect *E. coli* growth, but CsgA-WT elicits HLA-DR surface exposure and IL-8, MIP-1α chemokine release in human enteroendocrine cells.**

A) OD measurements at 600 nm of *E. coli* grown in LB with 50% HuTu-80 conditioned medium from cells pre-treated with PBS, CsgA-WT, or CsgA-R12343 for the indicated time points. Untreated and ampicillin-treated bacteria were used negative and positive controls, respectively. A starting OD of 1 was used. Mean ± SEM, one-way ANOVA with Tukey's correction for multiple comparisons, n=3 independent experiments.

B) OD measurements at 600 nm of *E. coli* grown for 16 hours in LB with 50% HuTu-80 conditioned medium from cells pre-treated with PBS, CsgA-WT, or CsgA-R12343 using different starting bacterial ODs. Mean ± SEM, one-way ANOVA with Tukey's correction for multiple comparisons, n=3 independent experiments.

C) Surface HLA-DR flow cytometry histograms and quantification of percentage of HLA-DR+ HuTu-80 cells for the indicated conditions. Mean ± SEM; *p<0.05, one-way ANOVA with Tukey's correction for multiple comparisons, n=4 independent experiments.

D) HuTu-80 chemokine release measurements (log2 transformed for graphical presentation) in the supernatant for the indicated conditions. Geometric mean ± geometric SD; *p<0.05, **p<0.01 (CsgA-WT vs PBS), #p<0.05, ##p<0.01 (CsgA-WT vs CsgA-R12343), one-way ANOVA with Tukey's correction for multiple comparisons (for MIP-3α, IP-10, I-TAC, and Eotaxin), lognormal one-way ANOVA with Tukey's correction for multiple comparisons (for IL-8, MCP-1, and RANTES), Kruskal-Wallis test with Dunn's correction for multiple comparisons (for MIP-1α), n= 3-8 independent experiments.

Considering intestinal epithelial EVs regulate gut immune cell responses [265], α-SYN and CD63 levels were increased in EVs from CsgA-WT-treated HuTu-80 cells (**Figures 14B, D**), and CsgA was detectable in EVs (**Figure 16A**), we proceeded to evaluate the HuTu-80 EV immunomodulatory function in macrophages. Control HuTu-80 EVs provoked a strong pro-inflammatory IL-1b, IL-6, TNFα, IL-23, IL-8 cytokine and IL-8, MCP-1 chemokine release in macrophages (**Figure 16B**). The macrophage anti-inflammatory cytokine IL-10 was also elevated by the addition of HuTu-80 EVs on macrophages implying a complex macrophage immune response. On the contrary, EVs from CsgA-WT-treated HuTu-80 dampened the acute secretion of the macrophage pro-inflammatory cytokines IL-1b, IL-6, and IL-23 (**Figure 16B**). To evaluate the effect of EVs from CsgA-treated HuTu-80 in macrophages over a longer duration, the EVs were withdrawn from the medium and the cells were allowed to recover fir 48 hours (**Figure 16C**). Cytokine release was evaluated under basal conditions (no stimulus - H2O control) or following exposure to a subsequent inflammatory LPS stimulus. Under basal conditions, macrophages exposed to EVs from CsgA-treated HuTu-80 displayed an elevated IL-1β, IL-6, and IL-10 secretion compared to macrophages exposed EVs from PBS-treated HuTu-80 (**Figure 16E**), suggesting a sustained inflammatory state of macrophages. LPS treatment augmented IL-1β, IL-10, TNFα, and IL-10 release in macrophages exposed to control HuTu-80 EVs (**Figure 16E**). Importantly, the effect of LPS on cytokine release was abolished in macrophages exposed to EVs from CsgA-treated HuTu-80 (**Figure 16E**), indicating the reduced responsiveness of these macrophages to a subsequent inflammatory stimulus. This effect was present for both CsgA-WT and CsgA-R12343, suggesting it is independent of amyloid formation.

Altogether, CsgA induces an immunomodulatory HuTu-80 phenotype, characterized by increased HLA-DR surface expression and chemokine release, while CsgA-associated EVs promote a sustained macrophage activation state with subsequent exhaustion.

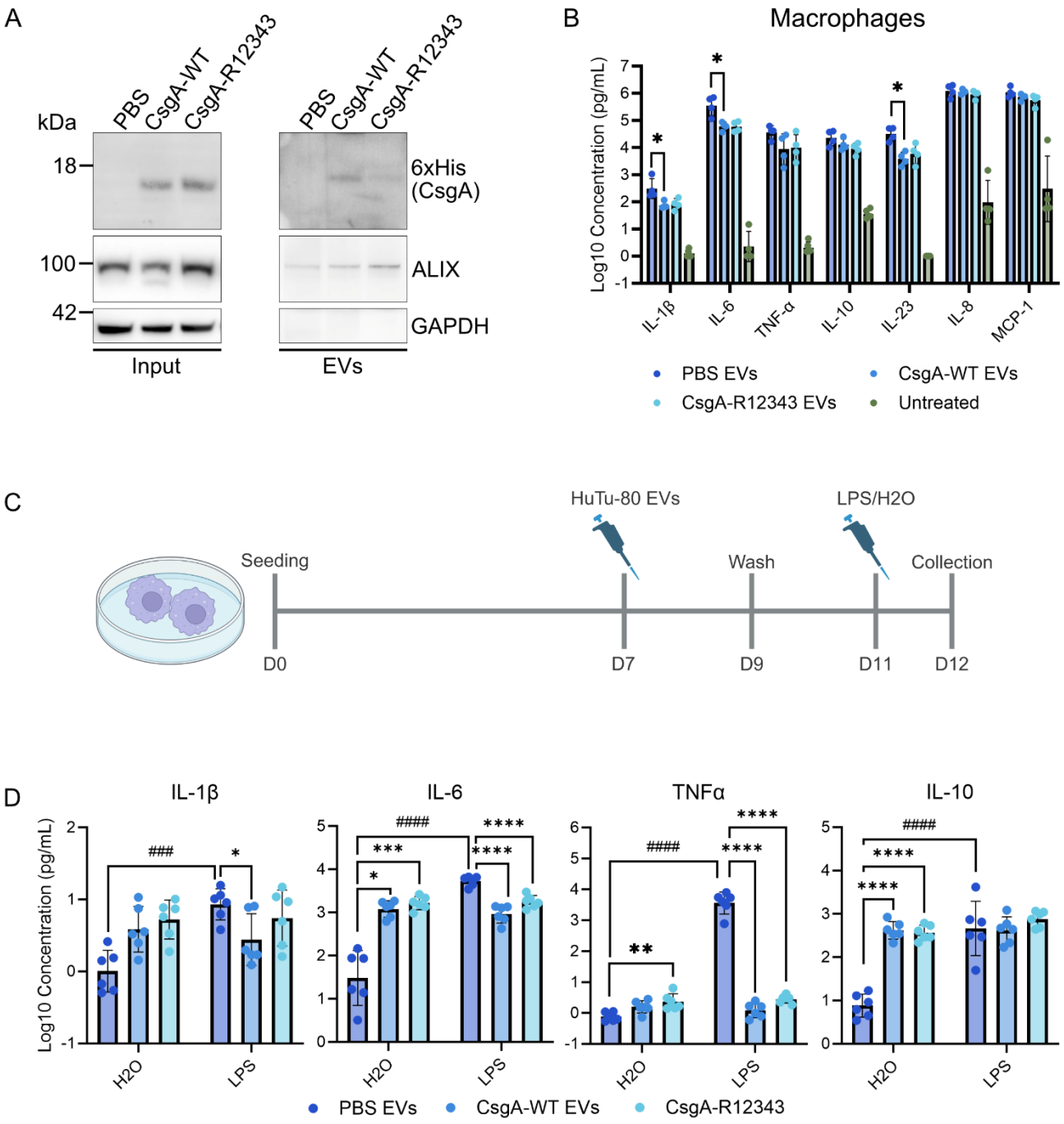


Figure 16. Extracellular vesicles from CsgA-treated HuTu-80 sustain cytokine release in KOLF2.J1 macrophages which show reduced responsiveness to secondary LPS stimulus.

A) Representative Western blots against 6xHis (CsgA), ALIX, and GAPDH for input and EV fractions of HuTu-80 for the indicated treatment conditions.

B) Cytokine release measurements (log10 transformed for graphical presentation) in the supernatant by macrophages cultured with extracellular vesicles derived from PBS, CsgA-WT, or CsgA-R12343-treated HuTu-80. Untreated macrophages were used as a negative control. Mean ± SEM; *p<0.05, Kruskal-Wallis test with Dunn's correction for multiple comparisons (between extracellular vesicle-treated macrophages), n= 4 independent experiments.

C) Schematic of the experimental set-up to study the effect of HuTu-80-derived extracellular vesicles on macrophage cytokine release following LPS exposure.
D) Cytokine release measurements in the supernatant by macrophages cultured with extracellular vesicles derived from PBS, CsgA-WT, or CsgA-R12343-treated HuTu-80 and treated with LPS (Figure 4E). Geometric mean ± geometric SD, *p<0.05, **p<0.01, ***p<0.001, ****p<0.0001 (comparisons between EVs from HuTu-80 with different bacterial amyloid exposure for the same second hit – H2O or LPS), ###p<0.001, ####p<0.0001 (comparisons between EVs from the same HuTu-80 treatment between H2O and LPS), two-way ANOVA with Tukey's correction for multiple comparisons (IL-1β, IL-6), two-way ANOVA of log10-transformed data with Tukey's correction for multiple comparisons (TNFα, IL-10), n=6 independent experiments.

5.1.4 Question 4: Can CsgA initiate α-SYN pathology in the human intestine?

5.1.4.1 CsgA does not promote α-SYN aggregation in enteroendocrine cells

CsgA cross-seeds with α-SYN *in vitro*, and PD animal models display faster pathology progression when fed with *E. coli* WT versus *E. coli* Δ*csgBAC* [121-125]. Furthermore, we found that CsgA and curli are trafficked to the lysosomes (**Figures 4-5**) where α-SYN is also present and degraded [215, 332]. Thus, we investigated whether amyloid cross-seeding occurs in CsgA-treated HuTu-80. Our cell model did not overexpress α-SYN and did not include any genetic variant involved in PD, thus we co-treated HuTu-80 with various molecules acting as secondary stressors (α-SYN, CBE, or LPS). Exogenous α-SYN monomers increased HuTu-80 α-SYN levels (**Figure 17A**). CBE is an enzymatic inhibitor of lysosomal GCase [333], which was used to mimic the loss of GCase enzymatic function caused by *GBA1* variants. Using a dose curve, the minimum CBE concentration conferring almost 100% loss of GCase activity was determined at 50 µM (**Figure 17B**). Finally, bacterial LPS from the pathogenic *E. coli* O111:B4 [334, 335] was used as a pro-inflammatory molecule [95, 96] that also augmented endogenous α-SYN levels in EECs [68]. As a positive control for α-SYN aggregation, HuTu-80 were exposed to α-SYN PFF. The cells were treated every other day, and the duration of the experiments was 10 DIV to permit sufficient time for α-SYN aggregation.

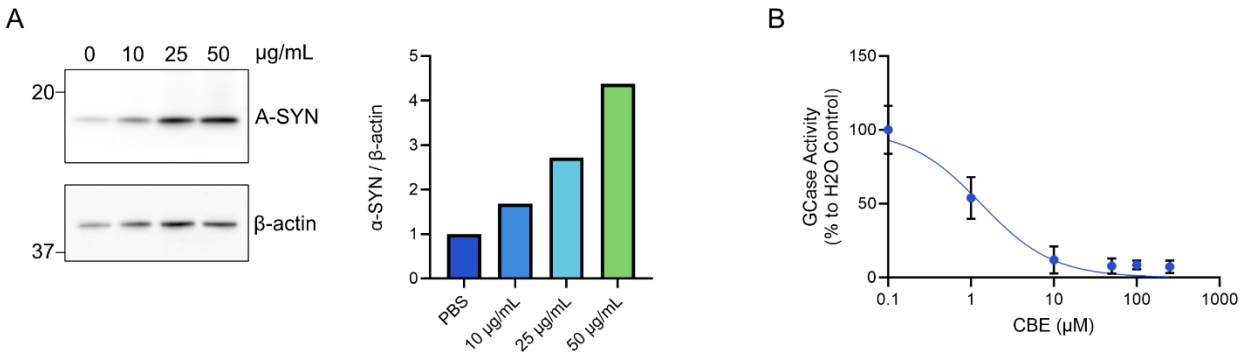


Figure 17. **A-SYN monomer treatment and CBE dose curve in HuTu-80.**
A) Western blot against α-SYN in HuTu-80 treated with exogenous α-SYN monomers with the concentrations indicated. Quantification of α-SYN levels normalized to β-actin and expressed as relative fold change to PBS.
B) GCase activity measured as fluorescence increase by 4-Methylumbelliferyl β-D-glucopyranoside digestion and expressed relative to the H_2O control for the indicated CBE concentrations.

Lysates from treated cells underwent Triton X-soluble and Triton X-insoluble fractionation to evaluate α-SYN aggregation. Aggregates of α-SYN are Triton X-insoluble and are visualized as higher molecular weight bands. CsgA-WT, CsgA-R12343, or curli fibers together with exogenous α-SYN monomers did not induce α-SYN aggregation in HuTu-80, and monomers (~17 kDa) were visible (**Figure 18A**). By contrast, α-SYN PFF caused the appearance of a smear and higher molecular bands when blotted against the α-SYN antibody (**Figure 18A**). The α-SYN band at 50 kDa was background signal detected by the antibody and it was also present in all conditions in whole blots of Triton X-soluble fraction against α-SYN. Similarly, CsgA or curli together with CBE did not promote α-SYN aggregation (**Figure 18B**). Finally, curli and LPS did not provoke any significant changes in Triton X-soluble or Triton X-insoluble α-SYN levels and did not induce α-SYN aggregation (**Figure 18C**). We detected α-SYN puncta formation in a subset of HuTu-80 treated with CsgA-WT together with α-SYN monomers (**Figure 19**), suggesting α-SYN accumulation in certain enteroendocrine cells.

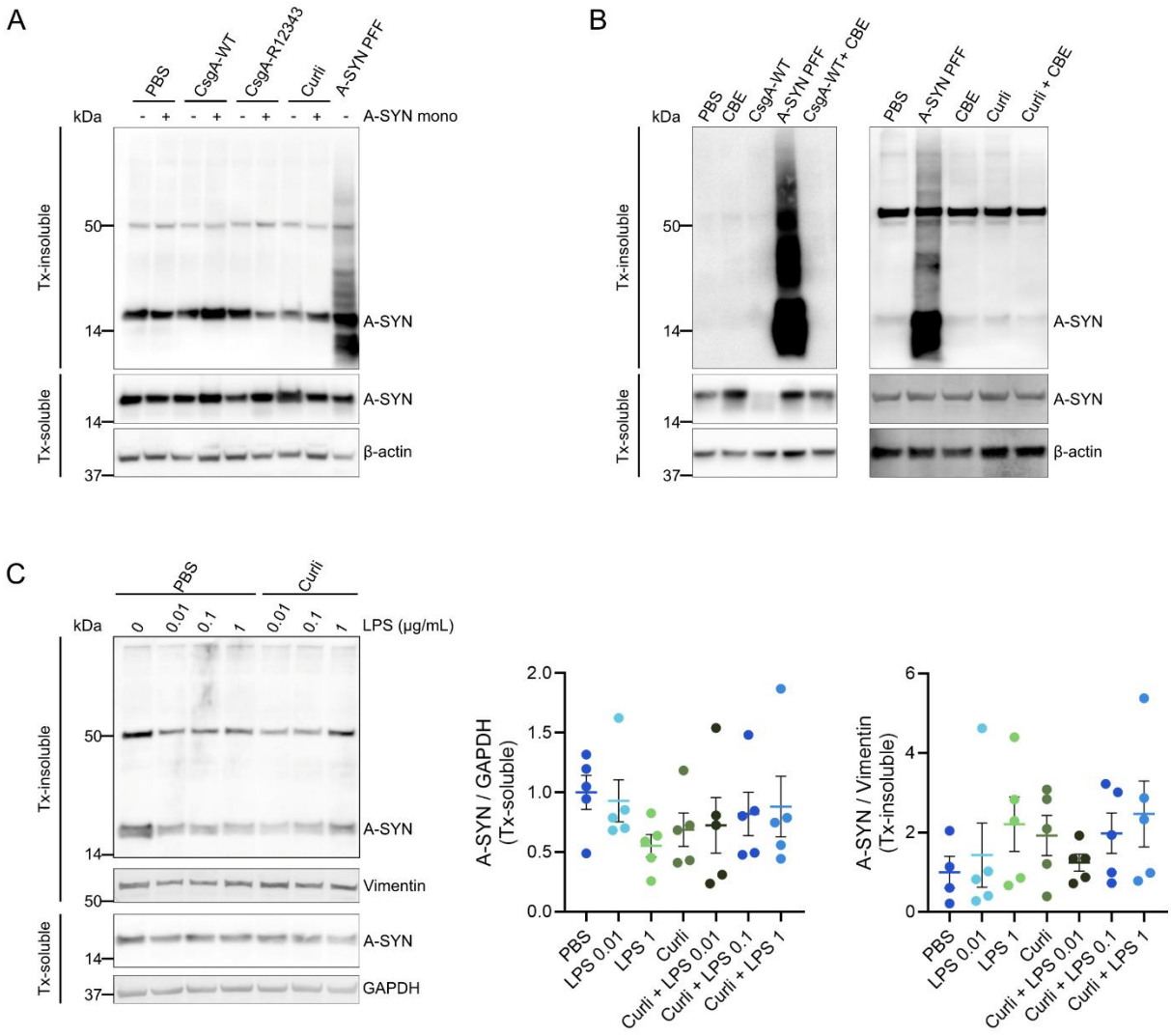


Figure 18. **Treatment with CsgA or curli does not promote α-SYN aggregation in in human enteroendocrine cells.**

A) Representative Western blots of Triton X-insoluble and Triton X-soluble lysates for the indicated conditions to assess α-SYN aggregation following CsgA and exogenous α-SYN treatment. B-actin was used as a housekeeping control. A-SYN PFF: α-SYN pre-formed fibrils (0.5 µM); A-SYN mono: α-SYN monomers (50 µg/mL). Tx: Triton X.

B) Representative Western blots of Triton X-insoluble and Triton X-soluble lysates for the indicated conditions to assess α-SYN aggregation following CsgA and CBE treatment. B-actin was used as a housekeeping control. CBE: conduritol-b-epoxide (50 µM). Tx: Triton X.

C) Representative Western blots of Triton X-insoluble and Triton X-soluble lysates for the indicated conditions to assess α-SYN aggregation following CsgA and LPS treatment. Quantifications of α-SYN levels normalized to GAPDH or vimentin for each fraction, expressed as relative fold-change to PBS. Mean ± SEM, one-way ANOVA with Tukey's correction for multiple comparisons, n=5 independent experiments. LPS: lipopolysaccharide; Tx: Triton X.

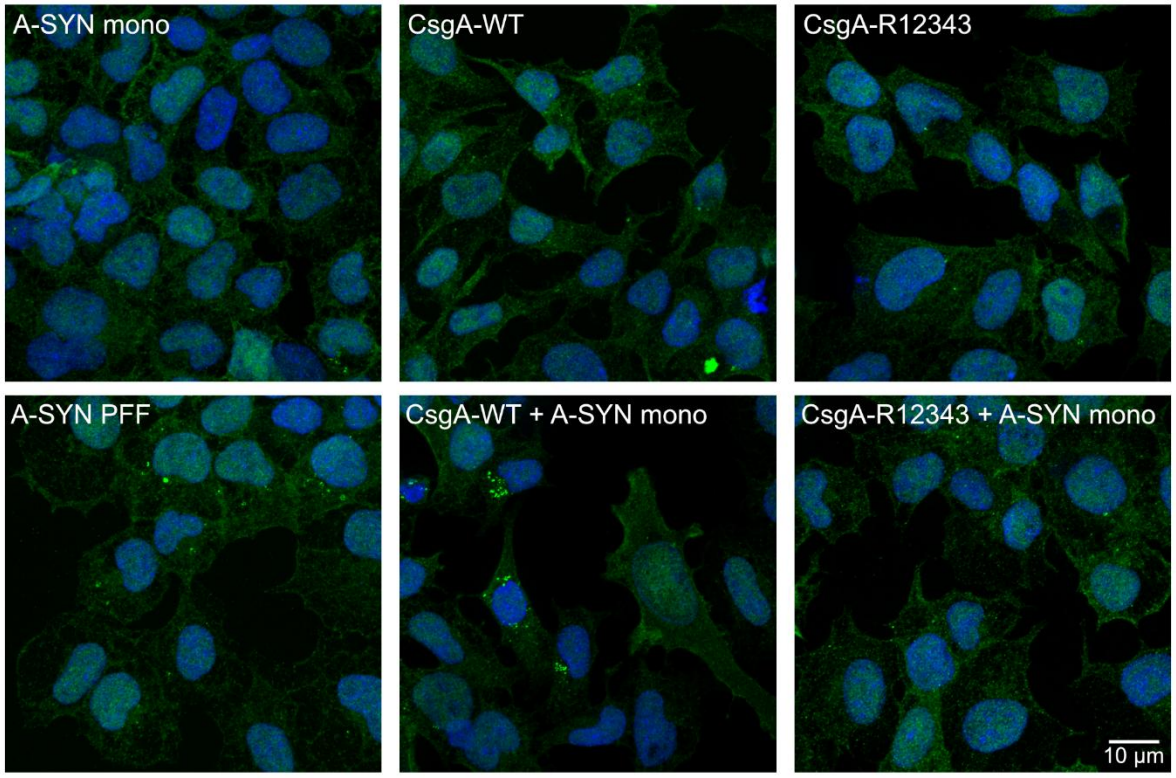


Figure 19. **Treatment with CsgA-WT and α-SYN monomers causes α-SYN puncta formation in a subset of in human enteroendocrine cells.**
Representative images of HuTu-80 stained against total α-SYN (green) for the treatment conditions indicated. DAPI (blue) was used as a nuclear counterstain. A-SYN mono = monomers (negative control); α-SYN PFF = pre-formed fibrils (positive control). Scale bar: 10 µm.

Next, we utilized the *E. coli* K12 strain either WT or *ΔcsgBAC* (negative control), since these strains accelerated α-SYN aggregation in PD animal models [122-124]. HuTu-80 were co-treated with CBE, $NaNO_2$, low α-SYN PFF concentration, *A. muciniphila* conditioned medium (CM), or IFNg. $NaNO_2$ is a source of nitric oxide and is associated with intestinal inflammation, gut microbiota balance disruption, and α-SYN pathology [336-338]. In the same line, *A. muciniphila* CM promoted α-SYN phosphorylation and aggregation in mouse STC-1 enteroendocrine cells [89]. Finally, IFNg is elevated in the serum of PD patients [49] and promoted Lewy body-like formation in human stem cell-derived dopaminergic neurons upon co-treatment with α-SYN PFF [50]. To induce biofilm formation and curli production, *E. coli* was initially grown on YESCA agar plates at 26^{o}C for 48 hours (**Figure 20A**). Congo Red staining, and sedimentation assay verified biofilm formation by *E. coli* WT but not by *E. coli* Δ*csgBAC* (**Figures 20A-B**). When the bacteria were centrifuged and the supernatant OD was measured at 500 nm, the reduction in absorbance in the medium by *E. coli* WT vs Δc*sgBAC* (**Figure 20C**) further suggested that Congo Red was incorporated in the bacterial biofilm. Subsequently, *E. coli* WT or *ΔcsgBAC* was co-cultured with

HuTu-80 for 10 DIV but did not induce any visible α-SYN aggregation in the Triton X-insoluble fractions alone or together with any of the molecules tested (**Figures 20D-G**). The levels of Triton X-soluble α-SYN were measured following treatment with *E. coli* and IFNg, but not significant changes were observed (**Figure 20G**). Thus, biofilm forming *E. coli* is not sufficient to promote α-SYN aggregation in HuTu-80 even in the presence of the stressors CBE, $NaNO_2$, α-SYN PFF, *A. muciniphila* CM, or IFNg.

Overall, these results indicated that CsgA-WT, curli fibers, or biofilm-forming *E. coli* did not initiate α-SYN aggregation under the tested conditions in HuTu-80 EECs.

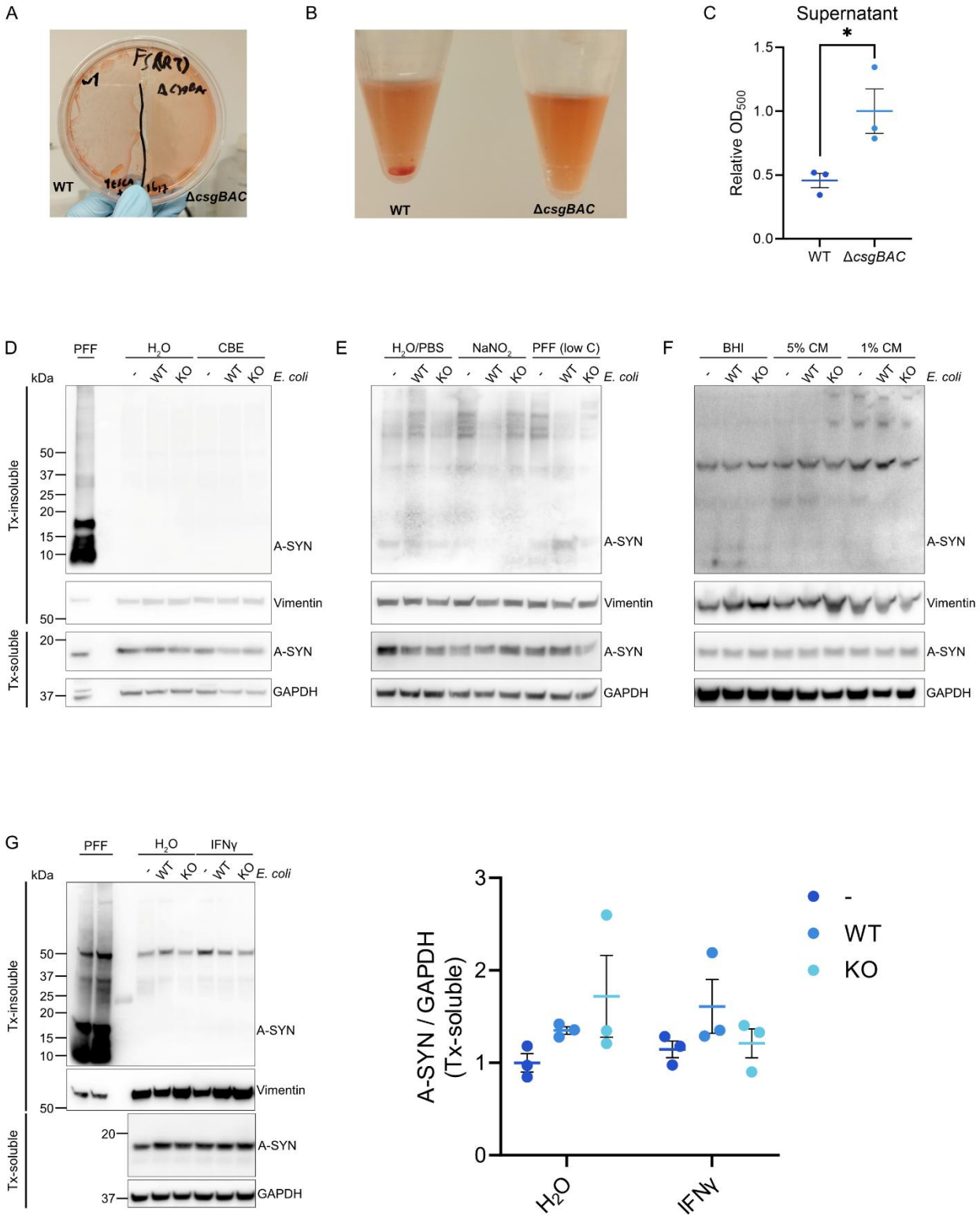


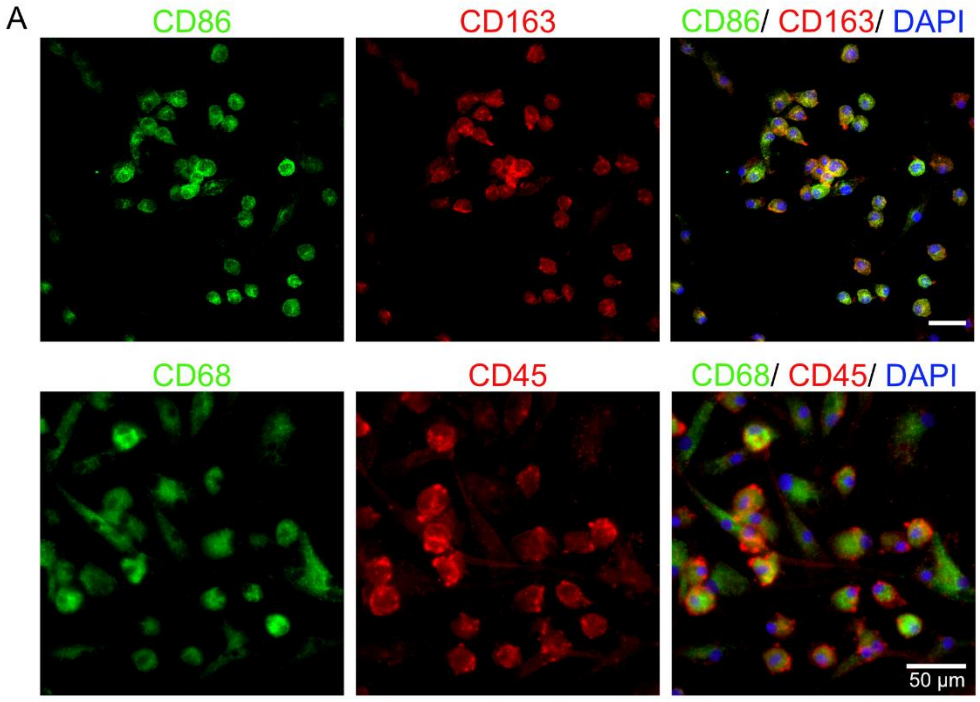
Figure 20. **Treatment with biofilm-producing *E. coli* does not lead to α-SYN aggregation in in human enteroendocrine cells.**

A) *E. coli* WT and Δ*csgBAC* grown on YESCA agar plates with Congo Red at 26°C for 48 hours.

B) *E. coli* WT and Δ*csgBAC* sedimentation assay in YESCA medium with Congo Red.
C) Quantification of OD at 500 nm of YESCA + Congo Red supernatant from *E. coli* WT and Δ*csgBAC* cultures. Mean ± SEM, *p<0.05, unpaired two-tailed t-test, n=3 independent experiments.
D) Representative Western blots of Triton X-insoluble and Triton X-soluble lysates for the indicated conditions to assess α-SYN aggregation following *E. coli* co-culture and CBE treatment. Vimentin and GAPDH were used as loading controls for each lysate fraction. CBE: conduritol-b-epoxide (50 μM). WT: *E. coli* WT; KO: *E. coli* Δ*csgBAC*; PFF: α-SYN pre-formed fibrils (0.5 μM).
E) Representative Western blots of Triton X-insoluble and Triton X-soluble lysates for the indicated conditions to assess α-SYN aggregation following *E. coli* co-culture and $NaNO_2$ or low α-SYN PFF concentration treatment. Vimentin and GAPDH were used as loading controls for each lysate fraction. $NaNO_2$: sodium nitrite (20 μM); PFF (low C): α-SYN pre-formed fibrils (25 ng/mL). The same ladder applies as in panel D.
F) Representative Western blots of Triton X-insoluble and Triton X-soluble lysates for the indicated conditions to assess α-SYN aggregation following *E. coli* co-culture and *A. muciniphila* CM treatment. Vimentin and GAPDH were used as loading controls for each lysate fraction. CM: conditioned medium. The 5% CM was added for a total of 2 DIV. The same ladder applies as in panel D.
G) Representative Western blots of Triton X-insoluble and Triton X-soluble lysates for the indicated conditions to assess α-SYN aggregation following *E. coli* co-culture and IFNg (0.2 ng/mL) treatment. Quantifications of Triton X-soluble α-SYN levels normalized to GAPDH expressed as relative fold-change to H_2O control. Mean ± SEM, one-way ANOVA with Tukey's correction for multiple comparisons, n=3 independent experiments.

5.1.4.2 Extracellular vesicles from CsgA-WT-treated HuTu-80 induce α-SYN seeding competency in peripheral neuron and macrophages

The enteric neurons and the intestinal immune system are integral gut components and are implicated in the early development and propagation of PD pathology [21, 52, 162, 339]. Considering HuTu-80-derived EVs show increased α-SYN levels, carry CsgA, and affect macrophage cytokine release (**Figures 14B, 16A-B**), we hypothesized that their exposure to peripheral neurons and macrophages would promote α-SYN aggregation. Peripheral neurons were derived as described by Reinhardt et al [301] and their detailed characterization is shown in the next section. Differentiated macrophages stained positive for the immune or macrophage cell surface markers CD45, CD68, CD86, and CD163 (**Figure 21A**). When co-cultured, peripheral neurons and macrophages retained TUJ1 and CD86 marker expression, respectively (**Figure 21B**). Notably, CD86 signal intensity was reduced, and macrophages appeared spherical in co-cultures compared to single cultures (**Figure 21A-B**). Using flow cytometry, CD56/NCAM and CD45 specifically stained neurons and macrophages, respectively (**Figure 22A**), and were employed for cell sorting experiments. In line with the CD86 immunocytochemistry (**Figure 21B**), CD45+ macrophages populations with different signal intensities were observed in co-cultures but not in single cultures (**Figure 22A**). This suggested that macrophages in co-cultures may lose their identity over time. Altogether, macrophages and peripheral neurons can be co-cultured and sorted for evaluating α-SYN aggregation.


A
CD86
CD163
CD86/ CD163/ DAPI
CD68
CD45
CD68/ CD45/ DAPI
50 µm

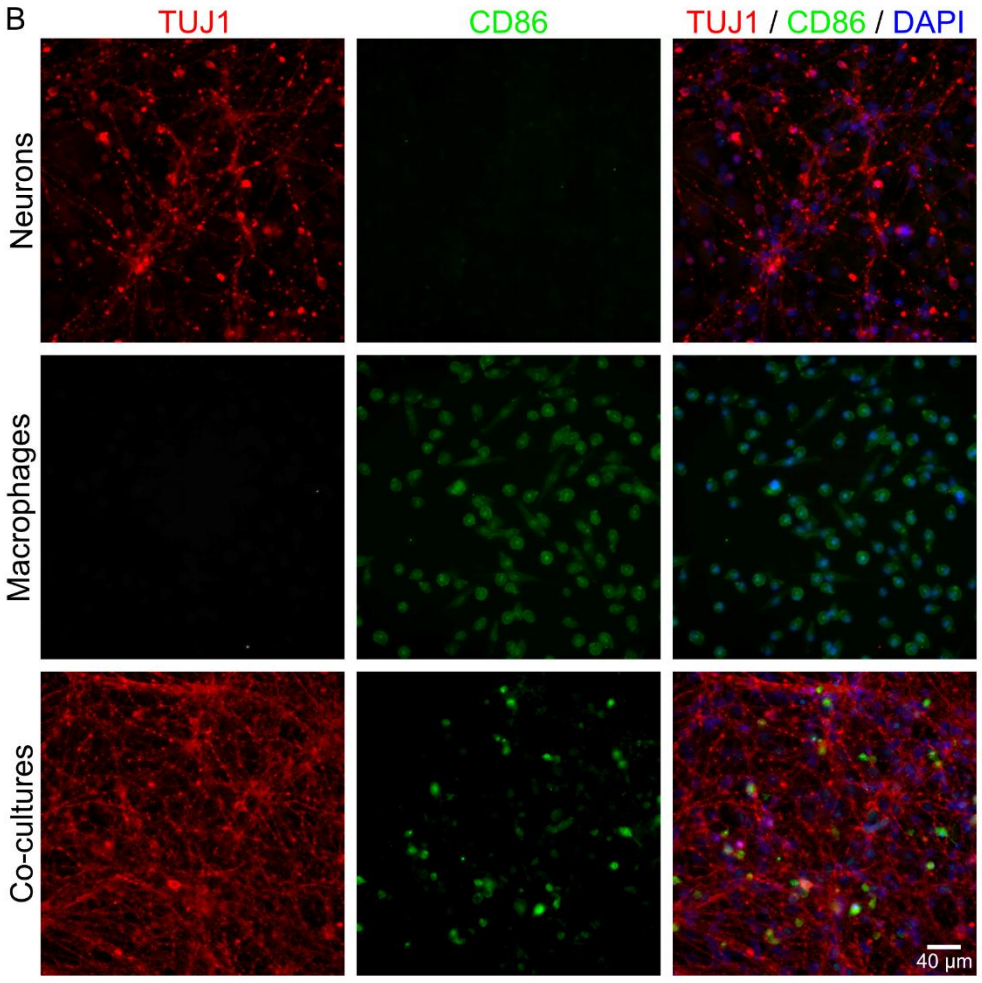

B
TUJ1
CD86
TUJ1 / CD86 / DAPI
Neurons
Macrophages
Co-cultures
40 µm

Figure 21. Control cell line 1 peripheral neuron and macrophage co-cultures.
A) Representative images of iPSC-derived macrophages stained against CD86 or CD68 (green), and CD163 or CD45 (red). DAPI (blue) was used as a nuclear counterstain. Scale bars: 50 µm. B) Representative immunofluorescence images of neurons, macrophages, and neuron/macrophage co-cultures corresponding to 8 DIV after seeding the cells in co-cultures and stained against TUJ1 (red, neurons) and CD86 (green, macrophages). DAPI (blue) was used as a nuclear counterstain. Scale bar: 40 µm.

Following flow cytometry optimization, the co-cultures were treated twice with 2 µg/mL EVs from HuTu-80 pre-treated with CsgA-WT, CsgA-R12343, or PBS, together with 50 µg/mL α-SYN monomers, to increase intracellular α-SYN load. Certain co-cultures were only exposed with α-SYN monomers or PFFs as negative and positive controls, respectively. Cells were detached and sorted (**Figure 22B**). The forward and side scatter (FSC, SSC) values were gated to filter out debris (**Figure 22B**, 1st column). Then, compensation matrices were prepared using the single-stained co-cultures for Sytox Blue (dead cell dye), NCAM, or CD56. The live cells were determined via the Sytox Blue-negative staining (**Figure 22B**, 2nd column). Neurons and macrophages were gated based on the NCAM and CD45 intensities (**Figure 22B**, 3rd column). Finally, singlets were selected using the FSC area and height values. Note that macrophages displayed high size heterogeneity, thus the singlet gate was larger (**Figure 22B**, 4th and 5th column).

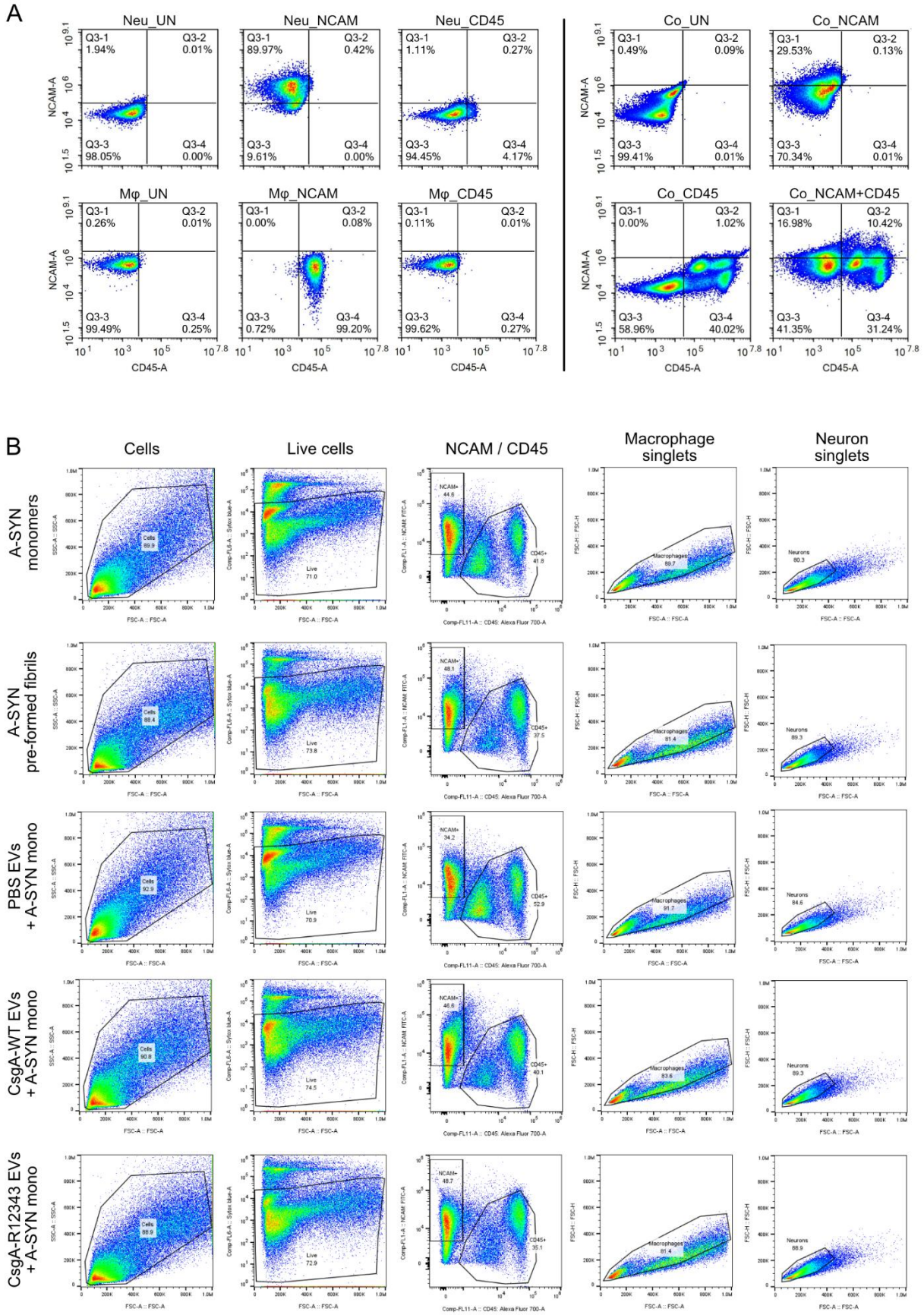
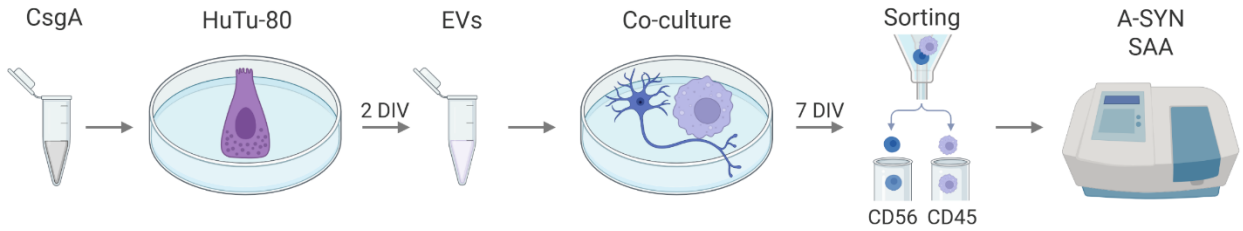

A
Neu_UN
Q3-1 1.94%
Q3-2 0.01%
Q3-3 98.05%
Q3-4 0.00%
Neu_NCAM
Q3-1 89.97%
Q3-2 0.42%
Q3-3 9.61%
Q3-4 0.00%
Neu_CD45
Q3-1 1.11%
Q3-2 0.27%
Q3-3 94.45%
Q3-4 4.17%
Co_UN
Q3-1 0.49%
Q3-2 0.09%
Q3-3 99.41%
Q3-4 0.01%
Co_NCAM
Q3-1 29.53%
Q3-2 0.13%
Q3-3 70.34%
Q3-4 0.01%
Mφ_UN
Q3-1 0.26%
Q3-2 0.01%
Q3-3 99.49%
Q3-4 0.25%
Mφ_NCAM
Q3-1 0.00%
Q3-2 0.08%
Q3-3 0.72%
Q3-4 99.20%
Mφ_CD45
Q3-1 0.11%
Q3-2 0.01%
Q3-3 99.62%
Q3-4 0.27%
Co_CD45
Q3-1 0.00%
Q3-2 1.02%
Q3-3 58.96%
Q3-4 40.02%
Co_NCAM+CD45
Q3-1 16.98%
Q3-2 10.42%
Q3-3 41.35%
Q3-4 31.24%
NCAM-A
CD45-A
B
Cells
Live cells
NCAM / CD45
Macrophage singlets
Neuron singlets
A-SYN monomers
A-SYN pre-formed fibrils
PBS EVs + A-SYN mono
CsgA-WT EVs + A-SYN mono
CsgA-R12343 EVs + A-SYN mono

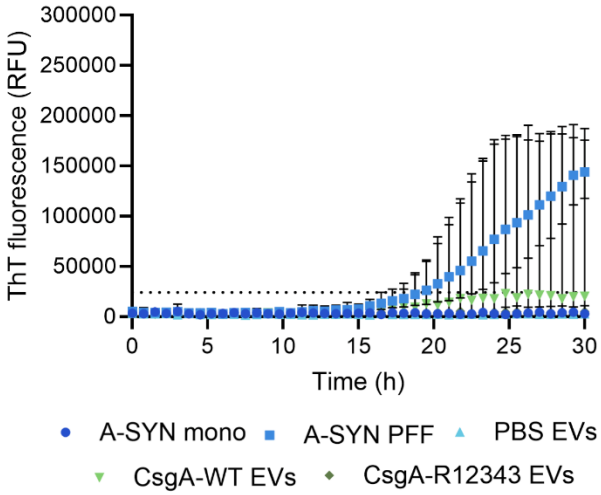
Figure 22. **FACS gating strategy to sort control cell line 1 peripheral neuron and macrophages to measure α-SYN seeding competency in cell lysates.**
A) Representative flow cytometry plots to verify surface staining of peripheral neurons and macrophages in single cultures or co-cultures with NCAM and CD45, respectively. Neu: neurons; Mφ: macrophages; Co: co-cultures; UN: unstained. NCAM and CD45 on the title of each graph corresponded to the antibody these cells were stained with.
B) Representative flow cytometry plots to isolate peripheral neurons and macrophages from co-cultures for the indicated treatments. Cells were initially chosen based on their forward and side scatter, then living cells were selected by including the Sytox Blue-negative population. Peripheral neurons and macrophages were separated from the co-culture based on the fluorescent signal of NCAM (CD56) and CD45, respectively. Single neurons and macrophages were finally sorted by gating the indicated forward scatter area and height.

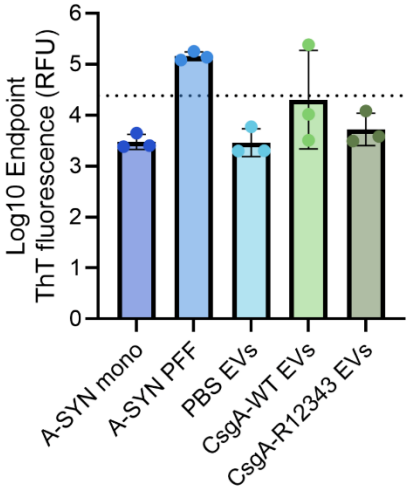
The lysates from sorted cells were analyzed by the α-SYN SAA using RT-QuIC (**Figure 23A**). In this assay, purified α-SYN monomers are incubated together with the lysates and ThT. If the preparation contains α-SYN seeds, then the assay's monomers will begin to aggregate leading to increase in ThT fluorescence. Neurons and macrophages treated with α-SYN PFF showed the expected increase in ThT fluorescence that surpassed the 10% cut-off value (**Figure 23B-C**). Instead, lysates from α-SYN monomer-treated neurons and macrophages were negative validating our experimental controls (**Figure 23B-C**). Treatment with EVs from CsgA-R12343- or PBS-exposed HuTu-80 did not show α-SYN seeding competency in either peripheral neurons or macrophages, while EVs from CsgA-WT-treated HuTu-80 had a tendency for increased ThT fluorescence vs the PBS control (**Figure 23B-C**). Thus, EVs from CsgA-WT-treated HuTu-80 promote modest α-SYN seeding capacity in recipient peripheral neurons and macrophages.

A

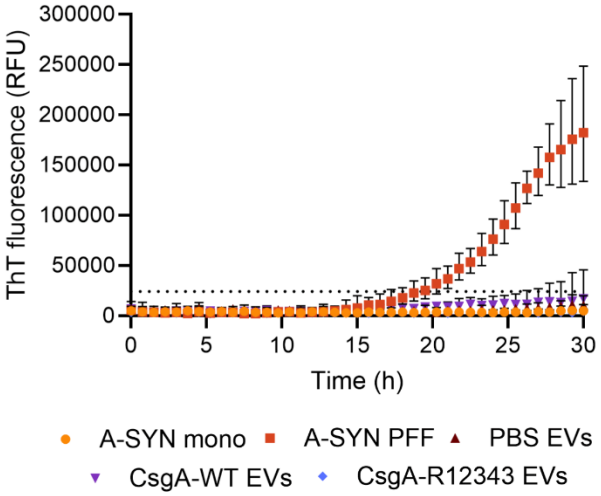

CsgA
HuTu-80
2 DIV
EVs
Co-culture
7 DIV
Sorting
CD56 CD45
A-SYN SAA

B


Neurons
ThT fluorescence (RFU)
Time (h)
A-SYN mono
A-SYN PFF
PBS EVs
CsgA-WT EVs
CsgA-R12343 EVs


Neurons
Log10 Endpoint ThT fluorescence (RFU)
A-SYN mono
A-SYN PFF
PBS EVs
CsgA-WT EVs
CsgA-R12343 EVs

C


Macrophages
ThT fluorescence (RFU)
Time (h)
A-SYN mono
A-SYN PFF
PBS EVs
CsgA-WT EVs
CsgA-R12343 EVs

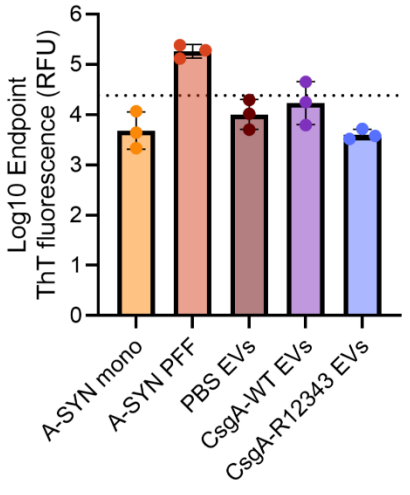

Macrophages
Log10 Endpoint ThT fluorescence (RFU)
A-SYN mono
A-SYN PFF
PBS EVs
CsgA-WT EVs
CsgA-R12343 EVs

Figure 23. **A-SYN seed amplification assay in control cell line 1 peripheral neuron and macrophage lysates from co-cultures treated with HuTu-80 EVs.**
A) Schematic of the experimental set-up to study the effect of HuTu-80-derived extracellular vesicles on α-SYN seeding competency in co-cultures of peripheral neurons and macrophages.
B) A-SYN seed amplification assay monitored with ThT fluorescence in neuron lysates for the time points and conditions indicated. The cut-off for positive signal (dotted line) was defined as 10% of the maximal fluorescence intensity (>24132). A-SYN mono = α-SYN monomers (negative control); A-SYN PFF = α-SYN pre-formed fibrils (positive control). Geometric mean ± geometric SD, Kruskal-Wallis test with Dunn's correction for multiple comparisons, n=3 independent experiments.
C) A-SYN seed amplification assay monitored with ThT fluorescence in macrophage lysates for the time points and conditions indicated. The cut-off (dotted line) for positive signal was defined as 10% of the maximal fluorescence intensity (>24132). A-SYN mono = α-SYN monomers (negative control); A-SYN PFF = α-SYN pre-formed fibrils (positive control). Geometric mean ± geometric SD, one-way ANOVA with Tukey's correction for multiple comparisons, n=3 independent experiments.

5.2 Part 2: Development of a neuron-enteroendocrine microfluidics co-culture model to monitor pathology propagation

5.2.1 Human iPSC-derived intestinal organoids

While HuTu-80 presented a practical and expandable enteroendocrine cell model to study the effect of the bacterial amyloid CsgA, the cells were limited by their cancer background. Human iPSC-derived models allow differentiation to cell types of interest, they permit personalized studies, and they can be modified to include a genetic variant of interest. Thus, they are highly adaptable based on the biological question investigated. Currently, EECs can be acquired from differentiation of iPSCs towards intestinal organoids. We employed an iPSC-to-colonic organoid differentiation protocol which developed EECs [300]. Using chemical modulators, the iPSCs were directed towards the endoderm fate, followed by the hindgut endoderm, and finally colonic organoids. The organoids were collected and cultured in Matrigel domes to promote their 3D growth. To increase EECs representation, we used organoids used between passage 3-8 which were maintained in culture for 8-10 days *in vitro* after splitting, since larger organoids showed reduced proliferation, improved differentiation, and increased invagination. These organoids were characterized by immunostaining or were dissociated and cultured in 2D transwells for an additional 10 days *in vitro*. As 2D, the cultures are more homogeneous and can be readily treated on the luminal side with CsgA. These 2D cultures were also fixed to be characterized by immunostaining. Successful HIO differentiation was revealed by the ubiquitous expression of CDX2, a transcription factor integral in intestinal epithelium specification and maintenance [340], both in 3D (**Figure 24A**) and 2D (**Figure 24B**). Chromogranin-A (CHGA), an EEC marker, was

also widely expressed in HIOs (**Figures 23A, B**) and co-labelled cells with 5-hydroxytryptamine (serotonin, **Figure 24A**), a neurotransmitter produced and released by EECs [159]. A-SYN was expressed by few CHGA-positive cells, yet its levels were barely detectable (**Figures 23C-D**). Therefore, while the iPSC-derived HIOs cultured in 3D or 2D contained EECs, this model was not appropriate for studying α-SYN pathology upon bacterial amyloid exposure.

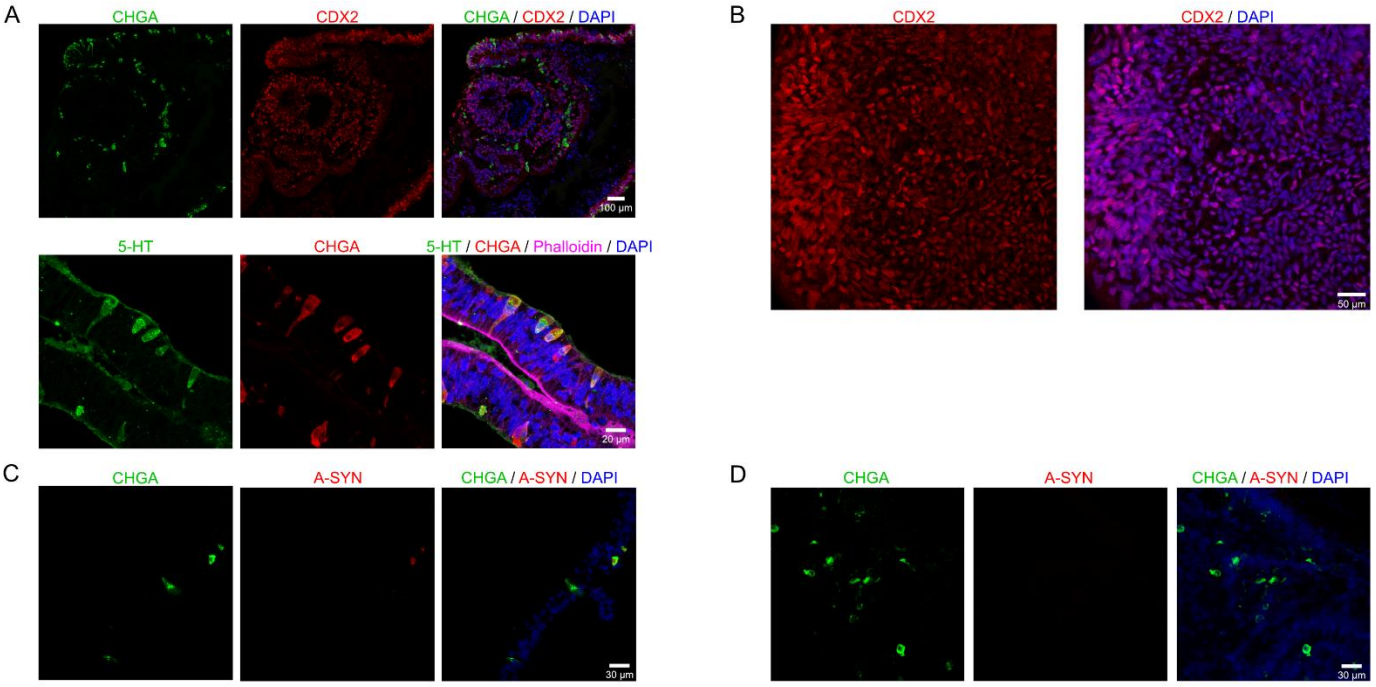


Figure 24. KOLF2.J1 iPSC-intestinal organoid characterization.
A) Representative images of immunostained 3D-cultured intestinal organoids sections against the indicated proteins. CHGA: chromogranin-A (green or red); CDX2: caudal-type homeobox transcription factor 2; 5-HT: 5-hydroxytryptamine/serotonin (green). Phalloidin (magenta) and DAPI (blue) were used as a cytoskeleton and nuclear counterstain, respectively. Scale bars (from top to bottom): 100 and 20 µm.
B) Representative image of immunostained 3D-cultured intestinal organoid sections against CHGA (green) and α-SYN (red). DAPI (blue) was used as a nuclear counterstain. Scale bar: 30 µm.
C) Representative image of intestinal organoids dissociated, cultured 10 DIV in 2D transwells, and immunostained against CDX2 (red). DAPI (blue) was used as a nuclear counterstain. Scale bar: 50 µm.
D) Representative image of intestinal organoids dissociated, cultured 10 DIV in 2D transwells, and immunostained against CHGA (green) and α-SYN (red). DAPI (blue) was used as a nuclear counterstain. Scale bar: 30 µm.

5.2.2 Human iPSC-derived peripheral neurons co-cultured with HuTu-80 in microfluidics chips

Intestinal α-SYN expression is not limited to EECs with the protein being produced by enteric neurons as well. As our neuron model, we differentiated NPCs into peripheral neurons following the protocol of Reinhardt et al [301]. Considering the protocol was established in the lab, a series of characterizations were performed. WNT signalling activation and BMP4 were used to induce K7 NPCs fate towards neural crest-like cells (NCLCs, 10 DIV, **Figure 25A**). NCLC gene expression was compared to iPSCs and showed proper patterning of vagal NCL lineage (*PAX3*, *HOXB3-4*, **Figure 25A**). The *HOXB5* levels displayed large variability between independent differentiations. However, *SOX10* transcription factor expression was not induced in NCLCs compared to iPSCs (**Figure 25A**), which could be a limitation of differentiating from pre-patterned NPCs [301], and, thus, this protocol did not derive pure enteric neurons. The early transition of NCLCs to neurons was verified by the increased expression of *ASCL1* and *PHOX2B* at D10 versus iPSCs (**Figure 25A**). *EDNRB* levels were unchanged between NCLCs and iPSCs. Subsequently, NCLCs were split and cultured with neuron maintenance medium for at least 11 days to allow for differentiation towards peripheral neurons. Neuronal-like morphology was visible already at 15 DIV and the neurons were positive for the neuronal cytoskeleton markers TUJ1 and PRPH (**Figure 25B**). This expression persisted at 30 DIV, where neuron projection outgrowth was present alongside the neuron marker MAP2 (**Figure 25C**). Finally, a subset of cells contained choline-O-acetyltransferase (ChAT, **Figure 25D**), the acetylcholine synthesis enzyme in cholinergic neurons. Therefore, we were able to obtain differentiated peripheral neurons derived from NPCs.

In the intestine, enteric neurons form synapses with EECs. To model the connection between the two cell types, peripheral neurons and HuTu-80 would be separated into two different microfluidics channels and connected via neuron projections. The commercial Netri Dualink Ultra microfluidics chip was selected since it consists of a middle channel further separating the cell types in the two side channels and minimizing medium mixing. The side and middle channels are all connected at the bottom through microgrooves. NCLCs were seeded into one side channel and were allowed to differentiate over 11 DIV (**Figure 25E**). Neuron projection outgrowth was promoted by doubling the concentration of BDNF and GDNF adding less medium volume in the unseeded channel to apply chemoattraction and a hydrostatic pressure towards that channel, respectively. At 21 DIV of the peripheral neuron differentiation protocol, HuTu-80 were seeded into the opposite channel (**Figure 25E**). Neuron projections could be seen with brightfield microscopy in the middle channel and on the side close to the HuTu-80 (**Figure 25F**). Following 7 DIV of co-culture, the cells were

fixed and stained with the neurofilament marker TUJ1 and the pre-synaptic marker SYP1. Certain TUJ1+/SYP1+ neuron projections spanned the middle channel and reached the HuTu-80 cells (**Figure 25G**), suggesting they may form synapses. HuTu-80 cells were also TUJ1+ probably due to their neuron-like properties of EECs. Hence, peripheral neurons can be co-cultured with HuTu-80 enteroendocrine cells in microfluidics devices as a model to study PD pathology propagation.

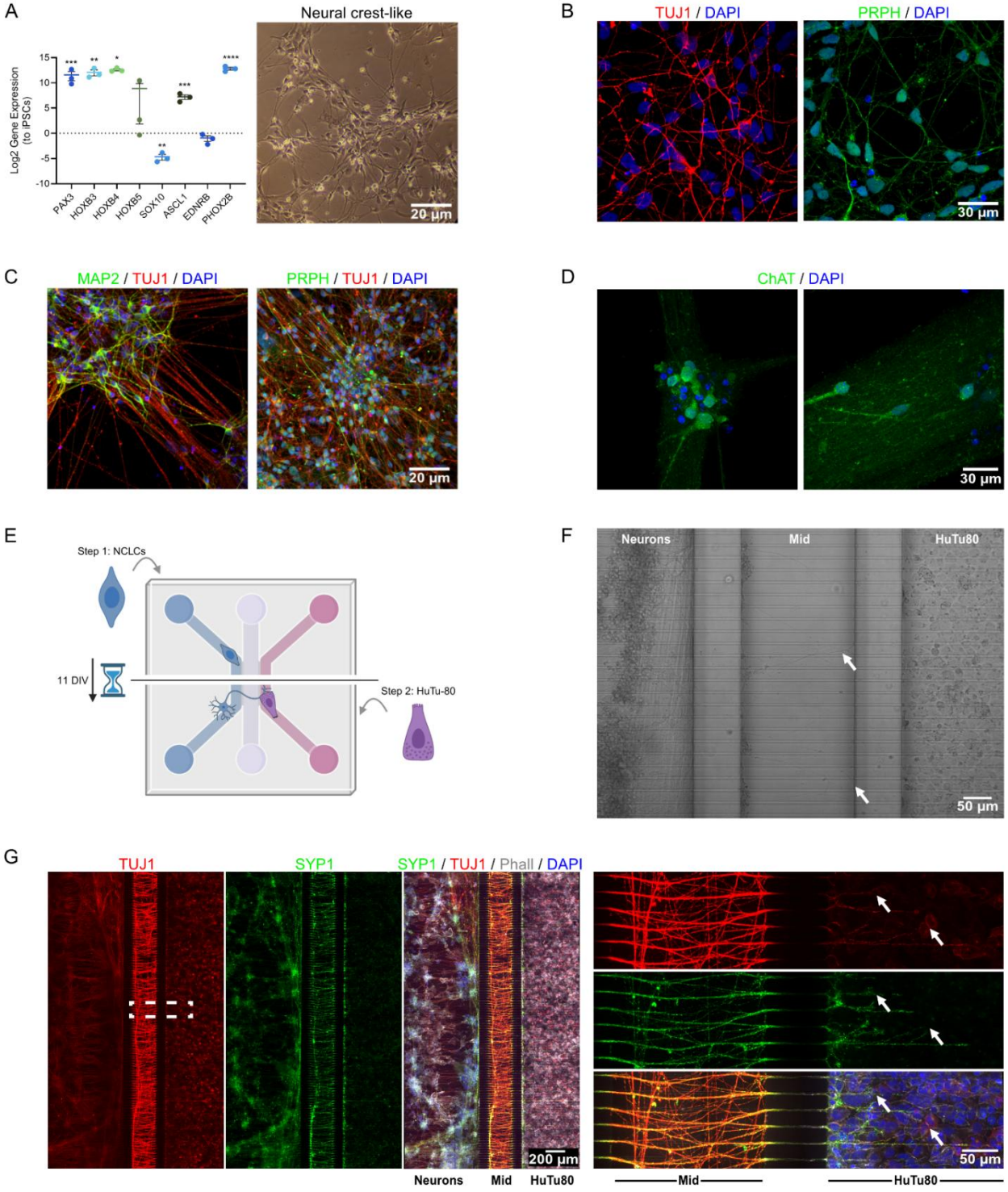


Figure 25. Control cell line 1 NPC-derived peripheral neuron characterization and co-culture in microfluidics chip with HuTu-80.
A) Neural crest patterning (*PAX3*, *HOXB3-5*, *SOX10*) and early neuronal fate (*ASCL1*, *EDNRB*, *PHOX2B*) gene expression in NPC-derived neural crest-like cells (D10) versus iPSCs. Representative brightfield image of neural crest-like cells dissociated at D11 of the differentiation protocol and cultured 1 DIV in maturation medium. Scale bar: 20 µm. Mean ± SEM, *p<0.05, **p<0.01, ***p<0.001, ****p<0.0001, unpaired two-tailed t-test of each gene's Ct in NCLCs vs iPSCs, n=3 independent experiments.
B) Representative immunofluorescence images of D15 peripheral neurons stained against TUJ1 (red) and PRPH (green). DAPI (blue) was used as a nuclear counterstain. Scale bar: 30 µm.
C) Representative immunofluorescence images of D30 peripheral neurons stained against MAP2 (green), TUJ1 (red), and PRPH (green). DAPI (blue) was used as a nuclear counterstain. Scale bar: 20 µm.
D) Representative immunofluorescence images of D65 peripheral neurons stained against ChAT (green). DAPI (blue) was used as a nuclear counterstain. Scale bar: 30 µm.
E) Schematic of the microfluidics chip seeding. NCLCs were initially seeded into one side channel and allowed to grow for 11 DIV (step 1), when the HuTu-80 were then pipetted (steps 2). Cells were kept in co-culture for 7 DIV.
F) Representative brightfield image of neurons at D21, 2 hours post-HuTu-80 seeding. Arrows indicate visible neuron projections in the middle channel towards the HuTu-80 compartment.
G) Representative immunofluorescence image of D30 peripheral neurons co-cultured in microfluidics together with HuTu-80 in separate channels. The cells were stained against SYP1 (green) and TUJ1 (red). Phalloidin (gray) and DAPI (blue) were used as a cytoskeleton and nuclear counterstain. The right section is a zoom-in of the white dashed square indicated on the left section. Arrows highlight neuron projections in proximity to HuTu-80. Scale bars: 200 µm (overview), 50 µm (zoom-in).

6. Discussion

The primary goal of this project was to identify how the bacterial amyloid CsgA perturbed EEC function to drive PD pathogenesis. HuTu-80 were selected as a human EEC cell model due to their high expression of α-SYN and they were treated with CsgA monomers (CsgA-WT or CsgA-R12343) or curli fibers. The first question was to investigate whether CsgA and curli are uptaken by EECs. Specifically, CsgA-WT and curli were targeted into the lysosomes of HuTu-80 for degradation 48 hours post-treatment. Despite the lysosomal trafficking and alterations in lysosomal morphology, there was no effect in the autophagy as assessed by the markers P62 and LC3B-II/LC3B-I by neither CsgA monomers nor curli.

The second question was to comprehensively evaluate the EEC response to the bacterial amyloids. Following the development of the HuTu-80-TMEM192-3xHA cell line, proteomics was performed in whole-cell and lysosome-specific lysates. Surprisingly, only CsgA-WT provoked proteome changes in both whole-cell and lysosome-enriched lysates in the HuTu-80, suggesting that the aggregation-prone monomers initiate an EEC response. The differences between CsgA-WT and curli could be attributed to the large size of curli fibers that may limit their uptake into cells. Overall, CsgA-WT decreased protein levels of mitochondrial respiratory complexes, mitochondrial-related redox components, the proteostasis machinery (chaperones and proteasome subunits), and intracellular trafficking elements. These changes were not sufficient to cause a significant dysregulation in mitochondrial respiration, superoxide production, or proteasome chymotrypsin-like activity, suggesting that CsgA-WT does not provoke a robust pathological phenotype in HuTu-80 EECs. Nonetheless, the downregulation of AP2S1, DYNC1I2, and LAMP2 in lysosomal fractions of CsgA-WT-treated cells suggested impaired lysosomal trafficking. Indeed, CsgA-WT induced a decrease in lysosomal α-SYN levels accompanied by an increase of α-SYN release in the extracellular space and EVs, indicating that EECs alter the trafficking machinery to transition towards intercellular communication. This was further corroborated by elevated RAB27A levels in whole-cell lysates and CD63 levels in EVs from HuTu-80 exposed to CsgA-WT, though there were no changes in the total number or size of released EVs. The concomitant elevation of α-SYN and CD63 in EVs suggested that enteroendocrine cells acquired immune modulatory properties in response to the bacterial amyloid CsgA.

In the same line, the third question was to evaluate the HuTu-80 immune response. CsgA-WT promoted upregulation of IL-8 and MIP-1α chemokine release accompanied by increased HLA-DR surface exposure. To further understand the immune effects of the enteroendocrine cell response, HuTu-80 EVs were treated to iPSC-derived macrophages. EVs from untreated cells

were inflammatory as evidenced by the elevated release of IL-1β, IL-6, TNFα, IL-10, and IL-23 cytokines, and IL-8 and MCP-1 chemokines. Instead, EVs from CsgA-WT-treated HuTu-80 diminished the IL-1β, IL-6, and IL-23 pro-inflammatory cytokine release. To evaluate the longer-term effect of CsgA-associated EVs, macrophages were allowed to recover prior to a secondary LPS stimulus. Even after a 48-hour recovery period, macrophages exposed to EVs from CsgA-treated HuTu-80 displayed sustained cytokine release. Importantly, these macrophages displayed abolished to LPS stimulus, indicating they acquire exhausted-like properties. Overall, these finding suggest the possibility of a chronic inflammatory effect of CsgA on macrophages that is not dependent on its amyloidogenic capacity. Thus, HuTu-80 acquire an immunomodulatory phenotype upon sensing CsgA by chemokine secretion, MHC class II surface exposure, and EV release that sustains an activated macrophage state with subsequent exhaustion.

Immunity and α-SYN trafficking perturbations are linked to PD pathogenesis; hence the fourth question of the study was to evaluate α-SYN aggregation in HuTu-80 following CsgA treatment. Cells were exposed to CsgA-WT, curli, and biofilm-producing *E. coli* alone or in combination with additional stressors (GCase inhibition, the inflammatory molecules LPS and IFNγ, exogenous a-SYN monomers or PFF, *A. muciniphila* secretome, or sodium nitrite), yet no detectable α-SYN aggregation was observed. Considering HuTu-80 EVs carried CsgA, increased α-SYN levels, and modulated immunity, they were treated to iPSC-derived peripheral neuron/macrophage co-cultures. CsgA-WT-associated EVs induced a modest increase in ThT fluorescence, suggesting that EECs exposed to CsgA transfer cargo to tissue-resident neurons and immune cells to initiate α-SYN seeding.

Finally, we developed an EEC-peripheral neuron microfluidics model that could be used to study the crosstalk between these two cell types in the context of intestinal PD. Initially, we differentiated hIPSCs into colonic organoids with CHGA+ EECs in 3D and 2D, however they lacked endogenous α-SYN expression. Therefore, the HuTu-80 were selected as the EEC model for the microfluidics co-culture. Peripheral neurons derived from human stem cells extended SYP1+ projections towards EECs, suggesting their synaptic connectivity. While the model requires further characterization, it is a promising tool to monitor PD pathology propagation between EECs and enteric neurons.

6.1 The HuTu-80 response to CsgA and relevance for Parkinson's disease

6.1.1 CsgA: lysosomes and intracellular trafficking

To our knowledge, this is the first study to show that bacterial amyloids are uptaken by human cells to be actively targeted to the lysosomes. Use of the inhibitors bafA1 or CQ showed accumulation of CsgA-WT and curli (but not CsgA-R12343) in the human EEC line HuTu-80, confirming lysosomes participate in bacterial amyloid degradation. Combined with the detection of CsgA-WT but not CsgA-R12343 in HuTu-80-TMEM192-3xHA lyso-IP fractions, these findings suggest the R5 domain of CsgA or the CsgA aggregation state affect its intracellular trafficking and processing. Notably, bafA1 and CQ block autophagy by increasing lysosomal pH while LysoTracker emits fluorescence only in acidic pH. While use of these inhibitors for less than 8 hours promoted robust reduction of LysoTracker fluorescent signal [341, 342], a 48-hour treatment duration did not affect detection of the LysoTracker signal [343] implying lysosomal pH recovery. Accordingly in our experimental setting, the LysoTracker signal was quantifiable at a low drug concentration (10 nM and 10 μM for bafA1 and CQ, respectively) and a 48-hour treatment duration. However, CsgA-WT itself may affect lysosomal acidity as suggested by the downregulation of ATP6V0C, a subunit of the vacuolar ATP-ase (V-ATPase) which is responsible for lysosomal acidification, in the lysosomal proteomics dataset. While lysosomal pH measurements are necessary (i.e., LysoSensor staining), these findings would be relevant for linking CsgA to lysosomal dysfunction implicated in PD [50, 215, 280, 284, 344-346]. Regarding lysosomal morphology, CsgA monomers caused a reduction in LysoTracker+ particle number with the decrease being significant only for CsgA-R12343. The effect of these changes was not sufficient to be detected at the autophagy marker (P62, LC3B) level. On the contrary, curli provoked a significant increase in the average LysoTracker+ particle size, suggesting an enlargement of lysosomes probably due to the large curli fiber size. Overall, CsgA-WT and curli are both trafficked to lysosomes for degradation, suggesting EECs internalized both the amyloid-prone monomers and mature fibers of CsgA, without affecting autophagy.

Both CsgA-WT and CsgA-R12343 induced a downregulation of LAMP2 in lysosomal fractions. There are three LAMP2 isoforms with each involved in a different component of the autophagic machinery: LAMP2A, LAMP2B, and LAMP2C participate in CMA, exosomal membranes, and degradation of nucleic acids or B-cell antigen presentation, respectively [214-216, 347-351]. The proteomics dataset and antibody used in this study did not distinguish between the three isoforms, thus while it is assumed that CMA is impaired, the levels of LAMP2A following CsgA-WT treatment should be measured. Following injection of *Staphylococcus* bacterial amyloid BapB as PFF in the

dorsal striatum of mice, Fernandez-Calvet et al [352] observed decreased midbrain LAMP2A levels accompanied by increased α-SYN levels and half-life compared to saline-injected mice. The effects were less robust in SH-SY5Y cells where BapB PFF treatment increased α-SYN levels without affect LAMP2A [352], suggesting that tissue complexity influences the response to the bacterial amyloid. In our experimental setting, the HuTu-80 were lysed immediately following CsgA treatment, while SH-SY5Y cells remained in culture for 10 DIV following BapB treatment [352] which could allow LAMP2 levels to recover. The mechanism leading to LAMP2 downregulation by CsgA *in vitro* or BapB *in vivo* is not known and CsgA does not contain a KFERQ-like motif. Thus, CsgA, unlike mutant α-SYN [215], is not expected to bind and block LAMP2 function. Instead, CsgA-WT would impact CMA primarily by inducing downregulation of LAMP2 and the co-chaperone HSPA8, as observed in the proteomics dataset. Therefore, both CsgA-WT and CsgA-R12343 downregulated the CMA-involved protein LAMP2, suggesting the bacterial origin of the protein is responsible for the observed effect and implying a predisposition to lysosomal dysfunction in EECs.

CsgA-WT decreased DYNC1I2 levels suggesting an impact in lysosomal trafficking through endo-lysosome fusion perturbation. Out of the 6 dynein chains detected in the lysosome proteomics dataset, DYNC1I2 and DYNC1H1 were downregulated, and the reduction was validated for DYNC1I2. Alongside LAMP2 downregulation, these findings could explain the downregulation of lysosomal α-SYN following CsgA-WT treatment in HuTu-80. The importance of dynein in α-SYN lysosomal trafficking has been studied in PD patient samples and neuron models. For instance, SN α-SYN inclusions are associated with declined dynein levels, decreased dynein/α-SYN co-localization, and impaired endo-lysosomal transport [353-355]. Conversely, silencing dynein heavy chains induced an increase in intracellular levels and half-life of α-SYN-A53T in rat PC12 cells [233]. Instead, boosting DYNLRB1 activation through NAGK overexpression induced α-SYN-A53T and HTT Q74 aggregate clearance in HEK293T cell models [234, 356]. Thus, dynein activity is linked to α-SYN degradation, whereas amyloid accumulation disrupts dynein function. In our CsgA-WT- versus PBS-treated proteomics datasets, DYNLRB1 was downregulated in whole-cell lysates and NAGK was decreased in both whole-cell and lysosome-enriched lysates, suggesting bacterial and human amyloids affect dynein function through similar mechanisms. The functions of dynein extend beyond endosomal localization to mitochondrial transport in neurons. A-SYN PFFs induced indirect downregulation of dynein which promoted a reduction of mitochondrial proteins implicated in anterograde transport (MTRITON X1, MTRITON X2, and Miro1) in the striatum of rats [357]. However, EECs have a short neuropod compared to the long axons in neurons, implying that dynein downregulation by CsgA-WT may not produce a robust mitochondrial transport impairment. Accordingly, there were no visible changes in mitochondrial

morphology, network, or cytosolic localization as visualized by MitoTracker live-cell imaging in HuTu-80 treated with CsgA-WT or curli. Thus, the CsgA-WT-mediated DYNC1I2 downregulation further corroborates lysosomal trafficking is impaired with subsequent decline in lysosomal α-SYN levels, suggesting EEC intracellular trafficking machinery perturbations in response to the the bacterial protein.

Overall, while both CsgA-WT and curli are trafficked to lysosomes for degradation, only CsgA-WT induced changes in lysosomal α-SYN and associated trafficking protein levels, suggesting the aggregate-prone monomers induce a robust EEC trafficking response.

6.1.2 Gut bacterial products and α-SYN aggregation

6.1.2.1 The bacterial-human amyloid cross-seeding: CsgA and α-SYN

Despite the downregulation in lysosomal α-SYN by CsgA-WT, whole-cell α-SYN levels remained unchanged. CsgA cross-seeds with α-SYN *in vitro* and accelerates α-SYN aggregation and S129 phosphorylation in animal models of PD [121-125, 358], yet there was no detectable aggregation in any of the experimental conditions tested in HuTu-80. In literature, PD animal models were either overexpressing human *SNCA* [121-124] or expressing human *LRRK2*-R1628P [125], two genotypes which promoted baseline α-SYN pathology. These studies provided a link between CsgA amyloids and PD progression *in vivo*, yet without describing an underlying pathological mechanism. To study CsgA/α-SYN cross-seeding in a simplified human model, the HuTu-80 EEC line endogenously expressing α-SYN was chosen. Nevertheless, our cell model lacked tissue complexity or PD-linked genetic manipulations, and included short experimental duration and exposure to *E. coli* compared to the animal models. These differences could partly explain the absence of endogenous α-SYN aggregation following CsgA treatment or biofilm-forming *E. coli* co-culture.

Few studies have investigated the effect of bacterial amyloids on α-SYN expression and aggregation in cell models. In neurons differentiated from SH-SY5Y cells, 16 µg/mL of CsgA did not alter *SNCA* and α-SYN levels [359], while the formation of α-SYN aggregates of α-SYN phosphorylation were not evaluated. The PFF of two different bacterial amyloids, BapB (from *S. aureus*) and EspN (from *Enterococcus faecalis*), promoted α-SYN aggregation and S129 phosphorylation in SH-SY5Y-derived neurons overexpressing human α-SYN with an HA tag, while the respective monomers had no effect on α-SYN levels [352]. Particularly, BapB PFF co-localized with α-SYN in puncta, suggesting their cross-seeding [352]. From a technical perspective, the bacterial amyloid treatment concentration was 20 µg/mL for 48 hours and cells were kept in culture

for an additional 10 days, replenishing the medium 2 days post-treatment. The CsgA concentration and treatment duration were similar in our study, thus the differences between our observations could be attributed to the HuTu-80 cell culture model that does not overexpress α-SYN. To overcome this, HuTu-80 were co-treated with CsgA and exogenous human α-SYN monomers every other day, yet no changes in soluble or insoluble α-SYN were detected. HuTu-80 is a highly replicating cell line, compared to differentiated SH-SY5Y neurons that do not proliferate. This could limit and dilute the strength of the effect of CsgA-WT cross-seeding with α-SYN in HuTu-80. Immunostaining of HuTu-80 treated with CsgA-WT together with α-SYN monomers showed α-SYN puncta formation in a subset of cells. These puncta indicate α-SYN accumulation and possibly early states of α-SYN aggregation, yet they were only visible in few EECs which could explain the lack of visible α-SYN aggregation by WB. A feasible alternative for measuring cross-seeding would be to generate an α-SYN-GFP HuTu-80 line and perform screening treatments with CsgA monomers or PFF, or *E. coli* alone or together with a second hit (i.e, α-SYN monomers, IFNγ, or CBE). A-SYN-GFP forms condensates under amyloid-inducing conditions which are readily visualized by fluorescent microscopy [89, 360]. The appearance of condensates is indicative of an early aggregation state, and their quantification permits comparison of the amyloid burden between conditions. In the human intestine, EECs are born from intestinal stem cells, and their estimated turnover ranges from 10 days to several months with EECs connected to neurons belonging to the longer lifespan range in the mouse colon [158, 361-363]. Therefore, a non-proliferative EEC line or intestinal organoids would be more appropriate to study intestinal amyloid cross-seeding.

Overall, the relevance of combinatory or two-hit treatments relied on the fact that PD is a complex disease with various genetic and environmental factors. Cells resist external stressors to maintain homeostasis, unless multiple hits strike simultaneously and/or for prolonged duration. This was signified *in vitro* using human amyloids (α-SYN PFF) and the pro-inflammatory cytokine IFNγ, the combination of which evoked LB-like pathology in human neuron cultures [50]. The experimental approach was replicated in our study but using the bacterial amyloid CsgA and decreased IFNγ levels (0.2 µg/mL instead of 200 µg/mL) to compensate for the repeated cytokine treatments mimicking a chronic low-dose scenario in the human intestine. Biofilm-forming *E. coli* and IFNγ had no significant effect on α-SYN levels or aggregation in HuTu-80. Overall, enteroendocrine cells do not develop detectable α-SYN aggregation upon CsgA or curli treatment, or biofilm-forming *E. coli* co-culture even under the presence of a secondary stimulus.

Interestingly, HuTu-80 responded to CsgA-WT by altering their proteome and initiated communication signals through EVs. Considering EVs carried CsgA and elevated α-SYN levels,

and exosomes are involved in α-SYN pathology propagation [281-283, 286-288], we evaluated the seeding capacity of EEC-derived EVs in tissue-resident cells. Enteric neurons and macrophages have been both implicated in early stages of PD pathogenesis [21, 52, 162, 339] and the underlying mechanisms are being uncovered. Intestinal macrophages uptake α-SYN aggregates, present α-SYN seeding capacity, and mount a T-cell immune response that induces dopaminergic neuron loss and motor impairments in mice [54]. Thus, we developed and characterized a human iPSC-derived peripheral neuron/macrophage co-culture model that we co-treated with HuTu-80 EVs and α-SYN monomers to increase intracellular α-SYN load. Particularly, EVs from CsgA-treated HuTu-80 instead of CsgA were used as an early PD model where intestinal barrier permeability should not be present, though we are aware that IBD patients with compromised gut barrier may develop PD [55, 56]. Importantly, CsgA-WT-associated EVs induced a modest increase in ThT fluorescence, indicating the presence of α-SYN seeds in both peripheral neurons and macrophages. Notably, exosomes from *E. coli* promoted pS129-α-SYN phosphorylation and autophagic impairment in the colon of LRRK2-R1628P mice while exosomes from *E. coli* Δ*csgBAC* did not [125], suggesting that exosomal transport of bacterial amyloids may induce α-SYN pathology. It would be interesting to identify whether the α-SYN seeds are present already within our HuTu-80 EVs or whether they manifest within the neurons and macrophages. While the reported pathology should be validated in detail, it provides a novel axis of α-SYN aggregation between the amyloidogenic CsgA and enteric neurons and macrophages with EECs acting as intermediaries through EV cargo transfer.

6.1.2.2 Other bacterial metabolites that promote α-SYN aggregation: A. muciniphila secretome and nitric oxide

Other bacterial metabolites and products have been reported to induce cellular dysfunction and α-SYN aggregation in mouse STC-1 EECs. The secretome from *A. muciniphila* cultivated in mucin-free medium triggered inositol triphosphate receptor-mediated Ca^{2+} release from the endosplamic reticulum that, in succession, induced mitochondrial ROS production followed by α-SYN upregulation, phosphorylation at serine 129, and aggregation [89]. Additionally, *A. muciniphila* culture in mucin-free medium induced α-SYN inclusions in CCK+ mouse EECs in mice as assessed by immunofluorescent staining, though the mechanism proposed in the STC-1 model was not validated *in vivo*. The effects described on α-SYN were rapid as they occurred only within 48 hours post-secretome addition. In our study, there was no increase in detergent-soluble α-SYN levels in HuTu-80 exposed to *A. muciniphila* secretome alone or together with CsgA for 48 hours or 10 DIV. Notably, the 10% secretome dose was reduced to 5% for HuTu-80 to minimize cell death, suggesting HuTu-80 are more sensitive or respond differently to *A. muciniphila* conditioned medium than STC-1 cells. It would be interesting to test whether *A.*

muciniphila secretome alters Ca^{2+} buffering [89] in HuTu-80 or in human intestinal organoids to validate the findings in a different EEC model and further understand *A. muciniphila*'s controversial role in promoting or hindering PD progression. Notably, the mucin-free experimental approach resembles an inflamed intestinal state, such as in the case of IBD where mucin production or structure is compromised [364], and secretome from mucin-cultured *A. muciniphila* should be included as a control.

The *Enterobacteriaceae*-derived metabolite nitrate (NO_3^-) is metabolized to nitrite (NO_2^-). A preprint reported that sodium nitrite elicited α-SYN accumulation in STC-1 cells within 24 hours, which was prevented by benserazide, a dopamine synthesis inhibitor [336]. A disrupted cell redox balance causes oxidation of dopamine intermediates that facilitate α-SYN aggregation via post-translational modifications [365, 366]. Reactive nitrogen species are also involved in α-SYN aggregation via tyrosine nitration or methionine oxidation [367, 368]. Sodium nitrite at 50 μM concentration elicited elevated mitochondrial superoxide production and reduced cell viability in STC-1 cells [336]. In the HuTu-80 experimental setup, biofilm-forming *E. coli* together with sodium nitrite did not provoke α-SYN aggregation. Knowing that curli can slightly elevate HuTu-80 mitochondrial superoxide levels, including sodium nitrite exposure may provide sufficient redox stress to initiate α-SYN pathology, though this hypothesis remains to be evaluated.

6.1.3 CsgA-mediated EEC immune response and macrophage activation

6.1.3.1 The immune response of enteroendocrine cells

The downregulation of lysosomal α-SYN levels was accompanied by an elevation in both supernatant and EV α-SYN levels. Notably, the degree of EV α-SYN increase by CsgA-WT (from 1.5 to 2.0 ng/mL) does not explain the increased supernatant α-SYN levels (20 to 38 ng/mL), indicating that most secreted α-SYN is not associated with EVs. A-SYN is both a chemoattractant and an activator of innate and adaptive immunity [13, 64-66] and could reflect a physiological response upon exposure to the bacterial protein. Indeed, the bacterial molecules LPS, Pam3CSK4, and sodium butyrate all induced an upregulation of *SNCA* and α-SYN in STC-1 cells [68], and α-SYN is upregulated following viral or bacterial exposure [13, 64-66]. One mechanism by which α-SYN was trafficked to HuTu-80 EVs for release could be the CsgA-WT-induced upregulation of RAB27A, a protein that promotes vesicle binding to the cell membrane prior their release [329]. Surprisingly, EV number, size, and marker ALIX and FLOT1 levels were unchanged between treatment conditions in both HuTu-80 whole-cel lysates and EV preparations. The exception was CD63, which was significantly upregulated in EV fractions from CsgA-WT-treated HuTu-80. CD63 is a member of the tetraspanin protein family that participates in exosome

formation, cargo sorting, and intensifies immune signal transduction [264, 268]. The tetraspanins CD9 and CD81 were also augmented in the whole-cell proteomics dataset by CsgA-WT, though their levels in HuTu-80 EVs were not measured. Considering IEC-derived exosomes partially modulate immunity via tetraspanins [265], the upregulation of both CD63 and α-SYN in EVs by the amyloidogenic CsgA may present a means of EEC-immune cell communication.

Concomitantly with the upregulation of α-SYN and CD63 in EVs, “antigen presentation” was upregulated in whole-cell lysates of treated HuTu-80. Combined with the known immune-regulatory properties of EECs [149, 154-157] and literature showing CsgA drives inflammatory response in macrophages [126-129], we measured antigen presentation markers and chemokine release in HuTu-80. CsgA-WT promoted an inflammatory HuTu-80 response by inducing HLA-DR surface expression, and IL-8 and MIP-1α chemokine secretion. HLA-DR is an MHC class II antigen presentation molecule that is loaded with cleaved peptides in intracellular antigen presentation compartments prior to surface exposure [369, 370]. Canonical presentation occurs by professional antigen presenting cells (APCs), namely dendritic cells macrophages, and B-cells [371], which expose foreign peptides to initiate T-cell-mediated immune responses. Due to the luminal exposure of IECs, they function as direct sensors of environmental changes (i.e., bacterial infections) and act as non-canonical APCs [372, 373]. Since they lack co-receptor molecules, IECs cannot always elicit T-cell activation [266, 374, 375] and, rather, facilitate professional APC activation to regulate adaptive immunity. The importance of EECs in antigen presentation has not yet been established, though the reported immunoregulatory roles and luminal exposure suggest EECs participate in this pathway. Indeed, concomitant to HLA-DR upregulation, whole-cell proteomics analysis revealed a substantial upregulation of MHC class I molecules (HLA-A, HLA-B, HLA-C, HLA-E, and HLA-H), further implying an EEC immunogenic response to the bacterial amyloid. It should be further evaluated whether CsgA peptides are actively loaded onto antigen presentation molecules on the cell surface by immunopeptidomics. With this experimental approach, the pathogenic presentation of α-SYN peptides [376], is also measurable. In line with antigen presentation marker upregulation, the levels of secreted IL-8, MIP-1α, and α-SYN increased post-CsgA-WT treatment. IL-8 regulates neutrophil, basophil, eosinophil, and T-cell attraction and activation, and is elevated in IBD [377-379]. MIP-1α, also known as CCL3, attracts various immune cell types, and correlates with immune cell infiltration in ulcerative colitis [380, 381]. While these are important chemokines during inflammation, their chronic elevation is associated with inflammatory bowel diseases linked to PD. In summary, HuTu-80 acquire immunoregulatory properties by upregulating chemokine secretion, antigen presentation markers, and extracellular vesicle release upon amyloidogenic CsgA exposure, suggesting they act as immune sensors of the bacterial amyloid.

6.1.3.2 The immune response of macrophages exposed to enteroendocrine cell extracellular vesicles

To evaluate the hypothesis of immunity modulation by EECs treated with CsgA, macrophages were exposed to HuTu-80-derived EVs. Macrophages were chosen due to their involvement in early enteric α-SYN pathology manifestation and T-cell activation [54]. Control EVs (from PBS-treated HuTu-80) promoted macrophage pro-inflammatory (IL-1β, IL-6, TNFα, IL-10, IL-23) and anti-inflammatory (IL-10) cytokine release, as well as chemokine (IL-8, MCP-1) secretion, suggesting a complex immune response to HuTu-80 EVs. Indeed, macrophages can be both activated and suppressed by tumour cell-derived EVs due to their recognition as hostile, while cancer cells suppress immunity to improve their survival [382]. Strikingly, EVs from CsgA-WT-treated HuTu-80 significantly downregulated the pro-inflammatory cytokine levels IL-1β, IL-6, and IL-23. A similar trend was observed with CsgA-R12343, although not significant, suggesting that the amyloidogenic capacity of CsgA is not the primary inducer for the observed effects. IL-1β is a strong pro-inflammatory molecule that activates lymphocytes, facilitates immune cell migration, and induces the expression of other cytokines [383] and is implicated in PD [384]. Similarly, IL-6 is a multifactorial cytokine involved in adaptive immune cell activation and proliferation, and the acute-phase response [49, 385]. Finally, IL-23 promotes Th17 cell expansion which defend against infections but are also involved in auto-immune diseases [386]. As a bacterial amyloid produced by commensal gut microbiota, CsgA can attenuate immune activation under inflammatory conditions as mentioned in the introduction [133-135, 387]. While CsgA, independent of its amyloidogenic capacity, induced diminished inflammatory cytokine release through EEC-derived EVs, the concentration of the released cytokines remained relatively high compared to untreated macrophages.

To further dissect the immune effect of CsgA-associated EVs on macrophages, we designed an experiment where the EVs were removed from the macrophage supernatant and the cells were allowed 48 hours to rest. Notably, macrophages treated with CsgA-associated HuTu-80 EVs sustained IL-1β, IL-6, and IL-10 release even after removal of the EVs suggesting an activated immune state, while macrophages exposed to control EVs displayed significantly reduced cytokine levels. Following a subsequent LPS stimulation, macrophages previously exposed to control HuTu-80 EVs mounted IL-1β, IL-6, TNFα, and IL-10 release, indicating their immune activation capacity to a secondary stimulus. However, the LPS-induced effect on cytokine secretion was abolished on macrophages previously exposed to CsgA-associated HuTu-80 EVs, resembling an immunosuppressed or chronically-activated state. Indeed, chronically-stimulated macrophages exhibit diminished levels of pro-inflammatory cytokines and augmented levels of anti-inflammatory cytokines [78, 388-391]. Combined with the cytokine release measurements at

48 hours, CsgA, irrespective of its amyloid state, acts a persistent inflammatory trigger in macrophages through EEC-associated EVs.

The term of exhausted macrophages has been recently introduced, and these cells differ to tolerized macrophages. While tolerized macrophages show increased bacterial phagocytosis, exhausted macrophages display declined phagocytic capacity [78, 388-390]. Using multiple LPS-hit models, the exhaustion phenotype is accompanied by reduced cytokine release, CD38 marker expression, TRAM(a TLR4 adaptor)-mediated STAT1 pathway activation and declined NF-κB activity, impaired mitochondrial metabolism, and increased ROS levels [78, 81]. Regarding neurodegenerative diseases, exhausted macrophages or their mechanisms have not yet been described. However, ongoing studies have been funded to evaluate overall peripheral immunity exhaustion in PD (Parkinson's Foundation [392], Michael J Fox [393]). An overall chronic activation of the immune system combined with reduced phagocytosis, altered cytokine release and inflammasome activation have been reported in PD [76, 394, 395]. In AD, amyloid pathology and cognitive decline are associated with declined TNFα, IFNg, IL-2, and granzyme B levels in T-cells [75]. Similarly, a 6-month exposure to curli-producing *E. coli* decreased the numbers of dendritic cells, activated T-helper cells and T-cytotoxic cells in the *SOD1*-G93A ALS mouse model [131], indicating that the bacterial amyloid dampens T-cell activation. Importantly, intestinal permeability was unaffected in this model [131], suggesting commensal *E. coli* affects the immune system through intestinal cell signalling. Due to the involvement of persistent immune stimulation and exhaustion as a driver of neurodegenerative diseases, further studies are required to understand the underlying pathological mechanisms. Relevant experiments to evaluate the macrophage phenotype and underlying mechanisms following EEC EV exposure are described in the "Outlook" section. Thus, EECs respond to amyloidogenic CsgA by mounting an immune response characterized by chemokine secretion and HLA-DR surface expression, while EEC-derived EVs promote a sustained macrophage activation state associated with immune exhaustion properties independent of CsgA amyloid status.

6.1.3.3 The mechanistic pathway driving the immune response to CsgA

Another important question raised is how EECs primed their inflammatory response against CsgA. While EECs express functional TLRs [154], HuTu-80 did not express TLR2 by Western blot or proteomics. The proteomics analysis did not detect either TLR1 or TLR9, which also participate in curli-induced macrophage responses [127, 129], implying that other CsgA receptors are involved. Curli bound to fibronectin at the RGD motif facilitated *E. coli* internalization in T24 and HeLa cells [142]. Fibronectin and RGD-binding integrins [396] (beta-1, beta-2, beta-5, and alpha-V) were elevated by CsgA-WT in whole-cell HuTu-80 lysates, suggesting a potential CsgA-

specific uptake and cellular response mechanism. Generally, integrins interact with the actin cytoskeleton [397, 398]. *Staphylococcus aureus* uses fibronectin binding proteins to initiate fibronectin/integrin-mediated actin cytoskeleton reorganization through the FAK-Src pathway leading to its internalization by host cells [399]. Accordingly, actin cytoskeleton was a significantly dysregulated GO term by CsgA-WT and could present a potential internalization pathway. Additionally, fibronectin-integrin signalling activates the NF-κB pathway [400, 401], a fundamental transcription factor guiding immune responses including cytokine expression [402] and implicated in CsgA-evoked immunity [129]. Another mechanism of curli-induced inflammatory responses is through the unfolded protein response (UPR). Chemical inhibition of the UPR sensor IRE1α prevented IL-6 upregulation in the curli-exposed HLA-B27 mouse model of reactive arthritis [403]. Within the cell, curli co-localized with the UPR regulator glucose regulatory protein 78 (GRP78) [403], an upstream IRE1a element initiating the proteostatic response [404]. Both the genetic hit and curli were required to alter GRP78 levels [403]. Accordingly, GRP78 was only slightly elevated by CsgA-WT (log2FC = 0.32) in the whole-cell HuTu-80 proteomics dataset, while curli did not alter GRP78 levels. Thus, CsgA alone is not sufficient to induce a robust proteostatic stress phenotype that would explain the reported immune responses. Overall, fibronectin together with integrins and the downstream NF-κB signalling may be cellular mechanisms driving CsgA uptake and EEC immune responses.

6.1.4 Mitochondrial changes by CsgA in EECs

The proteomics facility analyzed the lysosome-enriched dataset revealed altered mitochondrial pathways. Indeed, lyso-IP protocols are limited by contamination with mitochondrial proteins [315]. Using WB for validation, CsgA-WT significantly decreased the levels of NDUFV1 and COX2 subunits of complexes I and IV, respectively, in HuTu-80 whole-cell lysates, without significantly affecting mitochondrial respiration. Interestingly, the whole-cell proteomics dataset did not reveal changes in mitochondrial complex subunit levels, while the unfiltered lysosomal dataset displayed an upregulation in various complex I and IV subunits. These discrepancies could be caused by an increased lysosome-mitochondrial contact that occurs during mitophagy or an adapted metabolic response [405]. Various mitochondrial-related metabolic pathways appeared as dysregulated GO terms by CsgA-WT, including glycolysis, alanine, aspartate, and glutamate metabolism. Similarly, fatty acid β-oxidation and branched-chain amino acid (leucine, isoleucine, and valine) catabolism were two downregulated metabolic processes reported by transcriptomics analysis of α-SYN-A53T-expressing *C. elegans* fed with curli-producing *E. coli* compared to worms fed with *E. coli CsgA*-KO [123]. While the metabolic processes affected were different to

our study, the combined findings suggest CsgA impacts overall mitochondrial-associated metabolic function. In line with the HuTu-80 seahorse assay, WT *C. elegans* fed with curli producing-*E. coli* did not show changes in mitochondrial respiration. Instead, α-SYN-A53T *C. elegans* showed downregulation of mitochondrial respiration parameters that were further aggravated by curli producing-*E. coli* [123], indicating that curli alone is not sufficient to disrupt mitochondrial oxidative phosphorylation. Thus, the amyloid forms of CsgA impact the levels of mitochondrial subunit levels without impacting mitochondrial respiration, yet EECs may respond to CsgA through metabolic changes.

Other than mitochondrial subunits, SOD1 was decreased by CsgA-WT, but this was not accompanied by increased mitochondrial superoxide levels. Rather, curli were sufficient to induce a significant elevation in superoxide without affecting SOD1 expression. This rise could reflect a physiological response to the bacterial protein, as ROS are part of the host responses to pathogens and are involved in immune signalling [406, 407]. On the other hand, PARK7 was not significantly reduced despite its stark downregulation by CsgA-WT which is possibly explained by the data variability for the curli condition. The absence of an obvious change in mitochondrial area and, particularly, the lack of bacterial amyloid localization in mitochondria suggests CsgA and curli act in an indirect manner. This is contrast to α-SYN that can affect both as monomers or aggregates mitochondrial function by altering complex function and protein import [408-410]. Hence, bacterial amyloids appear to exert their effect on mitochondria in a manner different to human amyloids and/or EECs respond to bacterial amyloids by altering mitochondria-related protein expression.

Mitochondria in EECs are important for proper nutrient sensing and hormone release [192, 195], thus impacting EEC mitochondrial function could lead to gastrointestinal imbalance. Overall, the results of this project show that amyloidogenic CsgA predisposes to mitochondrial impairments by downregulating crucial mitochondrial proteins involved in respiration and ROS balance, that may necessitate a second trigger (i.e., genetics, toxins) to manifest observable mitochondrial dysfunction. Damaged mitochondrial can be a trigger of α-SYN aggregation via oxidation or nitration [367, 368, 411], and affected EECs may miscommunicate signals with neurons that could cause the intestinal symptoms observed in PD patients. Overall, amyloidogenic CsgA negatively impacts mitochondrial protein expression yet alone are not sufficient to perturb mitochondrial function in EECs.

6.1.5 Bacterial amyloids in the human intestine

Gut commensal bacteria are necessary for proper development and maintenance of intestinal homeostasis. Their exposure to host cells promotes immune tolerance at early life stages, and their presence contributes to nutrition and restriction of opportunistic pathogen growth [412, 413]. As in nature, bacteria are present either as planktonic or as a biofilm in the human intestine. The bacterial biofilm can be directly attached to the mucus surface, on mucin aggregates, or food particles in the lumen [139, 414-416]. The density of biofilm increases from proximal to distal gut, hence the colon has the highest biofilm concentration [136]. While the prevalence of biofilms is estimated around 10% in healthy individuals, it increases to 57% in IBS [136]. The non-healthy and invasive growth of biofilms in IBD, IBS, and gut cancers is associated with pathogen expansion, reduced bacterial diversity, impaired barrier function, and immune system activation which contribute to disease progression [136, 137, 417, 418]. Species-wise, adherent-invasive *E. coli* are overrepresented in biofilms of IBS and ulcerative colitis patients compared to healthy individuals [136, 419]. CsgA is produced by multiple members of the *Enterobacteriaceae* family and together with bacterial amyloids from other species (i.e., Pseudomonas aeruginosa, *Enterococcus faecalis*, *Lactobacillus johnsonii*, and *Enterococcus faecium*), their gene expression is enriched in intestinal tissue of PD patients versus non-affected controls [31, 352, 420, 421] further suggesting bacterial amyloids are involved in disease pathogenesis. Particularly, the *Pseudomonas* bacterial amyloid FapC accelerated α-SYN aggregation at high concentration (42 μM) [422]. The persistence of mucus invasive biofilm can contribute to chronic inflammation, direct exposure, and uptake of bacterial amyloids to intestinal cells. An alternative route of bacterial amyloid transfer to host cells has been reported via the carriage of CsgA within bacteria-derived exosomes [125]. Intestinal bacterial amyloid exposure under genetic predisposition (i.e., GBA1 or LRRK2 variants involved in sporadic PD) or infection-associated inflammation may act as body-first PD trigger in EECs. Alternatively, the intestinal inflammation and “leaky gut” often reported in PD individuals [423-426] implies bacterial amyloid exposure can accelerate disease progression in humans, as reported in PD animal models colonized with *E. coli* [121-125]. Despite the increasing relevance of biofilms and the gut-brain axis in PD, biofilm staining in PD tissue material is rare. Investigation of gut tissue biopsies from PD patients at different disease stages and versus non-affected individuals will allow for quantification and tissue localization of biofilm components during disease progression. Development and commercialization of antibodies against the known bacterial amyloids will permit evaluation of protein levels in patient tissue and intestinal cells. Finally, biofilms could be evaluated as a potential biomarker for PD or other gut dysbiosis-related diseases. Overall, the field of biofilm in humans is continuing to evolve and is expanding our knowledge in the importance of bacteria in host health and disease.

6.2 Human intestinal organoids and microfluidics co-culture systems

In vitro models are continuously being developed to improve the complexity and translatability of research findings. Human IPSCs are bankable and can be directed to differentiate towards cell types or tissue-like structures of interest, with the advantage of genetic modifications or personalized sampling. Microfluidics systems combine biology and physics to achieve a structure of interest and cell type or tissue-like separation compatible with high resolution imaging. In this section, the relevance of the models to the scope of the project will be discussed alongside possible ways to improve the model systems for answering relevant biological questions.

The protocol to derive intestinal organoids differentiated from hIPSCs towards the colon fate included CHGA+ EECs [300] and was previously established in the lab. The CHGA+ cells co-expressed 5-HT+ suggesting they are capable of neurotransmitter release and represent enterochromaffin-like cells. Despite the lack of robust α-SYN expression, the current colonic organoid model represents a potential tool for studying epithelial layer-mediated immune responses. However, the low number of EECs accompanied by the goal to establish an EEC-enteric neuron co-culture necessitate an organoid model with readily detectable α-SYN expression. In the mammalian intestine, enterochromaffin cells are more evenly distributed compared to other EECs with a slightly increased abundance in the colon [427, 428]. Furthermore, proteinatlas.org shows increased expression of α-SYN in the colon than in the small intestine, implying that differentiation towards a more proximal part of the gut would not prove beneficial in terms of proper EEC development. Interestingly, a preprint described the expression of α-SYN in CHGA+ cells in hiPSC-derived intestinal organoids [429]. The protocol included certain changes in growth factor timing and types, with the most important being the lack of Wnt signalling activation (CHIR99021) at the first day and the inclusion of the Wnt signalling enhancer R-spondin in the final medium composition [429]. Thus, proper timing and intensity of Wnt signalling may be important from patterning towards intestinal stem cells and downstream EEC development at least in terms of α-SYN expression in hIPSC-derived intestinal organoids. It is not known whether α-SYN expression is altered throughout EEC development, but perhaps a functional synaptic connection with enteric neurons is necessary considering neuronal α-SYN participates in presynaptic vesicle maintenance and release [11, 12] and neuron development [430]. Finally, human primary colonic organoids provide an alternative of mature intestinal tissue where EECs may express α-SYN to study triggers of endogenous seeding, though in this case it would be difficult to acquire and maintain an equal number of biopsies with enteric neurons. Irrespective of the protocol, the proposed approach to study EEC involvement in α-SYN aggregation using intestinal organoids would be to dissociate and seed them in 2D in transwells. This setup allows

for minimizing organoid variability due to their different size and invagination degree and provides access to both apical and luminal side of the cells. As an example, bacterial amyloids are treated on the apical side, and chemokine and α-SYN release are measured in the basal side. Thus, the current colonic organoid model requires further development for studying the effect of bacterial amyloids and EEC involvement in PD.

The field of microfluidics chips in biology has evolved to accommodate the need to separate cell types and media in compartments, to guide specific tissue anatomy, or to include constant medium flow [431]. We wanted to establish a microfluidics cell culture models which permits enteric neuron-EEC separation to study pathology propagation compatible with high resolution microscopy of isolated neuronal projections. Human iPSC-derived peripheral neuron precursors were generated and characterized prior to their seeding in microfluidics. The protocol employed here [301] produced vagal neural crest-like cells which were not expressing *SOX10*. Since *SOX10* is a crucial developmental transcription factor regulating the early stages of neural crest survival and identity as well as enteric neuron gene expression (i.e., *PHOX2B* and *EDNRB*) [432], this restricts the usability of the protocol for enteric neuron differentiation. While iPSC-derived enteric neuron protocols have been published [433-435], their batch-to-batch reproducibility and neuronal representation were limited and, thus, were not further established for use in microfluidics systems in the scope and timeline of this project. The neural crest-like cells were seeded on one channel and were allowed to grow neuronal projections towards the unseeded channel by a combination of mechanical (increased media volume and pressure in the seeded channel) and chemical (doubled BDNF and GDNF concentration in the unseeded channel) manipulations. By adding HuTu-80 EECs in the second side channel and allowing the cells to grow, we observed certain SYP1+/TUJ1+ projections reached the HuTu-80 cells. Notably, HuTu-80 were also labelled by TUJ1, suggesting the neuron-like identity of EECs. Thus far, *TUBB3* (the gene of TUJ1) expression has only been described in colon EECs (proteinatlas.org). The current microfluidics model requires further neuron/EEC characterization by evaluating synaptic connection between the two cell types. This could be achieved by potassium chloride-evoked calcium signal measurements and electrophysiological recordings from one channel to the other (EECs to neurons and vice versa) using commercial microfluidics chips with electrodes placed at the bottom of the three channels. In the described setup, EECs were seeded without enterocytes, hence there was no tight barrier formation. Thus, bacterial amyloid treatment to HuTu-80 must be performed outside the microfluidics followed by cell seeding in the chip to study EEC-derived neuron perturbations. The use and pathological relevance of the established microfluidics system is focused on EEC-to-enteric neuron pathology propagation and characterization. Indeed, EVs from CsgA-WT-treated HuTu-80 induced modest α-SYN seeding activity, yet the pathology and

associated neuronal perturbations require further evaluation. While the model requires further development, the incorporation of macrophages in the neuron compartment or Caco-2 cells in HuTu-80 channel, would enable cellular crosstalk and simultaneous study of the immune response and epithelial barrier integrity in CsgA-exposed cultures. Relevant and feasible experiments to investigate bacterial amyloid-induced EEC-neuronal dysfunction are described in the “Outlook” section.

6.3 Limitations of the study

HuTu-80 was selected as the enteroendocrine cell model, since it produced higher levels of α-SYN compared to the other human EEC lines tested (HT-29, and Colo-320DM). Despite the published differentiations protocols to enrich for EECs in human iPSC-derived intestinal organoid models [320, 321], the aim of the study was to dissect EEC-specific mechanisms upon CsgA exposure that are related to PD. Indeed, HuTu-80 is an easily expandable and screenable cell line model permitting the mechanistic dissection of intracellular processes and intercellular communication pathways, which we used to identify bacterial amyloid lysosomal trafficking and EV-mediated immune signalling. Indeed, a major finding of our study was the identification of CsgA-mediated immune exhaustion through EEC EVs. These results obtained from HuTu-80 are novel, yet they are derived from a cancer cell line which impacts the macrophage immune responses and overall weakens the translatability of our findings. Additionally, tissue complexity is absent removing the effect of other intestinal cell types or a microbiota community (and the associated biofilm) on EECs and immune cells which are relevant for the human intestine. Therefore, we decided to establish human stem cell-derived models (macrophages, peripheral neurons, intestinal organoids) that would be necessary to strengthen the impact of our study. While these models require further development prior to mechanistic validation, hIPSC or primary intestinal organoids present a more physiological system to investigate the translational relevance of the HuTu-80 results to human individuals. Overall, HuTu-80 permitted the discovery of molecular processes, while complex co-culture and organoid models are needed to validate these pathways for understanding and treating intestinal PD pathogenesis.

6.4 Conclusion

The aim of the study was to evaluate how CsgA or curli mechanistically affect EECs to predispose to PD. CsgA-WT and curli, being non-host proteins, were trafficked to the EEC lysosomes for degradation. The aggregate-prone form of CsgA induced proteome changes, implying that the bacterial amyloid function of the protein is primarily responsible for the EEC responses, yet CsgA-WT alone did not suffice to induce robust EEC dysfunction (mitochondrial respiration, autophagy, proteasome activity). Rather than inducing α-SYN aggregation in EECs, CsgA-WT altered α-SYN trafficking from lysosomes towards extracellular release into the medium and within EVs. The secretion of α-SYN was accompanied by elevated HLA-DR surface expression and IL-8 and MIP-1α release, suggesting that EECs recognize CsgA as an inflammatory trigger. EVs from HuTu-80 treated with CsgA-WT or CsgA-R12343 carried the bacterial amyloid and had increased α-SYN and CD63 levels. These EVs promoted sustained inflammatory cytokine release and absence of a subsequent response to LPS in treated macrophages, suggestive of an exhausted-like population. The induced immune response in macrophages was largely independent of the amyloidogenic capacity of CsgA, but CsgA-WT is expected to be a stronger inducer due to EEC chemokine secretion. Interestingly, CsgA-associated EVs from EECs promote modest α-SYN seeding capacity in peripheral neurons and macrophages, suggesting EECs may promote α-SYN pathology in tissue-resident cells upon exposure to bacterial amyloids. Conclusively, we identified EECs as upstream sensors of CsgA that respond by altering their α-SYN intracellular trafficking to elicit EV-mediated sustained immune response of macrophages associated with exhaustion. This novel CsgA-EEC-immune axis could promote dysregulation of host intestinal homeostasis accompanied by altered microbiota composition to predispose to early stages of PD. A graphical model of CsgA's mechanism of action in HuTu-80 EECs is provided (**Figure 26**).

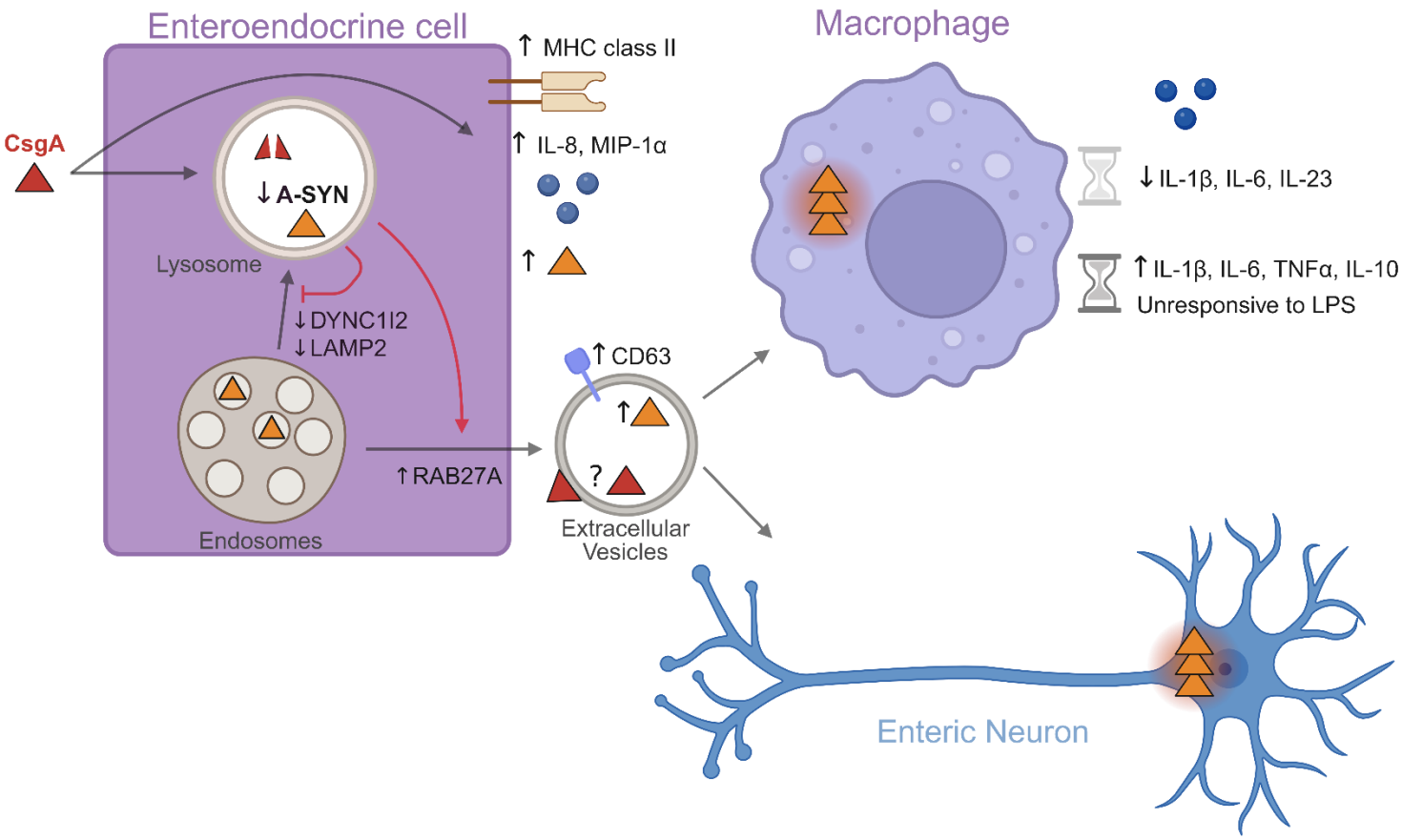


Figure 26. Graphical summary of the proposed CsgA-induced trafficking response in enteroendocrine cells and extracellular vesicle-mediated regulation of macrophages and neurons. The bacterial amyloid CsgA is uptaken and targeted to the lysosomes of EECs for degradation. Within the cell, CsgA provokes downregulation of lysosome trafficking proteins LAMP2 and DYNC1I2 and upregulation of extracellular vesicle release protein RAB27A. This is accompanied by reduced lysosomal α-SYN and increased supernatant and extracellular vesicle α-SYN levels. EECs respond to CsgA as an inflammatory trigger by surface exposure of the MHC class II molecule HLA-DR, IL-8 and MIP1-α chemokine release. Extracellular vesicles from CsgA-treated enteroendocrine cells carry CsgA (the "?" refers to the unknown localization of CsgA in the EVs) and show elevated CD63 levels, promote sustained macrophage inflammatory cytokine release and suppress the macrophage response to LPS, irrespective of CsgA's amyloidogenic properties. CsgA-WT-associated extracellular vesicles increase α-SYN seeding capacity in recipient macrophages and neurons.

7. Outlook

In this study, we discovered that CsgA-WT impacted the levels of intracellular trafficking and immune components in EECs, though a thorough functional understanding requires further validation. This section will focus on the most relevant experiments to investigate the mechanistic EEC response to bacterial amyloids, the role of EEC EVs, the exhausted macrophage phenotype, and to validate the findings in more physiological intestinal models. The optimization of the hIPSC-derived intestinal organoid cultures to detect α-SYN expression in EECs and the quality control experiments in microfluidics EEC-neuron co-cultures have already been described in the respective “Discussion” section.

The uptake mechanism of CsgA remains to be determined and its identification will help understand the participating downstream mechanisms involved. CsgA-WT and curli were localized to the lysosomes for degradation in HuTu-80 EECs and, accordingly, there was lack of co-localization of the bacterial amyloid with early endosomes labelled with RAB5A-GFP 48 hours post-treatment. However, at this time point of treatment, the majority of CsgA and curli are expected to have been uptaken. It would be interesting to study the early uptake of Alexa-594-labeled CsgA/curli uptake by live-cell imaging to identify the mechanism of internalization. Particularly, fibronectin and RGD integrins were upregulated in whole-cell proteomics dataset of cells treated for 48 hours with CsgA-WT. This implies the possible involvement of these components in the binding and endocytosis of CsgA [142] by EECs. Using RGD peptides that bind and block integrin-mediated internalization, we can evaluate whether fibronectin/integrins are involved in fluorescently labelled CsgA uptake in EECs. Interestingly, fibronectin/integrins are upstream activators of NF-κB [401] which is involved in CsgA-induced immunity [129]. Nuclear translocation of NF-κB (i.e., by immunostaining against a p65 antibody) as an activation readout can be used following CsgA treatment. Subsequently, IKKβ or IKKα inhibitors may discern whether the canonical or non-canonical pathway of NF-κB is activated. Overall, understanding the CsgA uptake mechanism and downstream pathways will provide a means of blocking CsgA internalization and insight into the EEC immune response, both of which potentially leading to targetable pathways to hinder PD pathology or ease gastrointestinal symptoms.

Secondly, EECs responded to CsgA by modifying intracellular trafficking pathways to facilitate intercellular communication through EVs. Elucidating the sorting mechanism and the EV protein cargo and function will help identify the mechanism of CsgA-mediated immune exhaustion. Despite RAB27A upregulation by CsgA-WT, there was no change in the number of secreted EVs, suggesting it is the EV cargo (CD63, α-SYN) that is altered by CsgA-WT. CsgA-WT did not alter

ESCRT-dependent protein levels (i.e., ALIX, TSG101, VPS22, VPS36 etc) and SMPD3 (involved in the ceramide-dependent exosomal pathway [436]) was not detected in the proteomics. Instead, ESCRT-independent sorting components (CD9, CD63, and CD81) were upregulated implying a potential cargo selection mechanism which should be validated by genetic silencing, and could represent a novel bacterial amyloid-induced EEC pathway driving immune regulation. It would also be interesting to assess CsgA localization in the EVs (lumen or membrane) to gain an initial understanding on how CsgA is sorted to EVs, and this could be achieved with the help of CsgA-WT-594 and imaging flow cytometry. Altogether, the sorting mechanisms of CsgA and associated cellular signals will aid the understanding of how EECs may impact intestinal homeostasis in response to bacterial amyloids.

In the same direction, CsgA-associated EVs induced immune exhaustion-like properties in macrophages and it is fundamental to comprehend the phenotype and molecular pathways driving this response. The response kinetics can be deduced by performing live-cell imaging of macrophages treated with fluorescently labelled (DiI or DiO [437]) EVs. How fast are EVs uptaken by macrophages and how long is the fluorescent signal visible in macrophages? Do EVs from CsgA-treated HuTu-80 persist in macrophages longer than EVs from PBS-treated HuTu-80? Is CsgA detectable in macrophage lysates? Considering the novelty and significance of our obtained results regarding bacterial amyloids as immunity deregulators in intestinal PD pathology, EEC-derived EV and macrophage proteomics analysis should be employed. Particularly, exhausted macrophages display an M2-like phenotype, reduced bacterial phagocytosis, decreased antigen presentation, and CD38 upregulation [78, 81], all of which could be initially evaluated through the proteomics analysis prior to validation. These proteomics experiments will be fundamental to understanding the EV signals and macrophage molecular pathways responsible for the observed phenotypes paving the way towards therapeutics.

Finally, the intestinal organoid and the developed EEC-peripheral neuron microfluidics model require further development, but they provide a physiologically relevant environment to validate the effects of bacterial amyloids on tissue-resident cells mediated by EECs. Relevant to the project, labelled CsgA-WT-594 retro-grade propagation can be investigated by live-cell imaging in microfluidics devices to assess whether bacterial amyloids can be transmitted from EECs to neurons where they may cross-seed with α-SYN. Particularly, EV release could be inhibited with GW4869 to assess whether CsgA-WT transport is involved in bacterial amyloid transfer. Due to the identification of modest α-SYN seeding capacity in peripheral neuron/macrophage co-cultures, neurons in microfluidics could be stained with total α-SYN and pS129-α-SYN to evaluate whether detectable α-SYN pathology via EV transfer occurs. Formation of detergent-insoluble α-

SYN can be verified by treating the samples with proteinase K. While these experiments focus on α-SYN pathology, neuronal electrophysiology can be measured to identify potential links between bacterial amyloids and gastrointestinal motility dysfunctions in PD patients. Lastly, intestinal organoids co-cultured with immune cells (i.e., macrophages) provide a final complex tissue-like system to validate the discovered pathways of EEC-mediated immune exhaustion. Human iPSC-derived microfluidics co-culture and intestinal organoid models are useful for understanding bacterial amyloid-mediated PD pathogenesis with translation relevance and could be an integral part of a drug discovery pipeline for disease therapeutics.

8. References

1. Su, D., Cui, Y., He, C., Yin, P., Bai, R., Zhu, J., Lam, J. S. T., Zhang, J., Yan, R., Zheng, X., Wu, J., Zhao, D., Wang, A., Zhou, M. & Feng, T. (2025) Projections for prevalence of Parkinson's disease and its driving factors in 195 countries and territories to 2050: modelling study of Global Burden of Disease Study 2021, *Bmj.* **388**, e080952.
2. Dorsey, E. R. & Bloem, B. R. (2024) Parkinson's Disease Is Predominantly an Environmental Disease, *J Parkinsons Dis.* **14**, 451–465.
3. Kline, E. M., Houser, M. C., Herrick, M. K., Seibler, P., Klein, C., West, A. & Tansey, M. G. (2021) Genetic and Environmental Factors in Parkinson's Disease Converge on Immune Function and Inflammation, *Mov Disord.* **36**, 25–36.
4. Nalls, M. A., Blauwendraat, C., Vallerga, C. L., Heilbron, K., Bandres-Ciga, S., Chang, D., Tan, M., Kia, D. A., Noyce, A. J., Xue, A., Bras, J., Young, E., von Coelln, R., Simón-Sánchez, J., Schulte, C., Sharma, M., Krohn, L., Pihlstrøm, L., Siitonen, A., Iwaki, H., Leonard, H., Faghri, F., Gibbs, J. R., Hernandez, D. G., Scholz, S. W., Botia, J. A., Martinez, M., Corvol, J. C., Lesage, S., Jankovic, J., Shulman, L. M., Sutherland, M., Tienari, P., Majamaa, K., Toft, M., Andreassen, O. A., Bangale, T., Brice, A., Yang, J., Gan-Or, Z., Gasser, T., Heutink, P., Shulman, J. M., Wood, N. W., Hinds, D. A., Hardy, J. A., Morris, H. R., Gratten, J., Visscher, P. M., Graham, R. R. & Singleton, A. B. (2019) Identification of novel risk loci, causal insights, and heritable risk for Parkinson's disease: a meta-analysis of genome-wide association studies, *Lancet Neurol.* **18**, 1091–1102.
5. Tran, J., Anastacio, H. & Bardy, C. (2020) Genetic predispositions of Parkinson's disease revealed in patient-derived brain cells, *NPJ Parkinsons Dis.* **6**, 8.
6. Spillantini, M. G., Schmidt, M. L., Lee, V. M., Trojanowski, J. Q., Jakes, R. & Goedert, M. (1997) Alpha-synuclein in Lewy bodies, *Nature.* **388**, 839–40.
7. George, J. M. (2002) The synucleins, *Genome Biol.* **3**, Reviews3002.
8. Burré, J., Vivona, S., Diao, J., Sharma, M., Brunger, A. T. & Südhof, T. C. (2013) Properties of native brain α-synuclein, *Nature.* **498**, E4–6; discussion E6–7.
9. Ferreon, A. C., Gambin, Y., Lemke, E. A. & Deniz, A. A. (2009) Interplay of alpha-synuclein binding and conformational switching probed by single-molecule fluorescence, *Proc Natl Acad Sci U S A.* **106**, 5645–50.
10. Sharma, M. & Burré, J. (2023) α-Synuclein in synaptic function and dysfunction, *Trends Neurosci.* **46**, 153–166.
11. Burré, J., Sharma, M., Tsetsenis, T., Buchman, V., Etherton, M. R. & Südhof, T. C. (2010) Alpha-synuclein promotes SNARE-complex assembly in vivo and in vitro, *Science.* **329**, 1663–7.
12. Wang, L., Das, U., Scott, D. A., Tang, Y., McLean, P. J. & Roy, S. (2014) α-synuclein multimers cluster synaptic vesicles and attenuate recycling, *Curr Biol.* **24**, 2319–26.
13. Alam, M. M., Yang, D., Li, X. Q., Liu, J., Back, T. C., Trivett, A., Karim, B., Barbut, D., Zasloff, M. & Oppenheim, J. J. (2022) Alpha synuclein, the culprit in Parkinson disease, is required for normal immune function, *Cell Rep.* **38**, 110090.
14. Uversky, V. N. (2007) Neuropathology, biochemistry, and biophysics of alpha-synuclein aggregation, *J Neurochem.* **103**, 17–37.
15. Kim, W. S., Kågedal, K. & Halliday, G. M. (2014) Alpha-synuclein biology in Lewy body diseases, *Alzheimers Res Ther.* **6**, 73.
16. Lim, S., Chun, Y., Lee, J. S. & Lee, S. J. (2016) Neuroinflammation in Synucleinopathies, *Brain Pathol.* **26**, 404–9.
17. Yasuda, T., Nakata, Y. & Mochizuki, H. (2013) α-Synuclein and neuronal cell death, *Mol Neurobiol.* **47**, 466–83.
18. Kyle, R. A. (2001) Amyloidosis: a convoluted story, *Br J Haematol.* **114**, 529–38.
19. Wolfe, K. J. & Cyr, D. M. (2011) Amyloid in neurodegenerative diseases: friend or foe?, *Semin Cell Dev Biol.* **22**, 476–81.

20. Wakabayashi, K., Takahashi, H., Takeda, S., Ohama, E. & Ikuta, F. (1988) Parkinson's disease: the presence of Lewy bodies in Auerbach's and Meissner's plexuses, *Acta Neuropathol.* **76**, 217–221.
21. Wakabayashi, K., Takahashi, H., Takeda, S., Ohama, E. & Ikuta, F. (1989) Lewy bodies in the enteric nervous system in Parkinson's disease, *Arch Histol Cytol.* **52 Suppl**, 191–4.
22. Hayes, M. T. (2019) Parkinson's Disease and Parkinsonism, *Am J Med.* **132**, 802–807.
23. Leite Silva, A. B. R., Gonçalves de Oliveira, R. W., Diógenes, G. P., de Castro Aguiar, M. F., Sallem, C. C., Lima, M. P. P., de Albuquerque Filho, L. B., Peixoto de Medeiros, S. D., Penido de Mendonça, L. L., de Santiago Filho, P. C., Nones, D. P., da Silva Cardoso, P. M. M., Ribas, M. Z., Galvão, S. L., Gomes, G. F., Bezerra de Menezes, A. R., Dos Santos, N. L., Mororó, V. M., Duarte, F. S. & Dos Santos, J. C. C. (2023) Premotor, nonmotor and motor symptoms of Parkinson's Disease: A new clinical state of the art, *Ageing Res Rev.* **84**, 101834.
24. Savica, R., Carlin, J. M., Grossardt, B. R., Bower, J. H., Ahlskog, J. E., Maraganore, D. M., Bharucha, A. E. & Rocca, W. A. (2009) Medical records documentation of constipation preceding Parkinson disease: A case-control study, *Neurology.* **73**, 1752–8.
25. Horsager, J. & Borghammer, P. (2024) Brain-first vs. body-first Parkinson's disease: An update on recent evidence, *Parkinsonism Relat Disord.* **122**, 106101.
26. Giachino, C. T., C., Caniglia, S., Serapide, M. F., L'Episcopo, F. L., Giuliano, C., Mearelli, M., Jakobi, M., Schneiderhan-Marra, N., Deleidi, M. & Marchetti, B. (2022) LRRK2-G2019S Synergizes with Ageing and Low-Grade Inflammation to Promote Gut and Peripheral Immune Cell Activation that Precede Nigrostriatal Degeneration in *BioRxiV*
27. Pei, J., Oliveira, N. L., Recinto, S. J., Kazanova, A., Queiroz-Junior, C. M., Li, Z., Couto, K., Westfall, S., Fahmy, A. M., Tiefensee-Ribeiro, C., King, I. L., Milnerwood, A. J., Desjardins, M., Thanabalasuriar, A., Stratton, J. A. & Gruenheid, S. (2025) Lrrk2 G2019S mutation incites increased cell-intrinsic neutrophil effector functions and intestinal inflammation in a model of infectious colitis, *NPJ Parkinsons Dis.* **11**, 267.
28. Welsh, J. A., Goberdhan, D. C. I., O'Driscoll, L., Buzas, E. I., Blenkiron, C., Bussolati, B., Cai, H., Di Vizio, D., Driedonks, T. A. P., Erdbrügger, U., Falcon-Perez, J. M., Fu, Q. L., Hill, A. F., Lenassi, M., Lim, S. K., Mahoney, M. G., Mohanty, S., Möller, A., Nieuwland, R., Ochiya, T., Sahoo, S., Torrecilhas, A. C., Zheng, L., Zijlstra, A., Abuelreich, S., Bagabas, R., Bergese, P., Bridges, E. M., Brucale, M., Burger, D., Carney, R. P., Cocucci, E., Crescitelli, R., Hanser, E., Harris, A. L., Haughey, N. J., Hendrix, A., Ivanov, A. R., Jovanovic-Talisman, T., Kruh-Garcia, N. A., Ku'ulei-Lyn Faustino, V., Kyburz, D., Lässer, C., Lennon, K. M., Lötvall, J., Maddox, A. L., Martens-Uzunova, E. S., Mizenko, R. R., Newman, L. A., Ridolfi, A., Rohde, E., Rojalin, T., Rowland, A., Saftics, A., Sandau, U. S., Saugstad, J. A., Shekari, F., Swift, S., Ter-Ovanesyan, D., Tosar, J. P., Useckaite, Z., Valle, F., Varga, Z., van der Pol, E., van Herwijnen, M. J. C., Wauben, M. H. M., Wehman, A. M., Williams, S., Zendrini, A., Zimmerman, A. J., Théry, C. & Witwer, K. W. (2024) Minimal information for studies of extracellular vesicles (MISEV2023): From basic to advanced approaches, *J Extracell Vesicles.* **13**, e12404.
29. McGee, D. J., Lu, X. H. & Disbrow, E. A. (2018) Stomaching the Possibility of a Pathogenic Role for Helicobacter pylori in Parkinson's Disease, *J Parkinsons Dis.* **8**, 367–374.
30. Meng, L., Shen, L. & Ji, H. F. (2019) Impact of infection on risk of Parkinson's disease: a quantitative assessment of case-control and cohort studies, *J Neurovirol.* **25**, 221–228.
31. Wallen, Z. D., Demirkan, A., Twa, G., Cohen, G., Dean, M. N., Standaert, D. G., Sampson, T. R. & Payami, H. (2022) Metagenomics of Parkinson's disease implicates the gut microbiome in multiple disease mechanisms, *Nat Commun.* **13**, 6958.
32. Bonaz, B. (2025) Enteric neuropathy and the vagus nerve: Therapeutic implications, *Neurogastroenterol Motil.* **37**, e14842.
33. Ayers, J. I., Riffe, C. J., Sorrentino, Z. A., Diamond, J., Fagerli, E., Brooks, M., Galaleldeen, A., Hart, P. J. & Giasson, B. I. (2018) Localized Induction of Wild-Type and Mutant Alpha-Synuclein Aggregation Reveals Propagation along Neuroanatomical Tracts, *J Virol.* **92**.

34. Ferreira, N., Gonçalves, N. P., Jan, A., Jensen, N. M., van der Laan, A., Mohseni, S., Vægter, C. B. & Jensen, P. H. (2021) Trans-synaptic spreading of alpha-synuclein pathology through sensory afferents leads to sensory nerve degeneration and neuropathic pain, *Acta Neuropathol Commun.* **9**, 31.
35. Kim, S., Kwon, S. H., Kam, T. I., Panicker, N., Karuppagounder, S. S., Lee, S., Lee, J. H., Kim, W. R., Kook, M., Foss, C. A., Shen, C., Lee, H., Kulkarni, S., Pasricha, P. J., Lee, G., Pomper, M. G., Dawson, V. L., Dawson, T. M. & Ko, H. S. (2019) Transneuronal Propagation of Pathologic α-Synuclein from the Gut to the Brain Models Parkinson's Disease, *Neuron.* **103**, 627–641.e7.
36. Svensson, E., Horváth-Puhó, E., Thomsen, R. W., Djurhuus, J. C., Pedersen, L., Borghammer, P. & Sørensen, H. T. (2015) Vagotomy and subsequent risk of Parkinson's disease, *Ann Neurol.* **78**, 522–9.
37. Braak, H., Del Tredici, K., Rüb, U., de Vos, R. A., Jansen Steur, E. N. & Braak, E. (2003) Staging of brain pathology related to sporadic Parkinson's disease, *Neurobiol Aging.* **24**, 197–211.
38. Calabrese, V., Santoro, A., Monti, D., Crupi, R., Di Paola, R., Latteri, S., Cuzzocrea, S., Zappia, M., Giordano, J., Calabrese, E. J. & Franceschi, C. (2018) Aging and Parkinson's Disease: Inflammaging, neuroinflammation and biological remodeling as key factors in pathogenesis, *Free Radic Biol Med.* **115**, 80–91.
39. Brochard, V., Combadière, B., Prigent, A., Laouar, Y., Perrin, A., Beray-Berthat, V., Bonduelle, O., Alvarez-Fischer, D., Callebert, J., Launay, J. M., Duyckaerts, C., Flavell, R. A., Hirsch, E. C. & Hunot, S. (2009) Infiltration of CD4+ lymphocytes into the brain contributes to neurodegeneration in a mouse model of Parkinson disease, *J Clin Invest.* **119**, 182–92.
40. McGeer, P. L., Itagaki, S., Boyes, B. E. & McGeer, E. G. (1988) Reactive microglia are positive for HLA-DR in the substantia nigra of Parkinson's and Alzheimer's disease brains, *Neurology.* **38**, 1285–91.
41. Tansey, M. G., Wallings, R. L., Houser, M. C., Herrick, M. K., Keating, C. E. & Joers, V. (2022) Inflammation and immune dysfunction in Parkinson disease, *Nat Rev Immunol.* **22**, 657–673.
42. Gao, H. M., Kotzbauer, P. T., Uryu, K., Leight, S., Trojanowski, J. Q. & Lee, V. M. (2008) Neuroinflammation and oxidation/nitration of alpha-synuclein linked to dopaminergic neurodegeneration, *J Neurosci.* **28**, 7687–98.
43. Tansey, M. G. & Goldberg, M. S. (2010) Neuroinflammation in Parkinson's disease: its role in neuronal death and implications for therapeutic intervention, *Neurobiol Dis.* **37**, 510–8.
44. Liddelow, S. A., Guttenplan, K. A., Clarke, L. E., Bennett, F. C., Bohlen, C. J., Schirmer, L., Bennett, M. L., Münch, A. E., Chung, W. S., Peterson, T. C., Wilton, D. K., Frouin, A., Napier, B. A., Panicker, N., Kumar, M., Buckwalter, M. S., Rowitch, D. H., Dawson, V. L., Dawson, T. M., Stevens, B. & Barres, B. A. (2017) Neurotoxic reactive astrocytes are induced by activated microglia, *Nature.* **541**, 481–487.
45. Chou, T. W., Chang, N. P., Krishnagiri, M., Patel, A. P., Lindman, M., Angel, J. P., Kung, P. L., Atkins, C. & Daniels, B. P. (2021) Fibrillar α-synuclein induces neurotoxic astrocyte activation via RIP kinase signaling and NF-κB, *Cell Death Dis.* **12**, 756.
46. Eo, H., Kim, S., Jung, U. J. & Kim, S. R. (2024) Alpha-Synuclein and Microglia in Parkinson's Disease: From Pathogenesis to Therapeutic Prospects, *J Clin Med.* **13**.
47. Scheiblich, H., Bousset, L., Schwartz, S., Griep, A., Latz, E., Melki, R. & Heneka, M. T. (2021) Microglial NLRP3 Inflammasome Activation upon TLR2 and TLR5 Ligation by Distinct α-Synuclein Assemblies, *J Immunol.* **207**, 2143–2154.
48. Forloni, G. (2023) Alpha Synuclein: Neurodegeneration and Inflammation, *Int J Mol Sci.* **24**.
49. Brodacki, B., Staszewski, J., Toczyłowska, B., Kozłowska, E., Drela, N., Chalimoniuk, M. & Stepien, A. (2008) Serum interleukin (IL-2, IL-10, IL-6, IL-4), TNFalpha, and INFgamma concentrations are elevated in patients with atypical and idiopathic parkinsonism, *Neurosci Lett.* **441**, 158–62.
50. Bayati, A., Ayoubi, R., Aguila, A., Zorca, C. E., Deyab, G., Han, C., Recinto, S. J., Nguyen-Renou, E., Rocha, C., Maussion, G., Luo, W., Shlaifer, I., Banks, E., McDowell, I., Del Cid Pellitero, E., Ding, X. E., Sharif, B., Séguéla, P., Yaqubi, M., Chen, C. X., You, Z., Abdian, N., McBride, H. M., Fon, E. A., Stratton, J. A., Durcan, T. M., Nahirney, P. C. & McPherson, P. S. (2024) Modeling Parkinson's disease pathology in human dopaminergic neurons by sequential exposure to α-synuclein fibrils and proinflammatory cytokines, *Nat Neurosci.* **27**, 2401–2416.

51. Campagnolo, M., Weis, L., Sandre, M., Tushevski, A., Russo, F. P., Savarino, E., Carecchio, M., Stocco, E., Macchi, V., De Caro, R., Parchi, P., Bubacco, L., Porzionato, A., Antonini, A. & Emmi, A. (2024) Immune landscape of the enteric nervous system differentiates Parkinson's disease patients from controls: The PADUA-CESNE cohort, *Neurobiol Dis.* **200**, 106609.
52. Garretti, F., Monahan, C., Sloan, N., Bergen, J., Shahriar, S., Kim, S. W., Sette, A., Cutforth, T., Kanter, E., Agalliu, D. & Sulzer, D. (2023) Interaction of an α-synuclein epitope with HLA-DRB1(∗)15:01 triggers enteric features in mice reminiscent of prodromal Parkinson's disease, *Neuron.* **111**, 3397–3413.e5.
53. White, Z., Cabrera, I., Mei, L., Clevenger, M., Ochoa-Raya, A., Kapustka, I., Dominguez, J. R., Zhou, J., Koster, K. P., Anwar, S., Wang, Q., Ng, C., Sagoshi, S., Matsuo, T., Jayawardena, D., Kim, S. H., Kageyama, T., Mitchell, B. J., Rivera, D., Dudeja, P. K., Lutz, S. E., Kim, K. W., Yoshii, A., Chevrier, N., Inoue, M. & Sano, T. (2025) Gut inflammation promotes microbiota-specific CD4 T cell-mediated neuroinflammation, *Nature.* **643**, 509–518.
54. De Schepper, S., Konstantellos, V., Conway, J. A., Sokolova, D., Zaccagnini, L., Cowley, M. V., Sierksma, A., Yudina, M., Edmonds, M., Gavriouchkina, D., Geary, B., Wallis, A., Celikag, M., Baykam, Z., Vara-Pérez, M., Crowley, G., Hager, F. T., Bijnen, M., Posner, D., Luk, K., Cerovic, V., Clatworthy, M., Videlock, E. J., Jaunmuktane, Z., Movahedi, K., Greter, M., Chain, B., Alessi, D. R., Hong, S. & Bartels, T. (2026) Intestinal macrophages modulate synucleinopathy along the gut-brain axis, *Nature*.
55. Zhang, X., Svn, Z., Liv, M., Yang, Y., Zeng, R., Huang, Q. & Sun, Q. (2021) Association Between Irritable Bowel Syndrome and Risk of Parkinson's Disease: A Systematic Review and Meta-Analysis, *Front Neurol.* **12**, 720958.
56. Zhu, Y., Yuan, M., Liu, Y., Yang, F., Chen, W. Z., Xu, Z. Z., Xiang, Z. B. & Xu, R. S. (2022) Association between inflammatory bowel diseases and Parkinson's disease: systematic review and meta-analysis, *Neural Regen Res.* **17**, 344–353.
57. Azeredo da Silveira, S., Schneider, B. L., Cifuentes-Diaz, C., Sage, D., Abbas-Terki, T., Iwatsubo, T., Unser, M. & Aebischer, P. (2009) Phosphorylation does not prompt, nor prevent, the formation of alpha-synuclein toxic species in a rat model of Parkinson's disease, *Hum Mol Genet.* **18**, 872–87.
58. Ghanem, S. S., Majbour, N. K., Vaikath, N. N., Ardah, M. T., Erskine, D., Jensen, N. M., Fayyad, M., Sudhakaran, I. P., Vasili, E., Melachroinou, K., Abdi, I. Y., Poggiolini, I., Santos, P., Dorn, A., Carloni, P., Vekrellis, K., Attems, J., McKeith, I., Outeiro, T. F., Jensen, P. H. & El-Agnaf, O. M. A. (2022) α-Synuclein phosphorylation at serine 129 occurs after initial protein deposition and inhibits seeded fibril formation and toxicity, *Proc Natl Acad Sci U S A.* **119**, e2109617119.
59. Karampetsou, M., Ardah, M. T., Semitekolou, M., Polissidis, A., Samiotaki, M., Kalomoiri, M., Majbour, N., Xanthou, G., El-Agnaf, O. M. A. & Vekrellis, K. (2017) Phosphorylated exogenous alpha-synuclein fibrils exacerbate pathology and induce neuronal dysfunction in mice, *Sci Rep.* **7**, 16533.
60. Smith, W. W., Margolis, R. L., Li, X., Troncoso, J. C., Lee, M. K., Dawson, V. L., Dawson, T. M., Iwatsubo, T. & Ross, C. A. (2005) Alpha-synuclein phosphorylation enhances eosinophilic cytoplasmic inclusion formation in SH-SY5Y cells, *J Neurosci.* **25**, 5544–52.
61. Tenreiro, S., Reimão-Pinto, M. M., Antas, P., Rino, J., Wawrzycka, D., Macedo, D., Rosado-Ramos, R., Amen, T., Waiss, M., Magalhães, F., Gomes, A., Santos, C. N., Kaganovich, D. & Outeiro, T. F. (2014) Phosphorylation modulates clearance of alpha-synuclein inclusions in a yeast model of Parkinson's disease, *PLoS Genet.* **10**, e1004302.
62. Espinosa-Oliva, A. M., Ruiz, R., Soto, M. S., Boza-Serrano, A., Rodriguez-Perez, A. I., Roca-Ceballos, M. A., García-Revilla, J., Santiago, M., Serres, S., Economopoulus, V., Carvajal, A. E., Vázquez-Carretero, M. D., García-Miranda, P., Klementieva, O., Oliva-Martín, M. J., Deierborg, T., Rivas, E., Sibson, N. R., Labandeira-García, J. L., Machado, A., Peral, M. J., Herrera, A. J., Venero, J. L. & de Pablos, R. M. (2024) Inflammatory bowel disease induces pathological α-synuclein aggregation in the human gut and brain, *Neuropathol Appl Neurobiol.* **50**, e12962.
63. Greten-Harrison, B., Polydoro, M., Morimoto-Tomita, M., Diao, L., Williams, A. M., Nie, E. H., Makani, S., Tian, N., Castillo, P. E., Buchman, V. L. & Chandra, S. S. (2010) αβγ-Synuclein triple knockout mice reveal age-dependent neuronal dysfunction, *Proc Natl Acad Sci U S A.* **107**, 19573–8.

64. Beatman, E. L., Massey, A., Shives, K. D., Burrack, K. S., Chamanian, M., Morrison, T. E. & Beckham, J. D. (2015) Alpha-Synuclein Expression Restricts RNA Viral Infections in the Brain, *J Virol.* **90**, 2767–82.
65. Tomlinson, J. J., Shutinoski, B., Dong, L., Meng, F., Elleithy, D., Lengacher, N. A., Nguyen, A. P., Cron, G. O., Jiang, Q., Roberson, E. D., Nussbaum, R. L., Majbour, N. K., El-Agnaf, O. M., Bennett, S. A., Lagace, D. C., Woulfe, J. M., Sad, S., Brown, E. G. & Schlossmacher, M. G. (2017) Holocranohistochemistry enables the visualization of α-synuclein expression in the murine olfactory system and discovery of its systemic anti-microbial effects, *J Neural Transm (Vienna).* **124**, 721–738.
66. Stolzenberg, E., Berry, D., Yang, D., Lee, E. Y., Kroemer, A., Kaufman, S., Wong, G. C. L., Oppenheim, J. J., Sen, S., Fishbein, T., Bax, A., Harris, B., Barbut, D. & Zasloff, M. A. (2017) A Role for Neuronal Alpha-Synuclein in Gastrointestinal Immunity, *J Innate Immun.* **9**, 456–463.
67. Abreu, M. T., Fukata, M. & Arditi, M. (2005) TLR signaling in the gut in health and disease, *J Immunol.* **174**, 4453–60.
68. Hurley, M. J., Menozzi, E., Koletsi, S., Bates, R., Gegg, M. E., Chau, K. Y., Blottière, H. M., Macnaughtan, J. & Schapira, A. H. V. (2023) α-Synuclein expression in response to bacterial ligands and metabolites in gut enteroendocrine cells: an in vitro proof of concept study, *Brain Commun.* **5**, fcad285.
69. Song, Y., Mo, Y., Chen, S., Chen, Y., Zhang, C., Deng, S., Liao, J., He, Y., Wang, W., Zheng, W. & Zeng, T. (2026) Immune Exhaustion in Chronic Infection and Cancer: Signaling Pathways and Therapeutic Interventions, *MedComm (2020).* **7**, e70635.
70. Wherry, E. J., Barber, D. L., Kaech, S. M., Blattman, J. N. & Ahmed, R. (2004) Antigen-independent memory CD8 T cells do not develop during chronic viral infection, *Proc Natl Acad Sci U S A.* **101**, 16004–9.
71. Wherry, E. J. & Kurachi, M. (2015) Molecular and cellular insights into T cell exhaustion, *Nat Rev Immunol.* **15**, 486–99.
72. Fuller, M. J. & Zajac, A. J. (2003) Ablation of CD8 and CD4 T cell responses by high viral loads, *J Immunol.* **170**, 477–86.
73. Moskophidis, D., Lechner, F., Pircher, H. & Zinkernagel, R. M. (1993) Virus persistence in acutely infected immunocompetent mice by exhaustion of antiviral cytotoxic effector T cells, *Nature.* **362**, 758–61.
74. Watowich, M. B., Gilbert, M. R. & Larion, M. (2023) T cell exhaustion in malignant gliomas, *Trends Cancer.* **9**, 270–292.
75. Grayson, J. M., Short, S. M., Lee, C. J., Park, N., Marsac, C., Sette, A., Lindestam Arlehamn, C. S., Leng, X. I., Lockhart, S. N. & Craft, S. (2023) T cell exhaustion is associated with cognitive status and amyloid accumulation in Alzheimer's disease, *Sci Rep.* **13**, 15779.
76. Bido, S., Muggeo, S., Massimino, L., Marzi, M. J., Giannelli, S. G., Melacini, E., Nannoni, M., Gambarè, D., Bellini, E., Ordazzo, G., Rossi, G., Maffezzini, C., Iannelli, A., Luoni, M., Bacigaluppi, M., Gregori, S., Nicassio, F. & Broccoli, V. (2021) Microglia-specific overexpression of α-synuclein leads to severe dopaminergic neurodegeneration by phagocytic exhaustion and oxidative toxicity, *Nat Commun.* **12**, 6237.
77. Hemati, S. & Mohsenipour, Z. (2026) Immune exhaustion in bacterial infections: mechanisms, consequences, and therapeutic implications, *Braz J Infect Dis.* **30**, 105809.
78. Padovani, C. M., Wilson, R. M., Rodriguez, A., Spur, B. W. & Yin, K. (2024) Resolvin D2 attenuates LPS-induced macrophage exhaustion, *Faseb j.* **38**, e23569.
79. Kurtz, J. R., Nieves, W., Bauer, D. L., Israel, K. E., Adcox, H. E., Gunn, J. S., Morici, L. A. & McLachlan, J. B. (2020) Salmonella Persistence and Host Immunity Are Dictated by the Anatomical Microenvironment, *Infect Immun.* **88**.
80. Stapels, D. A. C., Hill, P. W. S., Westermann, A. J., Fisher, R. A., Thurston, T. L., Saliba, A. E., Blommestein, I., Vogel, J. & Helaine, S. (2018) Salmonella persisters undermine host immune defenses during antibiotic treatment, *Science.* **362**, 1156–1160.
81. Pradhan, K., Yi, Z., Geng, S. & Li, L. (2021) Development of Exhausted Memory Monocytes and Underlying Mechanisms, *Front Immunol.* **12**, 778830.

82. Wang, L., Cui, Y., Han, B., Du, Y., Salewala, K. S., Wang, S., Zhao, W., Zhang, H., Wang, S., Xu, X., Ma, J., Zhu, Y. & Tuo, H. (2025) Gut microbiota and Parkinson's disease, *Chin Med J (Engl).* **138**, 289–297.
83. Nie, S., Wang, J., Deng, Y., Ye, Z. & Ge, Y. (2022) Inflammatory microbes and genes as potential biomarkers of Parkinson's disease, *NPJ Biofilms Microbiomes.* **8**, 101.
84. Scheperjans, F., Aho, V., Pereira, P. A., Koskinen, K., Paulin, L., Pekkonen, E., Haapaniemi, E., Kaakkola, S., Eerola-Rautio, J., Pohja, M., Kinnunen, E., Murros, K. & Auvinen, P. (2015) Gut microbiota are related to Parkinson's disease and clinical phenotype, *Mov Disord.* **30**, 350–8.
85. Cilia, R., Piatti, M., Cereda, E., Bolliri, C., Caronni, S., Ferri, V., Cassani, E., Bonvegna, S., Ferrarese, C., Zecchinelli, A. L., Barichella, M. & Pezzoli, G. (2021) Does Gut Microbiota Influence the Course of Parkinson's Disease? A 3-Year Prospective Exploratory Study in de novo Patients, *J Parkinsons Dis.* **11**, 159–170.
86. Ke, H., Li, F., Deng, W., Li, Z., Wang, S., Lv, P. & Chen, Y. (2021) Metformin Exerts Anti-inflammatory and Mucus Barrier Protective Effects by Enriching Akkermansia muciniphila in Mice With Ulcerative Colitis, *Front Pharmacol.* **12**, 726707.
87. Qu, S., Fan, L., Qi, Y., Xu, C., Hu, Y., Chen, S., Liu, W., Liu, W. & Si, J. (2021) Akkermansia muciniphila Alleviates Dextran Sulfate Sodium (DSS)-Induced Acute Colitis by NLRP3 Activation, *Microbiol Spectr.* **9**, e0073021.
88. Wu, Z., Xu, Q., Gu, S., Chen, Y., Lv, L., Zheng, B., Wang, Q., Wang, K., Wang, S., Xia, J., Yang, L., Bian, X., Jiang, X., Zheng, L. & Li, L. (2022) Akkermansia muciniphila Ameliorates Clostridioides difficile Infection in Mice by Modulating the Intestinal Microbiome and Metabolites, *Front Microbiol.* **13**, 841920.
89. Amorim Neto, D. P., Bosque, B. P., Pereira de Godoy, J. V., Rodrigues, P. V., Meneses, D. D., Tostes, K., Costa Tonoli, C. C., Faustino de Carvalho, H., González-Billault, C. & de Castro Fonseca, M. (2022) Akkermansia muciniphila induces mitochondrial calcium overload and α -synuclein aggregation in an enteroendocrine cell line, *iScience.* **25**, 103908.
90. Bai, X., Sun, Y., Li, Y., Li, M., Cao, Z., Huang, Z., Zhang, F., Yan, P., Wang, L., Luo, J., Wu, J., Fan, D., Chen, H., Zhi, M., Lan, P., Zeng, Z., Wu, X., Miao, Y. & Zuo, T. (2022) Landscape of the gut archaeome in association with geography, ethnicity, urbanization, and diet in the Chinese population, *Microbiome.* **10**, 147.
91. Ren, Y., Wu, J., Wang, Y., Zhang, L., Ren, J., Zhang, Z., Chen, B., Zhang, K., Zhu, B., Liu, W., Li, S. & Li, X. (2023) Lifestyle patterns influence the composition of the gut microbiome in a healthy Chinese population, *Sci Rep.* **13**, 14425.
92. Sung, J., Kim, S., Cabatbat, J. J. T., Jang, S., Jin, Y. S., Jung, G. Y., Chia, N. & Kim, P. J. (2017) Global metabolic interaction network of the human gut microbiota for context-specific community-scale analysis, *Nat Commun.* **8**, 15393.
93. Sperandeo, P., Martorana, A. M. & Polissi, A. (2019) Lipopolysaccharide Biosynthesis and Transport to the Outer Membrane of Gram-Negative Bacteria, *Subcell Biochem.* **92**, 9–37.
94. Chow, J. C., Young, D. W., Golenbock, D. T., Christ, W. J. & Gusovsky, F. (1999) Toll-like receptor-4 mediates lipopolysaccharide-induced signal transduction, *J Biol Chem.* **274**, 10689–92.
95. da Silva, A. A. F., Fiadeiro, M. B., Bernardino, L. I., Fonseca, C. S. P., Baltazar, G. M. F. & Cristóvão, A. C. B. (2024) "Lipopolysaccharide-induced animal models for neuroinflammation - An overview.", *J Neuroimmunol.* **387**, 578273.
96. Meng, F. & Lowell, C. A. (1997) Lipopolysaccharide (LPS)-induced macrophage activation and signal transduction in the absence of Src-family kinases Hck, Fgr, and Lyn, *J Exp Med.* **185**, 1661–70.
97. Lu, Y. C., Yeh, W. C. & Ohashi, P. S. (2008) LPS/TLR4 signal transduction pathway, *Cytokine.* **42**, 145–151.
98. Zogaj, X., Bokranz, W., Nimtz, M. & Römling, U. (2003) Production of cellulose and curli fimbriae by members of the family Enterobacteriaceae isolated from the human gastrointestinal tract, *Infect Immun.* **71**, 4151–8.
99. Blanco, L. P., Evans, M. L., Smith, D. R., Badtke, M. P. & Chapman, M. R. (2012) Diversity, biogenesis and function of microbial amyloids, *Trends Microbiol.* **20**, 66–73.

100. Raghupathi, P. K., Liu, W., Sabbe, K., Houf, K., Burmølle, M. & Sørensen, S. J. (2017) Synergistic Interactions within a Multispecies Biofilm Enhance Individual Species Protection against Grazing by a Pelagic Protozoan, *Front Microbiol.* **8**, 2649.
101. Petrova, O. E. & Sauer, K. (2009) A novel signaling network essential for regulating Pseudomonas aeruginosa biofilm development, *PLoS Pathog.* **5**, e1000668.
102. Sauer, K., Camper, A. K., Ehrlich, G. D., Costerton, J. W. & Davies, D. G. (2002) Pseudomonas aeruginosa displays multiple phenotypes during development as a biofilm, *J Bacteriol.* **184**, 1140–54.
103. Gallo, P. M., Rapsinski, G. J., Wilson, R. P., Oppong, G. O., Sriram, U., Goulian, M., Buttaro, B., Caricchio, R., Gallucci, S. & Tükel, Ç. (2015) Amyloid-DNA Composites of Bacterial Biofilms Stimulate Autoimmunity, *Immunity.* **42**, 1171–84.
104. Sauer, K., Stoodley, P., Goeres, D. M., Hall-Stoodley, L., Burmølle, M., Stewart, P. S. & Bjarnsholt, T. (2022) The biofilm life cycle: expanding the conceptual model of biofilm formation, *Nat Rev Microbiol.* **20**, 608–620.
105. Barnhart, M. M. & Chapman, M. R. (2006) Curli biogenesis and function, *Annu Rev Microbiol.* **60**, 131–47.
106. Olsén, A., Jonsson, A. & Normark, S. (1989) Fibronectin binding mediated by a novel class of surface organelles on Escherichia coli, *Nature.* **338**, 652–5.
107. Wang, X. & Chapman, M. R. (2008) Sequence determinants of bacterial amyloid formation, *J Mol Biol.* **380**, 570–80.
108. Wang, X., Hammer, N. D. & Chapman, M. R. (2008) The molecular basis of functional bacterial amyloid polymerization and nucleation, *J Biol Chem.* **283**, 21530–9.
109. Bu, F., Dee, D. R. & Liu, B. (2024) Structural insight into Escherichia coli CsgA amyloid fibril assembly, *mBio.* **15**, e0041924.
110. Sleutel, M., Pradhan, B., Volkov, A. N. & Remaut, H. (2023) Structural analysis and architectural principles of the bacterial amyloid curli, *Nat Commun.* **14**, 2822.
111. Brombacher, E., Baratto, A., Dorel, C. & Landini, P. (2006) Gene expression regulation by the Curli activator CsgD protein: modulation of cellulose biosynthesis and control of negative determinants for microbial adhesion, *J Bacteriol.* **188**, 2027–37.
112. Gerstel, U., Park, C. & Römling, U. (2003) Complex regulation of csgD promoter activity by global regulatory proteins, *Mol Microbiol.* **49**, 639–54.
113. Robbe-Saule, V., Jaumouillé, V., Prévost, M. C., Guadagnini, S., Talhouarne, C., Mathout, H., Kolb, A. & Norel, F. (2006) Crl activates transcription initiation of RpoS-regulated genes involved in the multicellular behavior of Salmonella enterica serovar Typhimurium, *J Bacteriol.* **188**, 3983–94.
114. Chorell, E., Andersson, E., Evans, M. L., Jain, N., Götheson, A., Åden, J., Chapman, M. R., Almqvist, F. & Wittung-Stafshede, P. (2015) Bacterial Chaperones CsgE and CsgC Differentially Modulate Human α-Synuclein Amyloid Formation via Transient Contacts, *PLoS One.* **10**, e0140194.
115. Evans, M. L., Chorell, E., Taylor, J. D., Åden, J., Götheson, A., Li, F., Koch, M., Sefer, L., Matthews, S. J., Wittung-Stafshede, P., Almqvist, F. & Chapman, M. R. (2015) The bacterial curli system possesses a potent and selective inhibitor of amyloid formation, *Mol Cell.* **57**, 445–55.
116. Nenninger, A. A., Robinson, L. S., Hammer, N. D., Epstein, E. A., Badtke, M. P., Hultgren, S. J. & Chapman, M. R. (2011) CsgE is a curli secretion specificity factor that prevents amyloid fibre aggregation, *Mol Microbiol.* **81**, 486–99.
117. Robinson, L. S., Ashman, E. M., Hultgren, S. J. & Chapman, M. R. (2006) Secretion of curli fibre subunits is mediated by the outer membrane-localized CsgG protein, *Mol Microbiol.* **59**, 870–81.
118. Epstein, E. A., Reizian, M. A. & Chapman, M. R. (2009) Spatial clustering of the curlin secretion lipoprotein requires curli fiber assembly, *J Bacteriol.* **191**, 608–15.
119. Hammer, N. D., Schmidt, J. C. & Chapman, M. R. (2007) The curli nucleator protein, CsgB, contains an amyloidogenic domain that directs CsgA polymerization, *Proc Natl Acad Sci U S A.* **104**, 12494–9.
120. Nenninger, A. A., Robinson, L. S. & Hultgren, S. J. (2009) Localized and efficient curli nucleation requires the chaperone-like amyloid assembly protein CsgF, *Proc Natl Acad Sci U S A.* **106**, 900–5.

121. Schmit, K. J., Garcia, P., Sciortino, A., Aho, V. T. E., Pardo Rodriguez, B., Thomas, M. H., Gérardy, J. J., Bastero Acha, I., Halder, R., Cialini, C., Heurtaux, T., Ostahi, I., Busi, S. B., Grandmougin, L., Lowndes, T., Singh, Y., Martens, E. C., Mittelbronn, M., Buttini, M. & Wilmes, P. (2023) Fiber deprivation and microbiome-borne curli shift gut bacterial populations and accelerate disease in a mouse model of Parkinson's disease, *Cell Rep.* **42**, 113071.
122. Sampson, T. R., Challis, C., Jain, N., Moiseyenko, A., Ladinsky, M. S., Shastri, G. G., Thron, T., Needham, B. D., Horvath, I., Debelius, J. W., Janssen, S., Knight, R., Wittung-Stafshede, P., Gradinaru, V., Chapman, M. & Mazmanian, S. K. (2020) A gut bacterial amyloid promotes α-synuclein aggregation and motor impairment in mice, *Elife.* **9**.
123. Wang, C., Lau, C. Y., Ma, F. & Zheng, C. (2021) Genome-wide screen identifies curli amyloid fibril as a bacterial component promoting host neurodegeneration, *Proc Natl Acad Sci U S A.* **118**.
124. Chen, S. G., Stribinskis, V., Rane, M. J., Demuth, D. R., Gozal, E., Roberts, A. M., Jagadapillai, R., Liu, R., Choe, K., Shivakumar, B., Son, F., Jin, S., Kerber, R., Adame, A., Masliah, E. & Friedland, R. P. (2016) Exposure to the Functional Bacterial Amyloid Protein Curli Enhances Alpha-Synuclein Aggregation in Aged Fischer 344 Rats and Caenorhabditis elegans, *Sci Rep.* **6**, 34477.
125. Liang, D., Liu, H., Jin, R., Feng, R., Wang, J., Qin, C., Zhang, R., Chen, Y., Zhang, J., Teng, J., Tang, B., Ding, X. & Wang, X. (2023) Escherichia coli triggers α-synuclein pathology in the LRRK2 transgenic mouse model of PD, *Gut Microbes.* **15**, 2276296.
126. Tükel, C., Raffatellu, M., Humphries, A. D., Wilson, R. P., Andrews-Polymenis, H. L., Gull, T., Figueiredo, J. F., Wong, M. H., Michelsen, K. S., Akçelik, M., Adams, L. G. & Bäumler, A. J. (2005) CsgA is a pathogen-associated molecular pattern of Salmonella enterica serotype Typhimurium that is recognized by Toll-like receptor 2, *Mol Microbiol.* **58**, 289–304.
127. Tursi, S. A., Lee, E. Y., Medeiros, N. J., Lee, M. H., Nicastro, L. K., Buttaro, B., Gallucci, S., Wilson, R. P., Wong, G. C. L. & Tükel, Ç. (2017) Bacterial amyloid curli acts as a carrier for DNA to elicit an autoimmune response via TLR2 and TLR9, *PLoS Pathog.* **13**, e1006315.
128. Tükel, C., Wilson, R. P., Nishimori, J. H., Pezeshki, M., Chromy, B. A. & Bäumler, A. J. (2009) Responses to amyloids of microbial and host origin are mediated through toll-like receptor 2, *Cell Host Microbe.* **6**, 45–53.
129. Tükel, C., Nishimori, J. H., Wilson, R. P., Winter, M. G., Keestra, A. M., van Putten, J. P. & Bäumler, A. J. (2010) Toll-like receptors 1 and 2 cooperatively mediate immune responses to curli, a common amyloid from enterobacterial biofilms, *Cell Microbiol.* **12**, 1495–505.
130. Das, T. K., Blasco-Conesa, M. P., Korf, J., Honarpisheh, P., Chapman, M. R. & Ganesh, B. P. (2022) Bacterial Amyloid Curli Associated Gut Epithelial Neuroendocrine Activation Predominantly Observed in Alzheimer's Disease Mice with Central Amyloid-β Pathology, *J Alzheimers Dis.* **88**, 191–205.
131. Kurlawala, Z., McMillan, J. D., Singhal, R. A., Morehouse, J., Burke, D. A., Sears, S. M., Duregon, E., Beverly, L. J., Siskind, L. J. & Friedland, R. P. (2023) Mutant and curli-producing E. coli enhance the disease phenotype in a hSOD1-G93A mouse model of ALS, *Sci Rep.* **13**, 5945.
132. Olsén, A., Wick, M. J., Mörgelin, M. & Björck, L. (1998) Curli, fibrous surface proteins of Escherichia coli, interact with major histocompatibility complex class I molecules, *Infect Immun.* **66**, 944–9.
133. Oppong, G. O., Rapsinski, G. J., Tursi, S. A., Biesecker, S. G., Klein-Szanto, A. J., Goulian, M., McCauley, C., Healy, C., Wilson, R. P. & Tükel, C. (2015) Biofilm-associated bacterial amyloids dampen inflammation in the gut: oral treatment with curli fibres reduces the severity of hapten-induced colitis in mice, *NPJ Biofilms Microbiomes.* **1**, 15019–.
134. Grabig, A., Paclik, D., Guzy, C., Dankof, A., Baumgart, D. C., Erckenbrecht, J., Raupach, B., Sonnenborn, U., Eckert, J., Schumann, R. R., Wiedenmann, B., Dignass, A. U. & Sturm, A. (2006) Escherichia coli strain Nissle 1917 ameliorates experimental colitis via toll-like receptor 2- and toll-like receptor 4-dependent pathways, *Infect Immun.* **74**, 4075–82.
135. Sturm, A., Rilling, K., Baumgart, D. C., Gargas, K., Abou-Ghazalé, T., Raupach, B., Eckert, J., Schumann, R. R., Enders, C., Sonnenborn, U., Wiedenmann, B. & Dignass, A. U. (2005) Escherichia coli Nissle 1917

distinctively modulates T-cell cycling and expansion via toll-like receptor 2 signaling, *Infect Immun.* **73**, 1452–65.
136. Baumgartner, M., Lang, M., Holley, H., Crepaz, D., Hausmann, B., Pjevac, P., Moser, D., Haller, F., Hof, F., Beer, A., Orgler, E., Frick, A., Khare, V., Evstatiev, R., Strohmaier, S., Primas, C., Dolak, W., Köcher, T., Klavins, K., Rath, T., Neurath, M. F., Berry, D., Makristathis, A., Muttenthaler, M. & Gasche, C. (2021) Mucosal Biofilms Are an Endoscopic Feature of Irritable Bowel Syndrome and Ulcerative Colitis, *Gastroenterology.* **161**, 1245–1256.e20.
137. Swidsinski, A., Weber, J., Loening-Baucke, V., Hale, L. P. & Lochs, H. (2005) Spatial organization and composition of the mucosal flora in patients with inflammatory bowel disease, *J Clin Microbiol.* **43**, 3380–9.
138. Tytgat, H. L. P., Nobrega, F. L., van der Oost, J. & de Vos, W. M. (2019) Bowel Biofilms: Tipping Points between a Healthy and Compromised Gut?, *Trends Microbiol.* **27**, 17–25.
139. Jandl, B., Dighe, S., Gasche, C., Makristathis, A. & Muttenthaler, M. (2024) Intestinal biofilms: pathophysiological relevance, host defense, and therapeutic opportunities, *Clin Microbiol Rev.* **37**, e0013323.
140. Zollinger, A. J. & Smith, M. L. (2017) Fibronectin, the extracellular glue, *Matrix Biol.* **60-61**, 27–37.
141. Mezu-Ndubuisi, O. J. & Maheshwari, A. (2021) The role of integrins in inflammation and angiogenesis, *Pediatr Res.* **89**, 1619–1626.
142. Gophna, U., Oelschlaeger, T. A., Hacker, J. & Ron, E. Z. (2002) Role of fibronectin in curli-mediated internalization, *FEMS Microbiol Lett.* **212**, 55–8.
143. York, I. A. & Rock, K. L. (1996) Antigen processing and presentation by the class I major histocompatibility complex, *Annu Rev Immunol.* **14**, 369–96.
144. Johansson, C., Nilsson, T., Olsén, A. & Wick, M. J. (2001) The influence of curli, a MHC-I-binding bacterial surface structure, on macrophage-T cell interactions, *FEMS Immunol Med Microbiol.* **30**, 21–9.
145. Clevers, H. (2013) The intestinal crypt, a prototype stem cell compartment, *Cell.* **154**, 274–84.
146. Miron, N. & Cristea, V. (2012) Enterocytes: active cells in tolerance to food and microbial antigens in the gut, *Clin Exp Immunol.* **167**, 405–12.
147. Bevins, C. L. & Salzman, N. H. (2011) Paneth cells, antimicrobial peptides and maintenance of intestinal homeostasis, *Nat Rev Microbiol.* **9**, 356–68.
148. Kim, Y. S. & Ho, S. B. (2010) Intestinal goblet cells and mucins in health and disease: recent insights and progress, *Curr Gastroenterol Rep.* **12**, 319–30.
149. Worthington, J. J., Reimann, F. & Gribble, F. M. (2018) Enteroendocrine cells-sensory sentinels of the intestinal environment and orchestrators of mucosal immunity, *Mucosal Immunol.* **11**, 3–20.
150. Grundeken, E. & El Aidy, S. (2025) Enteroendocrine cells: the gatekeepers of microbiome-gut-brain communication, *NPJ Biofilms Microbiomes.* **11**, 179.
151. Haber, A. L., Biton, M., Rogel, N., Herbst, R. H., Shekhar, K., Smillie, C., Burgin, G., Delorey, T. M., Howitt, M. R., Katz, Y., Tirosh, I., Beyaz, S., Dionne, D., Zhang, M., Raychowdhury, R., Garrett, W. S., Rozenblatt-Rosen, O., Shi, H. N., Yilmaz, O., Xavier, R. J. & Regev, A. (2017) A single-cell survey of the small intestinal epithelium, *Nature.* **551**, 333–339.
152. Habib, A. M., Richards, P., Cairns, L. S., Rogers, G. J., Bannon, C. A., Parker, H. E., Morley, T. C., Yeo, G. S., Reimann, F. & Gribble, F. M. (2012) Overlap of endocrine hormone expression in the mouse intestine revealed by transcriptional profiling and flow cytometry, *Endocrinology.* **153**, 3054–65.
153. Montero-Hadjadje, M., Elias, S., Chevalier, L., Benard, M., Tanguy, Y., Turquier, V., Galas, L., Yon, L., Malagon, M. M., Driouich, A., Gasman, S. & Anouar, Y. (2009) Chromogranin A promotes peptide hormone sorting to mobile granules in constitutively and regulated secreting cells: role of conserved N- and C-terminal peptides, *J Biol Chem.* **284**, 12420–31.
154. Bogunovic, M., Davé, S. H., Tilstra, J. S., Chang, D. T., Harpaz, N., Xiong, H., Mayer, L. F. & Plevy, S. E. (2007) Enteroendocrine cells express functional Toll-like receptors, *Am J Physiol Gastrointest Liver Physiol.* **292**, G1770–83.

155. Selleri, S., Palazzo, M., Deola, S., Wang, E., Balsari, A., Marincola, F. M. & Rumio, C. (2008) Induction of pro-inflammatory programs in enteroendocrine cells by the Toll-like receptor agonists flagellin and bacterial LPS, *Int Immunol.* **20**, 961–70.
156. Yusta, B., Baggio, L. L., Koehler, J., Holland, D., Cao, X., Pinnell, L. J., Johnson-Henry, K. C., Yeung, W., Surette, M. G., Bang, K. W., Sherman, P. M. & Drucker, D. J. (2015) GLP-1R Agonists Modulate Enteric Immune Responses Through the Intestinal Intraepithelial Lymphocyte GLP-1R, *Diabetes.* **64**, 2537–49.
157. Zhang, J. G., Cong, B., Li, Q. X., Chen, H. Y., Qin, J. & Fu, L. H. (2011) Cholecystokinin octapeptide regulates lipopolysaccharide-activated B cells co-stimulatory molecule expression and cytokines production in vitro, *Immunopharmacol Immunotoxicol.* **33**, 157–63.
158. Bohórquez, D. V., Shahid, R. A., Erdmann, A., Kreger, A. M., Wang, Y., Calakos, N., Wang, F. & Liddle, R. A. (2015) Neuroepithelial circuit formed by innervation of sensory enteroendocrine cells, *J Clin Invest.* **125**, 782–6.
159. Bellono, N. W., Bayrer, J. R., Leitch, D. B., Castro, J., Zhang, C., O'Donnell, T. A., Brierley, S. M., Ingraham, H. A. & Julius, D. (2017) Enterochromaffin Cells Are Gut Chemosensors that Couple to Sensory Neural Pathways, *Cell.* **170**, 185–198.e16.
160. Chandra, R., Hiniker, A., Kuo, Y. M., Nussbaum, R. L. & Liddle, R. A. (2017) α-Synuclein in gut endocrine cells and its implications for Parkinson's disease, *JCI Insight.* **2**.
161. Ortiz de Ora, L., Balsamo, J. M., Uyeda, K. S. & Bess, E. N. (2024) Discovery of a Gut Bacterial Metabolic Pathway that Drives α-Synuclein Aggregation, *ACS Chem Biol.* **19**, 1011–1021.
162. Chandra, R., Sokratian, A., Chavez, K. R., King, S., Swain, S. M., Snyder, J. C., West, A. B. & Liddle, R. A. (2023) Gut mucosal cells transfer α-synuclein to the vagus nerve, *JCI Insight.* **8**.
163. Rodrigues, P. V., de Godoy, J. V. P., Bosque, B. P., Amorim Neto, D. P., Tostes, K., Palameta, S., Garcia-Rosa, S., Tonoli, C. C. C., de Carvalho, H. F. & de Castro Fonseca, M. (2022) Transcellular propagation of fibrillar α-synuclein from enteroendocrine to neuronal cells requires cell-to-cell contact and is Rab35-dependent, *Sci Rep.* **12**, 4168.
164. Kouranti, I., Sachse, M., Arouche, N., Goud, B. & Echard, A. (2006) Rab35 regulates an endocytic recycling pathway essential for the terminal steps of cytokinesis, *Curr Biol.* **16**, 1719–25.
165. Lee, M. K., Stirling, W., Xu, Y., Xu, X., Qui, D., Mandir, A. S., Dawson, T. M., Copeland, N. G., Jenkins, N. A. & Price, D. L. (2002) Human alpha-synuclein-harboring familial Parkinson's disease-linked Ala-53 --> Thr mutation causes neurodegenerative disease with alpha-synuclein aggregation in transgenic mice, *Proc Natl Acad Sci U S A.* **99**, 8968–73.
166. Polymeropoulos, M. H., Lavedan, C., Leroy, E., Ide, S. E., Dehejia, A., Dutra, A., Pike, B., Root, H., Rubenstein, J., Boyer, R., Stenroos, E. S., Chandrasekharappa, S., Athanassiadou, A., Papapetropoulos, T., Johnson, W. G., Lazzarini, A. M., Duvoisin, R. C., Di Iorio, G., Golbe, L. I. & Nussbaum, R. L. (1997) Mutation in the alpha-synuclein gene identified in families with Parkinson's disease, *Science.* **276**, 2045–7.
167. Pacelli, C., Giguère, N., Bourque, M. J., Lévesque, M., Slack, R. S. & Trudeau, L. (2015) Elevated Mitochondrial Bioenergetics and Axonal Arborization Size Are Key Contributors to the Vulnerability of Dopamine Neurons, *Curr Biol.* **25**, 2349–60.
168. Bonifati, V., Rizzu, P., van Baren, M. J., Schaap, O., Breedveld, G. J., Krieger, E., Dekker, M. C., Squitieri, F., Ibanez, P., Joosse, M., van Dongen, J. W., Vanacore, N., van Swieten, J. C., Brice, A., Meco, G., van Duijn, C. M., Oostra, B. A. & Heutink, P. (2003) Mutations in the DJ-1 gene associated with autosomal recessive early-onset parkinsonism, *Science.* **299**, 256–9.
169. Liu, Y., Ma, X., Fujioka, H., Liu, J., Chen, S. & Zhu, X. (2019) DJ-1 regulates the integrity and function of ER-mitochondria association through interaction with IP3R3-Grp75-VDAC1, *Proc Natl Acad Sci U S A.* **116**, 25322–25328.
170. Thomas, K. J., McCoy, M. K., Blackinton, J., Beilina, A., van der Brug, M., Sandebring, A., Miller, D., Maric, D., Cedazo-Minguez, A. & Cookson, M. R. (2011) DJ-1 acts in parallel to the PINK1/parkin pathway to control mitochondrial function and autophagy, *Hum Mol Genet.* **20**, 40–50.
171. Irrcher, I., Aleyasin, H., Seifert, E. L., Hewitt, S. J., Chhabra, S., Phillips, M., Lutz, A. K., Rousseaux, M. W., Bevilacqua, L., Jahani-Asl, A., Callaghan, S., MacLaurin, J. G., Winklhofer, K. F., Rizzu, P., Rippstein, P.,

Kim, R. H., Chen, C. X., Fon, E. A., Slack, R. S., Harper, M. E., McBride, H. M., Mak, T. W. & Park, D. S. (2010) Loss of the Parkinson's disease-linked gene DJ-1 perturbs mitochondrial dynamics, *Hum Mol Genet.* **19**, 3734–46.
172. Taira, T., Saito, Y., Niki, T., Iguchi-Ariga, S. M., Takahashi, K. & Ariga, H. (2004) DJ-1 has a role in antioxidative stress to prevent cell death, *EMBO Rep.* **5**, 213–8.
173. Zhou, W., Zhu, M., Wilson, M. A., Petsko, G. A. & Fink, A. L. (2006) The oxidation state of DJ-1 regulates its chaperone activity toward alpha-synuclein, *J Mol Biol.* **356**, 1036–48.
174. Shendelman, S., Jonason, A., Martinat, C., Leete, T. & Abeliovich, A. (2004) DJ-1 is a redox-dependent molecular chaperone that inhibits alpha-synuclein aggregate formation, *PLoS Biol.* **2**, e362.
175. Sturtz, L. A., Diekert, K., Jensen, L. T., Lill, R. & Culotta, V. C. (2001) A fraction of yeast Cu,Zn-superoxide dismutase and its metallochaperone, CCS, localize to the intermembrane space of mitochondria. A physiological role for SOD1 in guarding against mitochondrial oxidative damage, *J Biol Chem.* **276**, 38084–9.
176. Bunton-Stasyshyn, R. K., Saccon, R. A., Fratta, P. & Fisher, E. M. (2015) SOD1 Function and Its Implications for Amyotrophic Lateral Sclerosis Pathology: New and Renascent Themes, *Neuroscientist.* **21**, 519–29.
177. Fischer, L. R., Igoudjil, A., Magrané, J., Li, Y., Hansen, J. M., Manfredi, G. & Glass, J. D. (2011) SOD1 targeted to the mitochondrial intermembrane space prevents motor neuropathy in the Sod1 knockout mouse, *Brain.* **134**, 196–209.
178. Abdeen, A. H., Trist, B. G., Nikseresht, S., Harwood, R., Roudeau, S., Rowlands, B. D., Kreilaus, F., Cottam, V., Mor, D., Richardson, M., Siciliano, J., Forkgen, J., Schaffer, G., Genoud, S., Li, A. A., Proschogo, N., Antonio, B., Falkenberg, G., Brueckner, D., Kysenius, K., Liddell, J. R., Fat, S. C. M., Wu, S., Fifita, J., Lockwood, T. E., Bishop, D. P., Blair, I., Ortega, R., Crouch, P. J. & Double, K. L. (2025) Parkinson-like wild-type superoxide dismutase 1 pathology induces nigral dopamine neuron degeneration in a novel murine model, *Acta Neuropathol.* **149**, 22.
179. Xiao, Y., Karam, C., Yi, J., Zhang, L., Li, X., Yoon, D., Wang, H., Dhakal, K., Ramlow, P., Yu, T., Mo, Z., Ma, J. & Zhou, J. (2018) ROS-related mitochondrial dysfunction in skeletal muscle of an ALS mouse model during the disease progression, *Pharmacol Res.* **138**, 25–36.
180. Helwig, M., Ulusoy, A., Rollar, A., O'Sullivan, S. A., Lee, S. S. L., Aboutalebi, H., Pinto-Costa, R., Jevans, B., Klinkenberg, M. & Di Monte, D. A. (2022) Neuronal hyperactivity-induced oxidant stress promotes in vivo α-synuclein brain spreading, *Sci Adv.* **8**, eabn0356.
181. La Vitola, P., Szegö, E. M., Pinto-Costa, R., Rollar, A., Harbachova, E., Schapira, A. H., Ulusoy, A. & Di Monte, D. A. (2024) Mitochondrial oxidant stress promotes α-synuclein aggregation and spreading in mice with mutated glucocerebrosidase, *NPJ Parkinsons Dis.* **10**, 233.
182. Scudamore, O. & Ciossek, T. (2018) Increased Oxidative Stress Exacerbates α-Synuclein Aggregation In Vivo, *J Neuropathol Exp Neurol.* **77**, 443–453.
183. Dionísio, P. A., Amaral, J. D. & Rodrigues, C. M. P. (2021) Oxidative stress and regulated cell death in Parkinson's disease, *Ageing Res Rev.* **67**, 101263.
184. Guan, S., Zhao, L. & Peng, R. (2022) Mitochondrial Respiratory Chain Supercomplexes: From Structure to Function, *Int J Mol Sci.* **23**.
185. Chen, C., McDonald, D., Blain, A., Sachdeva, A., Bone, L., Smith, A. L. M., Warren, C., Pickett, S. J., Hudson, G., Filby, A., Vincent, A. E., Turnbull, D. M. & Reeve, A. K. (2021) Imaging mass cytometry reveals generalised deficiency in OXPHOS complexes in Parkinson's disease, *NPJ Parkinsons Dis.* **7**, 39.
186. Kraytsberg, Y., Kudryavtseva, E., McKee, A. C., Geula, C., Kowall, N. W. & Khrapko, K. (2006) Mitochondrial DNA deletions are abundant and cause functional impairment in aged human substantia nigra neurons, *Nat Genet.* **38**, 518–20.
187. Salmonowicz, H. & Szczepanowska, K. (2025) The fate of mitochondrial respiratory complexes in aging, *Trends Cell Biol.* **35**, 955–970.
188. Flønes, I. H. & Tzoulis, C. (2022) Mitochondrial Respiratory Chain Dysfunction-A Hallmark Pathology of Idiopathic Parkinson's Disease?, *Front Cell Dev Biol.* **10**, 874596.

189. Brown, T. P., Rumsby, P. C., Capleton, A. C., Rushton, L. & Levy, L. S. (2006) Pesticides and Parkinson's disease--is there a link?, *Environ Health Perspect.* **114**, 156–64.
190. Paul, K. C., Krolewski, R. C., Lucumi Moreno, E., Blank, J., Holton, K. M., Ahfeldt, T., Furlong, M., Yu, Y., Cockburn, M., Thompson, L. K., Kreymerman, A., Ricci-Blair, E. M., Li, Y. J., Patel, H. B., Lee, R. T., Bronstein, J., Rubin, L. L., Khurana, V. & Ritz, B. (2023) A pesticide and iPSC dopaminergic neuron screen identifies and classifies Parkinson-relevant pesticides, *Nat Commun.* **14**, 2803.
191. Przedborski, S., Jackson-Lewis, V., Djaldetti, R., Liberatore, G., Vila, M., Vukosavic, S. & Almer, G. (2000) The parkinsonian toxin MPTP: action and mechanism, *Restor Neurol Neurosci.* **16**, 135–142.
192. Alsudayri, A., Perelman, S., Brewer, M., Chura, A., McDevitt, M., Drerup, C. & Ye, L. (2024) Gut microbiota regulate maturation and mitochondrial function of the nutrient-sensing enteroendocrine cell, *Development.* **151**.
193. Rangaraju, V., Lewis, T. L., Jr., Hirabayashi, Y., Bergami, M., Motori, E., Cartoni, R., Kwon, S. K. & Courchet, J. (2019) Pleiotropic Mitochondria: The Influence of Mitochondria on Neuronal Development and Disease, *J Neurosci.* **39**, 8200–8208.
194. Yu, S., Lee, Y., Boggess, S. C., Klein, N. R., Teyssier, N., Kampmann, M. & Knight, Z. A. (2026) A genetic screen in enteroendocrine cells reveals mechanisms that control protein sensing and GLP-1 release, *bioRxiv*.
195. McCauley, H. A., Riedman, A. M., Enriquez, J. R., Zhang, X., Watanabe-Chailland, M., Sanchez, J. G., Kechele, D. O., Paul, E. F., Riley, K., Burger, C., Lang, R. A. & Wells, J. M. (2023) Enteroendocrine Cells Protect the Stem Cell Niche by Regulating Crypt Metabolism in Response to Nutrients, *Cell Mol Gastroenterol Hepatol.* **15**, 1293–1310.
196. Singh, P. K. & Muqit, M. M. K. (2020) Parkinson's: A Disease of Aberrant Vesicle Trafficking, *Annu Rev Cell Dev Biol.* **36**, 237–264.
197. Rosenbloom, B. E. & Weinreb, N. J. (2013) Gaucher disease: a comprehensive review, *Crit Rev Oncog.* **18**, 163–75.
198. Sidransky, E., Nalls, M. A., Aasly, J. O., Aharon-Peretz, J., Annesi, G., Barbosa, E. R., Bar-Shira, A., Berg, D., Bras, J., Brice, A., Chen, C. M., Clark, L. N., Condroyer, C., De Marco, E. V., Dürr, A., Eblan, M. J., Fahn, S., Farrer, M. J., Fung, H. C., Gan-Or, Z., Gasser, T., Gershoni-Baruch, R., Giladi, N., Griffith, A., Gurevich, T., Januario, C., Kropp, P., Lang, A. E., Lee-Chen, G. J., Lesage, S., Marder, K., Mata, I. F., Mirelman, A., Mitsui, J., Mizuta, I., Nicoletti, G., Oliveira, C., Ottman, R., Orr-Urtreger, A., Pereira, L. V., Quattrone, A., Rogaeva, E., Rolfs, A., Rosenbaum, H., Rozenberg, R., Samii, A., Samaddar, T., Schulte, C., Sharma, M., Singleton, A., Spitz, M., Tan, E. K., Tayebi, N., Toda, T., Troiano, A. R., Tsuji, S., Wittstock, M., Wolfsberg, T. G., Wu, Y. R., Zabetian, C. P., Zhao, Y. & Ziegler, S. G. (2009) Multicenter analysis of glucocerebrosidase mutations in Parkinson's disease, *N Engl J Med.* **361**, 1651–61.
199. Mazzulli, J. R., Xu, Y. H., Sun, Y., Knight, A. L., McLean, P. J., Caldwell, G. A., Sidransky, E., Grabowski, G. A. & Krainc, D. (2011) Gaucher disease glucocerebrosidase and α-synuclein form a bidirectional pathogenic loop in synucleinopathies, *Cell.* **146**, 37–52.
200. Davis, M. Y., Johnson, C. O., Leverenz, J. B., Weintraub, D., Trojanowski, J. Q., Chen-Plotkin, A., Van Deerlin, V. M., Quinn, J. F., Chung, K. A., Peterson-Hiller, A. L., Rosenthal, L. S., Dawson, T. M., Albert, M. S., Goldman, J. G., Stebbins, G. T., Bernard, B., Wszolek, Z. K., Ross, O. A., Dickson, D. W., Eidelberg, D., Mattis, P. J., Niethammer, M., Yearout, D., Hu, S. C., Cholerton, B. A., Smith, M., Mata, I. F., Montine, T. J., Edwards, K. L. & Zabetian, C. P. (2016) Association of GBA Mutations and the E326K Polymorphism With Motor and Cognitive Progression in Parkinson Disease, *JAMA Neurol.* **73**, 1217–1224.
201. Gan-Or, Z., Amshalom, I., Kilarski, L. L., Bar-Shira, A., Gana-Weisz, M., Mirelman, A., Marder, K., Bressman, S., Giladi, N. & Orr-Urtreger, A. (2015) Differential effects of severe vs mild GBA mutations on Parkinson disease, *Neurology.* **84**, 880–7.
202. Schöndorf, D. C., Aureli, M., McAllister, F. E., Hindley, C. J., Mayer, F., Schmid, B., Sardi, S. P., Valsecchi, M., Hoffmann, S., Schwarz, L. K., Hedrich, U., Berg, D., Shihabuddin, L. S., Hu, J., Pruszak, J., Gygi, S. P., Sonnino, S., Gasser, T. & Deleidi, M. (2014) iPSC-derived neurons from GBA1-associated Parkinson's disease patients show autophagic defects and impaired calcium homeostasis, *Nat Commun.* **5**, 4028.

203. Smith, L. J., Bolsinger, M. M., Chau, K. Y., Gegg, M. E. & Schapira, A. H. V. (2023) The GBA variant E326K is associated with alpha-synuclein aggregation and lipid droplet accumulation in human cell lines, *Hum Mol Genet.* **32**, 773–789.
204. Manning-Boğ, A. B., Schüle, B. & Langston, J. W. (2009) Alpha-synuclein-glucocerebrosidase interactions in pharmacological Gaucher models: a biological link between Gaucher disease and parkinsonism, *Neurotoxicology.* **30**, 1127–32.
205. Noelker, C., Lu, L., Höllerhage, M., Vulinovic, F., Sturn, A., Roscher, R., Höglinger, G. U., Hirsch, E. C., Oertel, W. H., Alvarez-Fischer, D. & Andreas, H. (2015) Glucocerebrosidase deficiency and mitochondrial impairment in experimental Parkinson disease, *J Neurol Sci.* **356**, 129–36.
206. Papadopoulos, V. E., Nikolopoulou, G., Antoniadou, I., Karachaliou, A., Arianoglou, G., Emmanouilidou, E., Sardi, S. P., Stefanis, L. & Vekrellis, K. (2018) Modulation of β-glucocerebrosidase increases α-synuclein secretion and exosome release in mouse models of Parkinson's disease, *Hum Mol Genet.* **27**, 1696–1710.
207. Challis, C., Hori, A., Sampson, T. R., Yoo, B. B., Challis, R. C., Hamilton, A. M., Mazmanian, S. K., Volpicelli-Daley, L. A. & Gradinaru, V. (2020) Gut-seeded α-synuclein fibrils promote gut dysfunction and brain pathology specifically in aged mice, *Nat Neurosci.* **23**, 327–336.
208. Elkin, S. R., Lakoduk, A. M. & Schmid, S. L. (2016) Endocytic pathways and endosomal trafficking: a primer, *Wien Med Wochenschr.* **166**, 196–204.
209. Ogungbemi, D., Shorter, S., Asadollahi, R., Boussios, S. & Ovserpian, S. V. (2025) Molecular engines driving biogenesis, trafficking and release of exosomes: SNARE proteins, *Extracellular Vesicle.* **6**.
210. Eisbach, S. E. & Outeiro, T. F. (2013) Alpha-synuclein and intracellular trafficking: impact on the spreading of Parkinson's disease pathology, *J Mol Med (Berl).* **91**, 693–703.
211. Hoffmann, A. C., Minakaki, G., Menges, S., Salvi, R., Savitskiy, S., Kazman, A., Vicente Miranda, H., Mielenz, D., Klucken, J., Winkler, J. & Xiang, W. (2019) Extracellular aggregated alpha synuclein primarily triggers lysosomal dysfunction in neural cells prevented by trehalose, *Sci Rep.* **9**, 544.
212. Dilsizoglu Senol, A., Samarani, M., Syan, S., Guardia, C. M., Nonaka, T., Liv, N., Latour-Lambert, P., Hasegawa, M., Klumperman, J., Bonifacino, J. S. & Zurzolo, C. (2021) α-Synuclein fibrils subvert lysosome structure and function for the propagation of protein misfolding between cells through tunneling nanotubes, *PLoS Biol.* **19**, e3001287.
213. Parzych, K. R. & Klionsky, D. J. (2014) An overview of autophagy: morphology, mechanism, and regulation, *Antioxid Redox Signal.* **20**, 460–73.
214. Cuervo, A. M. & Dice, J. F. (1996) A receptor for the selective uptake and degradation of proteins by lysosomes, *Science.* **273**, 501–3.
215. Cuervo, A. M., Stefanis, L., Fredenburg, R., Lansbury, P. T. & Sulzer, D. (2004) Impaired degradation of mutant alpha-synuclein by chaperone-mediated autophagy, *Science.* **305**, 1292–5.
216. Mak, S. K., McCormack, A. L., Manning-Bog, A. B., Cuervo, A. M. & Di Monte, D. A. (2010) Lysosomal degradation of alpha-synuclein in vivo, *J Biol Chem.* **285**, 13621–9.
217. Yao, R. & Shen, J. (2023) Chaperone-mediated autophagy: Molecular mechanisms, biological functions, and diseases, *MedComm (2020).* **4**, e347.
218. Lee, H. J., Suk, J. E., Bae, E. J., Lee, J. H., Paik, S. R. & Lee, S. J. (2008) Assembly-dependent endocytosis and clearance of extracellular alpha-synuclein, *Int J Biochem Cell Biol.* **40**, 1835–49.
219. Hivare, P., Gadhavi, J., Bhatia, D. & Gupta, S. (2022) α-Synuclein fibrils explore actin-mediated macropinocytosis for cellular entry into model neuroblastoma neurons, *Traffic.* **23**, 391–410.
220. Oh, S. H., Kim, H. N., Park, H. J., Shin, J. Y., Bae, E. J., Sunwoo, M. K., Lee, S. J. & Lee, P. H. (2016) Mesenchymal Stem Cells Inhibit Transmission of α-Synuclein by Modulating Clathrin-Mediated Endocytosis in a Parkinsonian Model, *Cell Rep.* **14**, 835–849.
221. Schechter, M., Atias, M., Abd Elhadi, S., Davidi, D., Gitler, D. & Sharon, R. (2020) α-Synuclein facilitates endocytosis by elevating the steady-state levels of phosphatidylinositol 4,5-bisphosphate, *J Biol Chem.* **295**, 18076–18090.

222. Alam, P., Holst, M. R., Lauritsen, L., Nielsen, J., Nielsen, S. S. E., Jensen, P. H., Brewer, J. R., Otzen, D. E. & Nielsen, M. S. (2022) Polarized α-synuclein trafficking and transcytosis across brain endothelial cells via Rab7-decorated carriers, *Fluids Barriers CNS.* **19**, 37.
223. Shearer, L. J., Petersen, N. O. & Woodside, M. T. (2021) Internalization of α-synuclein oligomers into SH-SY5Y cells, *Biophys J.* **120**, 877–885.
224. Chavarría, C., Ivagnes, R. & Souza, J. M. (2022) Extracellular Alpha-Synuclein: Mechanisms for Glial Cell Internalization and Activation, *Biomolecules.* **12**.
225. Collins, B. M., McCoy, A. J., Kent, H. M., Evans, P. R. & Owen, D. J. (2002) Molecular architecture and functional model of the endocytic AP2 complex, *Cell.* **109**, 523–35.
226. Vargas, K. J., Wallace, J. N., Mooney, I., Owen, D. J. & Morgan, J. R. (2025) α-Synuclein interacts directly with AP2 and regulates its binding to synaptic membranes, *J Biol Chem.* **301**, 108502.
227. Vargas, K. J., Makani, S., Davis, T., Westphal, C. H., Castillo, P. E. & Chandra, S. S. (2014) Synucleins regulate the kinetics of synaptic vesicle endocytosis, *J Neurosci.* **34**, 9364–76.
228. McCormack, A., Keating, D. J., Chegeni, N., Colella, A., Wang, J. J. & Chataway, T. (2019) Abundance of Synaptic Vesicle-Related Proteins in Alpha-Synuclein-Containing Protein Inclusions Suggests a Targeted Formation Mechanism, *Neurotox Res.* **35**, 883–897.
229. Canty, J. T., Tan, R., Kusakci, E., Fernandes, J. & Yildiz, A. (2021) Structure and Mechanics of Dynein Motors, *Annu Rev Biophys.* **50**, 549–574.
230. Roberts, A. J., Kon, T., Knight, P. J., Sutoh, K. & Burgess, S. A. (2013) Functions and mechanics of dynein motor proteins, *Nat Rev Mol Cell Biol.* **14**, 713–26.
231. Mijaljica, D., Prescott, M. & Devenish, R. J. (2012) The intriguing life of autophagosomes, *Int J Mol Sci.* **13**, 3618–3635.
232. Kimura, S., Noda, T. & Yoshimori, T. (2008) Dynein-dependent movement of autophagosomes mediates efficient encounters with lysosomes, *Cell Struct Funct.* **33**, 109–22.
233. Li, D., Shi, J. J., Mao, C. J., Liu, S., Wang, J. D., Chen, J., Wang, F., Yang, Y. P., Hu, W. D., Hu, L. F. & Liu, C. F. (2013) Alteration of dynein function affects α-synuclein degradation via the autophagosome-lysosome pathway, *Int J Mol Sci.* **14**, 24242–54.
234. Ripon, M. K. H., Lee, H., Dash, R., Choi, H. J., Oktaviani, D. F., Moon, I. S. & Haque, M. N. (2020) N-acetyl-D-glucosamine kinase binds dynein light chain roadblock 1 and promotes protein aggregate clearance, *Cell Death Dis.* **11**, 619.
235. Myeku, N. & Figueiredo-Pereira, M. E. (2011) Dynamics of the degradation of ubiquitinated proteins by proteasomes and autophagy: association with sequestosome 1/p62, *J Biol Chem.* **286**, 22426–40.
236. Kabeya, Y., Mizushima, N., Ueno, T., Yamamoto, A., Kirisako, T., Noda, T., Kominami, E., Ohsumi, Y. & Yoshimori, T. (2000) LC3, a mammalian homologue of yeast Apg8p, is localized in autophagosome membranes after processing, *Embo j.* **19**, 5720–8.
237. Ichimura, Y., Kirisako, T., Takao, T., Satomi, Y., Shimonishi, Y., Ishihara, N., Mizushima, N., Tanida, I., Kominami, E., Ohsumi, M., Noda, T. & Ohsumi, Y. (2000) A ubiquitin-like system mediates protein lipidation, *Nature.* **408**, 488–92.
238. Mizushima, N., Yoshimori, T. & Levine, B. (2010) Methods in mammalian autophagy research, *Cell.* **140**, 313–26.
239. Seaman, M. N. (2012) The retromer complex - endosomal protein recycling and beyond, *J Cell Sci.* **125**, 4693–702.
240. Gambardella, S., Biagioni, F., Ferese, R., Busceti, C. L., Frati, A., Novelli, G., Ruggieri, S. & Fornai, F. (2016) Vacuolar Protein Sorting Genes in Parkinson's Disease: A Re-appraisal of Mutations Detection Rate and Neurobiology of Disease, *Front Neurosci.* **10**, 532.
241. Shannon, B., Soto-Ortolaza, A., Rayaprolu, S., Cannon, H. D., Labbé, C., Benitez, B. A., Choi, J., Lynch, T., Boczarska-Jedynak, M., Opala, G., Krygowska-Wajs, A., Barcikowska, M., Van Gerpen, J. A., Uitti, R. J., Springer, W., Cruchaga, C., Wszolek, Z. K. & Ross, O. A. (2014) Genetic variation of the retromer subunits VPS26A/B-VPS29 in Parkinson's disease, *Neurobiol Aging.* **35**, 1958.e1–2.

242. Bloom, G. S. (2014) Amyloid-β and tau: the trigger and bullet in Alzheimer disease pathogenesis, *JAMA Neurol.* **71**, 505–8.
243. Chae, C. W., Choi, G. E., Jung, Y. H., Lim, J. R., Cho, J. H., Yoon, J. H. & Han, H. J. (2022) High glucose-mediated VPS26a down-regulation dysregulates neuronal amyloid precursor protein processing and tau phosphorylation, *Br J Pharmacol.* **179**, 3934–3950.
244. Daly, J. L., Danson, C. M., Lewis, P. A., Zhao, L., Riccardo, S., Di Filippo, L., Cacchiarelli, D., Lee, D., Cross, S. J., Heesom, K. J., Xiong, W. C., Ballabio, A., Edgar, J. R. & Cullen, P. J. (2023) Multi-omic approach characterises the neuroprotective role of retromer in regulating lysosomal health, *Nat Commun.* **14**, 3086.
245. Xie, Y. X., Naseri, N. N., Fels, J., Kharel, P., Na, Y., Lane, D., Burré, J. & Sharma, M. (2022) Lysosomal exocytosis releases pathogenic α-synuclein species from neurons in synucleinopathy models, *Nat Commun.* **13**, 4918.
246. Bennett, M. C., Bishop, J. F., Leng, Y., Chock, P. B., Chase, T. N. & Mouradian, M. M. (1999) Degradation of alpha-synuclein by proteasome, *J Biol Chem.* **274**, 33855–8.
247. Gomes, A. V. (2013) Genetics of proteasome diseases, *Scientifica (Cairo).* **2013**, 637629.
248. Abi Habib, J., Lesenfants, J., Vigneron, N. & Van den Eynde, B. J. (2022) Functional Differences between Proteasome Subtypes, *Cells.* **11**.
249. Baumeister, W., Walz, J., Zühl, F. & Seemüller, E. (1998) The proteasome: paradigm of a self-compartmentalizing protease, *Cell.* **92**, 367–80.
250. Groll, M., Ditzel, L., Löwe, J., Stock, D., Bochtler, M., Bartunik, H. D. & Huber, R. (1997) Structure of 20S proteasome from yeast at 2.4 A resolution, *Nature.* **386**, 463–71.
251. Dick, T. P., Nussbaum, A. K., Deeg, M., Heinemeyer, W., Groll, M., Schirle, M., Keilholz, W., Stevanović, S., Wolf, D. H., Huber, R., Rammensee, H. G. & Schild, H. (1998) Contribution of proteasomal beta-subunits to the cleavage of peptide substrates analyzed with yeast mutants, *J Biol Chem.* **273**, 25637–46.
252. Vigneron, N., Abi Habib, J. & Van den Eynde, B. J. (2015) The capture proteasome assay: A method to measure proteasome activity in vitro, *Anal Biochem.* **482**, 7–15.
253. McNaught, K. S. & Jenner, P. (2001) Proteasomal function is impaired in substantia nigra in Parkinson's disease, *Neurosci Lett.* **297**, 191–4.
254. Bi, M., Du, X., Jiao, Q., Chen, X. & Jiang, H. (2021) Expanding the role of proteasome homeostasis in Parkinson's disease: beyond protein breakdown, *Cell Death Dis.* **12**, 154.
255. Galka, D., Ali, T. T., Bast, A., Niederleithinger, M., Gerhardt, E., Motosugi, R., Sakata, E., Knop, M., Outeiro, T. F., Popova, B. & Braus, G. H. (2024) Inhibition of 26S proteasome activity by α-synuclein is mediated by the proteasomal chaperone Rpn14/PAAF1, *Aging Cell.* **23**, e14128.
256. McKinnon, C., De Snoo, M. L., Gondard, E., Neudorfer, C., Chau, H., Ngana, S. G., O'Hara, D. M., Brotchie, J. M., Koprich, J. B., Lozano, A. M., Kalia, L. V. & Kalia, S. K. (2020) Early-onset impairment of the ubiquitin-proteasome system in dopaminergic neurons caused by α-synuclein, *Acta Neuropathol Commun.* **8**, 17.
257. Popova, B., Galka, D., Häffner, N., Wang, D., Schmitt, K., Valerius, O., Knop, M. & Braus, G. H. (2021) α-Synuclein Decreases the Abundance of Proteasome Subunits and Alters Ubiquitin Conjugates in Yeast, *Cells.* **10**.
258. Suzuki, G., Imura, S., Hosokawa, M., Katsumata, R., Nonaka, T., Hisanaga, S. I., Saeki, Y. & Hasegawa, M. (2020) α-synuclein strains that cause distinct pathologies differentially inhibit proteasome, *Elife.* **9**.
259. Zondler, L., Kostka, M., Garidel, P., Heinzelmann, U., Hengerer, B., Mayer, B., Weishaupt, J. H., Gillardon, F. & Danzer, K. M. (2017) Proteasome impairment by α-synuclein, *PLoS One.* **12**, e0184040.
260. Thibaudeau, T. A., Anderson, R. T. & Smith, D. M. (2018) A common mechanism of proteasome impairment by neurodegenerative disease-associated oligomers, *Nat Commun.* **9**, 1097.
261. Kalluri, R. (2024) The biology and function of extracellular vesicles in immune response and immunity, *Immunity.* **57**, 1752–1768.
262. Hurley, J. H. & Emr, S. D. (2006) The ESCRT complexes: structure and mechanism of a membrane-trafficking network, *Annu Rev Biophys Biomol Struct.* **35**, 277–98.

263. Zhan, Z., Ye, M. & Jin, X. (2023) The roles of FLOT1 in human diseases (Review), *Mol Med Rep.* **28**.
264. Andreu, Z. & Yáñez-Mó, M. (2014) Tetraspanins in extracellular vesicle formation and function, *Front Immunol.* **5**, 442.
265. Diaz-Garrido, N., Cordero, C., Olivo-Martinez, Y., Badia, J. & Baldomà, L. (2021) Cell-to-Cell Communication by Host-Released Extracellular Vesicles in the Gut: Implications in Health and Disease, *Int J Mol Sci.* **22**.
266. Mallegol, J., Van Niel, G., Lebreton, C., Lepelletier, Y., Candalh, C., Dugave, C., Heath, J. K., Raposo, G., Cerf-Bensussan, N. & Heyman, M. (2007) T84-intestinal epithelial exosomes bear MHC class II/peptide complexes potentiating antigen presentation by dendritic cells, *Gastroenterology.* **132**, 1866–76.
267. Lin, X. P., Almqvist, N. & Telemo, E. (2005) Human small intestinal epithelial cells constitutively express the key elements for antigen processing and the production of exosomes, *Blood Cells Mol Dis.* **35**, 122–8.
268. Van Niel, G., Mallegol, J., Bevilacqua, C., Candalh, C., Brugière, S., Tomaskovic-Crook, E., Heath, J. K., Cerf-Bensussan, N. & Heyman, M. (2003) Intestinal epithelial exosomes carry MHC class II/peptides able to inform the immune system in mice, *Gut.* **52**, 1690–7.
269. van Niel, G., Raposo, G., Candalh, C., Boussac, M., Hershberg, R., Cerf-Bensussan, N. & Heyman, M. (2001) Intestinal epithelial cells secrete exosome-like vesicles, *Gastroenterology.* **121**, 337–49.
270. Kropshofer, H., Spindeldreher, S., Röhn, T. A., Platania, N., Grygar, C., Daniel, N., Wölpl, A., Langen, H., Horejsi, V. & Vogt, A. B. (2002) Tetraspan microdomains distinct from lipid rafts enrich select peptide-MHC class II complexes, *Nat Immunol.* **3**, 61–8.
271. Mittelbrunn, M., Yáñez-Mó, M., Sancho, D., Ursa, A. & Sánchez-Madrid, F. (2002) Cutting edge: dynamic redistribution of tetraspanin CD81 at the central zone of the immune synapse in both T lymphocytes and APC, *J Immunol.* **169**, 6691–5.
272. Witherden, D. A., Boismenu, R. & Havran, W. L. (2000) CD81 and CD28 costimulate T cells through distinct pathways, *J Immunol.* **165**, 1902–9.
273. Wright, M. D., Moseley, G. W. & van Spriel, A. B. (2004) Tetraspanin microdomains in immune cell signalling and malignant disease, *Tissue Antigens.* **64**, 533–42.
274. Chen, X., Song, C. H., Feng, B. S., Li, T. L., Li, P., Zheng, P. Y., Chen, X. M., Xing, Z. & Yang, P. C. (2011) Intestinal epithelial cell-derived integrin αβ6 plays an important role in the induction of regulatory T cells and inhibits an antigen-specific Th2 response, *J Leukoc Biol.* **90**, 751–9.
275. Jiang, L., Shen, Y., Guo, D., Yang, D., Liu, J., Fei, X., Yang, Y., Zhang, B., Lin, Z., Yang, F., Wang, X., Wang, K., Wang, J. & Cai, Z. (2016) EpCAM-dependent extracellular vesicles from intestinal epithelial cells maintain intestinal tract immune balance, *Nat Commun.* **7**, 13045.
276. Kojima, M., Costantini, T. W., Eliceiri, B. P., Chan, T. W., Baird, A. & Coimbra, R. (2018) Gut epithelial cell-derived exosomes trigger posttrauma immune dysfunction, *J Trauma Acute Care Surg.* **84**, 257–264.
277. Wong, W. Y., Lee, M. M., Chan, B. D., Kam, R. K., Zhang, G., Lu, A. P. & Tai, W. C. (2016) Proteomic profiling of dextran sulfate sodium induced acute ulcerative colitis mice serum exosomes and their immunomodulatory impact on macrophages, *Proteomics.* **16**, 1131–45.
278. Dutta, S., Hornung, S., Kruayatidee, A., Maina, K. N., Del Rosario, I., Paul, K. C., Wong, D. Y., Duarte Folle, A., Markovic, D., Palma, J. A., Serrano, G. E., Adler, C. H., Perlman, S. L., Poon, W. W., Kang, U. J., Alcalay, R. N., Sklerov, M., Gylys, K. H., Kaufmann, H., Fogel, B. L., Bronstein, J. M., Ritz, B. & Bitan, G. (2021) α-Synuclein in blood exosomes immunoprecipitated using neuronal and oligodendroglial markers distinguishes Parkinson's disease from multiple system atrophy, *Acta Neuropathol.* **142**, 495–511.
279. Yan, S., Jiang, C., Janzen, A., Barber, T. R., Seger, A., Sommerauer, M., Davis, J. J., Marek, K., Hu, M. T., Oertel, W. H. & Tofaris, G. K. (2024) Neuronally Derived Extracellular Vesicle α-Synuclein as a Serum Biomarker for Individuals at Risk of Developing Parkinson Disease, *JAMA Neurol.* **81**, 59–68.
280. Abe, T., Kuwahara, T., Suenaga, S., Sakurai, M., Takatori, S. & Iwatsubo, T. (2024) Lysosomal stress drives the release of pathogenic α-synuclein from macrophage lineage cells via the LRRK2-Rab10 pathway, *iScience.* **27**, 108893.

281. Danzer, K. M., Kranich, L. R., Ruf, W. P., Cagsal-Getkin, O., Winslow, A. R., Zhu, L., Vanderburg, C. R. & McLean, P. J. (2012) Exosomal cell-to-cell transmission of alpha synuclein oligomers, *Mol Neurodegener.* **7**, 42.
282. Fussi, N., Höllerhage, M., Chakroun, T., Nykänen, N. P., Rösler, T. W., Koeglsperger, T., Wurst, W., Behrends, C. & Höglinger, G. U. (2018) Exosomal secretion of α-synuclein as protective mechanism after upstream blockage of macroautophagy, *Cell Death Dis.* **9**, 757.
283. Guo, M., Wang, J., Zhao, Y., Feng, Y., Han, S., Dong, Q., Cui, M. & Tieu, K. (2020) Microglial exosomes facilitate α-synuclein transmission in Parkinson's disease, *Brain.* **143**, 1476–1497.
284. Bayati, A. & McPherson, P. S. (2024) Alpha-synuclein, autophagy-lysosomal pathway, and Lewy bodies: Mutations, propagation, aggregation, and the formation of inclusions, *J Biol Chem.* **300**, 107742.
285. Dieriks, B. V., Park, T. I., Fourie, C., Faull, R. L., Dragunow, M. & Curtis, M. A. (2017) α-synuclein transfer through tunneling nanotubes occurs in SH-SY5Y cells and primary brain pericytes from Parkinson's disease patients, *Sci Rep.* **7**, 42984.
286. Minakaki, G., Menges, S., Kittel, A., Emmanouilidou, E., Schaeffner, I., Barkovits, K., Bergmann, A., Rockenstein, E., Adame, A., Marxreiter, F., Mollenhauer, B., Galasko, D., Buzás, E. I., Schlötzer-Schrehardt, U., Marcus, K., Xiang, W., Lie, D. C., Vekrellis, K., Masliah, E., Winkler, J. & Klucken, J. (2018) Autophagy inhibition promotes SNCA/alpha-synuclein release and transfer via extracellular vesicles with a hybrid autophagosome-exosome-like phenotype, *Autophagy.* **14**, 98–119.
287. Bayati, A., Banks, E., Han, C., Luo, W., Reintsch, W. E., Zorca, C. E., Shlaifer, I., Del Cid Pellitero, E., Vanderperre, B., McBride, H. M., Fon, E. A., Durcan, T. M. & McPherson, P. S. (2022) Rapid macropinocytic transfer of α-synuclein to lysosomes, *Cell Rep.* **40**, 111102.
288. Datta, A., Kim, H., Lal, M., McGee, L., Johnson, A., Moustafa, A. A., Jones, J. C., Mondal, D., Ferrer, M. & Abdel-Mageed, A. B. (2017) Manumycin A suppresses exosome biogenesis and secretion via targeted inhibition of Ras/Raf/ERK1/2 signaling and hnRNP H1 in castration-resistant prostate cancer cells, *Cancer Lett.* **408**, 73–81.
289. Trajkovic, K., Hsu, C., Chiantia, S., Rajendran, L., Wenzel, D., Wieland, F., Schwille, P., Brügger, B. & Simons, M. (2008) Ceramide triggers budding of exosome vesicles into multivesicular endosomes, *Science.* **319**, 1244–7.
290. Wu, S. & Schekman, R. W. (2024) Intercellular transmission of alpha-synuclein, *Front Mol Neurosci.* **17**, 1470171.
291. Miranda, I., Souza, A., Sousa, P., Ribeiro, J., Castanheira, E. M. S., Lima, R. & Minas, G. (2021) Properties and Applications of PDMS for Biomedical Engineering: A Review, *J Funct Biomater.* **13**.
292. Manz, A., Graber, N. & Widmer, H. M. (1990) Miniaturized total chemical analysis systems: A novel concept for chemical sensing, *Sensors and Actuators B: Chemical.* **1**, 244–248.
293. Kim, H., Girardi, G., Pickle, A., Kim, T. S. & Seker, E. (2025) Microfluidic tools to model, monitor, and modulate the gut-brain axis, *Biomicrofluidics.* **19**, 021301.
294. Kim, H. J., Li, H., Collins, J. J. & Ingber, D. E. (2016) Contributions of microbiome and mechanical deformation to intestinal bacterial overgrowth and inflammation in a human gut-on-a-chip, *Proc Natl Acad Sci U S A.* **113**, E7–15.
295. Kasendra, M., Tovaglieri, A., Sontheimer-Phelps, A., Jalili-Firoozinezhad, S., Bein, A., Chalkiadaki, A., Scholl, W., Zhang, C., Rickner, H., Richmond, C. A., Li, H., Breault, D. T. & Ingber, D. E. (2018) Development of a primary human Small Intestine-on-a-Chip using biopsy-derived organoids, *Sci Rep.* **8**, 2871.
296. De Gregorio, V., Sgambato, C., Urciuolo, F., Vecchione, R., Netti, P. A. & Imparato, G. (2022) Immunoresponsive microbiota-gut-on-chip reproduces barrier dysfunction, stromal reshaping and probiotics translocation under inflammation, *Biomaterials.* **286**, 121573.
297. Shah, P., Fritz, J. V., Glaab, E., Desai, M. S., Greenhalgh, K., Frachet, A., Niegowska, M., Estes, M., Jäger, C., Seguin-Devaux, C., Zenhausern, F. & Wilmes, P. (2016) A microfluidics-based in vitro model of the gastrointestinal human-microbe interface, *Nat Commun.* **7**, 11535.
298. Sedrani, C., Gomez-Giro, G., Grandmougin, L., Schwamborn, J. C. & Wilmes, P. (2023) A Gut-on-a-Chip Model to Study the Gut Microbiome-Nervous System Axis, *J Vis Exp*.

299. de Hoyos-Vega, J. M., Yu, X., Gonzalez-Suarez, A. M., Chen, S., Mercado-Perez, A., Krueger, E., Hernandez, J., Fedyshyn, Y., Druliner, B. R., Linden, D. R., Beyder, A. & Revzin, A. (2023) Modeling gut neuro-epithelial connections in a novel microfluidic device, *Microsyst Nanoeng.* **9**, 144.
300. Crespo, M., Vilar, E., Tsai, S. Y., Chang, K., Amin, S., Srinivasan, T., Zhang, T., Pipalia, N. H., Chen, H. J., Witherspoon, M., Gordillo, M., Xiang, J. Z., Maxfield, F. R., Lipkin, S., Evans, T. & Chen, S. (2017) Colonic organoids derived from human induced pluripotent stem cells for modeling colorectal cancer and drug testing, *Nat Med.* **23**, 878–884.
301. Reinhardt, P., Glatza, M., Hemmer, K., Tsytsyura, Y., Thiel, C. S., Höing, S., Moritz, S., Parga, J. A., Wagner, L., Bruder, J. M., Wu, G., Schmid, B., Röpke, A., Klingauf, J., Schwamborn, J. C., Gasser, T., Schöler, H. R. & Sterneckert, J. (2013) Derivation and expansion using only small molecules of human neural progenitors for neurodegenerative disease modeling, *PLoS One.* **8**, e59252.
302. Sivaranjani, M., Hansen, E. G., Perera, S. R., Flores, P. A., Tükel, Ç. & White, A. P. (2022) Purification of the Bacterial Amyloid "Curli" from Salmonella enterica Serovar Typhimurium and Detection of Curli from Infected Host Tissues, *Bio Protoc.* **12**, e4419.
303. Singh, V., Castellana-Cruz, M., Cremades, N. & Volpicelli-Daley, L. (2020) Generation and Sonication of α-synuclein Fibrils, *Protocolsio*.
304. Pérez, M. J., Ivanyuk, D., Panagiotakopoulou, V., Di Napoli, G., Kalb, S., Brunetti, D., Al-Shaana, R., Kaeser, S. A., Fraschka, S. A., Jucker, M., Zeviani, M., Viscomi, C. & Deleidi, M. (2021) Loss of function of the mitochondrial peptidase PITRM1 induces proteotoxic stress and Alzheimer's disease-like pathology in human cerebral organoids, *Mol Psychiatry.* **26**, 5733–5750.
305. Haenseler, W., Sansom, S. N., Buchrieser, J., Newey, S. E., Moore, C. S., Nicholls, F. J., Chintawar, S., Schnell, C., Antel, J. P., Allen, N. D., Cader, M. Z., Wade-Martins, R., James, W. S. & Cowley, S. A. (2017) A Highly Efficient Human Pluripotent Stem Cell Microglia Model Displays a Neuronal-Co-culture-Specific Expression Profile and Inflammatory Response, *Stem Cell Reports.* **8**, 1727–1742.
306. Théry, C., Amigorena, S., Raposo, G. & Clayton, A. (2006) Isolation and characterization of exosomes from cell culture supernatants and biological fluids, *Curr Protoc Cell Biol.* **Chapter 3**, Unit 3.22.
307. Eapen, V. V., Swarup, S., Hoyer, M. J., Paulo, J. A. & Harper, J. W. (2021) Quantitative proteomics reveals the selectivity of ubiquitin-binding autophagy receptors in the turnover of damaged lysosomes by lysophagy, *Elife.* **10**.
308. Stojkovska, I. & Mazzulli, J. R. (2021) Detection of pathological alpha-synuclein aggregates in human iPSC-derived neurons and tissue, *STAR Protoc.* **2**, 100372.
309. Mayberry, C. L., Wilson, J. J., Sison, B. & Chang, C. H. (2024) Protocol to assess bioenergetics and mitochondrial fuel usage in murine autoreactive immunocytes using the Seahorse Extracellular Flux Analyzer, *STAR Protoc.* **5**, 102971.
310. Hughes, C. S., Foehr, S., Garfield, D. A., Furlong, E. E., Steinmetz, L. M. & Krijgsveld, J. (2014) Ultrasensitive proteome analysis using paramagnetic bead technology, *Mol Syst Biol.* **10**, 757.
311. Thompson, A., Wölmer, N., Koncarevic, S., Selzer, S., Böhm, G., Legner, H., Schmid, P., Kienle, S., Penning, P., Höhle, C., Berfelde, A., Martinez-Pinna, R., Farztdinov, V., Jung, S., Kuhn, K. & Pike, I. (2019) TMTpro: Design, Synthesis, and Initial Evaluation of a Proline-Based Isobaric 16-Plex Tandem Mass Tag Reagent Set, *Anal Chem.* **91**, 15941–15950.
312. Reichel, M., Liao, Y., Rettel, M., Ragan, C., Evers, M., Alleaume, A. M., Horos, R., Hentze, M. W., Preiss, T. & Millar, A. A. (2016) In Planta Determination of the mRNA-Binding Proteome of Arabidopsis Etiolated Seedlings, *Plant Cell.* **28**, 2435–2452.
313. Huber, W., von Heydebreck, A., Sültmann, H., Poustka, A. & Vingron, M. (2002) Variance stabilization applied to microarray data calibration and to the quantification of differential expression, *Bioinformatics.* **18 Suppl 1**, S96–104.
314. Gatto, L. & Lilley, K. S. (2012) MSnbase-an R/Bioconductor package for isobaric tagged mass spectrometry data visualization, processing and quantitation, *Bioinformatics.* **28**, 288–9.

315. Akter, F., Bonini, S., Ponnaiyan, S., Kögler-Mohrbacher, B., Bleibaum, F., Damme, M., Renard, B. Y. & Winter, D. (2023) Multi-Cell Line Analysis of Lysosomal Proteomes Reveals Unique Features and Novel Lysosomal Proteins, *Mol Cell Proteomics.* **22**, 100509.
316. Perez-Riverol, Y., Bandla, C., Kundu, D. J., Kamatchinathan, S., Bai, J., Hewapathirana, S., John, N. S., Prakash, A., Walzer, M., Wang, S. & Vizcaíno, J. A. (2025) The PRIDE database at 20 years: 2025 update, *Nucleic Acids Res.* **53**, D543–d553.
317. Wang, X., Zhou, Y., Ren, J. J., Hammer, N. D. & Chapman, M. R. (2010) Gatekeeper residues in the major curlin subunit modulate bacterial amyloid fiber biogenesis, *Proc Natl Acad Sci U S A.* **107**, 163–8.
318. Al-Momani, H., Mashal, S. & AlGhawrie, H. (2025) Investigation of the effect of dimethyl sulfoxide on growth and biofilm formation of Pseudomonas aeruginosa, *Iran J Microbiol.* **17**, 942–953.
319. Summer, K., Browne, J., Hollanders, M. & Benkendorff, K. (2022) Out of control: The need for standardised solvent approaches and data reporting in antibiofilm assays incorporating dimethyl-sulfoxide (DMSO), *Biofilm.* **4**, 100081.
320. Sinagoga, K. L., McCauley, H. A., Múnera, J. O., Reynolds, N. A., Enriquez, J. R., Watson, C., Yang, H. C., Helmrath, M. A. & Wells, J. M. (2018) Deriving functional human enteroendocrine cells from pluripotent stem cells, *Development.* **145**.
321. Zeve, D., Stas, E., de Sousa Casal, J., Mannam, P., Qi, W., Yin, X., Dubois, S., Shah, M. S., Syverson, E. P., Hafner, S., Karp, J. M., Carlone, D. L., Ordovas-Montanes, J. & Breault, D. T. (2022) Robust differentiation of human enteroendocrine cells from intestinal stem cells, *Nat Commun.* **13**, 261.
322. Singh, J., Kaade, E., Muntel, J., Bruderer, R., Reiter, L., Thelen, M. & Winter, D. (2020) Systematic Comparison of Strategies for the Enrichment of Lysosomes by Data Independent Acquisition, *J Proteome Res.* **19**, 371–381.
323. Jackson, R. J., Hyman, B. T. & Serrano-Pozo, A. (2024) Multifaceted roles of APOE in Alzheimer disease, *Nat Rev Neurol.* **20**, 457–474.
324. O'Brien, R. J. & Wong, P. C. (2011) Amyloid precursor protein processing and Alzheimer's disease, *Annu Rev Neurosci.* **34**, 185–204.
325. Park, W. H. (2016) Exogenous H2O2 induces growth inhibition and cell death of human pulmonary artery smooth muscle cells via glutathione depletion, *Mol Med Rep.* **14**, 936–42.
326. Miyoshi, H. (2005) Inhibitors of Mitochondrial Respiratory Enzymes, *Journal of Pesticide Science.* **30**, 120–121.
327. Hu, S., Tan, J., Qin, L., Lv, L., Yan, W., Zhang, H., Tang, B. & Wang, C. (2021) Molecular chaperones and Parkinson's disease, *Neurobiol Dis.* **160**, 105527.
328. Qi, A., Wang, K., Li, Y., Hu, R., Hu, G., Li, Y., Shi, G. & Huang, M. (2024) The degradation of α--synuclein is limited by dynein to drive the AALP pathway through HDAC6 upon paraquat exposure, *Ecotoxicol Environ Saf.* **283**, 116841.
329. Ostrowski, M., Carmo, N. B., Krumeich, S., Fanget, I., Raposo, G., Savina, A., Moita, C. F., Schauer, K., Hume, A. N., Freitas, R. P., Goud, B., Benaroch, P., Hacohen, N., Fukuda, M., Desnos, C., Seabra, M. C., Darchen, F., Amigorena, S., Moita, L. F. & Thery, C. (2010) Rab27a and Rab27b control different steps of the exosome secretion pathway, *Nat Cell Biol.* **12**, 19–30; sup pp 1–13.
330. Yeung, L., Hickey, M. J. & Wright, M. D. (2018) The Many and Varied Roles of Tetraspanins in Immune Cell Recruitment and Migration, *Front Immunol.* **9**, 1644.
331. Park, S. C., Moon, J. C., Shin, S. Y., Son, H., Jung, Y. J., Kim, N. H., Kim, Y. M., Jang, M. K. & Lee, J. R. (2016) Functional characterization of alpha-synuclein protein with antimicrobial activity, *Biochem Biophys Res Commun.* **478**, 924–8.
332. Vogiatzi, T., Xilouri, M., Vekrellis, K. & Stefanis, L. (2008) Wild type alpha-synuclein is degraded by chaperone-mediated autophagy and macroautophagy in neuronal cells, *J Biol Chem.* **283**, 23542–56.
333. Dermentzaki, G., Dimitriou, E., Xilouri, M., Michelakakis, H. & Stefanis, L. (2013) Loss of β-glucocerebrosidase activity does not affect alpha-synuclein levels or lysosomal function in neuronal cells, *PLoS One.* **8**, e60674.

334. Coleman, W. G., Jr., Goebel, P. J. & Leive, L. (1977) Genetic analysis of Escherichia coli O111:B4, a strain of medical and biochemical interest, *J Bacteriol.* **130**, 656–60.
335. Viljanen, M. K., Peltola, T., Junnila, S. Y., Olkkonen, L., Järvinen, H., Kuistila, M. & Huovinen, P. (1990) Outbreak of diarrhoea due to Escherichia coli O111:B4 in schoolchildren and adults: association of Vi antigen-like reactivity, *Lancet.* **336**, 831–4.
336. Balsamo, J. M., Yan, Y., Thai, D., Cologna, S. M. & Bess, E. N. (2025) Multiomic Analysis Reveals Molecular Pathways Associated with Intestinal Aggregation of α-Synuclein, *bioRxiv*.
337. Leclerc, M., Bedu-Ferrari, C., Etienne-Mesmin, L., Mariadassou, M., Lebreuilly, L., Tran, S. L., Brazeau, L., Mayeur, C., Delmas, J., Rué, O., Denis, S., Blanquet-Diot, S. & Ramarao, N. (2021) Nitric Oxide Impacts Human Gut Microbiota Diversity and Functionalities, *mSystems.* **6**, e0055821.
338. Otzen, D. E., Gamon, L. F., Hägglund, P., Nielsen, J., Pedersen, J. N., Nybo, T., Nowak, J. S., Amstrup, S. K., Pirhaghi, M. & Davies, M. J. (2026) Nitrated products formed on α-synuclein are preferentially incorporated into oligomers but excluded from fibrils: A mechanism for accumulation of neurotoxic species, *Biochim Biophys Acta Proteins Proteom.* **1874**, 141118.
339. Pellegrini, C., D'Antongiovanni, V., Miraglia, F., Rota, L., Benvenuti, L., Di Salvo, C., Testa, G., Capsoni, S., Carta, G., Antonioli, L., Cattaneo, A., Blandizzi, C., Colla, E. & Fornai, M. (2023) Author Correction: Enteric α-synuclein impairs intestinal epithelial barrier through caspase-1-inflammasome signaling in Parkinson's disease before brain pathology, *NPJ Parkinsons Dis.* **9**, 83.
340. Sherwood, R. I., Maehr, R., Mazzoni, E. O. & Melton, D. A. (2011) Wnt signaling specifies and patterns intestinal endoderm, *Mech Dev.* **128**, 387–400.
341. Fedele, A. O. & Proud, C. G. (2020) Chloroquine and bafilomycin A mimic lysosomal storage disorders and impair mTORC1 signalling, *Biosci Rep.* **40**.
342. Steen, M., Kirchberger, T. & Guse, A. H. (2007) NAADP mobilizes calcium from the endoplasmic reticular Ca(2+) store in T-lymphocytes, *J Biol Chem.* **282**, 18864–71.
343. Min, D. H., Kim, D., Hong, S. T., Kim, J., Kim, M. J., Kwon, S. H., Kim, A. & Lee, J. Y. (2025) Bafilomycin A1 induces colon cancer cell death through impairment of the endolysosome system dependent on iron, *Sci Rep.* **15**, 5148.
344. Bae, E. J., Choi, M., Kim, J. T., Kim, D. K., Jung, M. K., Kim, C., Kim, T. K., Lee, J. S., Jung, B. C., Shin, S. J., Rhee, K. H. & Lee, S. J. (2022) TNF-α promotes α-synuclein propagation through stimulation of senescence-associated lysosomal exocytosis, *Exp Mol Med.* **54**, 788–800.
345. Jones-Tabah, J., He, K., Senkevich, K., Karpilovsky, N., Deyab, G., Cousineau, Y., Nikanorova, D., Goldsmith, T., Del Cid Pellitero, E., Chen, C. X., Luo, W., You, Z., Abdian, N., Pietrantonio, I., Goiran, T., Ahmad, J., Ruskey, J. A., Asayesh, F., Spiegelman, D., Waters, C., Monchi, O., Dauvilliers, Y., Dupré, N., Miliukhina, I., Timofeeva, A., Emelyanov, A., Pchelina, S., Greenbaum, L., Hassin-Baer, S., Alcalay, R. N., Milnerwood, A., Durcan, T. M., Gan-Or, Z. & Fon, E. A. (2023) The Parkinson's disease risk gene cathepsin B promotes fibrillar alpha-synuclein clearance, lysosomal function and glucocerebrosidase activity in dopaminergic neurons, *bioRxiv*.
346. Lin, L., Wu, Z., Luo, H. & Huang, Y. (2024) Cathepsin-mediated regulation of alpha-synuclein in Parkinson's disease: a Mendelian randomization study, *Front Aging Neurosci.* **16**, 1394807.
347. Endo, Y., Furuta, A. & Nishino, I. (2015) Danon disease: a phenotypic expression of LAMP-2 deficiency, *Acta Neuropathol.* **129**, 391–8.
348. Qiao, L., Hu, J., Qiu, X., Wang, C., Peng, J., Zhang, C., Zhang, M., Lu, H. & Chen, W. (2023) LAMP2A, LAMP2B and LAMP2C: similar structures, divergent roles, *Autophagy.* **19**, 2837–2852.
349. Fujiwara, Y., Furuta, A., Kikuchi, H., Aizawa, S., Hatanaka, Y., Konya, C., Uchida, K., Yoshimura, A., Tamai, Y., Wada, K. & Kabuta, T. (2013) Discovery of a novel type of autophagy targeting RNA, *Autophagy.* **9**, 403–9.
350. Fujiwara, Y., Kikuchi, H., Aizawa, S., Furuta, A., Hatanaka, Y., Konya, C., Uchida, K., Wada, K. & Kabuta, T. (2013) Direct uptake and degradation of DNA by lysosomes, *Autophagy.* **9**, 1167–71.

351. Pérez, L., McLetchie, S., Gardiner, G. J., Deffit, S. N., Zhou, D. & Blum, J. S. (2016) LAMP-2C Inhibits MHC Class II Presentation of Cytoplasmic Antigens by Disrupting Chaperone-Mediated Autophagy, *J Immunol.* **196**, 2457–65.
352. Fernández-Calvet, A., Matilla-Cuenca, L., Izco, M., Navarro, S., Serrano, M., Ventura, S., Blesa, J., Herráiz, M., Alkorta-Aranburu, G., Galera, S., Ruiz de Los Mozos, I., Mansego, M. L., Toledo-Arana, A., Alvarez-Erviti, L. & Valle, J. (2024) Gut microbiota produces biofilm-associated amyloids with potential for neurodegeneration, *Nat Commun.* **15**, 4150.
353. Chu, Y., Morfini, G. A., Langhamer, L. B., He, Y., Brady, S. T. & Kordower, J. H. (2012) Alterations in axonal transport motor proteins in sporadic and experimental Parkinson's disease, *Brain.* **135**, 2058–73.
354. Wang, Y., Sun, Z., Du, S., Wei, H., Li, X., Li, X., Shen, J., Chen, X. & Cai, Z. (2022) The increase of α-synuclein and alterations of dynein in A53T transgenic and aging mouse, *J Clin Neurosci.* **96**, 154–162.
355. Zhou, L., Wang, Y., Liu, Y., Zhu, F., Gao, G., Li, C., Ai, P., Xu, J., Wang, J., Guo, L., Guan, Y., Lee, V. M., Chen, J., Zheng, J. & Wu, Q. (2025) Dynein-Dependent Endo-Lysosomal Degradation Drives Lewy Body Disorders Accompanied by Aβ Pathology, *Adv Sci (Weinh).* **12**, e14860.
356. Islam, M. A., Sharif, S. R., Lee, H., Seog, D. H. & Moon, I. S. (2015) N-acetyl-D-glucosamine kinase interacts with dynein light-chain roadblock type 1 at Golgi outposts in neuronal dendritic branch points, *Exp Mol Med.* **47**, e177.
357. Yang, X., Ma, Z., Lian, P., Wu, Y., Liu, K., Zhang, Z., Tang, Z., Xu, Y. & Cao, X. (2025) Disruption of axonal transport in Parkinson's disease: the role of pathological α-Syn and AMPK/p38 MAPK signaling, *NPJ Parkinsons Dis.* **11**, 114.
358. Bhoite, S. S., Han, Y., Ruotolo, B. T. & Chapman, M. R. (2022) Mechanistic insights into accelerated α-synuclein aggregation mediated by human microbiome-associated functional amyloids, *J Biol Chem.* **298**, 102088.
359. Ioghen, O. C., Gaina, G., Lambrescu, I., Manole, E., Pop, S., Niculescu, T. M., Mosoia, O., Ceafalan, L. C. & Popescu, B. O. (2024) Bacterial products initiation of alpha-synuclein pathology: an in vitro study, *Sci Rep.* **14**, 30306.
360. Ziaunys, M., Sulskis, D., Veiveris, D., Sakalauskas, A., Mikalauskaite, K. & Smirnovas, V. (2024) Diverse effects of fluorescent labels on alpha-synuclein condensate formation during liquid-liquid phase separation, *Int J Biol Macromol.* **283**, 137688.
361. de Bruïne, A. P., Dinjens, W. N., Zijlema, J. H., Lenders, M. H. & Bosman, F. T. (1992) Renewal of enterochromaffin cells in the rat caecum, *Anat Rec.* **233**, 75–82.
362. Wei, L., Singh, R., Ha, S. E., Martin, A. M., Jones, L. A., Jin, B., Jorgensen, B. G., Zogg, H., Chervo, T., Gottfried-Blackmore, A., Nguyen, L., Habtezion, A., Spencer, N. J., Keating, D. J., Sanders, K. M. & Ro, S. (2021) Serotonin Deficiency Is Associated With Delayed Gastric Emptying, *Gastroenterology.* **160**, 2451–2466.e19.
363. Sesotyosari, S. L., Kinoshita, M., Sunardi, M., Lihan, M., Orii, A., Abe, T., Kiyonari, H., Nakai, T., Uesaka, T., Kodama, Y. & Enomoto, H. (2025) The long-term survival of enteroendocrine cells depends on their subtype and is linked to peripheral sensory innervation, *Dev Growth Differ.* **67**, 205–214.
364. Kang, Y., Park, H., Choe, B. H. & Kang, B. (2022) The Role and Function of Mucins and Its Relationship to Inflammatory Bowel Disease, *Front Med (Lausanne).* **9**, 848344.
365. Pham, C. L., Leong, S. L., Ali, F. E., Kenche, V. B., Hill, A. F., Gras, S. L., Barnham, K. J. & Cappai, R. (2009) Dopamine and the dopamine oxidation product 5,6-dihydroxylindole promote distinct on-pathway and off-pathway aggregation of alpha-synuclein in a pH-dependent manner, *J Mol Biol.* **387**, 771–85.
366. Bisaglia, M., Mammi, S. & Bubacco, L. (2007) Kinetic and structural analysis of the early oxidation products of dopamine: analysis of the interactions with alpha-synuclein, *J Biol Chem.* **282**, 15597–605.
367. Glaser, C. B., Yamin, G., Uversky, V. N. & Fink, A. L. (2005) Methionine oxidation, alpha-synuclein and Parkinson's disease, *Biochim Biophys Acta.* **1703**, 157–69.
368. Stykel, M. G. & Ryan, S. D. (2022) Nitrosative stress in Parkinson's disease, *NPJ Parkinsons Dis.* **8**, 104.
369. Watts, C. (2004) The exogenous pathway for antigen presentation on major histocompatibility complex class II and CD1 molecules, *Nat Immunol.* **5**, 685–92.

370. Roche, P. A. & Furuta, K. (2015) The ins and outs of MHC class II-mediated antigen processing and presentation, *Nat Rev Immunol.* **15**, 203–16.
371. Eiz-Vesper, B. & Schmetzer, H. M. (2020) Antigen-Presenting Cells: Potential of Proven und New Players in Immune Therapies, *Transfus Med Hemother.* **47**, 429–431.
372. Koyama, M., Mukhopadhyay, P., Schuster, I. S., Henden, A. S., Hülsdünker, J., Varelias, A., Vetizou, M., Kuns, R. D., Robb, R. J., Zhang, P., Blazar, B. R., Thomas, R., Begun, J., Waddell, N., Trinchieri, G., Zeiser, R., Clouston, A. D., Degli-Esposti, M. A. & Hill, G. R. (2019) MHC Class II Antigen Presentation by the Intestinal Epithelium Initiates Graft-versus-Host Disease and Is Influenced by the Microbiota, *Immunity.* **51**, 885–898.e7.
373. Heuberger, C. E., Janney, A., Ilott, N., Bertocchi, A., Pott, S., Gu, Y., Pohin, M., Friedrich, M., Mann, E. H., Pearson, C., Powrie, F. M., Pott, J., Thornton, E. & Maloy, K. J. (2024) MHC class II antigen presentation by intestinal epithelial cells fine-tunes bacteria-reactive CD4 T-cell responses, *Mucosal Immunol.* **17**, 416–430.
374. Campeau, J. L., Salim, S. Y., Albert, E. J., Hotte, N. & Madsen, K. L. (2012) Intestinal epithelial cells modulate antigen-presenting cell responses to bacterial DNA, *Infect Immun.* **80**, 2632–44.
375. Heuberger, C., Pott, J. & Maloy, K. J. (2021) Why do intestinal epithelial cells express MHC class II?, *Immunology.* **162**, 357–367.
376. Harms, A. S., Cao, S., Rowse, A. L., Thome, A. D., Li, X., Mangieri, L. R., Cron, R. Q., Shacka, J. J., Raman, C. & Standaert, D. G. (2013) MHCII is required for α-synuclein-induced activation of microglia, CD4 T cell proliferation, and dopaminergic neurodegeneration, *J Neurosci.* **33**, 9592–600.
377. Matsushima, K., Yang, D. & Oppenheim, J. J. (2022) Interleukin-8: An evolving chemokine, *Cytokine.* **153**, 155828.
378. Mazzucchelli, L., Hauser, C., Zgraggen, K., Wagner, H., Hess, M., Laissue, J. A. & Mueller, C. (1994) Expression of interleukin-8 gene in inflammatory bowel disease is related to the histological grade of active inflammation, *Am J Pathol.* **144**, 997–1007.
379. Nakase, H., Sato, N., Mizuno, N. & Ikawa, Y. (2022) The influence of cytokines on the complex pathology of ulcerative colitis, *Autoimmun Rev.* **21**, 103017.
380. Maurer, M. & von Stebut, E. (2004) Macrophage inflammatory protein-1, *Int J Biochem Cell Biol.* **36**, 1882–6.
381. Pan, Z., Lin, H., Fu, Y., Zeng, F., Gu, F., Niu, G., Fang, J. & Gu, B. (2023) Identification of gene signatures associated with ulcerative colitis and the association with immune infiltrates in colon cancer, *Front Immunol.* **14**, 1086898.
382. Xie, F., Zhou, X., Fang, M., Li, H., Su, P., Tu, Y., Zhang, L. & Zhou, F. (2019) Extracellular Vesicles in Cancer Immune Microenvironment and Cancer Immunotherapy, *Adv Sci (Weinh).* **6**, 1901779.
383. Pyrillou, K., Burzynski, L. C. & Clarke, M. C. H. (2020) Alternative Pathways of IL-1 Activation, and Its Role in Health and Disease, *Front Immunol.* **11**, 613170.
384. Hunot, S., Dugas, N., Faucheux, B., Hartmann, A., Tardieu, M., Debré, P., Agid, Y., Dugas, B. & Hirsch, E. C. (1999) FcepsilonRII/CD23 is expressed in Parkinson's disease and induces, in vitro, production of nitric oxide and tumor necrosis factor-alpha in glial cells, *J Neurosci.* **19**, 3440–7.
385. Tanaka, T., Narazaki, M. & Kishimoto, T. (2014) IL-6 in inflammation, immunity, and disease, *Cold Spring Harb Perspect Biol.* **6**, a016295.
386. Tang, C., Chen, S., Qian, H. & Huang, W. (2012) Interleukin-23: as a drug target for autoimmune inflammatory diseases, *Immunology.* **135**, 112–24.
387. Oppong, G. O., Rapsinski, G. J., Newman, T. N., Nishimori, J. H., Biesecker, S. G. & Tükel, Ç. (2013) Epithelial cells augment barrier function via activation of the Toll-like receptor 2/phosphatidylinositol 3-kinase pathway upon recognition of Salmonella enterica serovar Typhimurium curli fibrils in the gut, *Infect Immun.* **81**, 478–86.
388. Huang, X., Venet, F., Wang, Y. L., Lepape, A., Yuan, Z., Chen, Y., Swan, R., Kherouf, H., Monneret, G., Chung, C. S. & Ayala, A. (2009) PD-1 expression by macrophages plays a pathologic role in altering

microbial clearance and the innate inflammatory response to sepsis, *Proc Natl Acad Sci U S A.* **106**, 6303–8.
389. Rőszer, T. (2015) Understanding the Mysterious M2 Macrophage through Activation Markers and Effector Mechanisms, *Mediators Inflamm.* **2015**, 816460.
390. Zhou, M., Aziz, M., Yen, H. T., Ma, G., Murao, A. & Wang, P. (2023) Extracellular CIRP dysregulates macrophage bacterial phagocytosis in sepsis, *Cell Mol Immunol.* **20**, 80–93.
391. Zubair, K., You, C., Kwon, G. & Kang, K. (2021) Two Faces of Macrophages: Training and Tolerance, *Biomedicines.* **9**.
392. Wallings, R. & Tansey, M. (2024) Investigating the effects of LRRK2 mutations in immune exhaustion in *PF-LAUNCH-1263938* Parkinson's Foundation.
393. Tansey, M. d. G., Wallings, R. L., Smeyne, R. J., Bradshaw, E. M. & Weindel, C. (2026) Investigating the Role of Immune Cell Exhaustion (ICE) and Biological Immune Aging (BIA) in PD Risk and PD Heterogeneity, *Michael J Fox*.
394. Jiang, S. S., Wang, Y. L., Xu, Q. H., Gu, L. Y., Kang, R. Q., Yang, W. Y., Zhang, B. R., Tian, J. & Pu, J. L. (2023) Cytokine and chemokine map of peripheral specific immune cell subsets in Parkinson's disease, *NPJ Parkinsons Dis.* **9**, 117.
395. Nguyen, L. T. N., Nguyen, H. D., Kim, Y. J., Nguyen, T. T., Lai, T. T., Lee, Y. K., Ma, H. I. & Kim, Y. E. (2022) Role of NLRP3 Inflammasome in Parkinson's Disease and Therapeutic Considerations, *J Parkinsons Dis.* **12**, 2117–2133.
396. Barczyk, M., Carracedo, S. & Gullberg, D. (2010) Integrins, *Cell Tissue Res.* **339**, 269–80.
397. Joshi, S., Naha, A., Ene, J., Holmes, C., Li, Y. & Driscoll, T. (2026) Cellular Uptake of Nanoparticles is Regulated by Integrin-Based Adhesion to the Extracellular Matrix, *ACS Appl Mater Interfaces.* **18**, 3515–3526.
398. Wang, B., Yurecko, R. S., Dedhar, S. & Cleary, P. P. (2006) Integrin-linked kinase is an essential link between integrins and uptake of bacterial pathogens by epithelial cells, *Cell Microbiol.* **8**, 257–66.
399. Josse, J., Laurent, F. & Diot, A. (2017) Staphylococcal Adhesion and Host Cell Invasion: Fibronectin-Binding and Other Mechanisms, *Front Microbiol.* **8**, 2433.
400. Chen, J., Green, J., Yurdagul, A., Jr., Albert, P., McInnis, M. C. & Orr, A. W. (2015) αvβ3 Integrins Mediate Flow-Induced NF-κB Activation, Proinflammatory Gene Expression, and Early Atherogenic Inflammation, *Am J Pathol.* **185**, 2575–89.
401. Klein, S., de Fougerolles, A. R., Blaikie, P., Khan, L., Pepe, A., Green, C. D., Koteliansky, V. & Giancotti, F. G. (2002) Alpha 5 beta 1 integrin activates an NF-kappa B-dependent program of gene expression important for angiogenesis and inflammation, *Mol Cell Biol.* **22**, 5912–22.
402. Liu, T., Zhang, L., Joo, D. & Sun, S. C. (2017) NF-κB signaling in inflammation, *Signal Transduct Target Ther.* **2**, 17023–.
403. Grando, K., Bessho, S., Harrell, K., Kyrylchuk, K., Pantoja, A. M., Olubajo, S., Albicoro, F. J., Klein-Szanto, A. & Tükel, Ç. (2024) Bacterial amyloid curli activates the host unfolded protein response via IRE1α in the presence of HLA-B27, *Gut Microbes.* **16**, 2392877.
404. Ibrahim, I. M., Abdelmalek, D. H. & Elfiky, A. A. (2019) GRP78: A cell's response to stress, *Life Sci.* **226**, 156–163.
405. Wong, Y. C., Kim, S., Peng, W. & Krainc, D. (2019) Regulation and Function of Mitochondria-Lysosome Membrane Contact Sites in Cellular Homeostasis, *Trends Cell Biol.* **29**, 500–513.
406. Chandel, N. S., Schumacker, P. T. & Arch, R. H. (2001) Reactive oxygen species are downstream products of TRAF-mediated signal transduction, *J Biol Chem.* **276**, 42728–36.
407. Stoolman, J. S., Grant, R. A., Billingham, L. K., Poor, T. A., Weinberg, S. E., Harding, M. C., Lu, Z., Miska, J., Szibor, M., Budinger, G. S. & Chandel, N. S. (2025) Mitochondria complex III-generated superoxide is essential for IL-10 secretion in macrophages, *Sci Adv.* **11**, eadu4369.
408. Ludtmann, M. H., Angelova, P. R., Ninkina, N. N., Gandhi, S., Buchman, V. L. & Abramov, A. Y. (2016) Monomeric Alpha-Synuclein Exerts a Physiological Role on Brain ATP Synthase, *J Neurosci.* **36**, 10510–10521.

409. Rostovtseva, T. K., Gurnev, P. A., Protchenko, O., Hoogerheide, D. P., Yap, T. L., Philpott, C. C., Lee, J. C. & Bezrukov, S. M. (2015) α-Synuclein Shows High Affinity Interaction with Voltage-dependent Anion Channel, Suggesting Mechanisms of Mitochondrial Regulation and Toxicity in Parkinson Disease, *J Biol Chem.* **290**, 18467–77.
410. Mingo, Y. B., Escobar Galvis, M. L. & Henderson, M. X. (2025) α-Synuclein pathology and mitochondrial dysfunction: Toxic partners in Parkinson's disease, *Neurobiol Dis.* **209**, 106889.
411. Hokenson, M. J., Uversky, V. N., Goers, J., Yamin, G., Munishkina, L. A. & Fink, A. L. (2004) Role of individual methionines in the fibrillation of methionine-oxidized alpha-synuclein, *Biochemistry.* **43**, 4621–33.
412. Dommett, R., Zilbauer, M., George, J. T. & Bajaj-Elliott, M. (2005) Innate immune defence in the human gastrointestinal tract, *Mol Immunol.* **42**, 903–12.
413. Sanz, Y., Cryan, J. F., Deschasaux-Tanguy, M., Elinav, E., Lambrecht, R. & Veiga, P. (2025) The gut microbiome connects nutrition and human health, *Nat Rev Gastroenterol Hepatol.* **22**, 534–555.
414. Leitch, E. C., Walker, A. W., Duncan, S. H., Holtrop, G. & Flint, H. J. (2007) Selective colonization of insoluble substrates by human faecal bacteria, *Environ Microbiol.* **9**, 667–79.
415. Palestrant, D., Holzknecht, Z. E., Collins, B. H., Parker, W., Miller, S. E. & Bollinger, R. R. (2004) Microbial biofilms in the gut: visualization by electron microscopy and by acridine orange staining, *Ultrastruct Pathol.* **28**, 23–7.
416. Walker, A. W., Duncan, S. H., Harmsen, H. J., Holtrop, G., Welling, G. W. & Flint, H. J. (2008) The species composition of the human intestinal microbiota differs between particle-associated and liquid phase communities, *Environ Microbiol.* **10**, 3275–83.
417. Dejea, C. M., Wick, E. C., Hechenbleikner, E. M., White, J. R., Mark Welch, J. L., Rossetti, B. J., Peterson, S. N., Snesrud, E. C., Borisy, G. G., Lazarev, M., Stein, E., Vadivelu, J., Roslani, A. C., Malik, A. A., Wanyiri, J. W., Goh, K. L., Thevambiga, I., Fu, K., Wan, F., Llosa, N., Housseau, F., Romans, K., Wu, X., McAllister, F. M., Wu, S., Vogelstein, B., Kinzler, K. W., Pardoll, D. M. & Sears, C. L. (2014) Microbiota organization is a distinct feature of proximal colorectal cancers, *Proc Natl Acad Sci U S A.* **111**, 18321–6.
418. Yang, J., Yang, Y., Ishii, M., Nagata, M., Aw, W., Obana, N., Tomita, M., Nomura, N. & Fukuda, S. (2020) Does the Gut Microbiota Modulate Host Physiology through Polymicrobial Biofilms?, *Microbes Environ.* **35**.
419. López-Siles, M., Camprubí-Font, C., Gómez Del Pulgar, E. M., Sabat Mir, M., Busquets, D., Sanz, Y. & Martinez-Medina, M. (2022) Prevalence, Abundance, and Virulence of Adherent-Invasive Escherichia coli in Ulcerative Colitis, Colorectal Cancer, and Coeliac Disease, *Front Immunol.* **13**, 748839.
420. Golińska, E., Tomusiak, A., Gosiewski, T., Więcek, G., Machul, A., Mikołajczyk, D., Bulanda, M., Heczko, P. B. & Strus, M. (2013) Virulence factors of Enterococcus strains isolated from patients with inflammatory bowel disease, *World J Gastroenterol.* **19**, 3562–72.
421. Schult-Hannemann, D., Gassner, C., Thur, N., Hennig, C., Fricke, L., Liotta, L., Weidlich, S., Matchado, M. S., Stecher, B., Arps, L., Steiger, K., Shakhtour, J., Jesinghaus, M., List, M., Janssen, K. P., Pourjam, M., Neuhaus, K., Haller, D., Schmid, R. M., Quante, M., Middelhoff, M. & Maurer, H. C. (2026) Comparison of Different Sites of Microbiota Shows Increased Pseudomonas Species in the Gut Mucosa in Inflammatory Bowel Disease, *Inflamm Bowel Dis.* **32**, 339–349.
422. Christensen, L. F. B., Jensen, K. F., Nielsen, J., Vad, B. S., Christiansen, G. & Otzen, D. E. (2019) Reducing the Amyloidogenicity of Functional Amyloid Protein FapC Increases Its Ability To Inhibit α-Synuclein Fibrillation, *ACS Omega.* **4**, 4029–4039.
423. Devos, D., Lebouvier, T., Lardeux, B., Biraud, M., Rouaud, T., Pouclet, H., Coron, E., Bruley des Varannes, S., Naveilhan, P., Nguyen, J. M., Neunlist, M. & Derkinderen, P. (2013) Colonic inflammation in Parkinson's disease, *Neurobiol Dis.* **50**, 42–8.
424. Perez-Pardo, P., Dodiya, H. B., Engen, P. A., Forsyth, C. B., Huschens, A. M., Shaikh, M., Voigt, R. M., Naqib, A., Green, S. J., Kordower, J. H., Shannon, K. M., Garssen, J., Kraneveld, A. D. & Keshavarzian, A. (2019) Role of TLR4 in the gut-brain axis in Parkinson's disease: a translational study from men to mice, *Gut.* **68**, 829–843.

425. Chen, S. J. & Lin, C. H. (2022) Gut microenvironmental changes as a potential trigger in Parkinson's disease through the gut-brain axis, *J Biomed Sci.* **29**, 54.
426. Forsyth, C. B., Shannon, K. M., Kordower, J. H., Voigt, R. M., Shaikh, M., Jaglin, J. A., Estes, J. D., Dodiya, H. B. & Keshavarzian, A. (2011) Increased intestinal permeability correlates with sigmoid mucosa alpha-synuclein staining and endotoxin exposure markers in early Parkinson's disease, *PLoS One.* **6**, e28032.
427. Qin, H. Y., Xavier Wong, H. L., Zang, K. H., Li, X. & Bian, Z. X. (2019) Enterochromaffin cell hyperplasia in the gut: Factors, mechanism and therapeutic clues, *Life Sci.* **239**, 116886.
428. Sjölund, K., Sandén, G., Håkanson, R. & Sundler, F. (1983) Endocrine cells in human intestine: an immunocytochemical study, *Gastroenterology.* **85**, 1120–30.
429. Bonbardi, M. H., Xu, M., de Leeuw, J., Slingerland, S. v. d. Z., S., Sommer, I. E. C., Harmsen, H. J. M., van Laar, T. & van Ijzendoorn, S. C. D. (2025) A human multilineage gut organoid model for Parkinson disease, *BioRxiv*.
430. Garcia-Reitboeck, P., Anichtchik, O., Dalley, J. W., Ninkina, N., Tofaris, G. K., Buchman, V. L. & Spillantini, M. G. (2013) Endogenous alpha-synuclein influences the number of dopaminergic neurons in mouse substantia nigra, *Exp Neurol.* **248**, 541–5.
431. Farhang Doost, N. & Srivastava, S. K. (2024) A Comprehensive Review of Organ-on-a-Chip Technology and Its Applications, *Biosensors (Basel).* **14**.
432. Bondurand, N. & Sham, M. H. (2013) The role of SOX10 during enteric nervous system development, *Dev Biol.* **382**, 330–43.
433. Barber, K., Studer, L. & Fattahi, F. (2019) Derivation of enteric neuron lineages from human pluripotent stem cells, *Nat Protoc.* **14**, 1261–1279.
434. Gogolou, A., Frith, T. J. R. & Tsakiridis, A. (2021) Generating Enteric Nervous System Progenitors from Human Pluripotent Stem Cells, *Curr Protoc.* **1**, e137.
435. James, C., Wu, H. F., Art, J., Patel, A. & Zeltner, N. (2025) Protocol to derive postganglionic parasympathetic neurons using human pluripotent stem cells for electrophysiological and functional assessment, *STAR Protoc.* **6**, 104001.
436. Burgelman, M., Dujardin, P., Willems, A., Hochepied, T., Van Imschoot, G., Van Wonterghem, E., Van Hoecke, L., Vandendriessche, C. & Vandenbroucke, R. E. (2024) Challenging the conventional wisdom: Re-evaluating Smpd3's role in extracellular vesicle biogenesis, *J Extracell Biol.* **3**, e70015.
437. Fatima, H., Chen, X., Li, Q., Nie, X., Xie, J. & Nie, S. (2026) Advances in extracellular vesicle research: tools and techniques, *Nanoscale Horiz*.

9. Appendix

Supplementary table 1. PCR primers list

Primer Name	Sequence (5'-3')
CsgA_1_FW	ATCTTCCCCATCGGTGATGTC
CsgA_1_RV	AACTCAGCTTCCTTTCGGGC
CsgA_2_FW	CAACGTGGCTTCGGTAACAG
CsgA_2_RV	AGTCTGGTCAACTGCAGCAC

Supplementary table 2. Primary antibodies list

Target	Host	ICC/IHC	WB	Flow	Brand	Cat ID/RRID
5-HT	Rabbit	1:250			Sigma-Aldrich	S5545/ RRID:AB_477522
6xHis tag	Rabbit		1:1,000		Proteintech	10001-0-AP/ RRID:AB_11232228
Alix	Mouse		1:1,000		Santa Cruz	sc-271975/ RRID:AB_10707811
AP2S1	Rabbit		1:1,000		Proteintech	15634-1-AP/ RRID:AB_3669216
A-SYN	Mouse	1:500	1:1,000		BD Biosciences	610787/ RRID:AB_398107
ATP5A	Mouse		1:1,000		Santa Cruz	sc-136178/ RRID:AB_2061764
Beta-actin	Mouse		1:5,000		Santa Cruz	sc-47778/ RRID:AB_626632
Calnexin	Mouse		1:200		Santa Cruz	sc-80645/ RRID:AB_1119919
CD163	Mouse	1:250			Santa Cruz	sc-20066/ RRID:AB_626933
CD45	Mouse			1:100	Biolegend	304024/ RRID:AB_493761
CD56/ NCAM	Mouse			1:100	Biolegend	362546/ RRID:AB_2565964
CD63	Rabbit		1:1,000		Proteintech	25682-1-AP/ RRID:AB_2783831
CD68	Rat	1:300			Biorad	MCA1957GA/ RRID:AB_324217
CD86	Rabbit	1:250			Bethyl	A700-030/ RRID:AB_2891831

CDX2	Rabbit	1:400			ThermoFisher	PA5-95733/ RRID:AB_2807535
ChAT	Goat	1:100			Millipore	AB144P/ RRID:AB_11212924
CHGA	Mouse	1:250			Santa Cruz	sc-393941/ RRID:AB_2801371
COX2	Mouse		1:1,000		Santa Cruz	sc-514489
COX4	Mouse		1:1,000		Santa Cruz	sc-376731/ RRID:AB_2904544
CsgA	Rabbit		1:1,000		Cusabio	CSB-PA821944XA01EOD
DYNCI12	Rabbit		1:1,000		Proteintech	12219-1-AP/ RRID:AB_2093630
FLOT1	Rabbit		1:1,000		Santa Cruz	sc-25506/ RRID:AB_2106567
GAPDH	Mouse		1:15,000		Santa Cruz	sc-47724/ RRID:AB_627678
GCase	Mouse		1:1,000		Sigma Aldrich	WM0002629M1
HA tag	Rabbit	1:100	1:1,000		Proteintech	51064-2-AP/ RRID:AB_11042321
HEXB	Mouse		1:1,000		Santa Cruz	sc-376781/ RRID:AB_2909474
HLA-DR	Mouse			1:100	Biolegend	307658/ RRID:AB_2572101
HSP60	Mouse		1:2,000		Santa Cruz	sc-271215/ RRID:AB_10607973
HSP90	Rabbit		1:1,000		Enzo LifeSciences	ADI-SPA-836/ RRID:AB_10615944
LAMP1	Rabbit		1:1,000		Proteintech	21997-1-AP/ RRID:AB_2878966
LAMP1	Mouse	5 µg/mL			DSHB	H4A3/ RRID:AB_626853
LAMP2	Mouse	5 µg/mL			DSHB	H4B4/ RRID:AB_528129
LC3B	Rabbit		1:500		Proteintech	18725-1-AP/ RRID:AB_2137745
MAP2	Chicken	1:5,000			Biolegend	822501/ RRID:AB_2564858
NDUFS3	Mouse		1:1,000		Santa Cruz	sc-374282/ RRID:AB_10991315
NDUFV1	Mouse		1:1,000		Santa Cruz	sc-100566/ RRID:AB_2282460

P62	Mouse		1:2,000		Sigma Aldrich	P0067/ RRID:AB_1841064
PARK7	Mouse		1:500		Santa Cruz	sc-55572/ RRID:AB_831639
PRPH	Rabbit	1:2,000			Invitrogen	AB1530/ RRID:AB_90725
PSMA3	Mouse		1:250		Santa Cruz	sc-166205/ RRID:AB_2253046
PSMB2	Mouse		1:250		Santa Cruz	sc-58410/ RRID:AB_785340
PSMB5	Mouse		1:250		Santa Cruz	sc-393931/ RRID:AB_2800553
RAB27A	Rabbit		1:1,000		Proteintech	17817-1-AP/ RRID:AB_2176728
SOD1	Mouse		1:5,000		Santa Cruz	sc-17767/ RRID:AB_628301
SYP1	Rabbit	1:500			Cell Signalling Technology	36406/ RRID:AB_2799098
TLR2	Rabbit		1:1,000		Cell Signalling Technology	12276S/ RRID:AB_2797867
TUJ1	Mouse	1:1,000			Biolegend	801202/ RRID:AB_2313773
VDAC	Mouse		1:5,000		Santa Cruz	sc-390996/ RRID:AB_2750920
Vimentin	Mouse		1:2,000		BD Biosciences	550513/ RRID:AB_393716
VPS26A	Rabbit		1:1,000		Proteintech	12804-1-AP/ RRID:AB_2215033

Supplementary table 3. Secondary antibodies list

Target	**Host**	**ICC/IHC**	**WB**	**Brand**	**Cat ID/RRID**
Anti-Rabbit IgG, HRP-linked Antibody	Goat		1:5,000	Cell Signalling Technology	7074/ RRID:AB_2099233
Anti-Mouse IgG, HRP-linked Antibody	Goat		1:5,000	Cell Signalling Technology	7076/ RRID:AB_330924
IRDye 800CW anti-Rabbit IgG	Goat		1:5,000	LI-COR	926-32211/ RRID:AB_621843
IRDye 680RD Anti-Mouse IgG	Goat		1:5,000	LI-COR	926-68070/

					RRID:AB_10956588
Anti-Mouse IgG (H+L) Cross-Adsorbed Secondary Antibody, Alexa Fluor™ 488	Goat	1:1,000		ThermoFisher	A-11001/ RRID:AB_2534069
Anti-Mouse IgG (H+L) Cross-Adsorbed Secondary Antibody, Alexa Fluor™ 568	Goat	1:1,000		ThermoFisher	A11004/ RRID:AB_2534072
Anti-Rabbit IgG (H+L) Cross-Adsorbed Secondary Antibody, Alexa Fluor™ 488	Goat	1:1,000		ThermoFisher	A11008/ RRID:AB_143165
Anti-Rabbit IgG (H+L) Secondary Antibody, Alexa Fluor™ 568	Goat	1:1,000		ThermoFisher	A-11011/ RRID:AB_143157
Anti-Chicken IgY (H+L) Cross-Adsorbed Secondary Antibody, Alexa Fluor™ 647	Goat	1:1,000		ThermoFisher	A32933/ RRID:AB_2762845
Anti-Goat IgG (H+L) Cross-Adsorbed Secondary Antibody, Alexa Fluor™ 488	Donkey	1:1,000		ThermoFisher	A-11055/ RRID:AB_2534102

Supplementary table 4. qPCR primers list

Primer Name	**Sequence (5'-3')**
SNCA_FW	GGAGTGGCCATTCGACGAC
SNCA_FW	CCTGCTGCTTCTGCCACAC
ACTB_FW	TGACCCAGATCATGTTTGAGA
ACTB_RV	AGTCCATCACGATGCCAGT
HSP90AA1_FW	TCTGCCTCTGGTGATGAGATGG
HSP90AA1_RV	CGTTCCACAAAGGCTGAGTTAGC
HSP90AB1_FW	CTCTGTCAGAGTATGTTTCTCGC
HSP90AB1_RV	GTTTCCGCACTCGCTCCACAAA
PAX3_FW	AGCTCGGCGGTGTTTTTATCA
PAX3_RV	CTGCACAGGATCTTGGAGACG

HOXB3_FW	CCAGTGCCACTAGCAACAG
HOXB3_RV	CGTTTGCCTCGACTCTTTCATC
HOXB4_FW	CGTGAGCACGGTAAACCCC
HOXB4_RV	CGAGCGGATCTTGGTGTTG
HOXB5_FW	AACTCCTTCTCGGGGCGTTAT
HOXB5_RV	CATCCCATTGTAATTGTAGCCGT
SOX10_FW	CCTCACAGATCGCCTACACC
SOX10_RV	CATATAGGAGAAGGCCGAGTAGA
ASCL1_FW	CCCAAGCAAGTCAAGCGACA
ASCL1_RV	AAGCCGCTGAAGTTGAGCC
EDNRB_FW	GCAAACCGCAGAGATAATGACG
EDNRB_RV	GGACACAACCGTGTTGATGTATT
PHOX2B_FW	AACCCGATAAGGACCACTTTTG
PHOX2B_RV	AGAGTTTGTAAGGAACTGCGG

Supplementary table 5. Reagents lists (alphabetical order)

Reagent	**Company**	**Catalogue #**
2% Uranyl Acetate	Electron Microscope Scienes	Cat #22400-2
5x Colorless Reaction Buffer	Promega	Cat #M792A
Accutase	Stem Cell Technologies	Cat #07920
Advanced DMEM/F12	Fisher Scientific	Cat #12634010
Agar	Sigma-Aldrich	Cat #05040-250G
Agarose (low electroendoosmosis)	Sigma Aldrich	Cat #1168020250
Aluminium ammonium sulfate dodecahydrate	Merck Millipore	Cat #1010310500
Ampicillin	Carl Roth	Cat #K029.2
Anti-HA Magnetic Beads	ThermoFisher	Cat #88837
Ascorbic Acid	Sigma-Aldrich	Cat #A8960-5G
B-27 without vitamin A supplement	ThermoFisher	Cat #12587010
Bafilomycin A1	Invivogen	Cat #tlrl-baf1
BDNF	ThermoFisher	Cat #450-02-500ug
BigDye Terminator v3.1 Cycle Sequencing Kit	ThermoFisher	Cat #4337456
b-mercaptoethanol	Sigma-Aldrich	Cat #M3148-100ML
BMP4	Proteintech	Cat #HZ-1045
Bovine Serum Albumin (BSA)	Fisher Scientific	Cat #10053863
Casamino Acids	ThermoFisher	Cat #223050
CellLight Early Endosomes-GFP, BacMam 2.0	ThermoFisher	Cat #C10586
CHIR99021	Sigma-Aldrich	Cat #SML1046-5MG
Chloroquine	Invivogen	Cat #tlrl-chq-4
Congo Red	Sigma-Aldrich	Cat #C6277-25G

Coomassie Brilliant Blue G 250	Sigma-Aldrich	Cat #1.15444
DAPI	Sigma Aldrich	Cat #D9542-10MG
dibutyryl-cAMP (dbcAMP)	MedChem Express	Cat #HY-B0764
Dimethylsulfoxide (DMSO)	Sigma-Aldrich	Cat #276855-1L
Di-potassium hydrogen phosphate	Carl Roth	Cat #T875.1
DNase I	Sigma-Aldrich	Cat #10109169001
dNTPs 100 mM	ThermoFisher	Cat #R0182
Dulbecco's Modified Eagle Medium (DMEM)	Gibco	Cat #41965039
Ethanol	VWR	Cat #437435L
Ethylenediaminetetraacetic acid (EDTA)	Sigma-Aldrich	Cat #E6758-100G
Fetal Bovine Serum (FBS)	ThermoFisher	Cat #A5256801
Fluorescence Mounting Medium (DAKO)	Agilent Technologies	Cat #S302380-2
GDNF	ThermoFisher	Cat #450-10-500ug
Gentamycin sulphate	Carl Roth	Cat #0233.3
GlutaMAX Supplement	Gibco	Cat #35050038
Glycerol	Sigma-Aldrich	Cat #G5516-100ML
Glycine	Sigma Aldrich	Cat #1.00590.0001
GoTaq DNA Polymerase	Promega	Cat #M3005
Guanidine Hydrochloride	Sigma-Aldrich	Cat #50950-2.5KG
HEPES	Sigma-Aldrich	Cat #H3784-25G
Hydrochloric Acid (HCl)	Sigma-Aldrich	Cat #1.00317.1011
IFNg	ImmunoTools	Cat #11343536
IL-3	Immunotools	Cat #11340035
Imidazole	Sigma-Aldrich	Cat #I5513-25G
Isopropyl-β-D-thiogalactopyranoside (IPTG)	Fisher Scientific	Cat #10397642
Laemmli SDS sample buffer, reducing (6X)	Fisher Scientific	Cat #15493939
Laminin	R&D Systems	Cat #3400-010-03
Lipopolysaccharide (LPS)	Invivogen	Cat #tlrl-3pelps
Luria-Bertani broth (LB) medium powder	Carl Roth	Cat #X964.2
LysoTracker Blue DND-22	ThermoFisher	Cat #L7525
Lysozyme	Sigma-Aldrich	Cat #L6876-1G
Magnesium Chloride	Sigma-Aldrich	Cat #8147330100
Matrigel	Dutscher	Cat #354230
M-CSF	Proteintech	Cat #HZ-1192
Micro BCA Protein Assay Kit	ThernoFisher	Cat #23235
Midori Green Advance	Dutscher	Cat #523268
mTeSR Plus	Stem Cell Technologies	Cat #100-0276
N-2 supplement	Fisher Scientific	Cat #17502048
NaCl	Sigma Aldrich	Cat #S9625-5KG
Neurobasal	Fisher Scientific	Cat #21103049
Normal Goat Serum	ThermoFisher	Cat #50062Z
Paraformaldehyde, 4%	ThermoFisher	Cat #J61899.AP
Penicillin / Streptomycin	ThermoFisher	Cat #15140122
Phenylmethylsulfonyl fluoride (PMSF)	Sigma-Aldrich	Cat #P7626
Phorbol 12-myristate 13-acetate	Sigma-Aldrich	Cat #P8139-5MG
Phosphate Buffered Saline (PBS)	ThermoFisher	Cat #10010023
Phosphoric Acid, 85%	Sigma-Aldrich	Cat #345245-100ML
Pierce BCA Protein Assay Kit	Fisher Scientific	Cat #23225
Pierce Protease and Phosphatase Inhibitor	Fisher Scientific	Cat #A32959
Polybrene	Sigma-Aldrich	Cat #TR-1003-G

Potassium Chloride	Carl Roth	Cat #P017.1
Potassium phosphate monobasic	Sigma-Aldrich	Cat #P5379-500G
Purmorphamine	Merck Millipore	Cat #540220-5MG
Puromycin	Invivogen	Cat #ant-pr-1
RNase A	Sigma-Aldrich	Cat #10109169001
RPMI	Sigma Aldrich	Cat #R0883-6X500ML
SCF	ImmunoTools	Cat #11343325
SignalFire Elite ECL Reagent	Cell Signalling Technology	Cat #12757S
Skimmed milk	Dutscher	Cat #711160
Sodium Chloride	Sigma-Aldrich	Cat #S9625-5KG
Sodium dodecyl sulfate (SDS)	Carl Roth	Cat #CN30.3
Sodium Fluoride (NaF)	Sigma-Aldrich	Cat #201154-5G
Sodium Hydroxide (NaOH)	Sigma-Aldrich	Cat #S5881-500G
Sodium orthovanadate (Na3VO4)	Sigma-Aldrich	Cat #450243-10G
Sytox Blue	ThermoFisher	Cat #S34857
Thioflavin T (ThT)	Sigma-Aldrich	Cat #T3516
Tris-HCl	Sigma-Aldrich	Cat #T3253-1KG
Triton X	Carl Roth	Cat #3051.4
Trypan Blue Solution	Sigma Aldrich	Cat #T8154-100ML
Tryptone	Fisher Scientific	Cat #16279751
Tween 20	Sigma-Aldrich	Cat #P9416-100ML
VEGF	ImmunoTools	Cat #11343665
Wheat Germ Agglutinin Alexa Fluor 488	ThermoFisher	Cat #W11261
X-Vivo 15	Lonza	Cat #02-060Q
Y-27632	Selleck Chemicals	Cat #S1049
Yeast Extract	Fisher Scientific	Cat #16279781
ZombieNIR Fixable Viability Kit	Biolegend	Cat #423106

Plasmid and oligonucleotide sequences

>pET-CsgA-WT-6xHis

CsgA-WT-6xHis

TTCTTGAAGACGAAAGGGCCTCGTGATACGCCTATTTTTATAGGTTAATGTCATGATAATAATGGTTTCTTAGACGTC
AGGTGGCACTTTTCGGGGAAATGTGCGCGGAACCCCTATTTGTTTATTTTTCTAAATACATTCAAATATGTATCCGC
TCATGAGACAATAACCCTGATAAATGCTTCAATAATATTGAAAAAGGAAGAGTATGAGTATTCAACATTTCCGTGTCG
CCCTTATTCCCTTTTTTGCGGCATTTTGCCTTCCTGTTTTTGCTCACCCAGAAACGCTGGTGAAAGTAAAAGATGC
TGAAGATCAGTTGGGTGCACGAGTGGGTTACATCGAACTGGATCTCAACAGCGGTAAGATCCTTGAGAGTTTTCG
CCCCGAAGAACGTTTTCCAATGATGAGCACTTTTAAAGTTCTGCTATGTGGCGCGGTATTATCCCGTGTTGACGCC
GGGCAAGAGCAACTCGGTCGCCGCATACACTATTCTCAGAATGACTTGGTTGAGTACTCACCAGTCACAGAAAAG
CATCTTACGGATGGCATGACAGTAAGAGAATTATGCAGTGCTGCCATAACCATGAGTGATAACACTGCGGCCAACT
TACTTCTGACAACGATCGGAGGACCGAAGGAGCTAACCGCTTTTTTGCACAACATGGGGGATCATGTAACTCGCC
TTGATCGTTGGGAACCGGAGCTGAATGAAGCCATACCAAACGACGAGCGTGACACCACGATGCCTGCAGCAATG
GCAACAACGTTGCGCAAACTATTAACTGGCGAACTACTTACTCTAGCTTCCCGGCAACAATTAATAGACTGGATGG
AGGCGGATAAAGTTGCAGGACCACTTCTGCGCTCGGCCCTTCCGGCTGGCTGGTTTATTGCTGATAAATCTGGAG
CCGGTGAGCGTGGGTCTCGCGGTATCATTGCAGCACTGGGGCCAGATGGTAAGCCCTCCCGTATCGTAGTTATCT
ACACGACGGGGAGTCAGGCAACTATGGATGAACGAAATAGACAGATCGCTGAGATAGGTGCCTCACTGATTAAGC
ATTGGTAACTGTCAGACCAAGTTTACTCATATATACTTTAGATTGATTTAAAACTTCATTTTTAATTTAAAAGGATCTAG
GTGAAGATCCTTTTTGATAATCTCATGACCAAAATCCCTTAACGTGAGTTTTCGTTCCACTGAGCGTCAGACCCCG
TAGAAAAGATCAAAGGATCTTCTTGAGATCCTTTTTTTCTGCGCGTAATCTGCTGCTTGCAAACAAAAAAACCACC
GCTACCAGCGGTGGTTTGTTTGCCGGATCAAGAGCTACCAACTCTTTTTCCGAAGGTAACTGGCTTCAGCAGAGC
GCAGATACCAAATACTGTCCTTCTAGTGTAGCCGTAGTTAGGCCACCACTTCAAGAACTCTGTAGCACCGCCTACA
TACCTCGCTCTGCTAATCCTGTTACCAGTGGCTGCTGCCAGTGGCGATAAGTCGTGTCTTACCGGGTTGGACTCA

AGACGATAGTTACCGGATAAGGCGCAGCGGTCGGGCTGAACGGGGGGTTCGTGCACACAGCCCAGCTTGGAGC
GAACGACCTACACCGAACTGAGATACCTACAGCGTGAGCTATGAGAAAGCGCCACGCTTCCCGAAGGGAGAAAG
GCGGACAGGTATCCGGTAAGCGGCAGGGTCGGAACAGGAGAGCGCACGAGGGAGCTTCCAGGGGGAAACGCC
TGGTATCTTTATAGTCCTGTCGGGTTTCGCCACCTCTGACTTGAGCGTCGATTTTTGTGATGCTCGTCAGGGGGG
CGGAGCCTATGGAAAAACGCCAGCAACGCGGCCTTTTTACGGTTCCTGGCCTTTTGCTGGCCTTTTGCTCACATG
TTCTTTCCTGCGTTATCCCCTGATTCTGTGGATAACCGTATTACCGCCTTTGAGTGAGCTGATACCGCTCGCCGCA
GCCGAACGACCGAGCGCAGCGAGTCAGTGAGCGAGGAAGCGGAAGAGCGCCTGATGCGGTATTTTCTCCTTAC
GCATCTGTGCGGTATTTCACACCGCATATATGGTGCACTCTCAGTACAATCTGCTCTGATGCCGCATAGTTAAGCC
AGTATACACTCCGCTATCGCTACGTGACTGGGTCATGGCTGCGCCCCGACACCCGCCAACACCCGCTGACGCGC
CCTGACGGGCTTGTCTGCTCCCGGCATCCGCTTACAGACAAGCTGTGACCGTCTCCGGGAGCTGCATGTGTCAG
AGGTTTTCACCGTCATCACCGAAACGCGCGAGGCAGCTGCGGTAAAGCTCATCAGCGTGGTCGTGAAGCGATTC
ACAGATGTCTGCCTGTTCATCCGCGTCCAGCTCGTTGAGTTTCTCCAGAAGCGTTAATGTCTGGCTTCTGATAAAG
CGGGCCATGTTAAGGGCGGTTTTTTCCTGTTTGGTCACTGATGCCTCCGTGTAAGGGGGATTTCTGTTCATGGGG
GTAATGATACCGATGAAACGAGAGAGGATGCTCACGATACGGGTTACTGATGATGAACATGCCCGGTTACTGGAA
CGTTGTGAGGGTAAACAACTGGCGGTATGGATGCGGCGGGACCAGAGAAAAATCACTCAGGGTCAATGCCAGCG
CTTCGTTAATACAGATGTAGGTGTTCCACAGGGTAGCCAGCAGCATCCTGCGATGCAGATCCGGAACATAATGGT
GCAGGGCGCTGACTTCCGCGTTTCCAGACTTTACGAAACACGGAAACCGAAGACCATTCATGTTGTTGCTCAGG
TCGCAGACGTTTTGCAGCAGCAGTCGCTTCACGTTCGCTCGCGTATCGGTGATTCATTCTGCTAACCAGTAAGGC
AACCCCGCCAGCCTAGCCGGGTCCTCAACGACAGGAGCACGATCATGCGCACCCGTGGCCAGGACCCAACGCT
GCCCGAGATGCGCCGCGTGCGGCTGCTGGAGATGGCGGACGCGATGGATATGTTCTGCCAAGGGTTGGTTTGC
GCATTCACAGTTCTCCGCAAGAATTGATTGGCTCCAATTCTTGGAGTGGTGAATCCGTTAGCGAGGTGCCGCCGG
CTTCCATTCAGGTCGAGGTGGCCCGGCTCCATGCACCGCGACGCAACGCGGGGAGGCAGACAAGGTATAGGGC
GGCGCCTACAATCCATGCCAACCCGTTCCATGTGCTCGCCGAGGCGGCATAAATCGCCGTGACGATCAGCGGTC
CAGTGATCGAAGTTAGGCTGGTAAGAGCCGCGAGCGATCCTTGAAGCTGTCCCTGATGGTCGTCATCTACCTGC
CTGGACAGCATGGCCTGCAACGCGGGCATCCCGATGCCGCCGGAAGCGAGAAGAATCATAATGGGGAAGGCCA
TCCAGCCTCGCGTCGCGAACGCCAGCAAGACGTAGCCCAGCGCGTCGGCCGCCATGCCGGCGATAATGGCCTG
CTTCTCGCCGAAACGTTTGGTGGCGGGACCAGTGACGAAGGCTTGAGCGAGGGCGTGCAAGATTCCGAATACC
GCAAGCGACAGGCCGATCATCGTCGCGCTCCAGCGAAAGCGGTCCTCGCCGAAAATGACCCAGAGCGCTGCCG
GCACCTGTCCTACGAGTTGCATGATAAAGAAGACAGTCATAAGTGCGGCGACGATAGTCATGCCCCGCGCCCAC
CGGAAGGAGCTGACTGGGTTGAAGGCTCTCAAGGGCATCGGTCGAGATCCCGGTGCCTAATGAGTGAGCTAACT
TACATTAATTGCGTTGCGCTCACTGCCCGCTTTCCAGTCGGGAAACCTGTCGTGCCAGCTGCATTAATGAATCGG
CCAACGCGCGGGGAGAGGCGGTTTGCGTATTGGGCGCCAGGGTGGTTTTTCTTTTCACCAGTGAGACGGGCAA
CAGCTGATTGCCCTTCACCGCCTGGCCCTGAGAGAGTTGCAGCAAGCGGTCCACGCTGGTTTGCCCCAGCAGG
CGAAAATCCTGTTTGATGGTGGTTAACGGCGGGATATAACATGAGCTGTCTTCGGTATCGTCGTATCCCACTACCG
AGATATCCGCACCAACGCGCAGCCCGGACTCGGTAATGGCGCGCATTGCGCCCAGCGCCATCTGATCGTTGGCA
ACCAGCATCGCAGTGGGAACGATGCCCTCATTCAGCATTTGCATGGTTTGTTGAAAACCGGACATGGCACTCCAG
TCGCCTTCCCGTTCCGCTATCGGCTGAATTTGATTGCGAGTGAGATATTTATGCCAGCCAGCCAGACGCAGACGC
GCCGAGACAGAACTTAATGGGCCCGCTAACAGCGCGATTTGCTGGTGACCCAATGCGACCAGATGCTCCACGCC
CAGTCGCGTACCGTCTTCATGGGAGAAAATAATACTGTTGATGGGTGTCTGGTCAGAGACATCAAGAAATAACGCC
GGAACATTAGTGCAGGCAGCTTCCACAGCAATGGCATCCTGGTCATCCAGCGGATAGTTAATGATCAGCCCACTG
ACGCGTTGCGCGAGAAGATTGTGCACCGCCGCTTTACAGGCTTCGACGCCGCTTCGTTCTACCATCGACACCAC
CACGCTGGCACCCAGTTGATCGGCGCGAGATTTAATCGCCGCGACAATTTGCGACGGCGCGTGCAGGGCCAGA
CTGGAGGTGGCAACGCCAATCAGCAACGACTGTTTGCCCGCCAGTTGTTGTGCCACGCGGTTGGGAATGTAATT
CAGCTCCGCCATCGCCGCTTCCACTTTTTCCCGCGTTTTCGCAGAAACGTGGCTGGCCTGGTTCACCACGCGGG
AAACGGTCTGATAAGAGACACCGGCATACTCTGCGACATCGTATAACGTTACTGGTTTCACATTCACCACCCTGAA
TTGACTCTCTTCCGGGCGCTATCATGCCATACCGCGAAAGGTTTTGCGCCATTCGATGGTGTCCGGGATCTCGAC
GCTCTCCCTTATGCGACTCCTGCATTAGGAAGCAGCCCAGTAGTAGGTTGAGGCCGTTGAGCACCGCCGCCGCA
AGGAATGGTGCATGCAAGGAGATGGCGCCCAACAGTCCCCCGGCCACGGGGCCTGCCACCATACCCACGCCGA
AACAAGCGCTCATGAGCCCGAAGTGGCGAGCCCGATCTTCCCCATCGGTGATGTCGGCGATATAGGCGCCAGCA
ACCGCACCTGTGGCGCCGGTGATGCCGGCCACGATGCGTCCGGCGTAGAGGATCGAGATCTCGATCCCGCGAA
ATTAATACGACTCACTATAGGGGAATTGTGAGCGGATAACAATTCCCC*TCTAGA*AATAATTTTGTTTAACTTTAAGAA
GGAGATATACCATGGGTGTTGTTCCTCAGTACGGCGGCGGCGGTAACCACGGTGGTGGCGGTAATAATAGCGGC
CCAAATTCTGAGCTGAACATTTACCAGTACGGTGGCGGTAACTCTGCACTTGCTCTGCAAACTGATGCCCGTAACT
CTGACTTGACTATTACCCAGCATGGCGGCGGTAATGGTGCAGATGTTGGTCAGGGCTCAGATGACAGCTCAATCG
ATCTGACCCAACGTGGCTTCGGTAACAGCGCTACTCTTGATCAGTGGAACGGCAAAAATTCTGAAATGACGGTTA
AACAGTTCGGTGGTGGCAACGGTGCTGCAGTTGACCAGACTGCATCTAACTCCTCCGTCAACGTGACTCAGGTT
GGCTTTGGTAACAACGCGACCGCTCATCAGTACCATCACCATCACCATCACTAAGGATCCGGCTGCTAACAAAGC
CCGAAAGGAAGCTGAGTTGGCTGCTGCCACCGCTGAGCAATAACTAGCATAACCCCTTGGGGCCTCTAAACGGG
TCTTGAGGGGTTTTTTGCTGAAAGGAGGAACTATATCCGGATATCCCGCAAGAGGCCCGGCAGTACCGGCATAAC
CAAGCCTATGCCTACAGCATCCAGGGTGACGGTGCCGAGGATGACGATGAGCGCATTGTTAGATTTCATACACGG

TGCCTGACTGCGTTAGCAATTTAACTGTGATAAACTACCGCATTAAAGCTTATCGATGATAAGCTGTCAAACATGAG
AA

>CsgA-R12343-6xHis_oligonucleotide

R3 sequence

ATGCACCCATGGGTGTTGTTCCTCAGTACGGCGGCGGCGGTAACCACGGTGGTGGCGGTAATAATAGCGGCCCA
AATTCTGAGCTGAACATTTACCAGTACGGTGGCGGTAACTCTGCACTTGCTCTGCAAACTGATGCCCGTAACTCTG
ACTTGACTATTACCCAGCATGGCGGCGGTAATGGTGCAGATGTTGGTCAGGGCTCAGATGACAGCTCAATCGATC
TGACCCAACGTGGCTTCGGTAACAGCGCTACTCTTGATCAGTGGAACGGCAAAAATTCTGAAATGACGGTTAAAC
AGTTCGGTGGTGGCAACGGTGCTGCAGTTGACCAGACTGCATCTAACAGTTCGATTGACCTAACGCAGAGAGGT
TTCGGAAATTCTGCAACTCTTGACCAATGGAATGGCAAGAATCATCACCATCACCATCACTAAGGATCCATGCAC

10. Acknowledgements

I would like to first thank Michela for the opportunity to do my PhD in this interesting and ever-evolving field. I would like to also thank everyone that I met during my stay in Tübingen and Paris and helped me develop both professionally and individually.

I am grateful to my colleagues for all the discussions and support they provided me. Particularly, it was a pleasure to work together with Malvina as she greatly supported me with the work, organisation, and the French language. I would like to thank Anouk, the first student I supervised, that was always motivated and engaged in evolving the project and she was always positive and optimistic which helped brighten the environment. I would also like to thank Hariam who helped me optimize the iPSC differentiation and microfluidics seeding protocols.

Next, I would like to thank my friends, both those who are still around, always make me smile and enjoy my cakes, as well as those who continued their career in different places with whom I will cherish the moments spent together and look forward to seeing them again in the future.

Finally, I am grateful to my family, it is always a pleasure to see all of them when I travel back to Greece. Especially, I would like to thank my parents which continue to support me during our weekly online meetings and help me keep the fluency of my mother tongue.